Final Dissertation for the Degree Of Philosophiae Doctor in Astronomy, Astrophysics and Space Science

EXPLORING INFLATION WITH COSMIC MICROWAVE BACKGROUND AND GRAVITATIONAL WAVES

Supervisors
Prof. Nicola Vittorio
University of Rome Tor Vergata

Prof. Sabino Matarrese
University of Padova

PhD Candidate
Giacomo Galloni

Student ID
1947388

Academic Year MMXX-MMXXIII (XXXVI cycle)

Exploring Inflation with Cosmic Microwave Background and Gravitational Waves
Final Dissertation for the Degree Of Philosophiae Doctor in Astronomy, Astrophysics and Space Science
Università di Roma "Tor Vergata", Università di Roma "La Sapienza", Istituto Nazionale di Astrofisica - INAF

Author's email: giacomo.galloni@roma2.infn.it

We'll ride the spiral to the end
and may just go where no one's been

— Maynard James Keenan - TOOL

ABSTRACT

The exploration of primordial Gravitational Waves (GWs) stands as a pivotal force in modern Cosmology, providing a unique window into the mechanisms at the birth of the Universe. Particularly, in the early moments of the cosmos, we hypothesize an extreme accelerated expansion, known as *inflation*. One of its main predictions is a primordial background of GWs, which have propagated almost undisturbed to our present time. Due to their nature, these GWs retain information about their production mechanism, enabling us to investigate inflation by observing them or their indirect imprints on various aspects of the Universe, as the Cosmic Microwave Background (CMB) polarization. In this Thesis, we leverage GWs and their relics to address two key questions: Does the standard cosmological model sufficiently explain our observations? What is known about these primordial GWs with current data?

Before delving into these questions, Part I describes a Universe devoid of GWs, characterized by an inflationary period with only scalar perturbations. The *hot Big-Bang* model and its thermal history are explained through the concept of thermal decoupling (see Chap. 2). After addressing some inconsistencies in this model in Chap. 3, we turn our attention to the inflationary model in Chap. 4 as a solution to these issues. In this context, we explore two key components: the physics of scalar perturbations and the CMB, which serves as a cornerstone in contemporary Cosmology.

This initial part lays the groundwork for highlighting the imprints of GWs in Part II, where tensor perturbations are introduced into the inflationary paradigm. In Chap. 5, we explore predictions for single-field slow-roll inflation and beyond. Additionally, we present a comprehensive computation of the Boltzmann equations for GWs, yielding key observable quantities related to the Cosmological Gravitational Wave Background (CGWB) (see Chap. 6). For example, the observation of CMB B-mode polarization offers invaluable information on inflation, as it is directly linked to the presence of primordial GWs.

At this juncture of the manuscript, we possess a holistic view of the Universe with both scalar and tensor perturbations, enabling us to address the first question mentioned earlier. In Part III, we challenge aspects such as the cosmological principle, which advocates the homogeneity and isotropy of the Universe. The CMB reveals signatures of a departure from statistical isotropy, manifested in the form of the *hemispherical power asymmetry* (see Chap. 7). This feature suggests a preferred direction in the sky, prompting an investigation of the role of GWs in understanding its physical origin in Chap. 8 and Chap. 9. Another intriguing aspect of the CMB is the lack-of-correlation anomaly observed in its two-point angular correlation. It seems that this correlation is almost null on scales larger than 60°, in contrast to

what we would expect from our current understanding. Chap. 10 discusses the possibility of detecting a similar characteristic in the CGWB.

In Part IV, the focus shifts to data analysis in pursuit of answering the second question. Bayesian and frequentist statistics are introduced in Chap. 11 and Chap. 12, emphasizing two well-known techniques in Cosmology: Markov-Chain Monte-Carlo (MCMC) and Profile Likelihood (PL). Subsequently, Chap. 13 delves into the Bayesian perspective on the tensor sector of parameter space, considering different prior choices and assumptions. This analysis highlights the strengths and weaknesses of MCMC, prompting a frequentist test on the same datasets in Chap. 14 using the PL. By the end of these chapters, the current status of the search for primordial GWs from the perspectives of CMB and GW interferometers' observations becomes clear.

Although these chapters may not fully answer our driving questions due to their broad and ambitious nature, they underscore my contribution to the field. The original results obtained during this Philosophiae Doctor (PhD) degree include theoretical predictions for the CGWB, accounting for CMB anomalies, statistical tools for simulating and estimating the significance of the lack-of-correlation, novel forecasts on the CGWB, and a comprehensive and statistically sound analysis of CMB B-mode data using both Bayesian and frequentist tools, alongside direct GW observations.

Not covered in this Thesis is the research within the Lite (Light) satellite for the studies of B-mode polarization and Inflation from cosmic background Radiation Detection (LiteBIRD) collaboration. LiteBIRD represents a significant future venture for exploring CMB B-mode polarization, providing a unique opportunity to inspect its largest scales, being a space-based mission. As an active member of different working groups, my contributions encompass forecasts on LiteBIRD's capability to distinguish different inflationary models, forecasts on the science achievable through cross-correlating LiteBIRD with galaxy surveys, validation tests on simulations, likelihood analysis, and parameter estimation in various contexts.

CONTENTS

LIST OF FIGURES

ACRONYMS

ABS Atacama B-Mode Search

ACTPol Atacama Cosmology Telescope Polarimeter

AGWB Astrophysical Gravitational Wave Background

BAO Barionic Acoustic Oscillation

BBN Big Bang Nucleosynthesis

BBO Big Bang Observer

BH Black Hole

BICEP Background Imaging of Cosmic Extragalactic Polarization

CDM Cold Dark Matter

CE Cosmic Explorer

CGWB Cosmological Gravitational Wave Background

CL Confidence Level

CLASS Cosmic Linear Anisotropy Solving System

CMB Cosmic Microwave Background

CNB Cosmic Neutrinos Background

COBE COsmic Background Explorer

CPU Central Processing Unit

CS Cut-Sky

CV Cosmic Variance

DASI Degree Angular Scale Interferometer

DECIGO DECi-hertz Interferometer Gravitational wave Observatory

DOF Degree Of Freedom

EFT Effective Field Theory

EM Electro-Magnetic

EOM Equation Of Motion

ET Einstein Telescope

EW Electro-Weak

FC Feldman-Cousins

FLRW Friedmann-Lemâitre-Robertson-Walker

FS Full-Sky

FWHM Full Width Half Maximum

GR General Relativity

GUT Grand Unified Theory

GW Gravitational Wave

HFI High-Frequency Instrument

H-Z Harrison-Zel'dovich

HiLLiPoP High ℓ Likelihood for Polarized Planck

ISW Integrated Sachs-Wolfe

JCV Joint Cosmic Variance

KAGRA Kamioka Gravitational Wave Detector

K-G Klein-Gordon

ΛCDM Λ Cold Dark Matter

LFI Low-Frequency Instrument

LHS Left Hand Side

LIGO Laser Interferometer Gravitational-Wave Observatory

LISA Laser Interferometer Space Antenna

LiteBIRD Lite (Light) satellite for the studies of B-mode polarization and Inflation from cosmic background Radiation Detection

LoLLiPoP Low ℓ Likelihood for Polarized Planck

LSS Last Scattering Surface

LVK Laser Interferometer Gravitational-Wave Observatory (LIGO)-Virgo-Kamioka Gravitational Wave Detector (KAGRA)

MCMC Markov-Chain Monte-Carlo

NANOGrav North American Nanohertz Observatory for Gravitational Waves

PD Percentage Displacement

PDF Probability Density Function

PDG Particle Data Group

PhD Philosophiae Doctor

PL Profile Likelihood

POLARBEAR POLARization of the Background Radiation

PR3 *Planck* Release 3

PR4 *Planck* Release 4

PT Phase Transition

PTA Pulsar Timing Array

QCD Quantum Chromo-Dynamics

QUaD QUIET at DASI

QUIET Q and U Extragalactic Sub-mm Telescope

RHS Right Hand Side

RS Rees-Sciama

SBF Spherical Bessel Function

SED Spectral Energy Distribution

SGWB Stochastic Gravitational Wave Background

SH Spherical Harmonic

SPTpol South Pole Telescope polarimeter

SSA Single-Scale Approach

SW Sachs-Wolfe

TSA Two-Scales Approach

TT Transverse-Traceless

WMAP Wilkinson Microwave Anisotropy Probe

Part I

A "SCALAR" UNIVERSE

In this part of the Thesis, we will explore essential aspects of modern Cosmology. Specifically, we will present the hot Big-Bang model along with its limitations, which led to the introduction of an inflationary phase in the Universe, a concept we will also elucidate. Throughout this exploration, we will consider a "scalar" Universe, devoid of Gravitational Waves (GWs), and shed light on the intricacies of primordial quantum fluctuations during the early stages of the Universe. This approach enables us to scrutinize the observable quantities measured today, providing insights into the physics underlying the birth of our Universe.

1 BASICS OF COSMOLOGY

In this chapter, we will cover fundamental concepts that are crucial for a better grasp of the subsequent discussions. The focal points include the Einstein field equations and the Friedmann-Lemâitre-Robertson-Walker (FLRW) metric.
The primary references for this chapter are [1–4], serving as valuable starting points for a more in-depth exploration of these topics.

1.1 EINSTEIN'S EQUATIONS AND FLRW METRIC

The famous Einstein's equations read [1]

$$G_{\mu\nu} \equiv R_{\mu\nu} - \frac{1}{2} R g_{\mu\nu} = 8\pi G T_{\mu\nu} \tag{1}$$

where: $R^{\lambda}_{\sigma\mu\nu} \equiv \partial_\mu \Gamma^{\lambda}_{\sigma\nu} - \partial_\nu \Gamma^{\lambda}_{\sigma\mu} + \Gamma^{\lambda}_{\mu\rho}\Gamma^{\rho}_{\nu\sigma} - \Gamma^{\lambda}_{\nu\rho}\Gamma^{\rho}_{\mu\sigma}$ is the Riemann tensor;

$R_{\mu\nu}$ = Ricci tensor, defined as the contraction of the first and third indexes of the Riemann one;

R = is the Ricci scalar, defined as the full contraption of the Ricci tensor;

$\Gamma^{\mu}_{\nu\lambda} \equiv \frac{1}{2} g^{\mu\rho}\left(\frac{\partial g_{\rho\nu}}{\partial x^\lambda} + \frac{\partial g_{\rho\lambda}}{\partial x^\nu} - \frac{\partial g_{\nu\lambda}}{\partial x^\rho}\right)$ are the Christoffel symbols;

$g_{\mu\nu}$ = metric tensor;

G = gravitational constant;

$T_{\mu\nu}$ = stress-energy tensor.

Eq. 1 can be derived from the variation w. r. t. the metric of the total action $S_{TOT} = S_{HE} + S_m$ [5, 6], where

$$S_{HE} \equiv \int d^4x \sqrt{-g} \frac{R}{16\pi G} \tag{2}$$

is the Hilbert-Einstein action that accounts for gravity, in which g is the determinant of the metric tensor, while

$$S_m = \int d^4x \sqrt{-g} \mathscr{L}_m \tag{3}$$

is the action associated to all the other particles (scalar fields, fermions, gauge bosons, ...), where $\mathscr{L}_m$ indicates their Lagrangian density. In particular, from the variation $\frac{\delta S_{HE}}{\delta g^{\mu\nu}}$ one derives the geometric Left Hand Side (LHS)

of Eq. 1 while the stress-energy tensor $T_{\mu\nu}$ on the Right Hand Side (RHS) is defined as [6]

$$T_{\mu\nu} \equiv -\frac{2}{\sqrt{-g}}\frac{\delta S_m}{\delta g^{\mu\nu}} \,. \tag{4}$$

This tensor can be computed in two ways:

- if one focuses on the global properties of the Universe and treats its content as a perfect fluid, this leads to the very well-known form (true for a generic reference frame) [1]

$$T_{\mu\nu} = u_\mu u_\nu(\rho + P) + P g_{\mu\nu} \,,^2 \tag{5}$$

  where: ρ = energy density;
  P = isotropic pressure;
  u_μ = 4-velocity of the fluid in its reference frame.

- One can also study this tensor accounting for every field contribution to the action. Of course, this road requires a very detailed theory on the content of the Universe.

There are two other important relations that must be taken into account every time that Einstein's equations enter the game; these are the Bianchi identity $\nabla_\mu G^{\mu\nu} = 0$ and the continuity equation $\nabla_\mu T^{\mu\nu} = 0$ (∇ here indicates the covariant derivative), which indeed are consequences of one another, given the Einstein equations. Eq. 1 can be used to find a metric that satisfies some symmetries. Indeed, looking for a metric that describes an expanding Universe with curvature κ while being symmetric under rotation and spatial translation (isotropic and homogeneous)[3], we find the FLRW metric [2]

$$ds^2 = -c^2dt^2 + a^2(t)\left[\frac{dr^2}{1-\kappa r^2} + r^2 d\Omega^2\right] \,, \tag{6}$$

where: t = cosmic time, whereas the time coordinate of an observer comoving with the cosmic fluid;
r = radial coordinate;
$a(t)$ = scale factor, which spans the expansion of the Universe;
$d\Omega^2 = d\theta^2 + sin^2\theta d\phi^2$ is the infinitesimal solid angle;
κ = curvature, which can be either positive (closed Universe), null (flat Universe), or negative (open Universe)[4].

2 Actually a fluid can be characterized also by some form of anisotropies, as viscosity or thermal conductivity; these effects can be taken into account adding to the previous $T_{\mu\nu}$ an appropriate tensor $\Pi_{\mu\nu}$ (see for example the discussion in Sec. 5.2). Since here we only want to briefly summarize some fundamental tools and concepts, from now on we will use a perfect fluid, unless otherwise stated.

3 We do not ask for the time translation invariance because we want a Universe able to change throughout time.

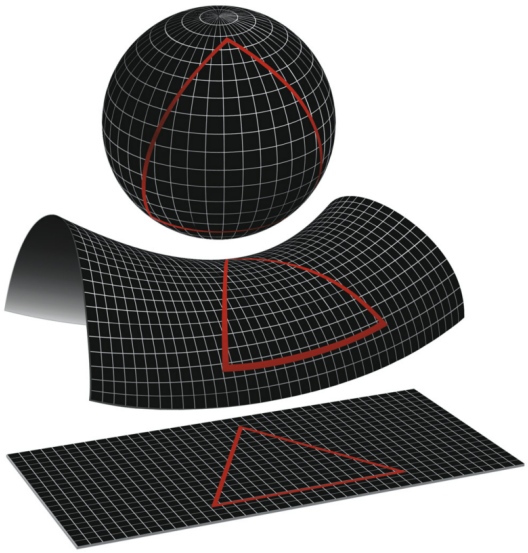

Figure 1: Different geometries encoded in the FLRW metric. Figure taken from [http://wmap.gsfc.nasa.gov/media/990006/990006_2048.jpg].

Usually, one parametrizes κ as

$$\kappa = \begin{cases} -1 & \text{open} \\ 0 & \text{flat} \\ +1 & \text{close} \end{cases} . \tag{7}$$

It is important to underline that the set (r, θ, ϕ) is made of comoving coordinates, i. e. they do not depend on the evolution and remain constant, so that, once they are multiplied by the scale factor, the physical coordinates are recovered[5]. From the symmetry properties of Eq. 6, it can be found the very easy form for the stress-energy tensor [3]

$$T_{\mu\nu} = \text{diag}[\rho(t), P(t), P(t), P(t)], \tag{9}$$

where $\rho(t)$ and $P(t)$ are respectively the energy density and the isotropic pressure of the fluid, which do not depend on $\vec{x}$ because of isotropy and homogeneity [6]. We emphasize that this description of the topology of the Universe is just the most simple description of a universe where the cos-

4 One can show that these three cases represent respectively the geometry of a sphere, a plane and an hyperboloid. It is intuitive that in all these cases, the "landscape" around a specific point is completely isotropic and remains the same while changing the considered point, hence they indeed are isotropic and homogeneous.

5 Considering the comoving coordinates, one can show that the coordinate separation between two points remain constant in time. Then the spatial splices of the metric in parentheses are rescaled by the scale factor, so that for any distance λ, it holds

$$\lambda_{physical}(t) = a(t) \cdot \lambda_{comoving} . \tag{8}$$

6 In this Thesis, 3-vectors will be indicated with a $\rightarrow$, whereas the same quantity without this symbol will indicate its modulus.

mological principle[7] is valid and is characterized by a curvature parameter. However, one could consider less trivial topologies, which would carry sizable differences to the characteristics of the Universe. Suppose, for example, that we consider a flat Universe with some periodic boundary conditions; this means that the Universe would have the topology of a 3D torus, which means that if the torus is not too large, we should be able to observe the same galaxy in multiple directions in the sky [7]. Another typical feature of these models are the so-called *circles-in-the-sky*, which should appear in our Cosmic Microwave Background (CMB) sky (see Chap. 2 and Chap. 4 for a description of the CMB) [8, 9]. For more details on this topic, see, for example, [10–12].

Furthermore, one could even consider some models where the cosmological principle is not valid. For example, spacetimes that are homogeneous but non-isotropic are called *Bianchi* models. These are classified into a total of 11 classes: 9 characterized by a single Lie algebra and 2 by a continuous family of Lie algebras in the real 3-dimensional space [13, 14]. The associated Lie group will then constitute the symmetry group on the manifold. E. g. the Bianchi I universe has different scale factors in the three spatial directions, meaning that they expand independently:

$$ds^2 = -dt^2 + a^2dx^2 + b^2dy^2 + c^2dz^2 \, . \tag{10}$$

On the other hand, one could consider strongly inhomogeneous space-times as *Szekeres spacetime* and *Lemaitre-Tolman-Boldi spacetime* [15].

Despite this, in this Thesis we will work in the assumptions of FLRW.

1.2 FRIEDMANN EQUATIONS

The dynamics of the expanding Universe can be explicitly seen by unfolding Einstein's equations.

$$R_{\mu\nu} - \frac{1}{2}g_{\mu\nu}R + \Lambda g_{\mu\nu} = 8\pi G T_{\mu\nu} \, , \tag{11}$$

where, w. r. t. Eq. 1, we have added, for the sake of completeness Λ, the cosmological constant. Initially introduced by Einstein to obtain a static Universe (supposedly Einstein's "biggest blunder" [16]), this quantity is now at the center of modern Cosmology as it explains phenomenologically the accelerated expansion we observe around us.

We have already seen what the main actors are appearing in Eq. 11 while discussing Eq. 1, thus, one can find the Friedmann equations by explicitly

7 On sufficiently large scales, all observers see the same Universe around them. This implies isotropy and homogeneity.

writing the $_{00}$ and $_{ij}$ components of the Einstein equations and by exploiting the conservation laws $\nabla_\mu T^{\mu\nu} = 0$. Hence, one can find

$$H^2 + \frac{\kappa}{a^2} = \frac{8\pi G}{3}\rho + \frac{\Lambda}{3} \,, \tag{12}$$

$$\frac{\ddot{a}}{a} = -\frac{4\pi G}{3}(\rho + 3P) + \frac{\Lambda}{3} \,, \tag{13}$$

$$\dot{\rho} + 3H(\rho + P) = 0 \,, \tag{14}$$

where: $\cdot \;=\;$ derivative w. r. t. cosmic time t;
$H \equiv\;$ $\frac{\dot{a}}{a}$ is the Hubble rate.

These equations are in fact dependent on each other through the Bianchi identities, so that only two of them are independent [1]. Once again, we emphasize that the simplicity of these equations is given by the cosmological principle. For example, if we consider a non-isotropic Universe, we would obtain more complex equations with extra parameters. E. g. considering a Bianchi I Universe [14, 17] one would obtain the results of Emir Gümrükçüo, Contaldi, and Peloso [18].

To close the system, one needs an additional relation linking $P(t)$ and $\rho(t)$, named the equation of state $P(\rho)$. The simplest choice is

$$P = \omega\rho \quad \text{with} \quad \omega = \text{constant} \,, \tag{15}$$

where ω depend on the energy content considered

$$\omega = \begin{cases} 0 & \text{dust or pressureless matter} \\ \frac{1}{3} & \text{radiation} \\ -1 & \Lambda \end{cases} \,. \tag{16}$$

Solving this system of equations, one finds the explicit expression of the scale factor $a(t)$, which in FLRW has the usual solution with a singularity back in time

$$a(t) = a_* \left(\frac{t}{t^*}\right)^{\frac{2}{3(\omega+1)}} \,, \tag{17}$$

where $_*$ indicates a reference scale[8].
For what regards ρ:

$$\rho = \rho_* \left(\frac{a}{a_*}\right)^{-3(1+\omega)} \quad \Rightarrow \quad \rho \propto \begin{cases} a^{-3} & \omega = 0 \\ a^{-4} & \omega = \frac{1}{3} \\ \text{constant} & \omega = -1 \end{cases} . \tag{18}$$

These dependency can be intuitively derived if one thinks at how energy gets diluted with the expansion of the Universe: in the case of pressureless matter (e.g. a bunch of protons), the energy density will scale as volume^{-1}, so a^{-3}, since the number of particles in that volume will not change; for radiation, the energy gets an extra a^{-1} factor because the wave length of radiation will also be diluted by expansion; finally Λ is by definition a constant, so even if the Universe expands, its value will not change.

All these relations and definitions can be written in function of conformal time η exploiting the transformation $dt = a(\eta)d\eta$ in order to obtain a metric in which $a(\eta)$ factorizes in front of all terms[9].

1.3 COSMOLOGICAL HORIZON

What is the maximum distance from which we have received a light signal during the whole life of the Universe t? This quantity is called the cosmological horizon and represents the radius of the region of causal connection centered on us

$$d_H(t) \equiv a(t) \int_0^t \frac{cdt'}{a(t')} . \tag{19}$$

It is related to its comoving counterpart

$$l \equiv \int_0^t \frac{cdt'}{a(t')} , \tag{20}$$

called comoving distance[10]. This horizon is similar to the event horizon of a Black Hole (BH), but it is a past horizon, instead of a future one. Also, if

8 From this relation one can appreciate the fact that only ratios of scale factors are physical, assuming a spatially flat Universe. In fact, the coordinate can always be rescaled by a constant without any physical consequence.
In the case of $\kappa \neq 0$ the normalization of $a(t)$ becomes physical, since in the Friedmann equations, specifically in Eq. 12, the term $\propto \kappa$ cannot be rescaled freely.

9 For any generic function of cosmic time $f(t)$ hold

$$\dot{f}(t) = \frac{f'(\eta)}{a(\eta)} , \qquad \ddot{f}(t) = \frac{f''(\eta)}{a^2(\eta)} - \mathcal{H}\frac{f'(\eta)}{a^2(\eta)} ,$$

where the prime refers to the derivative w. r. t. conformal time. The Hubble rate in cosmic time H is then named $\mathcal{H} \equiv \frac{a'}{a}$ in conformal one.

10 This quantity also represents the physical interpretation of conformal time, given that $d\eta = dt/a$.

$d_H(t)$ exists and its finite, it is called particle horizon. In particular in a FLRW Universe, $d_H(t)$ is finite if $\omega > -1/3$, in fact [19]

$$d_H(t) = \frac{3(1+\omega)ct}{1+3\omega} \simeq ct \simeq \frac{1}{H(t)} \,, \tag{21}$$

and

$$d_H(t) = \begin{cases} 3ct & \omega = 0 \\ 2ct & \omega = 1/3 \\ \infty & \omega = -1/3 \end{cases} \,. \tag{22}$$

Furthermore, exploiting the Friedman equations, one can find that $d_H(t)$ is finite iff $\ddot{a}(t) < 0$, so iff the acceleration of the Universe is negative.

1.4 HUBBLE RADIUS

The Hubble radius is defined as [3]

$$R_C(t) \equiv \frac{c}{H(t)} = c\tau_H \,, \tag{23}$$

where τ_H is Hubble time defined as the inverse of the Hubble rate $H(t)$, representing the characteristic time of expansion[11].

Making explicit the expression of H, we can find the relation between R_C and d_H

$$R_C(t) = \frac{3}{2}(1+\omega)ct = \frac{1+3\omega}{2} d_H(t) \,, \tag{24}$$

which in standard FLRW means $R_C(t) \sim d_H(t)$. However, they have a significant physical difference: if d_H accounts for the causal connection over the whole history of the Universe, R_C only accounts for the connection over one Hubble time.
Also R_C has its comoving counterpart called comoving Hubble radius r_H, defined as

$$r_H(t) \equiv \frac{R_C(t)}{a(t)} = \frac{1}{\dot{a}(t)} \,, \tag{25}$$

which is related to the comoving particle horizon through

$$\frac{d_H(t)}{a(t)} = \int_0^t \frac{cdt'}{a(t')} = \int_0^a \frac{cda'}{a'\dot{a}'} = \int_0^a \frac{cda'}{a'} r_H(t) \,. \tag{26}$$

11 One can show that for every τ_H passing by, the scale factor doubles.

2

HOT BIG-BANG MODEL

The Hot Big-Bang model stems from a straightforward concept: by observing the current expansion of the Universe, we can infer that, when running the cosmic clock backward, the Universe was once smaller and denser (i.e., hotter). This apparently simple idea unfolds into various predictions and implications for our understanding of the cosmos.
In conjunction with Einstein's equations, the Boltzmann equations play a pivotal role in characterizing the evolution of such a Universe.
In the subsequent sections, we will dive into these equations, introducing fundamental concepts such as thermal equilibrium (or departure from equilibrium) of different particle species. These concepts are instrumental in depicting the thermal history of the Universe.
As in the preceding chapter, refer to [1–4], and the references therein for more comprehensive details.

2.1 THERMALIZATION

Before we discuss the characteristics of the Big-Bang model, we introduce the key concept of thermalization. Indeed, we know that the Universe today is expanding, and thus we can imagine that going back in time all the elements present today were closer w. r. t. now. Give enough time, and we can also think of a very hot and very dense primordial soup containing only elementary particles. At this point, we may ask ourselves: are these particle species in thermal equilibrium or not?

A very general (and pretty rough) rule to check whether a given species i is decoupled from the thermal bath is to compare the interaction rate Γ_i and the expansion rate H: if $\Gamma_i \gg H$ i-particles are coupled with the plasma, meaning that, at a given time t, the species i interacts more frequently with the-rest-of-the-world w. r. t. how the universe is expanding, in some sense separating apart the actors of the interaction[12], otherwise it is decoupled.

The interaction rate is strictly related to the total cross section σ through the relation $\Gamma = n\langle\sigma v\rangle$, where n is the number density of the target particles and v is a properly averaged relative velocity.

12 In this context the coupling implies that the i-particles can maintain, or establish, a thermodynamic equilibrium with the plasma. In fact, we now that $T \propto a^{-1}$ and so

$$\frac{\dot{T}}{T} = -H \,,$$

thus if the particles are in equilibrium, they have to be able to follow the change in temperature of the plasma through interactions.

Focusing on $2 \leftrightarrow 2$ scatterings of relativistic particles ($v \sim 1$), we can recognize two main cases:

A. for processes mediated by massless gauge boson (e. g. by the photon γ), on can find that the cross-section goes as

$$\sigma \simeq \frac{\alpha^2}{T^2} \tag{27}$$

where $\alpha = \frac{g^2}{4\pi}$ is the fine structure constant for that particular theory and g is the gauge coupling strength. Assuming to deal with relativistic particles we can also write $\Gamma \simeq T^3\sigma$, thus we can deduce that particles whose interactions are mediated by a massless boson are decoupled when

$$\begin{aligned} \Gamma &\ll H \\ T^3\frac{\alpha^2}{T^2} &\ll \frac{T^2}{M_P} \\ T &\gg \alpha^2 M_P \, . \end{aligned} \tag{28}$$

B. For processes mediated by massive bosons (e.g $W^{\pm}$, Z boson in weak interaction), we can write instead

$$\sigma \simeq G_x^2 T^2 = \frac{\alpha^2}{M_x^4} T^2 \, , \tag{29}$$

where M_x is the mass of the particle involved. Repeating the same argument as before, we find that the decoupling condition is

$$T \ll G_x^{-2/3} M_P^{-1/3} \, . \tag{30}$$

At the end of the day, these prescriptions give us a simple way of understanding what happens when Γ and H are very different from each other ($\Gamma \ll H$ or $\Gamma \gg H$), but how does i behave at decoupling?

2.2 BOLTZMANN EQUATIONS

Boltzmann equations represent a fundamental tool in studying the evolution of the number density of a given species i, particularly in the case of the transition from thermal equilibrium to decoupling, i. e. $\Gamma_i \simeq H$.

The general and compact form is as follows:

$$\mathscr{L}[f(x^\mu, p^\mu)] = \mathscr{C}[f(x^\mu, p^\mu)] \, , \tag{31}$$

where:

- $\mathscr{L}$ is the Liouville operator providing the evolution of the distribution function. In fact, in General Relativity (GR), it can be written as

$$\mathscr{L} \equiv \frac{\mathrm{d}}{\mathrm{d}\lambda} = p^\alpha \frac{\partial}{\partial x^\alpha} - \Gamma^\alpha{}_{\beta\gamma} p^\beta p^\gamma \frac{\partial}{\partial p^\alpha} \,, \tag{32}$$

  where $\Gamma^\alpha_{\beta\gamma}$ are the Christoffel symbols associated with the metric considered.

- $\mathscr{C}$ is the collision operator that accounts for any scattering. For a generic process involving a particle σ that interacts with other $\alpha = a, b, \ldots$ particles to produce $\beta = 1, 2, \ldots$ particles, it can be written as [4]

$$\begin{aligned}\mathscr{C}[f_\sigma] = -\int \prod_{\alpha=a,b,\ldots} \prod_{\beta=1,2,\ldots} & d\Pi_\alpha d\Pi_\beta (2\pi)^4 \\ & \times \delta^{(4)}\left(p_\sigma + p_a + p_b + \ldots - p_1 - p_2 - \ldots\right) \\ & \times \Big[|M|_{\sigma+a+b+\ldots\to 1+2+\ldots} f_\sigma f_a f_b \ldots (1 \pm f_1)(1 \pm f_2)\ldots \\ & - |M|^2_{1+2+\ldots\to\sigma+a+b+\ldots} f_1 f_2 \ldots (1 \pm f_\sigma)(1 \pm f_1)(1 \pm f_2)\ldots \Big] \,,\end{aligned} \tag{33}$$

  where: $d\Pi_\alpha \equiv g_\alpha \frac{d^3 p_\alpha}{(2\pi)^3 2E_\alpha}$;
  g_α = intrinsic degrees of freedom of the species;
  E_α = energy of the species;
  $\delta^{(4)} \to$ assures the conservation of momentum through the process;
  $|M|$ = amplitudes of the processes involved;
  f_α = distribution functions;
  $(1 \pm f_\alpha) \to$ accounts for the nature of the particles, either bosonic $(+)$ or fermionic $(-)$.

In the fully relativistic case, f depends on the full 4-vectors x^a and p^a, leading to a Liouville operator of the form

$$\begin{aligned}\mathscr{L}[f(x^a, p^a)] = \frac{dx^a}{d\lambda}\frac{\partial f}{\partial x^a} + \frac{dp^a}{d\lambda}\frac{\partial f}{\partial p^a} = \frac{dx^a}{d\lambda}\frac{\partial f}{\partial x^a} - \Gamma^a_{bc} p^b p^c \frac{\partial f}{\partial p^a} = \\ = \left(p^a \frac{\partial}{\partial x^a} - \Gamma^a_{bc} p^b p^c \frac{\partial}{\partial p^a}\right) f \,,\end{aligned} \tag{34}$$

where the indexes a, b, c run from 0 to 3, λ is the affine parameter which parametrizes the trajectory of a given particle and $p^a = \frac{dx^a}{d\lambda}$ is its the 4-

momentum such that $g^{ab}p_a p_b = p^2 = -m^2$ [13]. Moreover, in the second equality, we used the geodesics equation

$$\frac{dp^a}{d\lambda} + \Gamma^a_{bc} p^b p^c = 0 \,, \tag{35}$$

where Γ^a_{bc} is the Christoffel symbol (or affine connection), which reads

$$\Gamma^a_{bc} = \frac{1}{2} g^{ad} \left(\frac{\partial g_{db}}{\partial x^c} + \frac{\partial g_{dc}}{\partial x^b} - \frac{\partial g_{bc}}{\partial x^d} \right) \quad [14] \,. \tag{36}$$

From now on, obviously, we will focus on the relativistic expression for $\mathscr{L}$, implementing a FLRW metric. In this context, the dependence of the distribution function f on x^a and p^a greatly simplifies, taking advantage of the homogeneity and isotropy of the system. It turns out to depend only on the time t and the modulus of the 4-momentum p, or alternatively on the whole energy. This clearly makes the expression for the Liouville operator easier: indeed a lot of derivatives vanish, and the surviving Christoffel symbols are only a few:

$$\Gamma^0_{ij} = a\dot{a}\delta_{ij} \quad ; \quad \Gamma^i_{0j} = \Gamma^i_{j0} = \delta^i_j \frac{\dot{a}}{a} \,. \tag{37}$$

This leads to the following expression for $\mathscr{L}$

$$\begin{aligned} \mathscr{L}[f(t,p)] &= E\frac{\partial f}{\partial t} - \Gamma^0_{ij} p^i p^j \frac{\partial f}{\partial E} = E\frac{\partial f}{\partial t} - H\delta_{ij} p^i p^j a^2 \frac{\partial f}{\partial E} \\ &= E\frac{\partial f}{\partial t} - Hp^2 \frac{\partial f}{\partial E} \end{aligned} \tag{38}$$

and to this temporary form of the Boltzmann equation

$$E\frac{\partial f}{\partial t} - Hp^2 \frac{\partial f}{\partial E} = \mathscr{C}[f(t,p)] \,. \tag{39}$$

Note that p is the proper momentum, i. e. such that it is the contraction of the physical momentum $p \propto 1/a$ and $E = \sqrt{p^2 + m^2}$, while p_i and p_j are the components of the comoving one.

However, we can manipulate this relation in order to recast the LHS in a more convenient form. Multiplying both sides for the factor $\frac{g}{(2\pi)^3}$, dividing for the energy E and integrating in d^3p, Eq. 39 becomes

$$\frac{g}{(2\pi)^3} \int d^3p \frac{\partial f}{\partial t} - \frac{g}{(2\pi)^3} \int d^3p H \frac{p^2}{E} \frac{\partial f}{\partial E} = \frac{g}{(2\pi)^3} \int \frac{d^3p}{E} \mathscr{C}[f(t,p)] \,. \tag{40}$$

13 If $\mathscr{C}[f] = 0$, one obtains the Liouville theorem saying that the distribution function in phase-space is conserved.

This operations start to seem useful once we realize that the two terms in the LHS recall something similar to the definition of the number density: indeed the first piece can be immediately rewritten as

$$\frac{\partial}{\partial t}\frac{g}{(2\pi)^3}\int d^3p f(t,p) = \dot{n}(t)\ , \tag{41}$$

while the second one requires a little bit of work. Indeed, using $E^2 = m^2 + p^2 \Rightarrow EdE = pdp \Rightarrow dE = \frac{p}{E}dp$ it becomes

$$\begin{aligned}
&\frac{g}{(2\pi)^3}\int d^3p H\frac{p^2}{E}\frac{\partial f}{\partial E} = \frac{g}{(2\pi)^3}H\int dp\frac{p^4}{E}\frac{\partial f}{\partial E}\int d\Omega = \\
&= \frac{g}{(2\pi)^3}H\int dp p^3\frac{\partial f}{\partial p}\int d\Omega \\
&= \frac{g}{(2\pi)^3}H\left(\left[p^3 f\right]_0^\infty - 3\int dp p^2 f\right)\int d\Omega\ .
\end{aligned} \tag{42}$$

The term in the square brackets is null since it vanishes in $p = 0$, but also for $p \to \infty$ due to the properties of the distribution function (it tends to zero quite rapidly, so that the term goes to zero before p becomes too big). This leaves the expression

$$-3H\frac{g}{(2\pi)^3}\int dp p^2 f\int d\Omega, \tag{43}$$

which is nothing else that $-3Hn(t)$. Now the Boltzmann equations read

$$\dot{n(t)} + 3Hn(t) = \frac{g}{(2\pi)^3}\int\frac{d^3p}{E}\mathscr{C}[f(t,p)] \tag{44}$$

and we immediately realize that if $\mathscr{C} = 0$, i. e. the particle do not interact in any way, than the RHS vanishes and this equation tell us that the number density depletes as $n(t) \propto a^{-3}(t)$ only due to the expansion of the universe, as we expect. As aforementioned, this is nothing else that the Liouville theorem.

Now, let us implement the collisions and try to see how Eq. 44 changes; for simplicity we will focus on scattering processes of the kind $1 + 2 \leftrightarrow 3 + 4$, i. e. that involve four different particle species, and suppose that we want to control how the number density of the species 1 evolves in time[15]. The previous equation now becomes

$$\dot{n_1} + 3Hn_1 = \frac{g_1}{(2\pi)^3}\int\frac{d^3p_1}{E_1}\mathscr{C}[f_1] \tag{45}$$

15 This is a particular case, but it is easily generalizable to any kind of process, including decays. This will be done in the next section, where we will analyze how the number density of a particle X changes taking into account its decays and scatterings with other Degree Of Freedom (DOF)

where the RHS's explicit expression is

$$\int d\Pi_1 d\Pi_2 d\Pi_3 d\Pi_4 (2\pi)^4 \delta(p_1 + p_2 - p_3 - p_4) \times \\ \times \left[|M_{3+4\to 1+2}|^2 f_3 f_4 (1 \pm f_1)(1 \pm f_2) - |M_{1+2\to 3+4}|^2 f_1 f_2 (1 \pm f_3)(1 \pm f_4) \right]. \tag{46}$$

Here $d\Pi_i$ is the phase-space factor for the particle species $i \in [1, 4]$ and the two amplitudes $M_{3+4\to 1+2}$ and $M_{1+2\to 3+4}$, respectively, for processes that create and destroy species 1 (which explains the two signs $+$ and $-$), are in principle different.

The terms of the kind $1 \pm f_i$, instead, are the *Bose enhancement factor* $(+)$ and the *Pauli blocking term* $(-)$; they simply describe the tendency of the production of species i to be favored if it is a boson or to be "slowed down" if it is a fermion. Naively, we can think of the latter effect as a consequence of the Pauli exclusion principle: since we cannot have two fermions with the same quantum numbers in a system, as long as they are produced, they must gain higher and higher energies, making their production more and more difficult. This is no more valid in the case of a boson; indeed, there is an enhancement instead of a suppression.

The RHS of Eq. 46 is quite complicated to solve being an integral-differential equation, so we will now make some simplifications:

- the two amplitudes squared $|M_{3+4\to 1+2}|^2$ and $|M_{1+2\to 3+4}|^2$ will be taken as equal, i. e. we suppose time invariance;
- we suppose that all the particles are in kinetic equilibrium due to the efficiency of the scattering processes. This allows us to use the Bose-Einstein and Fermi-Dirac distributions.

  $$f_{\substack{FD \\ BE}} = \frac{1}{e^{\frac{E-\mu}{T}} \pm 1}. \tag{47}$$

  n is related to $\mu(t, \vec{x})$ through an integral and, in the case of chemical equilibrium, μ regulates the fluxes of particles during the interactions, being the chemical potential;
- when we assume both kinetic and chemical equilibria, it results in having local thermodynamic equilibrium in which we can assume $\mu_i = 0$[16];

16 Heuristically speaking, since the chemical potential represents the energy required to add a particle i to a population of such particles, one can argue that to be in thermodynamic equilibrium means that from a generic interaction between $j, \bar{j}$ one can easily produce i particles (e. g. if $T \gg m_i$, $2\gamma \to i + \bar{i}$ will occur efficiently). For this reason even if the chemical potentials are not null, they surely are negligible.

- we will neglect both the *Bose enhancement factor* and the *Pauli blocking term* supposing that $E - \mu > T$. Indeed, in this limit, the distribution function becomes

$$f \simeq e^{\frac{\mu}{T}} e^{-\frac{E}{T}} = e^{\frac{\mu}{T}} f_{eq} \tag{48}$$

  and we completely lose the dependence on the nature of the particle (fermionic or bosonic).

At this point, Eq. 46 simplifies a lot and becomes [17]

$$\int d\Pi_1 d\Pi_2 d\Pi_3 d\Pi_4 (2\pi)^4 \delta(p_1 + p_2 - p_3 - p_4)(f_3 f_4 - f_1 f_2)|M|^2 \,. \tag{49}$$

Now let us focus on the term $(f_3 f_4 - f_1 f_2)$; exploiting the second assumption and the condition of energy conservation $E_1 + E_2 = E_3 + E_4$, it can be written also as

$$e^{-\frac{E_1+E_2}{T}} \left(e^{\frac{\mu_3}{T}} e^{\frac{\mu_4}{T}} - e^{\frac{\mu_1}{T}} e^{\frac{\mu_2}{T}} \right) \,, \tag{50}$$

which is nothing else that

$$e^{-\frac{E_1+E_2}{T}} \left(\frac{n_3(t) n_4(t)}{n_3^{eq}(t) n_4^{eq}(t)} - \frac{n_1(t) n_2(t)}{n_1^{eq}(t) n_2^{eq}(t)} \right) . \tag{51}$$

This cannot be so obvious, so let us see why Eq. 50 and Eq. 51 are the same. It follows from the definition of number density:

$$n(t) = \frac{g}{(2\pi)^3} \int d^3 p f = e^{\frac{\mu}{T}} \frac{g}{(2\pi)^3} \int d^3 p f_{eq} = e^{\frac{\mu}{T}} n_{eq}(t) \,, \tag{52}$$

where the explicit expressions for the number density at the equilibrium are

$$n_{eq}(t) = \begin{cases} g \left(\frac{mT}{2\pi} \right)^{3/2} e^{-\frac{m}{T}} & m \gg T \\ \frac{g}{\pi^2} T^3 & m \ll T \end{cases} . \tag{53}$$

17 In order to make a realistic theoretical prediction, one should proceed more carefully without making such a huge amount of assumptions: all the effects must be taken into account and the Boltzmann equations become solvable only numerically. However, for our purposes, this is not necessary because making these approximations permits us to proceed analytically while understanding the underlying physics.

Finally, putting together Eq. 45, Eq. 46, Eq. 49 and Eq. 51, we find the general form

$$\dot{n_1}(t) + 3Hn_1(t) = \int d\Pi_1 d\Pi_2 d\Pi_3 d\Pi_4 (2\pi)^4 \delta(p_1 + p_2 - p_3 - p_4) \times \\ \times |M|^2 \left(\frac{n_3(t) n_4(t)}{n_3^{eq}(t) n_4^{eq}(t)} - \frac{n_1(t) n_2(t)}{n_1^{eq}(t) n_2^{eq}(t)} \right) e^{-\frac{E_1+E_2}{T}} \tag{54}$$

which, once recognized that almost all the RHS correspond to the formal definition of thermally averaged cross section, can be finally put in the handy form

$$\dot{n_1}(t) + 3Hn_1(t) = n_1^{eq} n_2^{eq} \langle \sigma v \rangle \left[\frac{n_3(t) n_4(t)}{n_3^{eq}(t) n_4^{eq}(t)} - \frac{n_1(t) n_2(t)}{n_1^{eq}(t) n_2^{eq}(t)} \right] , \tag{55}$$

with

$$\langle \sigma v \rangle = \frac{1}{n_1^{eq} n_2^{eq}} \int d\Pi_1 d\Pi_2 d\Pi_3 d\Pi_4 (2\pi)^4 \delta(p_1 + p_2 - p_3 - p_4) |M|^2 e^{-\frac{E_1+E_2}{T}} . \tag{56}$$

These two equations represent the evolution of the particle number density as a function of the expansion of the Universe and its temperature, which determine the coupling of the particle studied.

With this representation, we can meticulously track the evolution of any given particle. For instance, a particle denoted as ψ might have been in thermal equilibrium with the primordial plasma during the Universe's hot phase, subsequently decoupled at a specific time, and continued evolving up to the present day. Naturally, variations arise depending on the specific particle in question and its interactions. If one were to repeat this process for each particle, it would yield a system of coupled differential equations dictating the evolution of the particle content of the Universe.

2.3 THERMAL HISTORY OF THE UNIVERSE

As the Universe undergoes expansion, the temperature of the thermal bath decreases, initiating various phenomena. In the hot Big-Bang model, we can trace this decline in temperature to outline the thermal history of the Universe, capturing key events along the way.

SINGULARITY: Following the contraction of the Universe back in time to its extreme consequences, in the hot Big-Bang model everything stems from a singularity with infinite density and temperature. This represents our starting point; however, we cannot describe it with current knowledge. Apart from the inherent "unnatural" infinities that this singularity implies, we would need at least a theory of quantum gravity.

This remains the case if we consider any event happening from this point up to Planck time, i. e. the smallest unit of time we can think of, when the Universe had a temperature of about 10^{19} GeV.

ELECTRO-WEAK PHASE TRANSITION: When the Universe cooled to 150 GeV, the Higgs mechanism gives mass to fermions, while the Electro-Weak (EW) force separates into the Electro-Magnetic (EM) and the weak ones triggering a Phase Transition (PT).

QUANTUM CHROMO-DYNAMICS PHASE TRANSITION: Quarks and gluons cannot remain separated anymore on-setting the Quantum Chromo-Dynamics (QCD) PT when the temperature drops below 150 MeV. As a consequence, hadrons are formed. Despite what one may expect, more matter is produced w. r. t. to antimatter. *Baryogenesis*, the mechanism behind this asymmetry, is still unknown.

NEUTRINOS DECOUPLING: Neutrinos decouple from thermal equilibrium while being relativistic at $T = 1$ MeV. As a consequence, they evolve quite independently from the rest of the thermal bath and generate a Cosmic Neutrinos Background (CNB), which has not been observed yet.

BIG BANG NUCLEOSYNTHESIS: Light elements (up to lithium) are formed at Big Bang Nucleosynthesis (BBN) when $T \sim 100$ keV. This represents one of the main predictions (and successes) of the tot Big-Bang model. In fact, there is a very good agreement between its predictions and the measured abundance of these light elements [20].

RECOMBINATION: Photons are decoupled as a consequence of the formation of neutral hydrogen. Photons start to free-stream to us, generating the CMB (see Sec. 4.5 for more details). This is another fundamental prediction of the hot Big-Bang model proven by observation [21–23]. At this time, the Universe has a temperature of ~ 0.3 eV. Before this moment, the Universe was opaque to light; thus, this represents the last moment in time that we can directly inspect with photons.

DARK AGES: After recombination, the Universe is mainly populated by clouds of hydrogen, which are essentially the only source of light. This epoch is still relatively unexplored and represents one of the future challenges of cosmology, exploiting the 21 cm emission line of hydrogen [24].

REIONIZATION: Structures start to form, giving birth to the first stars and galaxies. Thus, more and more gas is reionized. This means that CMB photons can interact again with matter. Furthermore, the presence of matter distributions modifies the geodesics of photons, bending their trajectories. The epoch of large-scale structures is very prolific of information on our Universe: e. g. the presence of Cold Dark Matter (CDM) and its features, the full nonlinear regime of its evolution, all the physics of galaxy clustering, and many other physical phenomena

that go down from cosmological scales to the physics of our solar system (for example, [25–28]).

3

SHORTCOMINGS OF HOT BIG-BANG MODEL

Even though in Chap. 2 we saw that the hot Big-Bang Model has successfully described a broad range of phenomena characterizing our Universe, it is flawed by the existence of the so-called "shortcomings". They are not intrinsic problems of the model, but still, they are inconsistencies in the form of strangely precise requirements on the initial conditions, in order to obtain what we observe today.
In this chapter, we will present these issues and we will introduce their solution by adding an extra ingredient to our recipe of the Universe: a period of accelerated expansion in early times, "inflation", which will be treated in more detail in Chap. 4.
The aspects we are going to treat in this chapter can be explored in more detail in many different references, such as [1–4].

3.1 HORIZON PROBLEM

The first inconsistency we discuss is known as the *horizon problem*. To fully understand it, let us first observe that in a FLRW Universe the comoving Hubble radius is always growing; indeed, recalling that in FLRW

$$r_H = \frac{1}{\dot{a}(t)}, \tag{57}$$

it is easy to see that its time derivative

$$\dot{r_H} = -\frac{\ddot{a}(t)}{\dot{a}(t)^2} \tag{58}$$

is positive when we consider radiation, or pressureless matter, whereas becomes negative when considering for example the cosmological constant (see Chap. 1). In other words, for the equation of states for the cosmic fluid with $\omega > -1/3$, the comoving Hubble radius always increases.

This means that sooner or later all scales λ will enter in the horizon and the region of causal connection around the observer will become larger and larger. This is illustrated in Fig. 2. At first sight one does not notice any problem: as time flows the Hubble radius grows and larger scales can cross it, starting to communicate with the rest of the causal connected region. However, the problem comes from an "experimental" point of view, looking at CMB. Indeed, we know that a crucial prediction of the hot Big-Bang model is a left-over thermal radiation generated when radiation and matter are decoupled (see Sec. 2.3).

The CMB radiation is found to be nearly isotropic, having the same temperature in every direction in the sky and showing a nearly perfect black-body

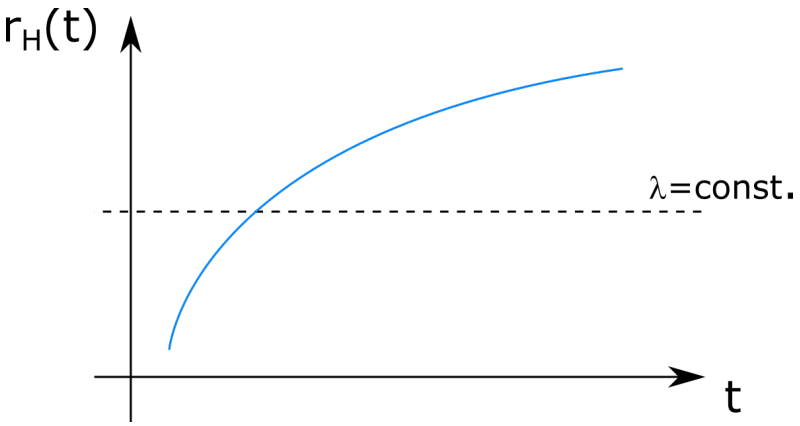

Figure 2: Comoving Hubble radius evolution in a Big-Bang model.

distribution peaked in the microwave region. Actually, this is not completely true; we will briefly explore the CMB anisotropies in Sec. 4.5, but for the purpose of this section, it suffices to state that we can observe regions that share the same statistical properties (in particular the same temperature T up to very tiny fluctuations) without having ever been in causal connection. In fact, they are separated by distances that are much larger than the largest distance traveled by light in all the history of the Universe. This is a clear inconsistency with our theoretical expectations.

In the hot Big-Bang framework, one has to assume that the initial condition of the Universe was extremely isotropic and homogeneous to consistently explain what we observe[18]. However, even doing so hides some further difficulties as one would have to deal with the fact that small anisotropies are indeed present on the CMB. In the hot Big-Bang model, it is not trivial at all to obtain these small anisotropies (see Sec. 4.5).

3.2 FLATNESS PROBLEM

Another issue is related to the importance of the curvature term, which leads to the so-called *Flatness problem*. The easiest way to see it is to analyze the first Friedmann equation

$$H^2 = \frac{8}{3}\pi G\rho - \frac{\kappa}{a^2}. \tag{59}$$

In the standard FLRW Universe, during the radiation- and matter-domination epochs, the energy density scales, respectively, as a^{-4} and a^{-3}. Now, the probability of having $\kappa = 0$ is almost null: indeed κ could take, in principle, whatever finite value so that the probability that it is exactly 0 is infinitesimally small. We immediately realize that as long as $\kappa \neq 0$, there will be a moment such that the curvature term κ/a^2 overcomes the other ones, since it decreases slower than ρ with the expansion of the Universe.

18 This explanation is not satisfactory for us, firstly because is essentially a zero-measure condition, which have basically zero probability to have occurred. Also, as physicists we would like to have an actual explanation, or a mechanism, of how things ended up this way from the most general set of initial conditions.

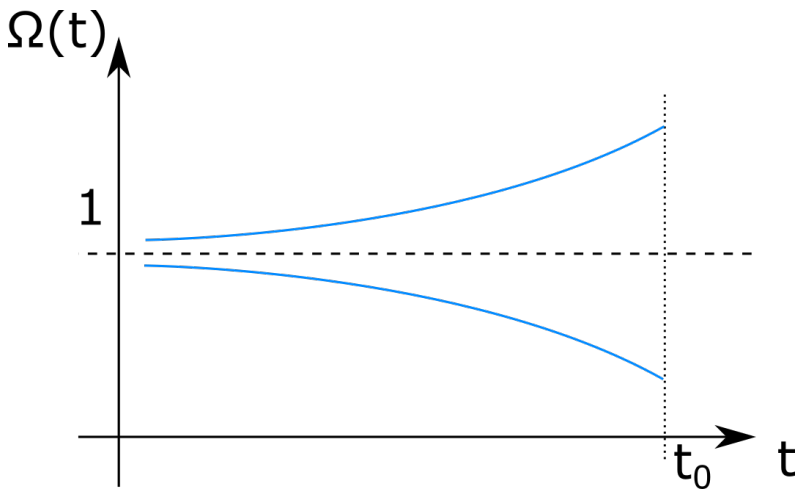

Figure 3: Density parameter behavior in a hot Big-bang model context.

Also, introducing the density parameter $\Omega(t) \equiv \rho(t)/\rho_c(t)$, where $\rho_c(t) \equiv 3H^2(t)M_P^2$ is the total energy density for a flat Universe, this contribution given by curvature is fated to increase more and more as time goes by; Fig. 3 summarizes visually these concepts and shows that, independently of the value of the curvature, at very early times Ω is approximately 1. Indeed, going back with time translates into a decrease of the scale factor, which implies that the curvature term becomes negligible so that (as happens in $\kappa = 0$ case) the density parameter becomes 1.

As time flows, we can write [1]

$$\Omega(t) - 1 = \frac{\kappa}{a^2(t)H^2(t)} = \kappa r_H^2(t) \equiv \Omega_\kappa(t) \tag{60}$$

and, besides of the sign κ, the total parameter density Ω departs from the initial value.

Here comes the problem: today, thanks to our cosmological observations, we know that $\Omega_\kappa = -0.012 \pm 0.010$ [29], which is very compatible with zero; however, since we know that κ is different from zero[19], how is it possible that today the energy contribution of the curvature term is so small?

A possible answer is that the initial value of Ω was so close to 1 that even today not enough time has passed to see its effects. However, if we want to remain in the standard hot Big-Bang model, accepting the previous explanation would result in the so-called *fine-tuning problem*.

Indeed, one can show that in order to account for the nowadays observations, the difference between the density parameter and 1, at the Planck epoch t_P which corresponds to a temperature $T_P \approx 10^{19} GeV$, has to be

$$\left[\Omega^{-1}(t_P) - 1\right] \simeq \left(\Omega_0^{-1} - 1\right)\left(\frac{T_0}{T_P}\right)^2 10^3 \approx 10^{-60}. \tag{61}$$

The problem is clear: if we want to explain the smallness of Ω_κ today we have to *fine tune* (i. e. put by hand with an high precision) the initial value

19 We can say to know this because the probability of it being exactly zero is itself null.

of Ω to 1 up the 60^{th} decimal place. This seems to be quite unnatural, in particular if we consider that such a tiny interval of acceptable initial values substantially has a "null measure" w. r. t. the whole possible ones[20].

3.3 UNWANTED RELICS

Another problem related to the hot Big-Bang model is the presence of "unwanted relics" [4] produced in the early Universe as a consequence of the spontaneous symmetry breaking of some Grand Unified Theory (GUT) at $T_{GUT} \sim 10^{14} \div 10^{16}$ GeV. An example is domain walls, i. e. topological objects (non-perturbative solutions), which can arise after spontaneous symmetry breaking in a given theory. Generally speaking, these relics are massive and very stable, since they are characterized by a small annihilation cross section; in fact, it is this last property that makes them *unwanted*, because their density parameter has the form $\Omega_x \sim 1/\sigma_x \sim 10^{14} \gg 1$. In this context, this problem is *unavoidable*, becoming a very serious flaw of the theory.

3.4 INFLATION AS A SOLUTION TO THESE SHORTCOMINGS

A solution that solves the aforementioned problems as a natural consequence of its very characteristics is a phase of accelerated expansion in the early times, called *inflation*.

3.4.1 *Horizon Problem Solution*

Inflation has the net effect of pushing to $-\infty$ the initial singularity [4]. This allows photons to be at some point in causal connection with all the others.

From the point of view of the Hubble radius, inflation caused it to decrease, forcing the scales to leave the horizon. Then, once this period ended and r_H started to grow again, all scales λ started to reenter the horizon. This time, they would have been causally connected with the rest when they were inside the horizon for the first time. Then, if we suppose that the largest scale that we can probe experimentally today, i. e. the CMB one, was within the horizon when inflation took place, there are no problems with causality anymore.

At this point, one could argue: how much did the Universe have to expand to solve the problem?

Introducing the useful quantity

$$N \equiv \int_{t_i}^{t_f} H(t)dt = ln\left(\frac{a_f}{a_i}\right), \tag{62}$$

20 We stress again that this last sentences are not properly "true". Indeed, from a pragmatic point of view, one could argue that the Universe had that exact initial condition and then evolved following the Big-Bang model until now, stopping there to question himself/herself. However, physicists do not usually like such an explanation, finding it unsatisfactory. We then want to find some mechanism that pushes the Universe to such a conclusion, without imposing any particular initial condition.

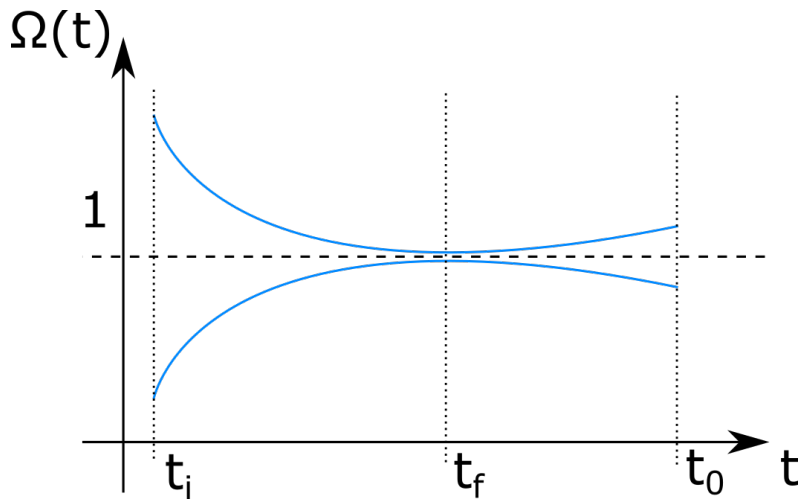

Figure 4: In this plot the expansion of the Universe occurring nowadays is neglected for the sake of simplicity. In any way it would only mean that the value of $\Omega(t)$ is getting pushed toward 1 even more, as happened during inflation.

which is called *number of e-folds*[21], and applying an exponential on both sides, Eq. 62 reads also as

$$\frac{a_f}{a_i} = e^N. \tag{63}$$

We can see that N immediately tell us how much bigger was the Universe at the end of inflation w. r. t. its beginning.

One can show that solving the horizon problem results in asking for at least $N \approx 60 \div 70$ [1], which approximately corresponds to an expansion of a factor 10^{26}, from the atomic scales to the size of the solar system.

3.4.2 *Flatness Problem Solution*

The solution can be argued taking Eq. 60 and observing that, if we consider inflation, making the Universe expand exponentially makes Ω_κ reach a value so small that even today it is still negligible. This means that even if at the beginning of this epoch the value of the total parameter density was very different from 1, as a consequence of the tremendous expansion, at the end of this phase it was pushed incredibly close to it. This solution would explain, then, the reason why even if the value of the curvature is different from zero, nowadays the measurements are consistent with a flat Universe, without imposing any initial condition. The condition $r_H(t_i) \geq r_H(t_0)$ that was needed to solve the *horizon problem* now translates into

$$\frac{\Omega^{-1}(t_i) - 1}{\Omega^{-1}(t_0) - 1} \geq 1 \tag{64}$$

and one can show that it solves also this problem with a required number of e-folds of again $60 \div 70$ [1].

21 Here with the subscripts "i" and "f" we are referring, respectively, to the start and the end of inflation.

Intuitively speaking this solution can be visualized if one thinks of an inflating balloon: if it is very small, an ant onto its surface could see the curvature; however, inflating the balloon to the size of the Earth, the curvature would get severely diluted and our ant would think to live on a flat Earth.

3.4.3 *Unwanted Relics Solution*

Inflation naturally solves the problem of unwanted relics. In fact, an inflationary scenario would lead to an expansion epoch, with $a(t) \propto e^{Ht}$, strongly suppressing the number density of these relics, being $n_x \propto a^{-3Ht}$. In this way one ends up having ≈ 1 of these objects in all the observable Universe, without concerns of its contribution to the overall energy density [4].

3.5 THE DARK SECTOR

Even though we just showed that an accelerated period at very early times can solve the shortcomings of the hot Big-Bang model, there are of course many remaining issues that are still open questions in modern Cosmology.

We already commented in Sec. 2.3 that, for example, the nature of the matter-antimatter asymmetry is still unknown. However, we cannot proceed in this Thesis without mentioning one of the biggest mysteries in our current understanding of the Universe, its *dark sector*. Indeed, to obtain a compelling picture of the cosmos, we require the existence of both some kind of CDM and of some form of *dark energy*. The former actually accounts for $\sim 25\%$ of the total energy budget of the Universe today, whereas ordinary baryonic matter covers just 5%. We have independent proofs of the existence of a CDM component essentially from any period of the history of the Universe we can inspect, from CMB all the way to the very local Universe.

Therefore, where is the missing $\sim 70\%$ of the energy budget today? That is actually stored in dark energy. This evanescent entity permeates the Universe, while providing a negative pressure that makes it expand, which explains our local observations. The simplest way to describe it is actually what we showed in Eq. 11: a cosmological constant. These two dark elements are actually what give the name to the standard model of Cosmology, i. e. the Λ Cold Dark Matter (ΛCDM) model.

Despite this, and the best efforts of the scientific community, the nature of both of these elements is obscure to us, and a period of accelerated expansion itself provides no explanation.

4

INFLATION

In Chap. 3 we introduced inflation as a solution to the shortcomings of the hot Big-Bang model. Now, we will discuss in more detail the standard inflationary model of the Universe. Specifically, we will consider the most simple example of a single-field model with a real scalar inflaton. Indeed, we have seen in Chap. 1, that in order to have accelerated expansion it is required to have

$$\ddot{a} > 0 \iff P < -\frac{1}{3}\rho \,, \tag{65}$$

which are attained by a simple simple scalar field under specific conditions.
Furthermore, after having developed some intuition on how primordial perturbations can be translated into temperature perturbations, we will conclude this chapter by taking a closer look at the CMB, introduced in Chap. 2.
Similarly to Chap. 3, the information contained in this chapter can be found in many references, such as [1–4].

4.1 WHY A SCALAR FIELD?

Once again, we can write the Einstein's equations as

$$R_{\mu\nu} - \frac{1}{2}g_{\mu\nu}R + \Lambda g_{\mu\nu} = 8\pi G T_{\mu\nu} \,. \tag{66}$$

Here, the cosmological constant Λ accounting for dark energy is associated to a stress-energy tensor, which can be written as [4]

$$T^{\Lambda}_{\mu\nu} \equiv (P_\Lambda + \rho_\Lambda)u_\mu u_\nu + P_\Lambda g_{\mu\nu} = P_\Lambda g_{\mu\nu} \,, \tag{67}$$

where we define $P_\Lambda = -\rho_\Lambda = -\frac{\Lambda}{8\pi G}$ ($\omega_\Lambda = -1$). From Eq. 12, it is possible to see that in a Universe where Λ dominates, the scale factor will be $a(t) \propto e^{Ht}$, meaning that it expands exponentially. This is very similar to what we want to achieve with our scalar field, however, since Λ is a constant, the expansion would never end.

Thus, we can then generate an effective Λ by assuming that the Universe has a scalar field φ in its ground state. In fact, φ would have the lagrangian density equal to [1]

$$\mathscr{L} = \frac{1}{2}g^{\mu\nu}\partial_\mu\varphi\,\partial_\nu\varphi - V(\varphi), \tag{68}$$

where $V(\varphi)$ is the potential and to which we can associate a stress-energy tensor [1]

$$T^{\varphi}_{\mu\nu} = \partial_\mu\varphi\,\partial_\nu\varphi + g_{\mu\nu}\mathscr{L}. \tag{69}$$

In the ground state, $\langle\varphi\rangle$ is constant, meaning that it is constant both in time and space; thus, we end up with having a stress-energy tensor, contributing to the total energy of the vacuum state, of the form

$$T_{\mu\nu} = -V(\langle\varphi\rangle)g_{\mu\nu}\ , \tag{70}$$

where we have neglected the kinetic term being in the vacuum state.

Even if this simple trick to generate such an effective vacuum energy seems to work, as mentioned, this calculation hides a flaw: inflation must end at some point. There must be some dynamics regulating such a process, so the simplest acceptable system will give [22]

$$\varphi(\vec{x},t) \quad\rightarrow\quad \langle 0|\varphi|0\rangle = f(t) \neq \text{constant}\ . \tag{71}$$

Still, the previous example with $\langle\varphi\rangle$ = constant already suggests the solution: requiring that the potential $V(\varphi)$ is *sufficiently* constant.

In Chap. 1, we mentioned that more complex models of the Universe abandon isotropy and homogeneity (cosmological principle). Is it possible to achieve inflation in those scenarios? The answer is *yes* and actually it can be shown that the examples we mention in Sec. 1.1 admit FLRW as an asymptotic state after inflation.

In a model with a real scalar field, the full action is

$$\begin{aligned} S^{TOT} =& S_{HE} + S_\varphi + S_m = \\ =& \frac{1}{16\pi G}\int d^4x\sqrt{-g}\big(R + \mathscr{L}_\varphi[\varphi,\partial_\mu\varphi] + \mathscr{L}_{\text{fields}}\big)\ , \end{aligned} \tag{72}$$

where S_{HE} is the Hilbert-Einstein action, S_φ is the action of the inflaton and S_m is the action of the "rest-of-the-world" (i. e. fermions, gauge fields, other scalars, etc). In the following, we will neglect S_m because, in general, it is subdominant at early times, since, by definition, the inflaton φ dominates the energy density.

The generic Lagrangian of a real scalar field has the form shown by Eq. 68, where the potential can have different forms depending on the model and is usually assumed to be minimally coupled (for the sake of simplicity); for example, a simple quadratic potential is $V(\varphi) = \frac{1}{2}m_\varphi^2\varphi^2$, where m_φ is the mass of the particle associated to φ.

22 Giving away simplicity one can consider a wide variety of cases, which however must respect the underlying symmetries of the considered system. What if, for example, we consider the case of a vector gauge field A^μ? This is not a viable choice in the standard scenario, since taking a $\langle 0|\,A^\mu\,|0\rangle \neq 0$ violates rotational invariance (isotropy), resulting in observational consequences. Other choices can be a spinor field ψ, but $\langle 0|\,\psi\,|0\rangle \neq 0$ gives the same problem. A way to solve it is to consider scalar condensates $\langle 0|\bar{\psi}\psi|0\rangle$, from which to build the model.

4.2 EVOLUTION OF φ

To characterize the evolution of a scalar field in an expanding Universe, we can associate to φ its stress-energy momentum $T_{\mu\nu}$, thus reminding Eq. 4 we can write

$$T_{\mu\nu} \equiv \frac{-2}{\sqrt{-g}}\frac{\delta S}{\delta g^{\mu\nu}} = \frac{-2}{\sqrt{-g}}\left[-\frac{\partial(\sqrt{-g}\mathscr{L})}{\partial g^{\mu\nu}} + \partial_\alpha \frac{\partial(\sqrt{-g}\mathscr{L})}{\partial \partial_\alpha g^{\mu\nu}} + \dots\right] , \quad (73)$$

where higher order derivatives terms can arise in case $\mathscr{L}$ depends on higher derivatives of the metric. Plugging Eq. 68, one obtains

$$\begin{aligned} T^{\varphi}_{\mu\nu} &= -2\frac{\partial \mathscr{L}_\varphi}{\partial g^{\mu\nu}} + g^{\mu\nu}\mathscr{L}_\varphi \\ &= \partial_\mu\varphi\,\partial_\nu\varphi + g_{\mu\nu}\left[-\frac{1}{2}g^{\alpha\beta}\varphi_{;\alpha}\,\varphi_{;\beta} - V(\varphi)\right] . \end{aligned} \quad (74)$$

Then, we can express φ as the sum of the classical background value and the field fluctuations as

$$\begin{aligned} \varphi \equiv \varphi(\vec{x},t) &= \langle 0|\,\varphi(\vec{x},t)\,|0\rangle + \delta\varphi(\vec{x},t) \\ &= \varphi_0(t) + \delta\varphi(\vec{x},t) \end{aligned} \quad (75)$$

This approach is useful in order to do perturbation theory, thus if

$$\langle \delta\varphi^2(\vec{x},t)\rangle \ll \varphi_0^2(t) \quad (76)$$

we can perform expansions in orders of the fluctuations.

Furthermore, the fact that $\langle\delta\varphi\rangle = 0$ means that Eq. 76 is in fact the variance of the fluctuation of φ.

4.2.1 *Classical Dynamics*

The background value $\varphi_0(t)$ is an homogeneous and isotropic scalar field in FLRW, so we can associate an stress-energy tensor such as [1]

$$\begin{aligned} T^0_{\ 0} &= -\left[\frac{1}{2}\dot{\varphi}_0^2(t) + V(\varphi_0)\right] = -\rho_\varphi(t) , \\ T^i_{\ j} &= \left[\frac{1}{2}\dot{\varphi}_0^2(t) - V(\varphi_0)\right]\delta^i_{\ j} = \delta^i_{\ j}P_\varphi(t) , \end{aligned} \quad (77)$$

where $\rho_\varphi(t)$ is the energy density and $P_\varphi(t)$ the isotropic pressure[23]. The fact that $T_{\mu\nu}$ is diagonal and the spatial part is the same in every direction is a consequence of isotropy and homogeneity, resulting in a tensor typical of perfect fluids.

23 In the following we will refer to background field with φ and fluctuations with $\delta\varphi$, without writing every time φ_0.

Recalling that for inflation, a negative isotropic pressure is required $P_\varphi < 0$, we can see that taking $V(\varphi) \gg \frac{1}{2}\dot{\varphi}^2$ brings to $P_\varphi \approx -V(\varphi) \approx -\rho_\varphi$, which gives rise to a quasi-de Sitter phase.

This can be achieved simply by considering a sufficiently flat potential. Suppose that initially we have the unsuitable condition (for inflation) $\frac{1}{2}\dot{\varphi}^2 \gg V(\varphi)$; therefore, from Eq. 77 $\omega_\varphi = \frac{P_\varphi}{\rho_\varphi} = 1$ and knowing the scaling of the energy density with the scale factor, we obtain $\rho_\varphi \sim \rho_{\text{KIN}} \propto a^{-3(1+\omega_\varphi)} = a^{-6}$. Due to this strong dependency and a sufficiently flat potential configuration, the latter will come to dominate, washing completely away the kinetic energy. This is called the *slow roll* regime, during which inflation is realized: the constant $V(\varphi)$ provides an accelerated expansion driven by the vacuum energy density of φ, which mimics an effective Λ.

Most importantly, this solution is an attractor because, whatever are the initial conditions of kinetic energy and potential, at some point this regime will make the potential to act as a cosmological constant, allowing also some dynamics to it, enabling to exit inflation. This attractive behavior is crucial to avoid fine-tuning issues and other artifacts.

4.2.2 *Equation of Motion*

The Equation Of Motion (EOM) for the scalar field φ comes from the variational principle[24] [2]

$$\frac{\delta S}{\delta \varphi} = 0 \rightarrow \Box\varphi = \frac{\partial V}{\partial \varphi} \,, \tag{78}$$

where the D'Alambertian operator $\Box$ in a curved spacetime gives

$$\varphi^{;\mu}{}_{;\mu} = \frac{1}{\sqrt{-g}}(g^{\mu\nu}\sqrt{-g}\,\varphi_{;\mu})_{;\nu} \,. \tag{79}$$

In a spatially flat ($\kappa = 0$) FLRW spacetime $\sqrt{-g} = a^3(t)$, therefore

$$\Box\varphi = -\ddot{\varphi} - 3H\dot{\varphi} + \frac{\nabla^2\varphi}{a^2} \,. \tag{80}$$

The resulting equation is the Klein-Gordon (K-G) equation for a quantum scalar field in FLRW [25]

$$\ddot{\varphi} + 3H\dot{\varphi} - \frac{\nabla^2\varphi}{a^2} = -\frac{\partial V}{\partial \varphi} \,. \tag{81}$$

24 The plus sign in front of the derivative of the potential come from the metric signature $(-,+,+,+)$.

25 Having considered $\kappa \neq 0$ would have only changed the explicit expression of ∇^2, but the equation would have appeared in the same form.

Through $3H\dot{\varphi}$, the field "feels" a friction due to the expansion of the Universe, which will play a crucial role in the following paragraphs.

Focusing on the background field $\varphi_0(t) \equiv \varphi(t)$ as in Eq. 75, we can study the background dynamics

$$\begin{cases} \ddot{\varphi} + 3H\dot{\varphi} = -\frac{\partial V}{\partial \varphi} \\ H^2 = \frac{8\pi G}{3}\left(\frac{1}{2}\dot{\varphi}^2 + V(\varphi)\right) = \frac{8\pi G}{3}\rho_\varphi \end{cases} \quad [26]. \tag{82}$$

Let us now introduce two conditions required to realize inflation for a sufficiently long amount of time while solving the Big-Bang shortcomings.

We have already presented the *first slow-roll condition*

$$V(\varphi) \gg \dot{\varphi}^2 \,, \tag{84}$$

which brings the potential to dominate over the kinetic energy during inflation. This is realized if the potential is sufficiently flat w. r. t. φ. Furthermore, we expect that its derivatives w. r. t. φ also depend weakly on φ[27].

Then, we can introduce a *second slow-roll condition*

$$\ddot{\varphi} \ll 3H\dot{\varphi} \,, \tag{85}$$

which brings to

$$\dot{\varphi} \sim -\frac{V'}{3H} \,. \tag{86}$$

This means that Eq. 82 are expressed as functions of $a(t)$ and $\varphi(t)$ once the model, i. e. the potential $V(\varphi)$, is specified.

4.2.3 *Slow-roll Parameters*

Now, we need a way to quantify the dynamics of the slow-roll regime in order to give predictions of specific models and compare it with observations. In particular, we will use the so-called *slow-roll parameters* ε and η.

Firstly, from an intuitive point of view, one can check how much H changes during inflation in order to define ε. In fact, in the cosmological constant case

26 In full generality we would have to account also for other contributions to the Hubble rate as

$$H^2 = \frac{8\pi G}{3}(\rho_\varphi + \rho_r + \rho_m) - \frac{k}{a^2} \,, \tag{83}$$

however $\rho_m \propto a^{-3}$, $\rho_r \propto a^{-4}$, $\rho_k \propto a^{-2}$ and $\rho_\varphi \simeq V(\varphi) \simeq$ constant, so the latter will come to dominate resulting in $a \simeq e^{Ht}$. This strong dependence of the other energy densities will wash them away very proficiently, so we can safely neglect them.

27 Here, we will indicate the derivative w. r. t. φ as $' \equiv \frac{\partial}{\partial \varphi}$. Be aware of the ambiguity with the derivative in conformal time, which, however, can be easily solved by looking at the context.

H is a constant, so we can expect that adding some dynamics to the system would make H change. Thus, we define [1]

$$\varepsilon \equiv -\frac{\dot{H}}{H^2} \,. \tag{87}$$

Using the Friedmann equations and the attractor solution, one can show that the first slow-roll parameter can be expressed as

$$\varepsilon \simeq \frac{3}{2}\frac{\dot{\varphi}^2}{V(\varphi)} \simeq \frac{1}{16\pi G}\left(\frac{V'}{V}\right)^2 \,. \tag{88}$$

Therefore, we can interpret ε as the ratio between the kinetic energy and the potential. Hence, assuming $V(\varphi) \gg \dot{\varphi}^2$, one obtains

$$\varepsilon \ll 1 \,. \tag{89}$$

Furthermore, if $\varepsilon \ll 1$, V' is small and the potential is flat. In this sense ε quantifies the flatness of the potential.

Exploiting now the second slow-roll condition $\ddot{\varphi} \ll 3H\dot{\varphi}$, we can define the second slow-roll parameter as [1]

$$\eta \equiv -\frac{\ddot{\varphi}}{H\dot{\varphi}} \ll 1 \,. \tag{90}$$

Again, one can show that

$$\eta \simeq \frac{V''}{3H^2} - \frac{\dot{H}}{H^2}\frac{V'}{3H\dot{\varphi}} \simeq \eta_V - \varepsilon \,, \tag{91}$$

where $\frac{V'}{3H\dot{\varphi}} \simeq -1$ and $\eta_V \equiv \frac{V''}{3H^2} \simeq \frac{1}{8\pi G}\frac{V''}{V}$ since during slow-roll H^2 is dominated by the potential. Thus, again having $\eta_V \ll 1$, means having a flat potential [28].

Indeed, ε alone can be sufficient to realize inflation when $\varepsilon < 1$, however, having also $\eta_V \ll 1$ will ensure that inflation lasts long enough.

ε and η_V are merely the first two parameters of a whole hierarchy of higher-order ones, but in the simplest case of inflation, one considers only these two. Also, at first order, they can be considered as constants.

It is also interesting to note that in the simple case of a single-field scalar inflation ε is always positive, given that $\dot{H} < 0$.

28 Note that there is an ambiguity between the symbol used for conformal time and the slow-roll parameter, i. e. η. From now on, we will refer to the second slow-roll parameter as η_V just introduced. In fact, this quantity is directly related to the potential of the inflaton. This will break the degeneracy between these two quantities.

4.3 QUANTUM FLUCTUATIONS OF THE INFLATON FIELD

How is it possible to generate cosmological perturbations $\frac{\delta\rho}{\rho}$ on large cosmological scales, $\lambda \gg H^{-1}$, from the fluctuations $\delta\varphi$ of the inflaton field?

Let us start from the EOM for the inflaton

$$\ddot{\varphi} + 3H\dot{\varphi} - \frac{\nabla^2\varphi}{a^2} = -\frac{\partial V}{\partial \varphi} \,. \tag{92}$$

Looking for the background evolution one obtains Eq. 75; however including the perturbations and focusing on the linear level, one obtains the following relations [2]

$$\begin{cases} \ddot{\delta\varphi} + 3H\dot{\delta\varphi} - \frac{\nabla^2\delta\varphi}{a^2} = -V''\delta\varphi \\ (\dot{\varphi}_0)^{\cdot\cdot} + 3H(\dot{\varphi}_0)^{\cdot} = -V''\dot{\varphi}_0 \end{cases} . \tag{93}$$

Indeed on large-scales where $\lambda_{\text{phys}} \gg H^{-1} \iff k \ll aH$, $\dot{\varphi}_0$ and $\delta\varphi$ evolve following the same identical equation. Looking at the Wronskian, one can in fact notice that they are related; specifically [1]

$$\delta\varphi(\vec{x}, t) = -\delta t(\vec{x})\dot{\varphi}_0(t) \,. \tag{94}$$

In other words, the perturbation can be thought as a slight time shift of the evolution of φ_0. Quantitatively, the scalar field is related to its background evolution as [1]

$$\varphi(\vec{x}, t) = \varphi_0(t - \delta t(\vec{x})) \,. \tag{95}$$

Thus, on large scales φ will assume the same value φ_0 everywhere, making every point in the Universe experience the same history, but at slightly different times.

4.3.1 *Approximated Solutions*

Eq. 93 can be solved easily in Fourier space, where

$$\delta\varphi(\vec{x}, t) = \frac{1}{(2\pi)^3}\int d^3k e^{i\vec{k}\cdot\vec{x}}\delta\varphi(k, t) \,, \tag{96}$$

with $\delta\varphi(k, t) = \delta\varphi^*(k, t)$, since $\delta\varphi(\vec{x}, t)$ is real[29], and where different modes as $\delta\varphi(k, t)$ and $\delta\varphi(k', t)$ evolve independently (only at linear level).

29 We use 3d Fourier transform because it is not invariant under time translation, and we use plane waves to transform because spatially flat FLRW is assumed, for $\kappa \neq 0$ we have to use solutions of Helmholtz equation: $\nabla^2 Q_k + k^2 Q_k = 0$.

The EOM reads, for a given Fourier component,

$$\delta\ddot{\varphi}_k + 3H\delta\dot{\varphi}_k + \frac{k^2\delta\varphi_k}{a^2} = -V''\delta\varphi_k \,. \tag{97}$$

We must now quantize the field, considering a field rescaled as $\delta\varphi \equiv \frac{\delta\widehat{\varphi}}{a(t)}$, hence [2]

$$\delta\widehat{\varphi}(\eta, \vec{x}) = \frac{1}{(2\pi)^3}\int d^3k \left[u_k(\eta)\widehat{a}_k e^{-i\vec{k}\cdot\vec{x}} + u_k^*(\eta)\widehat{a}_k^\dagger e^{i\vec{k}\cdot\vec{x}}\right] \,, \tag{98}$$

where $\widehat{a}, \widehat{a}^\dagger$ are the annihilation and creation operators, $a_k\,|0\rangle = 0\;\forall\; k$ and η is the conformal time. Here $|0\rangle$ is the free vacuum state, because linearizing we are not considering any interaction, except for the quadratic term that gives mass to the field.

The normalization condition for $u_k(\eta)$ is [30] $u_k^*(\eta)u_k^{'}(\eta) - u_k(\eta)u_k^{*'}(\eta) = -i$, which ensures the canonical quantization conditions for $\widehat{a}, \widehat{a}^\dagger$ operators [2]:

$$[\widehat{a}_k, \widehat{a}_{k'}] = 0\,; \qquad \left[\widehat{a}_k, \widehat{a}_{k'}^\dagger\right] = \hbar\,\delta^3(k - k^{'}) \,. \tag{99}$$

In a flat spacetime

$$u_k(\eta) = \frac{e^{-i\omega_k\eta}}{\sqrt{2\omega_k}} \quad \text{with} \quad \omega_k = \sqrt{k^2 + m^2} \,, \tag{100}$$

but in a curved spacetime u_k is not necessarily a plane wave; there is indeed an ambiguity in the definition of the vacuum state. At early times and small scales $k \gg aH$, we have $\omega_k \sim k$ and we require to be able to reproduce a flat space-time metric, due to the equivalence principle; thus we can assume

$$u_k(\eta) \approx \frac{e^{-ik\eta}}{\sqrt{2k}} \,. \tag{101}$$

These requirements are called the *Bunch-Davis vacuum choice*. Let us obtain the K-G equation in Fourier space starting by Eq. 92. Passing to conformal time, it is recast to

$$\varphi'' + 2\frac{a'}{a}\varphi' - \nabla^2\varphi = -a^2\frac{\partial V}{\partial\varphi} \,, \tag{102}$$

thus looking at the perturbation one obtains

$$\delta\varphi'' + 2\frac{a'}{a}\delta\varphi' - \nabla^2\delta\varphi = -a^2\frac{\partial^2 V}{\partial\varphi^2}\delta\varphi \,. \tag{103}$$

30 Here we use $' = \frac{\partial}{\partial\eta}$.

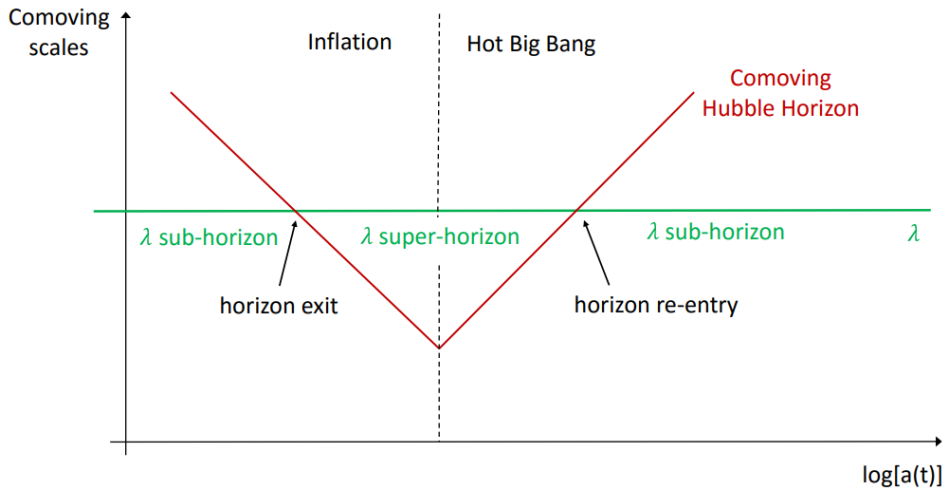

Figure 5: Summary representation of the relation between the comoving Hubble radius and a generic comoving scale λ. During the accelerated expansion the comoving Hubble horizon decreases in time, while it grows during the radiation and matter dominated epochs, making the scale λ exit and re-enter the horizon [30].

Applying then $\delta\varphi = \frac{\delta\widehat{\varphi}}{a(\eta)}$, we get

$$\delta\widehat{\varphi}'' - \frac{a''}{a}\delta\widehat{\varphi} - \nabla^2\delta\widehat{\varphi} = -a^2\frac{\partial^2 V}{\partial\varphi^2}\delta\widehat{\varphi}\,. \tag{104}$$

At this point, going to Fourier space and using $|\delta\widehat{\varphi}_k| = |u_k|$, we can finally write [2]

$$u_k''(\eta) + \left[k^2 - \frac{a''}{a} + \frac{\partial^2 V}{\partial\varphi^2}a^2\right] u_k(\eta) = 0\,. \tag{105}$$

This equation describes an harmonic oscillator with a frequency changing in time, due to the expansion of the Universe.

Considering a massless scalar field, $m_\varphi^2 = V''(\varphi) = 0$ in pure de Sitter ($H =$ constant), the equation is

$$u_k''(\eta) + \left[k^2 - \frac{a''}{a}\right] u_k(\eta) = 0\,. \tag{106}$$

Before studying more in depth the solutions to this equation, let us firstly clarify the role of conformal time. We know that it is related to cosmic time through $ad\eta = dt$, so in this case we can write

$$d\eta \propto \frac{dt}{e^{Ht}} \quad\longrightarrow\quad \eta \propto -\frac{1}{H}e^{-Ht} = -\frac{1}{aH} < 0\,, \tag{107}$$

hence during inflation η belongs to $]-\infty\,,\ 0[$. So, we can relate this to

$$\frac{a''}{a} = \frac{2}{\eta^2} = 2a^2H^2 = \frac{2}{r_H^2}\,. \tag{108}$$

Let us now solve the EOM of u_k in two different regimes:

SUB-HORIZON: we have $\lambda_{\rm phys} \ll H^{-1} \longleftrightarrow k \gg aH \to \frac{a''}{a}$, thus the EOM reduces to

$$u_k'' + k^2 u_k = 0 \longrightarrow u_k(\eta) = \frac{1}{\sqrt{2k}} e^{-ik\eta} \,, \tag{109}$$

whereas an oscillating solution. For what regard the field

$$\delta\varphi_k = \frac{u_k}{a} = \frac{1}{a}\frac{1}{\sqrt{2k}} e^{-ik\eta} \,, \tag{110}$$

from which we can observe that it has a decreasing amplitude $|\delta\varphi| = \frac{1}{a\sqrt{2k}}$, which depends on the inverse of a, so during inflation it decreases extremely fast.

SUPER-HORIZON: we have $\lambda_{\rm phys} \gg H^{-1} \longleftrightarrow k \ll aH \to \frac{a''}{a}$, thus the EOM reduces to

$$u_k'' - \frac{a''}{a} u_k = 0 \,. \tag{111}$$

This kind of equations are solved by [2]

$$u_k(\eta) = B(k) a(\eta) + A(k) a^{-2}(\eta) \,, \tag{112}$$

where A, B are integration constants in η which depend on k. In terms of field we get

$$\delta\varphi_k = B(k) + A(k) a^{-3}(\eta) \simeq B(k) = \text{constant} \,, \tag{113}$$

where we have neglected the decaying term that is washed away by inflation. Such a frozen solution makes sense intuitively if one argues that microphysics cannot play any role in such large-scale phenomena.

We can find the amplitude in this regime making a matching between the two regimes at horizon crossing, since from that moment on it will become constant. At horizon crossing $k = aH$, thus

$$u_k^{sup} = |B(k)| a = \frac{1}{\sqrt{2k}}\Big|_{k=aH} = u_k^{sub} \,, \tag{114}$$

therefore

$$|\delta\varphi_k| = |B(k)| = \frac{1}{a\sqrt{2k}}\Big|_{k=aH} = \frac{H}{\sqrt{2k^3}} \,. \tag{115}$$

In general averaging on sub-horizon scales one gets $\langle\delta\varphi\rangle_t = 0$ if t is a macroscopic time interval. However, we are considering an expanding background in which $\lambda_{\rm phys} \propto a \propto e^{Ht}$. This means that the fluctuations do not remain in the vacuum state, but the fluctuations become frozen and $\langle\delta\varphi\rangle \neq 0$. In

other words, we are generating classical perturbations of φ, so in some sense we have realized a state characterized by a net number of particles.

Finally, one can show that the exact solution of massless scalar field in pure de-Sitter is [3]

$$u_k(\eta) = \frac{e^{ik\eta}}{\sqrt{2k}}\left(1 - \frac{i}{k\eta}\right) \qquad \forall\, k \quad \text{and} \quad \forall \eta\ , \tag{116}$$

which gives the aforementioned solutions in the two asymptots.

4.3.2 *Exact Solutions in Quasi de-Sitter Spacetime*

Let us now consider a massless scalar field in quasi de-Sitter, reminding that the slow-roll parameter is $\varepsilon \equiv -\frac{\dot{H}}{H^2} \ll 1$. By definition of conformal time, as we have done before, we can write [2]

$$\eta \simeq -\frac{1}{aH(1-\varepsilon)}\ , \qquad \frac{a''}{a} = \frac{2}{\eta^2}\left[1 + \frac{3}{2}\varepsilon\right]\ , \tag{117}$$

at lowest order in ε. The EOM can be rewritten in terms of the slow-roll parameter as

$$u_k''(\eta) + \left[k^2 - \frac{\nu^2 - \frac{1}{4}}{\eta^2}\right] u_k(\eta) = 0, \tag{118}$$

where $\nu = \frac{9}{4} + 3\varepsilon$. In this form, it is equivalent to the Bessel equation [31]

$$z^2 y''(z) + z y'(z) + (z^2 - \nu^2) y(z) = 0\ , \tag{119}$$

whose solutions are known to be of the form [2]

$$u_k(\eta) = \sqrt{-\eta}\left[c_1(k) H_\nu^{(1)}(-k\eta) + c_2(k) H_\nu^{(2)}(-k\eta)\right]\ ^{31}, \tag{120}$$

- On sub-horizon scales we require $u_k(\eta) \sim \frac{e^{-ik\eta}}{\sqrt{2k}}$ for $\left(\frac{k}{aH}\right) \to \infty$, so introducing $x = -k\eta$ and given that

$$H_\nu^{(1)}(x) \simeq \sqrt{\frac{2}{\pi x}} e^{i\left(x - \frac{\pi}{2}\nu - \frac{\pi}{4}\right)} \xrightarrow{x \gg 1} \frac{e^{ix}}{\sqrt{x}}\sqrt{\frac{2}{\pi}}\ , \tag{121}$$

31 $H_\nu^{(i)}(-k\eta)$ are the Hankel functions of i^{th} species and order ν [31]. Also, it holds $H_\nu^{(2)}(-k\eta) = H_\nu^{(1)*}(-k\eta)$. Instead, the c_i are integration constants.

we must impose $c_2(k) = 0$ and $c_1(k) = \frac{\sqrt{\pi}}{2} \exp\left\{ i\left(\nu + \frac{1}{2}\right)\frac{\pi}{2} \right\}$, resulting in [2]

$$u_k(\eta) = \sqrt{-\eta}\frac{\sqrt{\pi}}{2} \exp\left\{ i\left(\nu + \frac{1}{2}\right)\frac{\pi}{2} \right\} \frac{e^{-ik\eta}}{\sqrt{-k\eta}} \,. \tag{122}$$

- On super-horizon scales ($k \ll aH$), we have instead

$$H_\nu^{(1)}(x) \simeq \sqrt{\frac{2}{\pi}} e^{-\frac{\pi}{2}} 2^{\nu-\frac{3}{2}} \left(\frac{\Gamma(\nu)}{\Gamma(\frac{3}{2})}\right) x^{-\nu} \xrightarrow{x\ll 1} x^{-\nu}\ ^{32}, \tag{123}$$

where $\nu^2 = \frac{9}{4} + 3\varepsilon \to \nu \simeq \frac{3}{2} + \varepsilon$, therefore $\nu - \frac{3}{2} = \varepsilon$. Thus [2]

$$u_k(\eta) \simeq \frac{1}{\sqrt{2k}} e^{i(\nu-\frac{1}{2})\frac{\pi}{2}} 2^{\nu-\frac{3}{2}} \left(\frac{\Gamma(\nu)}{\Gamma(\frac{3}{2})}\right) (-k\eta)^{\frac{1}{2}-\nu} \,. \tag{125}$$

The solution for the perturbation is, using $\frac{1}{a} \propto -\eta$ at lowest order in the slow roll parameters

$$|\delta\varphi_k| = \frac{|u_k|}{a} = 2^{\nu-\frac{3}{2}} \left(\frac{\Gamma(\nu)}{\Gamma(\frac{3}{2})}\right) \frac{H}{\sqrt{2k^3}} \left(\frac{k}{aH}\right)^{\frac{3}{2}-\nu} \,, \tag{126}$$

which can be approximated by

$$|\delta\varphi_k| \simeq \frac{H}{\sqrt{2k^3}} \left(\frac{k}{aH}\right)^{\frac{3}{2}-\nu} \,, \tag{127}$$

where one can notice that the de-Sitter solution is recovered with $\varepsilon = 0 \iff \nu = \frac{3}{2}$.

Being *quasi* de-Sitter switches on a scale dependency on $k^{-\varepsilon}$, which is a unique prediction of inflationary models

The form of this solution is maintained even if we consider more general frameworks. In particular in the most general case, one considers a massive inflaton and substitutes to the perturbations $\delta\varphi$ the so-called Sasaki-Mukhanov variable [1]

$$Q_\varphi \equiv \delta\varphi + \frac{\dot{\varphi}}{H}\widehat{\phi} \,, \tag{128}$$

32 Here, $\Gamma(x)$ is the Euler-Gamma function [31], defined as

$$\Gamma(z) \equiv \int_0^\infty x^{z-1} e^{-x}\, dx \quad \text{for} \quad \mathrm{Re}\,(z) > 0 \,. \tag{124}$$

where $\widehat{\phi}$ is related to the scalar perturbations of the spatial part of the metric δg_{ij},

$$g_{ij} = a^2(\eta)\left[(1-2\phi)\delta_{ij} + \chi_{ij}\right] \ . \tag{129}$$

One can show that even in this case the following holds [2]

$$\widehat{Q}''_{\varphi}(\eta) + \left[k^2 - \frac{\nu^2 - \frac{1}{4}}{\eta^2}\right]\widehat{Q}_{\varphi}(\eta) = 0 \ , \tag{130}$$

with $\nu^2 = \frac{9}{4} + 9\varepsilon - 3\eta_V$, thus at first order $\frac{3}{2} - \nu \simeq \eta_V - 3\varepsilon$. The amplitude will be

$$|Q_{\varphi}| \simeq \frac{H}{\sqrt{2k^3}}\left(\frac{k}{aH}\right)^{\frac{3}{2}-\nu} \ , \tag{131}$$

which is the most general solution we can consider.

4.3.3 *Correlation Functions and Power Spectrum*

Quantum fluctuations are not deterministic, but can be characterized by the statistics of the quantum random field $\delta\varphi(\vec{x}, t)$ that describes the amplitude of these fluctuations at each point of spacetime (i. e. the variance of φ). These fluctuations are correlated at different points; hence, even if the ensemble average is zero by definition (it is, in fact, the vacuum expectation value), one can compute the two-point correlation function

$$\xi \equiv \langle \delta(\vec{x} + \vec{r}, t)\, \delta(\vec{x}, t)\rangle \ , \tag{132}$$

which in a homogeneous and isotropic Universe is a function of $|\vec{r}|$ [33]. If we take the two-point correlation function of the Fourier transform of a generic stochastic field

$$\delta(\vec{x}, t) = \frac{1}{(2\pi)^3}\int d^3k e^{i\vec{k}\cdot\vec{x}}\delta_k(t) \ , \tag{133}$$

the result is

$$\langle \delta(\vec{k}, t)\, \delta(\vec{k}', t)\rangle = (2\pi)^3 P(k)\delta^3(\vec{k} + \vec{k}') \text{ [34]} \ , \tag{134}$$

where P is the *power spectrum*, that depends only on the modulus of $\vec{k}$ due to isotropy, while homogeneity causes the presence of the delta function.

33 It is very similar to a propagator, but it regards only the spatial part.

34 An equivalent definition of power spectrum is

$$\langle \delta(\vec{k}, t)\, \delta^*(\vec{k}', t)\rangle = (2\pi)^3 P(|\vec{k}|)\delta^3(\vec{k} - \vec{k}') \tag{135}$$

since $\delta(\vec{x}, t)$ is real we have $\delta^*(\vec{k}, t) = \delta(-\vec{k}, t)$.
In addition, the notation in Fourier space reads $\delta(\vec{k}, t) = \delta_{\vec{k}}(t)$.

Furthermore, the power spectrum P is the Fourier transform of ξ, namely using Eq. 134

$$\xi(\vec{r}) = \frac{1}{(2\pi)^3} \int d^3k' e^{i\vec{k}'\vec{r}} P(k_1) \, . \tag{136}$$

The variance results

$$\langle \delta^2(\vec{x}, t) \rangle = \xi(0) = \frac{1}{2\pi^2} \int_0^\infty \frac{dk}{k} k^3 P(k) = \int_0^\infty \frac{dk}{k} \Delta(k) \, , \tag{137}$$

where we defined the *adimensional power spectrum* as $\Delta(k) \equiv \frac{k^3}{2\pi^2} P(k)$, which is the contribution to the variance per logarithmic integral. It is used mostly in Cosmology, more than $P(k)$, for inflationary physics[35].

For inflaton field quantum fluctuations $|\delta\varphi_k| = \frac{|u_k|}{a}$ [2],

$$\langle \delta\varphi_{\vec{k}_1}, \delta\varphi^*_{\vec{k}_2} \rangle = (2\pi)^3 |\delta\varphi_{\vec{k}_1}|^2 \delta^3(\vec{k}_1 - \vec{k}_2) \, , \tag{138}$$

therefore [1]

$$P(k) = |\delta\varphi_k|^2 = \frac{|u_k|^2}{a^2} \qquad \rightarrow \qquad \Delta(k) = \frac{k^3}{2\pi^2} \frac{|u_k|^2}{a^2} \, . \tag{139}$$

On super horizon scales, $\delta\varphi_k = \frac{H}{\sqrt{2k^3}} \left(\frac{k}{aH}\right)^{\frac{3}{2}-\nu}$

$$P_\varphi(k) = \frac{H^2}{2k^3} \left(\frac{k}{aH}\right)^{3-2\nu} \qquad \Delta_\varphi(k) = \left(\frac{H}{2\pi}\right)^2 \left(\frac{k}{aH}\right)^{3-2\nu} \, , \tag{140}$$

where in the most general case $3 - 2\nu = 2\eta_V - 6\varepsilon$ [4]. We can then define the *spectral index* $n(k)$ as [1]

$$n(k) - 1 \equiv \frac{\mathrm{d} \ln \Delta(k)}{\mathrm{d} \ln k} \, , \tag{141}$$

which describes the shape of the power spectrum.

1. $n = 1 \leftrightarrow$ Harrison-Zel'dovich (H-Z) spectrum: it means that the amplitude of $\delta\varphi$ does not depend on the cosmological scale.
2. $n =$ constant $\leftrightarrow \Delta(k)$ can be written w. r. t. a "pivot scale" k_0 as

$$\Delta(k) = \Delta(k_0) \left(\frac{k}{k_0}\right)^{n-1} \, . \tag{142}$$

35 Note that here we are reporting the historical nomenclature of these quantities, but often in Cosmology the adimensional power spectrum is indicated with $P_i(k)$ where $i = s, t$ to indicate the spectrum of scalar or tensor perturbation, respectively. Indeed, a general rule of thumb is to assume that one always refers to the adimensional version of the spectrum. Even in this work, we will shift to this nomenclature in the following chapters, for example, in Chap. 5.

n and $\Delta(k_0)$ are indeed the two main observables one can constrain observing the CMB.

4.3.4 *Super-horizon Perturbations*

Firstly, let us introduce a couple of definitions. ζ is called *curvature perturbation on uniform energy density hypersurfaces*:

i) ζ is a gauge invariant quantity defined as[36] [1]

$$\zeta \equiv -\widehat{\phi} - H\frac{\delta\rho}{\dot{\rho}}\,, \tag{143}$$

where $\delta\rho$ is the scalar perturbation of the energy density.
In the $\widehat{\phi} = 0$ gauge, therefore, we have

$$\zeta = -H\frac{\delta\rho}{\dot{\rho}}. \tag{144}$$

ii) This is a very general definition, since in the case of inflation the density is the density of the scalar field, but it also applies during all the evolution of the Universe:

$$\zeta \to \frac{\delta\rho_\varphi}{\dot{\rho}_\varphi}, \quad \frac{\delta\rho_m}{\dot{\rho}_m}, \quad \frac{\delta\rho_\gamma}{\dot{\rho}_\gamma}, \quad \frac{\delta\rho_\Lambda}{\dot{\rho}_\Lambda}. \tag{145}$$

iii) On super horizon scales it is constant in time (adiabaticity in single-field models of inflation)

$$\zeta\Big|_{t_H^{(1)}(k)} = \zeta\Big|_{t_H^{(2)}(k)}\,. \tag{146}$$

These properties give us the ability to compare the amplitude of primordial inflaton perturbations with known quantities, such as CMB temperature fluctuations.

Let us now suppose to look at two different scales λ, λ', where the latter re-enters during matter-dominated epoch and the former during radiation domination. Let us then call $t_H^{(1)}(k)$ the time at which λ crosses out the horizon and $t_H^{(2)}(k)$ the time in which it re-enters. The same applies to $\lambda' \to k'$. Thanks to Eq. 146, we can compare density perturbation at the time of inflation with respect to radiation epoch

36 $\widehat{\phi}$ is related to the spatial perturbations of the metric $\delta g_{\mu\nu}$.

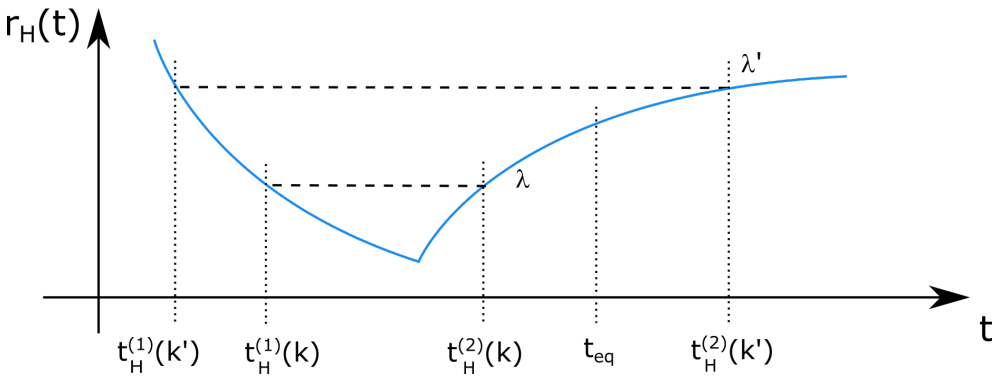

Figure 6: Comparison between different epochs using ζ conservation

$$\begin{aligned} \zeta\Big|_{t_H^{(1)}(k)} &= \zeta\Big|_{t_H^{(2)}(k)} \\ -H\,\frac{\delta\varphi}{\dot{\varphi}}\Big|_{t_H^{(1)}(k)} &= \frac{1}{4}\,\frac{\delta\rho_\gamma}{\rho_\gamma}\Big|_{t_H^{(2)}(k)} \end{aligned} \,, \tag{147}$$

since during radiation domination the density is given by $\rho = \rho_\gamma \propto T^4 \rightarrow \frac{\delta\rho}{\dot{\rho}} = 4\frac{\delta T}{T}$ and $\dot{\rho}_\gamma \simeq -4H\rho_\gamma$. In other words, there is a direct link between temperature fluctuation and primordial inflaton fluctuations

$$\zeta_\varphi \simeq \frac{\delta T}{T} \simeq 10^{-5}. \tag{148}$$

This seemingly naive argument actually solves one of the issues of the hot Big-Bang model: even though we mentioned in Chap. 3 that this model predicts the existence of CMB, it is very difficult to equip it with tiny anisotropies that we observe today. Instead, inflation naturally explains them as a direct consequence of the quantum fluctuations of the field that drive it, which got enhanced to microscopical scales and left their imprint on the temperature of CMB photons.

4.4 PRIMORDIAL DENSITY PERTURBATION

We have just seen that the adimensional power spectrum for primordial energy perturbations is related to the inflaton power spectrum (see Eq. 147), thus

$$\begin{aligned} \Delta_{\frac{\delta\rho}{\rho}}(k) = \frac{H^2}{\dot{\varphi}^2}\Delta_{\delta\varphi}(k)\big|_{t_H^{(1)}(k)} &= \left(\frac{H^2}{2\pi\dot{\varphi}}\right)^2 \left(\frac{k}{aH}\right)^{3-2\nu} = \\ &= \left(\frac{H^2}{2\pi\dot{\varphi}}\right)^2\Bigg|_{t_H^{(1)}(k)} . \end{aligned} \tag{149}$$

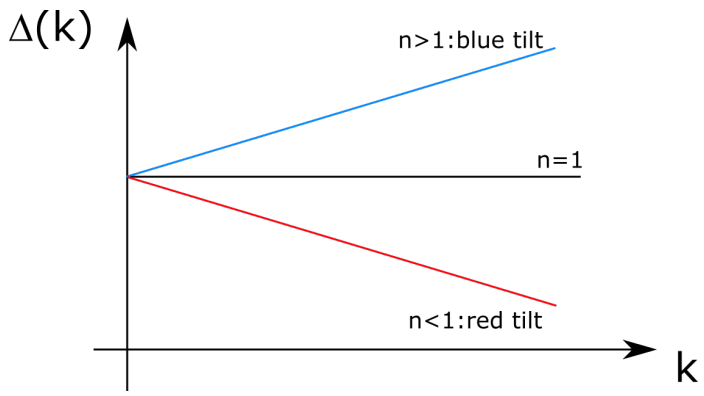

Figure 7: Spectral index classification. In a more general context, the distinction between blue/red-tilted and scale-invariant spectra is made w. r. t. 0, where, respectively $n > 0$, $n < 0$ and $n = 0$. In this case, we use 1 as the watershed because we refer to the particular notation used for the spectrum in Eq. 149.

We can now compute the scalar spectral index of primordial density perturbations, which is one of the most important prediction of inflationary models, defined as [1]

$$n_s - 1 \equiv \frac{\mathrm{d}\ln \Delta_{\frac{\delta\rho}{\rho}}(k)}{\mathrm{d}\ln k} = 3 - 2\nu = 2\eta_V - 6\varepsilon \,. \tag{150}$$

Inflationary models predict a power spectrum of density perturbations to have a spectral index which deviates from one by $\mathcal{O}(\varepsilon, \eta_V)$. Indeed, we have found a power spectrum very different from H-Z. At 68% Confidence Level (CL) we have [29]

$$n_s = 0.9681 \pm 0.0039 \,. \tag{151}$$

Indeed, the measured value is incompatible with $n_s = 1$ at $\sim 8\sigma$, which is a very robust statement.

To conclude, a classification of power spectra is given in terms of its spectral index (see Fig. 7). This will be useful in Chap. 5 and Chap. 13.

4.5 MORE DETAILS ON THE COSMIC MICROWAVE BACKGROUND

Now that we have gained some intuition on how the primordial fluctuations of the inflaton can be translated into temperature fluctuations, we can go into some more details about the CMB, introduced back in Chap. 2.

The CMB represents literally the most ancient point in time that we are able to explore via EM radiation, coming from the moment when the Universe was only 380 thousands of years old.

Before then, photons and electrons scattered efficiently and, thus, were in thermal equilibrium (see Chap. 2). This fact ensures that photons coming from that epoch should have a black-body spectrum. Indeed, this is true and has been the subject of many observations over the years. For example, COsmic Background Explorer (COBE) [32, 33] showed that the CMB is actually the most perfect blackbody we know (see Fig. 8). As mentioned in Chap. 2, the phenomenon that triggers the free-streaming behavior of photons is called "recombination" [3, 4].

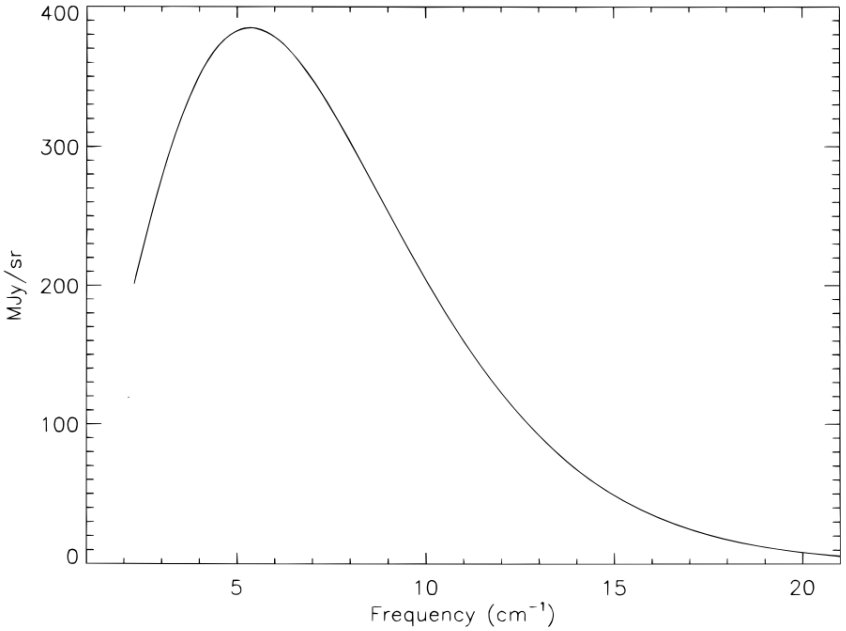

Figure 8: Monopole spectrum of CMB. The error bars of data are so small that it is impossible to distinguish them from the underlying theoretical prediction for a blackbody spectrum. Figure extracted from [22].

As the Universe expanded, the temperature of the plasma kept dropping, thus one can expect that, once it reached energies of the order of the atomic bounds (13.6 eV for the hydrogen), electrons and protons would start to combine in the more energetic-convenient hydrogen. Indeed, this is broadly what happened at recombination, with the caveat of the energy scale: it is necessary to wait until the plasma reached $\approx 1\,\mathrm{eV}$ to have the actual recombination, since the photons in the tails of the Gaussian distribution were still energetic enough to ionize hydrogen at higher energies [3].

However, the outcome is the same: after a transient, the Universe became full of neutral hydrogen atoms. From then on, photons traveled almost undisturbed to us.

In spite of this, CMB is far more interesting than a completely smooth picture of the Universe, since it is characterized by small anisotropies. Indeed, every phenomenon that interacts with photons traveling to us leaves some relic on their distribution.

4.5.1 *CMB Anisotropies*

In Chap. 2, we have mentioned that a way to describe CMB photons is following a Boltzmann approach to track their distribution throughout the history of the Universe. In Chap. 6, we show the detailed computation of the Boltzmann equations for GWs, so here we only show some passages. These two species share a very similar computation, especially in a collision-less scenario.

Considering only scalar perturbations of the metric, one can write [3]

$$\frac{\partial f}{\partial t} + \frac{\widehat{p}^i}{a}\frac{\partial f}{\partial x^i} - p\frac{\partial f}{\partial p}\left[H + \frac{\partial \Psi}{\partial t} + \frac{\widehat{p}^i}{a}\frac{\partial \Phi}{\partial x^i}\right] = 0\,. \tag{152}$$

The first two terms accounts for free-streaming, leading to the continuity and Euler equations [3]. The third one tells us that photons lose energy while the Universe keeps expanding, whereas the last two keep track of the effects caused by the scalar perturbations of the metric.

In the case of photons, we know that the distribution function takes the form of a Bose-Einstein distribution, perturbed by the presence of inhomogeneities [3]:

$$f(\vec{x}, p, \widehat{p}, t) \equiv \left[\exp\left\{\frac{p}{T(t)(1+\Theta(\vec{x}, \widehat{p}, t))}\right\} - 1\right]^{-1}, \tag{153}$$

which can be written as [3]

$$\begin{aligned} f =& \bar{f} - p\frac{\partial \bar{f}}{\partial p}\Theta \\ \simeq& \frac{1}{e^{p/T}-1} + \left[\frac{\partial}{\partial T}\left(\frac{1}{e^{p/T}-1}\right)\right] T\Theta\,. \end{aligned} \tag{154}$$

Here, the factor $-p\frac{\partial \bar{f}}{\partial p}\Theta$ represents a parametrization of the first order perturbation of the distribution function f, which allows to simplify the Boltzmann equation [3]. Note that here $\Theta = \Theta(\vec{x}, \widehat{p}, t)$ does not depend on p. This is a consequence of the photons being thermalized before recombination.

We have just sketched the beginning of the CMB photon treatment via the Boltzmann approach (for more details, see [3]). For the purpose of this section, it is sufficient to know that from this simple description one can consider a number of different interactions between photons and other particle species, which would appear in the RHS of Eq. 154, would affect the distribution function in many different ways and would lead to a complex solution of $\Theta(\vec{x}, \widehat{p}, t)$.

At the end of the day, assuming that one properly recovers such a solution, it is convenient to decompose it in Spherical Harmonics (SHs), given that we want to describe a quantity in the celestial sphere.

The decomposition amounts of doing

$$\Theta(\widehat{n}) = \sum_{\ell}\sum_{m=-\ell}^{\ell}\Theta_{\ell m}Y_{\ell m}(\widehat{n}) \quad \text{inverted by} \quad \Theta_{\ell m} = \int d^2n\Theta(\widehat{n})Y^*_{\ell m}(\widehat{n})\,, \tag{155}$$

where: $Y_{\ell m}(\theta, \varphi)$ = are the SHs;
$\Theta_{\ell m}$ = coefficients of the SH decomposition.

For completion, we remind the reader a few definitions behind SH: firstly

$$Y_\ell^m(\theta,\varphi) \equiv \sqrt{\frac{(2\ell+1)}{4\pi}\frac{(\ell-m)!}{(\ell+m)!}}\, P_\ell^m(\cos\theta)\, e^{im\varphi} \ , \tag{156}$$

where $P_\ell^m(\cos\theta)$ are the associate Legendre polynomials defined as a function of the Legendre polynomials as

$$P_\ell^m(x) \equiv (-1)^m(1-x^2)^{m/2}\frac{d^m}{dx^m}\left(P_\ell(x)\right) \ , \tag{157}$$

with the Rodriguez's formula expression of the Legendre polynomials yielding

$$P_n(x) \equiv \frac{1}{2^n n!}\frac{d^n}{dx^n}(x^2-1)^n \ . \tag{158}$$

Now, in the standard case of Gaussian fluctuations in a statistically isotropic Universe, the $a_{\ell m}$ coefficients encode completely the statistical properties of Θ.

At this point, one can define the angular power spectrum $\mathcal{C}_\ell$ as[3]

$$\langle a_{\ell m} a^*_{\ell' m'}\rangle = \delta_{\ell\ell'}\delta_{mm'}\mathcal{C}_\ell \ . \tag{159}$$

This is one of the main quantities that we want to measure today when analyzing CMB data. Indeed, it encodes all the processes that affected photons from Last Scattering Surface (LSS) to us today.

4.5.2 *Some Examples of Anisotropies*

Without entering into the details, which are beyond the goals of this Thesis, let us mention from a phenomenological and observational point of view what these anisotropies can look like.

- As mentioned above, before decoupling, photons and electrons were able to interact efficiently through Compton/Thompson scattering. This would also generate a competing pressure, provided by photons, to the gravitational attraction of matter.

  In other words, the gravitational infall compresses the fluid until the resistance of photon pressure reverses the motion [34], in such a way that acoustic waves were generated. These left visible relics on the CMB spectrum, named Barionic Acoustic Oscillations (BAOs) [35, 36].

- Studying in detail the CMB Boltzmann equations in the presence of scalar perturbations Φ, one can find that as the photons climb out of the potential wells at LSS (so after decoupling), gravity redshifts the temperature from $\frac{\delta T}{T}$ to $\frac{\delta T}{T}+\Phi$. Therefore, the effective perturbation at LSS will thus result in a similar result to $[\frac{\delta T}{T}+\Phi](\eta_{\rm cmb})$. The particu-

lar combination of intrinsic temperature fluctuations and gravitational redshift is called the ordinary Sachs-Wolfe (SW) effect [34, 37].

In fact, intuitively speaking, Φ represents a perturbation of the gravitational potential in the form of potential wells. These potential wells "attract" mainly matter, which tends to gather in them; however, the highly efficient coupling between matter and photons makes the latter in the same way "fall" in these wells. Subsequently, when the decoupling happens, photons start to free-stream and their frequency acquire a redshift equal to Φ while climbing back the potential well towards us [34].

Effects as the SW effect are called "primary" anisotropies, since they happened at the LSS, whereas subsequent effects are called "secondary" anisotropies and affect CMB photons along their journey to us [37].

Let us now cite some examples of secondary anisotropies:

- if the gravitational potentials vary with time, the photon will experience differential redshifts due to the gradient of Φ, which no longer yield equal and opposite contributions as the photons enter and exit the potential well, and time dilation effect relate to Ψ [34]. The sum of these contributions along the line of sight is called the Integrated Sachs-Wolfe (ISW) effect. Usually, this effect is divided in a early-ISW effect and a late-ISW, accounting for the Λ-dominated epoch [34, 37]. Another similar effect is the Rees-Sciama (RS) one, where higher order corrections to the density evolution cause time dependence in the gravitational potentials from the Poisson equation [38].

- After the reionization of the Universe, the radiation scattering onto free charges gets polarized and deviated, tending to erase small-scale peaks in the spectrum [39].

- Gravitational lensing causes the geodetics of CMB photons to change based on the spacetime distortions induced by massive objects [40].

All these anisotropies, along with many others we are not mentioning, carry information on a number of cosmological parameters and physical phenomena, allowing us to draw a comprehensive picture of the Universe.

4.5.3 *CMB Polarization*

Given the relevance for this Thesis, we spend some words on CMB polarization.

37 The more careful reader should have noticed that the over-densities are indeed $3D$ inhomogeneities and not anisotropies, thus an explanation is due. The LSS is a $2D$ surface of radius η_{CMB}, corresponding to the length covered by light from the moment of recombination to now, where we observe the effects of the inhomogeneities. Thus, the fact that the $3D$ inhomogeneities are projected on a $2D$ surface causes the fact that we see them as anisotropies on the CMB, meaning that changing the direction in the full-sky, we observe a slightly different temperature of the radiation.

Indeed, CMB photons are expected to be polarized by Compton scattering. There are two moments in time when this could leave measurable imprints on the CMB: recombination and reionization.

Without entering into detail, it can be shown that the fundamental requirement for polarization to be produced is the presence of a quadrupole perturbation of the photon distribution impeding on ionized electrons.

In the 2D plane perpendicular to propagation, the intensity can be decomposed into

$$I_{ij} = \begin{pmatrix} T+Q & U \\ U & T-Q \end{pmatrix}, \tag{160}$$

where T, Q, U are three of the 4 Stokes parameters. The fourth, that is, V is expected to be null in the standard cosmological picture [3].

Q and U can be further rearranged and decomposed into SHs, similarly to intensity:

$$(Q \pm iU)(\hat{n}) = \sum_{\ell m} {}_{\pm 2}a_{\ell m}(\hat{n})\, {}_{\pm 2}Y_{\ell m}\,, \tag{161}$$

where this time

$${}_sY_{\ell m} = \sqrt{\frac{(l-s)!}{(l+s)!}}\left(\partial^+\right)^s Y_{\ell m} \quad \text{and} \quad {}_sY_{\ell m} = (-1)^s\sqrt{\frac{(l+s)!}{(l-s)!}}\left(\partial^-\right)^{-s} Y_{\ell m} \tag{162}$$

are the spin-weighted SHs ensuring the proper rotation properties on the sphere to Q and U, and

$$\left(\partial^\pm\right)^s f(\theta,\phi) = -\sin^s\theta\left(\partial_\theta \pm \frac{i}{\sin\theta}\partial_\phi\right)\sin^{\mp s}\theta\, {}_sf(\theta,\phi) \tag{163}$$

are the spin-raising and spin-lowering operators acting on a generic function $f(\theta,\phi)$.

By defining

$$a^E_{\ell m} = -\frac{1}{2}\left({}_{+2}a_{\ell m} + {}_{-2}a_{\ell m}\right) \quad \text{and} \quad a^B_{\ell m} = -\frac{1}{2i}\left({}_{+2}a_{\ell m} - {}_{-2}a_{\ell m}\right), \tag{164}$$

we defined a decomposition of the polarization of CMB photons divided in a gradient and a curl component, i. e. the *E-modes* and *B-modes* (analogous to the electric and magnetic field of electromagnetism). One can show that only E-modes are generated in the presence of scalar perturbations. In fact, the E-mode varies in strength in the same direction as its orientation (or perpendicular to it) [3], so it makes sense that it is generated by a scalar quantity that carries only one DOF. Instead, B-modes need more than that to be produced, e. g. a GW perturbation (see Chap. 5), which carries two DOFs due to its tensorial nature.

The detection of primordial B-modes in CMB would be a clear proof of the presence of a Stochastic Gravitational Wave Background (SGWB). However, we must emphasize that GWs are not the only source of the curl component of polarization: for example, the deflection photons geodesics by mass distributions can also generate B-modes (this is called CMB lensing). This, together with many other complications, makes the detection of primordial B-modes extremely challenging.

An honorable mention must be given to foregrounds: on top of the very faint CMB B-mode signal, there are many more coming from galactic and extra-galactic phenomena, which often are also much stronger than CMB (i. e. thermal dust or synchrotron radiation). Fortunately, all these phenomena are characterized by specific Spectral Energy Distributions (SEDs), which are also different from the black-body we expect from CMB. This crucial feature allows us to disentangle the various signals if we measure B-modes at different frequencies through the so-called *component separation* techniques. Without entering into the details of this very prolific field of research, we mention that these techniques are separated into two macrocategories: in *parametric methods*, one describes different phenomena with different SEDs and essentially tries to fit their parameters [41–43]. On the other hand, *blind methods* do not assume any shape for SEDs, as the name suggests, and instead minimize the variance of the CMB component [44–48].

Part II

ADDING TENSOR PERTURBATIONS

So far, we have examined the primary features of a ΛCDM Universe characterized by scalar perturbations. In this part, we investigate the implications of introducing tensor perturbations, namely GWs. Our exploration will focus on one of the key predictions of inflationary models, a primordial background of GWs. After exploring the characteristics of this background within the standard single-field model, we will delve into examples of more intricate inflationary models. Additionally, we will briefly touch upon the ramifications that the existence of such a background introduces into our understanding of the Universe outlined in the preceding part. This will allow us to underscore the physical phenomena that can be examined to explore the tensor component of the Universe. Lastly, we will employ the Boltzmann approach to model the distribution of GWs and derive the angular power spectrum of the primordial GW background.

5

GRAVITATIONAL WAVES FROM INFLATION

At this point, we have followed the entire course leading to one of the fundamental predictions of inflationary models, the Cosmological Gravitational Wave Background (CGWB). In this chapter, we explore the implications of the standard single-field slow-roll model of inflation and go beyond, momentarily setting aside the criterion of simplicity. For example, we touch upon multifield inflation at the second order in perturbations. Ultimately, we examine how the presence of GWs modifies the aspects of the "scalar" Universe discussed in the preceding chapters. For additional insights, refer to [30, 49, 50].

5.1 SINGLE-FIELD SLOW-ROLL INFLATION

Even in the simplest model of inflation described in Chap. 4, tensor perturbations of the metric generate a SGWB. Such a background is a continuous set of waves fully characterized by their global statistical properties. In fact, they consist of a signal coming from every direction in the sky and having an entire spectrum in the frequency domain; on the contrary, a couple of merging neutron stars produces GWs with a specific direction in the sky and peaked at a specific frequency at coalescence. However, if we consider a large enough number of merging astrophysical objects, one can obtain the astrophysical analogue of the CGWB, i. e. an Astrophysical Gravitational Wave Background (AGWB). The number of objects must exceed the confusion limit to make it impossible to distinguish one from the other on our detectors [51, 52].

Neglecting scalar and vector perturbations, the perturbed spatially flat FLRW metric is[38],

$$ds^2 = -dt^2 + a^2(t)\left[\delta_{ij} + h_{ij}\right] dx_i dx_j \ , \tag{165}$$

with h_{ij} such that

$$h_{ij} = h_{ji} \quad , \quad h^i{}_i = 0 \quad , \quad h^i{}_{j|i} = 0 \ ^{39}. \tag{166}$$

The gauge choice bringing to these relations is called Transverse-Traceless (TT) gauge.

38 At linear level scalar, vector and tensor perturbations are decoupled, meaning that their evolution do not depend on one another. For this reason considering only the tensor ones is not a physical simplification, but only a way to obtain easier calculi.

39 The expression $h^i{}_{j|i}$ indicate the spatial covariant derivative built from the FLRW background metric g_{ij}, which for $k = 0$ is the normal covariant derivative.

At the linear level, the EOM for h_{ij} reads [1]

$$\ddot{h}_{ij} + 3H\dot{h}_{ij} - \frac{\nabla^2 h_{ij}}{a^2} = \Pi_{ij}^{TT} \,, \tag{167}$$

where Π_{ij}^{TT} is a tensor with the same properties as Eq. 166, which is a source term coming from possible anisotropic stress of the matter source. It is related to the last term of the stress-energy tensor of a perfect fluid $T_{\mu\nu} = (\rho + P)u_\mu u_\nu + P g_{\mu\nu} + \pi_{\mu\nu}$, called the anisotropic stress tensor, which, for example, can get a contribution by the quadrupole momentum of two merging objects (see also next section Sec. 5.2). At first order, it is vanishing for single field inflation, therefore during inflation holds

$$\ddot{h}_{ij} + 3H\dot{h}_{ij} - \frac{\nabla^2 h_{ij}}{a^2} = 0 \,, \tag{168}$$

which is the same equation we solved for the quantum vacuum fluctuation of a massless scalar field (see Chap. 4). Here, we are looking at the quantum fluctuations of the metric itself, since there is no source term. In fact, these primordial GWs are the result of intrinsic quantum fluctuations of the metric, and if we can detect them, we will have found a "smoking gun" of inflation. Also, they would be the first ever detected evidence of quantum gravity.

Eq. 168 describes the evolution of a tensor object, with 2 independent DOFs[40], corresponding to the two possible polarizations of GWs $\lambda = (+, \times)$. We can decompose such an object in the Fourier space as [1]

$$h_{ij}(\vec{x}, \eta) = \sum_{+\times} \int \frac{d^3k}{(2\pi)^3} e^{i\vec{k}\,\vec{x}} h_\lambda(\vec{k}, \eta) \varepsilon_{ij}^{\lambda}(\vec{k}) \,, \tag{169}$$

where $\varepsilon_{ij}^{\lambda}(\vec{k})$ are the polarization tensors, which satisfy $\forall\lambda$

$$\varepsilon_{ij} = \varepsilon_{ji} \quad , \quad \varepsilon^i{}_i = 0 \quad , \quad k^i \varepsilon_{ij}(\vec{k}) = 0, \tag{170}$$

and the normalization conditions

$$\varepsilon_{ij}^{\lambda}(\vec{k}) \varepsilon_{\lambda'}^{*ij}(\vec{k}) = \delta_{\lambda\lambda'} \quad , \quad \left(\varepsilon_{ij}^{\lambda}(\vec{k})\right)^* = \varepsilon_{ij}^{\lambda}(-\vec{k}) \,. \tag{171}$$

Suppose to have a plane monochromatic gravitational wave propagating in the $\hat{z}$ direction, in Fourier space we obtain

$$\varepsilon_{ij}^{+} = \begin{pmatrix} 1 & 0 \\ 0 & -1 \end{pmatrix} \quad , \quad \varepsilon_{ij}^{\times} = \begin{pmatrix} 0 & 1 \\ 1 & 0 \end{pmatrix} \quad , \tag{172}$$

$$h_{ij}(\vec{k}, \eta) = h_+(\vec{k}, \eta) \varepsilon_{ij}^{+}(\vec{k}) + h_\times(\vec{k}, \eta) \varepsilon_{ij}^{\times}(\vec{k}) \,. \tag{173}$$

40 h_{ij} is a 3×3 object, symmetric condition reduces the 9 initial DOF into 6, while "traceless" and "transverse" conditions consist in other 4 constraints. Therefore, h_{ij} has 2 DOF

The EOM in Fourier becomes

$$\ddot{h}_\lambda + 3H\dot{h}_\lambda + k^2\frac{h_\lambda}{a^2} = 0\,, \tag{174}$$

which is the same for each polarization state and it is again analog to the equation of motion of a minimally coupled scalar field ($h_{+,\times} \leftrightarrow \sqrt{32\pi G}\phi_{+,\times}$).

On super-horizon scales, $k \ll aH$, the solution is $h_{+,\times}$ =constant plus a decaying mode (see Chap. 4). The amplitude is, due to canonical normalization [1]:

$$|h_{+,\times}| = \sqrt{32\pi G}|\phi_{+,\times}| = \sqrt{32\pi G}\frac{H}{\sqrt{2k^3}}\left(\frac{k}{aH}\right)^{-\varepsilon}. \tag{175}$$

On subhorizon scales, $k \gg aH$, $h_{+,\times} = \frac{e^{-ik\eta}}{a(\eta)}$.

5.1.1 *Stochastic Background of GWs*

Let us analyze the power spectrum for a single polarization state of tensor perturbations of the metric, which corresponds to gravitational waves; remembering Eq. 175 it is given by

$$\begin{aligned}\Delta_t^{+,\times}(k) =& 32\pi G\frac{k^3}{2\pi^2}|h_{+,\times}|^2 = 32\pi G\left(\frac{H}{2\pi}\right)^2\left(\frac{k}{aH}\right)^{-2\varepsilon} \\ =& \frac{8}{\pi}\left(\frac{H}{M_P}\right)^2\Big|_{t_H^{(1)}(k)}\,,\end{aligned} \tag{176}$$

where $t_H^{(1)}(k)$ is the time of horizon exit, in which the scale of gravitational waves gets fixed, and k is the GW one $k = \frac{2\pi}{\lambda_{GW}}$. The total power spectrum is the sum of the two polarizations

$$\Delta_t(k) = \frac{16}{\pi}\left(\frac{H}{M_P}\right)^2\Big|_{t_H^{(1)}(k)} = \frac{16}{\pi}\left(\frac{H}{M_P}\right)^2\left(\frac{k}{aH}\right)^{-2\varepsilon}. \tag{177}$$

Therefore the spectral index of inflationary GWs is defined as

$$n_t \equiv \frac{\mathrm{d}\ln\Delta_t(k)}{\mathrm{d}\ln k} = -2\varepsilon\,. \tag{178}$$

As aforementioned, in the simplest models one has $\varepsilon > 0$ so n_t is always red tilted, thus on smaller and smaller scales the amplitude decreases. This fact will play a key role in assessing the feasibility of a detection of such a background with future GW detectors (see e. g. [53]). Note also that scale-invariance is defined as $n_t = 0$, whereas for scalar perturbations $n_s = 1$ (see Chap. 4).

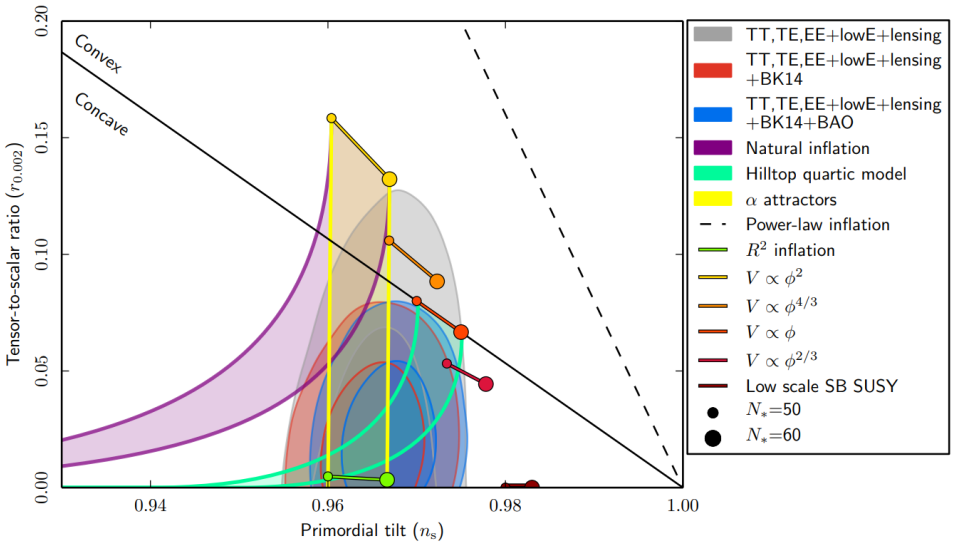

Figure 9: Marginalized joint 68% and 95% CL regions for n_S and r at $k = 0.002\,\mathrm{Mpc}^{-1}$. Note that the marginalized joint 68% and 95% CL regions assume $\frac{dn_S}{d\ln k} = 0$ (no index running). Figure extracted from [54].

In addition, we can define the *tensor-to-scalar perturbation ratio* as [1]

$$r \equiv \frac{\Delta_t}{\Delta_{\frac{\delta\rho}{\rho}}} = \frac{\Delta_t}{\Delta_\zeta} \,. \tag{179}$$

One can notice that since Δ_t at horizon crossing depends only on H^2, measuring it would indeed provide us information of the energy scale of inflation because $V \simeq E_{INF}^4$.

We can also rewrite it as function of the slow-roll parameters. In fact, recalling $\varepsilon = -\frac{\dot{H}}{H^2} = 4\pi G\frac{\dot{\varphi}^2}{H^2}$, we can express Δ_ζ as

$$\Delta_\zeta = \left.\frac{H^4}{4\pi\dot{\varphi}^2}\right|_{t_H} = \left.\frac{H^2}{4\pi^2}\frac{4\pi G}{\varepsilon}\right|_{t_H} = \frac{H^2}{\pi M_P^2\varepsilon} \,, \tag{180}$$

with which

$$r = \frac{\Delta_t}{\Delta_\zeta} = \frac{\frac{16H^2}{\pi M_P^2}}{\frac{H^2}{\pi M_P^2\varepsilon}} = 16\varepsilon \,. \tag{181}$$

Also, since we know the spectral index of tensor modes, $n_t = -2\varepsilon$ we have the so-called *single-field slow-roll consistency relation* [1]

$$r = -8n_t \,, \tag{182}$$

which is a relation between two observable quantities. Observing it is a clear proof of inflation, given that there are no other scenarios in the early Universe providing this same prediction. This is not an easy task at all, it requires a full measurement of the CGWB in its amplitude and spectral index,

but it would be so crucial to the Cosmology community that this is also referred to as "*holy grail of inflation*".

5.2 BEYOND SINGLE-FIELD SLOW-ROLL INFLATION AT FIRST-ORDER

Until now, we have considered only single-field slow-roll inflation at first-order in the perturbations; however, a plethora of more complex models have been explored in the literature, each with its own predictions on the SGWB produced. Here, we will very briefly mention some alternatives to the standard picture that we presented above.

5.2.1 *Second-order GWs*

First, suppose that we stick to single-field slow-roll inflation. At first order, scalar, vector, and tensor perturbations are independent; however, at higher order, this is not true. For example, the combination of first-order scalar perturbations gives rise to second-order GWs. In other words, even neglecting completely tensor perturbations of the metric, the very existence of scalar perturbations gives rise to tensor modes. It can be shown that the EOM of GWs is essentially Eq. 167 where Π in this case is the source function that accounts for the second-order production of GWs. Of course, if we consider the scenario in which the scalar primordial perturbations are the origin of this second-order term, this source term will be related to the scalar primordial spectrum defined in Eq. 149 [55–60].

Of course, this scenario becomes even more important if we consider more than one scalar field during inflation. For example, second-order GWs can be sourced by the presence of a *curvaton* [61, 62] or *spectator* scalar fields [63–65].

5.2.2 *GWs from Particle Production*

Another interesting mean of producing GWs is particle production. Indeed, if the inflaton is coupled with some other field (minimally or non-minimally), its energy can move to other sectors and produce extra quanta of other particles [66]. These would contribute to the anisotropic component of the stress-energy tensor and source GWs (again through the RHS of Eq. 167). These models are typically divided into two groups, depending on when particle production occurred. The first consists of models where the inflaton is coupled to some field during inflation; for example, the inflaton might be coupled to scalar fields [67, 68], axions [69–71], or gauge fields [72, 73]. The latter group consists of models where the inflaton interacts during *reheating* [74, 75]. We have not mentioned this period before, which represents the bridge between inflation and the hot Big-Bang evolution of the Universe. Indeed, we need to convert the energy stored in the inflaton into other particles to account for the predictions, and observations, related to the hot Big-Bang theory. The mechanisms behind the physics of reheating are still unknown

and very difficult to test. In fact, any feature born during that phase would be washed out by thermalization; also, such a feature evolves throughout the entire history of the Universe without leaving imprints of their initial conditions. For this reason, GWs represent a unique window in the physics of reheating [76–78].

5.2.3 *Modified Gravity Models*

Of course, modified gravity models change the physics of GWs. Relatively recently, the possibility of GWs propagating with a velocity different from c has been essentially ruled out (or severely restricted) by [51, 52]; however, many other models of modified gravity are still viable alternatives to GR [79–83]. Notable mentions are $f(R)$ theories, where higher-order terms as R^2 appear in Eq. 2, and scalar-tensor theories, which allow for scalar fields in the gravitational sector.

Among these, R^2-inflation (also called *Starobinski inflation*) is regarded as one of the most promising models today [84]. Indeed, looking at Fig. 9, one can notice that this model fits well the posterior distribution in the $r - n_s$ plane. The difference w. r. t. GR is given by this substitution:

$$R \longrightarrow R + \frac{R^2}{6M_P^2} \tag{183}$$

in the Hilbert-Einstein action of Eq. 2.

5.2.4 *General Consistency Relations*

We saw that in standard single-field inflation the consistency relation of Eq. 182 is enforced, i. e. a relation between r and n_t. Other models may predict different consistency relations; thus, here we list some of them.

GENERAL SINGLE-FIELD INFLATION In these models [85, 86], the inflaton sound speed can be $c_s \neq c$ and the consistency relation reads

$$r = -8c_s n_t \ . \tag{184}$$

MULTI-FIELDS INFLATION If, for example, inflation is driven dynamically by multiple scalar fields, both adiabatic and isocurvature perturbations are generated [87, 88]. The consistency relation becomes

$$r = -8n_t \sin^2 \Delta \ , \tag{185}$$

where $\cos \Delta$ parametrize the correlation between adiabatic and isocurvature perturbations at horizon exit.

SPACE-TIME VARIATIONS OF INFLATON DECAY We mentioned that during reheating the inflaton decays to ordinary particles, which we can

generally call χ. While the inflaton decays at a rate Γ, χ can fluctuate and leave imprinted these variations on super-horizon scales. In this scenario, Γ cannot be considered constant causing a change in the perturbation of the curvature ζ [89]. Parameterizing it with $\Delta = (\zeta_f - \zeta_i)/\zeta_i$, where i and f indicate the beginning and end of the reheating, we can write the consistency relation as

$$r = -8(1 - 2\Delta)n_t \,. \tag{186}$$

EFT INFLATION In the context of Effective Field Theories (EFTs) of inflation [90–93], one can find a very general consistency relation:

$$r = -\frac{32}{\pi}\frac{n_t - s_t}{c_t c_s'^2}\left(\alpha_0 + \sqrt{\beta_0}\right)^{3/2}\left|\Gamma\left(\frac{5}{4} + \frac{\alpha_0}{4\alpha_0 - 4i\sqrt{\beta_0}}\right)\right|^2 \tag{187}$$

where: c_s' = parameter related to the kinetic energy of a scalar field in the action [41];
c_t = tensor perturbation speed;
s_t = $-\frac{\dot{c}_t}{Hc_t}$ is a slow-roll parameter associated with c_t;
α_0 = parameter controlling the term in the dispersion relation $\propto k^2$;
β_0 = parameter controlling another term $\propto k^4$;
Γ = Euler Gamma function.

Despite the multitude of possibilities offered by inflation, from now on we will stick to the single-field slow-roll model, until it is differently specified. Also, we must mention that inflation is not the only production mechanism in the early Universe. For example, both PTs, as the EW one introduced in Chap. 2, or the presence of cosmic strings, i. e. topological defects due to some spontaneous symmetry breaking (see also Chap. 3), can produce primordial GWs that can be treated through a Boltzmann approach as we are about to present in Chap. 6 (see, for example, [94, 95]).

5.3 IMPRINTS OF GWS ON THE "SCALAR" UNIVERSE

First, GWs can be a probe for the thermal history of the Universe (see Chap. 2). It can be shown that the GW energy density for modes inside the horizon can be written as [30]

$$\Omega_{GW}(k,\eta) = \frac{1}{12}\left(\frac{k}{aH}\right)^2 \Delta_t^2(k) T_h^2(k,\eta) \tag{188}$$

41 Unlike the sound speed c_s, it can be negative.

where: Δ_t = is the primordial power spectrum defined in Eq. 177;
$T_h(k,\eta)$ = is the transfer function describing the evolution of GW modes when they enter the horizon ($T_h(k,\eta) \to 1$ for $k \to 0$).

The transfer function can be written as

$$T_h^2(k) = \Omega_m^2 \left(\frac{g_*(T_{in})}{g_{*0}}\right)\left(\frac{g_{*s0}}{g_{*s}(T_{in})}\right)^{4/3}\left(\frac{\overline{3j_1(k\eta_0)}}{k\eta_0}\right)^2 T_1^2(x_{eq})T_2^2(x_R)\,, \tag{189}$$

where: g_* = is the number of relativistic DOFs;
g_{*s} = is its counterpart in entropy;
0 = indicates a quantity evaluated at present time;
T_{in} = is the temperature at the horizon entry;
j_1 = is the spherical Bessel function for $\ell = 1$, which is averaged over time to extract the amplitude behavior (the bar indicates the average);
$T_1^2(x_{eq}) = 1 + 1.57x_{eq} + 3.42x_{eq}^2$ is a function that accounts for GWs entering before and after the matter-radiation equality;
x_{eq} = $\frac{k}{k_{eq}}$;
$T_2^2(x_R) = 1 - 0.32x_R + 0.99x_R^2$ is a function to describe the change in the expansion rate after reheating;
x_R = $\frac{k}{k_R}$.

This means that accurately measuring Ω_{GW} provides information about decoupling of relativistic species and about the physics of reheating. For example, assuming that the reheating stage is matter-dominated, the shift to the subsequent radiation-domination causes the presence of a knee in Ω_{GW}. If we take $10^6\,\text{GeV} \lesssim T_R \lesssim 10^9\,\text{GeV}$, the knee would affect the frequencies of $10^{-1} - 10^2\,\text{Hz}$, which is in the frequency band of Laser Interferometer Gravitational-Wave Observatory (LIGO)-Virgo-Kamioka Gravitational Wave Detector (KAGRA) [96–100].

Furthermore, being GWs relativistic DOFs, they contribute to the radiation energy density. This implies that BBN physics is affected by the presence of a CGWB, providing a bound at frequencies of $f \gtrsim 10^{-15}\,\text{Hz}$ [101–103].

Moving to another imprint, during the history of the Universe, free-streaming particles and generate an anisotropic stress-energy contribution, which would modify the GW EOM. The most studied particle species in this context are neutrinos [104]. At first-order, this effect provides a damping of GWs [105, 106], while the second-order acts as a source term [107, 108]. The damping effect would act on scales corresponding to neutrinos decoupling, thus $f \sim 10^{-11}\,Hz$, which is close to the band of Pulsar Timing Arrays (PTAs).

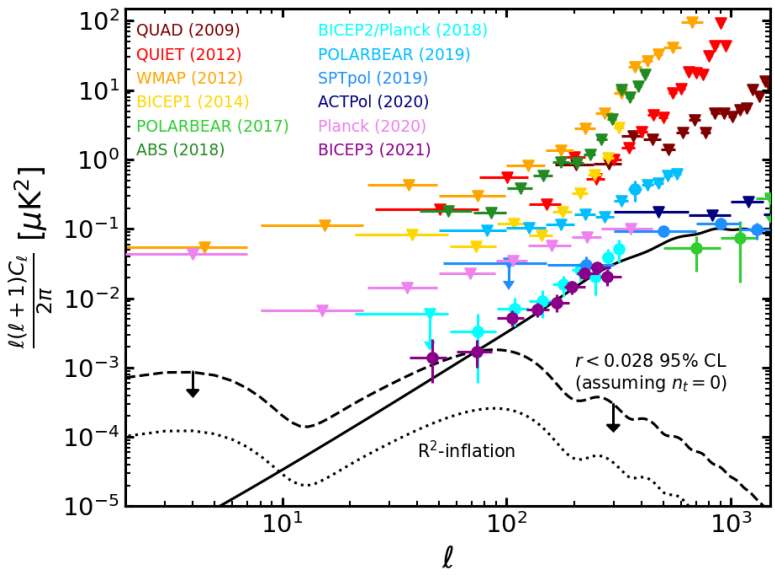

Figure 10: CMB B-mode measurements: Background Imaging of Cosmic Extragalactic Polarization (BICEP)3/Keck Array [113], Planck's satellite [114], Atacama Cosmology Telescope Polarimeter (ACTPol) [115], South Pole Telescope polarimeter (SPTpol) [116], POLARization of the Background Radiation (POLARBEAR) [117, 118], BICEP2/Keck Array [119], Atacama B-Mode Search (ABS) [120], BICEP1 [121], Wilkinson Microwave Anisotropy Probe (WMAP) [122], Q and U Extragalactic Sub-mm Telescope (QUIET) [123] and QUIET at Degree Angular Scale Interferometer (DASI) (QUaD) [124]. The solid line represents the lensing signal, whereas the dashed and dotted ones are respectively the primordial signal obtained assuming scale invariance and $r = 0.028$ and 0.004, the former being the 95% CL upper bound of this work, assuming scale-invariance, and the latter the prediction of the Starobinski model [84].

In Chap. 4, we briefly discuss CMB polarization, mentioning that B-modes are generated in the presence of GW perturbations. In fact, this is one of the most promising imprints of GWs. Currently, we have quite a zoology of CMB B-mode measurements, some of which are shown in figure 10. However, CMB experiments are mostly sensitive to the large-scale part of the primordial B-mode spectrum (at least by assuming a tensor spectral tilt close to scale invariance). The small scales are hidden below several orders of magnitude of the lensing B-mode as a result of photons passing through the gravitational potential of the large-scale structure (compare the dashed, or dotted, line of figure 10 with the solid one and see Sec. 4.5). In addition, any peculiar feature of the primordial GWs would induce additional signatures on the CMB, such as non-Gaussianity or chirality [67, 109–112].

Besides the CMB, GWs leave imprints on the large-scale structures too. For example, at late times they induce: a tidal effect during structure formation in the presence of long-wavelength tensor modes, which manifest in a quadrupole anisotropy contribution [125, 126]; a correlation on the galaxy shear [127, 128]; and projection effect due to the space-time perturbation caused by GW [127, 129]. They would also affect the propagation of light from close objects, which can be tracked by looking at microsecond pulsars (PTAs sensitive to $f \sim 10^{-9} - 10^{-7}$ Hz) [130, 131]. This channel of observation has gained a lot of momentum in the last few years. Indeed, PTA collaboration all over the world has claimed to have detected for the first time a SGWB (see, for example, [132, 133]). Finally, GW interferometers can detect single merger events, but in principle they can detect any background permeating space-time if the energy contribution at their scales is large enough [52, 130, 134, 135].

This list is not meant to be complete at all; however, it should convey the idea that the presence of GWs affects a vast range of frequencies that can be probed with very different experiments to unveil various physical

properties of our Universe. In this Thesis, we will consider three ways to inspect primordial GWs: CMB, PTAs and GW interferometers.

6

BOLTZMANN APPROACH TO THE CGWB

In Chap. 5, we explored the general characteristics of a CGWB generated by single-field slow-roll inflation (and beyond). Here, we utilize the Boltzmann framework introduced in Chap. 2 to analyze GWs and derive the expression for the angular power spectrum of the CGWB.
For further details, refer to [49, 50].

6.1 BOLTZMANN EQUATIONS

In Chap. 2 we have already introduced the basics of the Boltzmann approach to track the behavior of a particle species. In particular, we showed the main steps to obtain the scalar angular power spectrum of CMB photons.

Here, we do the same in much more detail for GWs. First, we define a distribution function for "gravitons" as $f = f(x^\mu, p^\mu)$, which generally depends on their position x^μ and the momentum along their trajectory $p^\mu(x)$, parameterized by an affine parameter λ. This function will evolve according to the well-known Boltzmann equation [3, 136, 137]

$$\mathscr{L}[f(x^\mu, p^\mu)] = \mathscr{C}[f(x^\mu, p^\mu)] + \mathscr{I}[f(x^\mu, p^\mu)] \,, \tag{190}$$

where:

- $\mathscr{L}$ is the Liouville operator.
- $\mathscr{C}$ is the collision operator that accounts for the GW scatterings.
- $\mathscr{I}$ is the emission operator [138]. In principle, this operator can contain contributions coming from a number of possible sources of GWs. E. g. from an astrophysical point of view, we know that merging binary systems emit GWs, thus they would appear in terms of their changing quadrupole momenta [52, 139].

  From a cosmological point of view, instead, we know that many production mechanisms of GWs can come into play (e. g. phase transitions [140] or enhanced density perturbations leading to primordial BHs [141–143], which occur at energies well below the Planck scale). However, in our case, we consider only inflation as a production mechanism (see e. g. [66, 69]).

It must be emphasized that here we are interested in the GWs that we can measure (or we forecast to be able to detect in the next future), which have a typical wavelength much smaller than the scales where the background is

varying. This means that we are in the limit of geometric optics and that we can treat them separately [94].

Going back to Eq. 190, in our treatment we will disregard both the collision term, given that graviton scatterings affect the distribution function at higher orders in the gravitational strength M_{Pl}^{-1}, where M_{Pl} is the reduced Planck mass (see [144] for a discussion on collisional effects involving gravitons), and the source terms coming from astrophysical sources, since we are only interested in the CGWB. The GW emission coming from inflation is treated as an initial condition on the distribution, thus the Boltzmann equation are recast to

$$\frac{\mathrm{d}f}{\mathrm{d}\lambda} = 0 = \frac{\mathrm{d}\lambda}{\mathrm{d}\eta}\frac{\mathrm{d}f}{\mathrm{d}\lambda} = \frac{\mathrm{d}f}{\mathrm{d}\eta} = \frac{\partial f}{\partial \eta} + \frac{\partial f}{\partial x^i}\frac{\mathrm{d}x^i}{\mathrm{d}\eta} + \frac{\partial f}{\partial q}\frac{\mathrm{d}q}{\mathrm{d}\eta} + \frac{\partial f}{\partial n^i}\frac{\mathrm{d}n^i}{\mathrm{d}\eta} = 0\,, \quad (191)$$

where: η = conformal time;
$\widehat{n}$ = GW direction of motion;
$q = a|\vec{p}|$ is the comoving momentum modulus.

In order to proceed further we need to explore how gravitons travel in a perturbed Universe. This will provide us with the necessary tool to make explicit the above expression for the evolution of the distribution function.

We know that the metric of a flat and unperturbed FLRW Universe is

$$ds^2 = a^2(\eta)\left[-d\eta^2 + \delta_{ij}dx^i dx^j\right]\,. \quad (192)$$

In full generality the perturbed FLRW metric can be decomposed in [30]

$$g_{00} = -a^2(\eta)\left(1 + 2\sum_{r=1}^{+\infty}\frac{1}{r!}\Phi^{(r)}\right)\,, \quad (193)$$

$$g_{i0} = g_{0i} = a^2(\eta)\sum_{r=1}^{+\infty}\frac{1}{r!}\omega_i^{(r)}\,, \quad (194)$$

$$g_{ij} = a^2(\eta)\left\{\left[1 - 2\left(\sum_{r=1}^{+\infty}\frac{1}{r!}\Psi^{(r)}\right)\right]\delta_{ij} + \sum_{r=1}^{+\infty}\frac{1}{r!}\chi_{ij}^{(r)}\right\}\,, \quad (195)$$

where: (r) = order of the perturbation ;
Φ, Ψ = scalar perturbations called "gravitational potentials" ;
ω_i = vector perturbations;
χ_{ij} = TT tensor perturbations, for which $\chi_i^{i(r)} = 0 = \partial^i\chi_{ij}$.

It is easy to notice that sending all the perturbations to zero recovers the background metric.

Considering only first-order perturbations, we can recast the metric to

$$ds^2 = a^2(\eta)\left[-(1+2\Phi)d\eta^2 + 2\omega_i d\eta dx^i + \left[(1-2\Psi)\,\delta_{ij} + \chi_{ij}\right]dx^i dx^j\right]\,.$$

(196)

Now, exploiting the Helmholtz's theorem one can always decompose a N-vector to identify the nature of the DOF embedded in it [1]. Therefore, $\omega_i = \omega_i^{\perp} + \partial_i \omega^{||}$, where $\omega^{||}$ is an irrotational, or curl-free, scalar component (also called potential flow); on the other hand, $\omega_i^{\perp}$ is a divergence-free, or solenoidal, vector with $\partial^i \omega_i^{\perp} = 0$ (also called vorticity), which is perpendicular to $\widehat{k}$ in Fourier space. Decomposing in a similar way a tensor, one can distinguish scalar, vector and tensor DOF resulting in[42]:

$$\chi_{ij} = D_{ij}\chi^{||} + \partial_i \chi_j^{\perp} + \partial_j \chi_i^{\perp} + \chi_{ij}^{T} \,, \tag{197}$$

where $D_{ij} = \left(\partial_i \partial_j - \frac{1}{3}\delta_{ij}\nabla^2\right)$ is the trace-free operator, $\chi^{||}$ is a scalar function and $\chi_i^{\perp}$ is a solenoidal vector field.

At this point, we have identified all the DOFs, so we can choose a gauge in which to perform our calculations. In this case, we use the Poisson gauge, which is translated as $\omega^{||} = \chi^{||} = \chi_i^{\perp} = 0$. In addition, we neglect the remaining vectorial perturbations, given that they are rapidly diluted by the accelerated expansion [1]. This results in having

$$ds^2 = a^2(\eta)\Big[-(1+2\Phi)d\eta^2 + \left[(1-2\Psi)\,\delta_{ij} + \chi_{ij}\right] dx^i dx^j\Big] \,, \tag{198}$$

where $\chi_{ij} = \chi_{ij}^{T}$ for the sake of notation.
Mimicking the procedure typical of CMB (see e. g. [136]), in this metric the Christoffel symbols take the form

$$\begin{aligned}
\Gamma^0_{00} &= \mathcal{H} + \phi' \,, \\
\Gamma^0_{0i} &= \partial_i \phi \,, \\
\Gamma^i_{00} &= \partial^i \phi \,, \\
\Gamma^i_{0j} &= \delta^i_j \left[\mathcal{H} - \psi'\right] + \frac{1}{2}\chi'^i_j \,, \\
\Gamma^0_{ij} &= \mathcal{H}\delta_{ij} + \frac{1}{2}\chi'_{ij} - \psi'\delta_{ij} + \mathcal{H}\chi_{ij} - 2\mathcal{H}\delta_{ij}\phi - 2\mathcal{H}\delta_{ij}\psi \,, \\
\Gamma^i_{jk} &= -\frac{1}{2}\partial^i \chi_{jk} + \delta_{jk}\partial^i\psi + \frac{1}{2}\partial_j \chi^i_k - \delta^i_k \partial_j \psi + \frac{1}{2}\partial_k \chi^i_j - \delta^i_j \partial_k \psi \,,
\end{aligned} \tag{199}$$

where: $'$ = derivative w. r. t. conformal time;
$\partial_i \equiv$ $\frac{\partial}{\partial x^i}$ are the spatial derivatives;
$\mathcal{H} \equiv$ $\frac{a'}{a}$ is the conformal Hubble parameter.

At this point, we need to look into the explicit expression of the graviton momenta. Indeed, recalling Eq. 32, we need an expression for $p^\alpha \equiv \frac{dx^\alpha}{d\lambda}$.

42 These properties hold: $\chi_{ij}^T = \chi_{ji}^T$, $\partial^i \chi_{ij}^T = 0$ and $\chi^{j\ T}_{\ i} = 0$.

The first thing we can do is to exploit some basic property of momenta in GR; indeed, calling p the modulus of spatial momentum $\vec{p}$ and $\hat{n}$ its versor, we know that both the following expressions will hold

$$g_{ij}p^i p^j = p^2 \quad \text{and} \quad p^\mu p^\nu g_{\mu\nu} = -m^2 \,. \tag{200}$$

Asking now that the spatial momentum takes the form [136] $p^i = G(p, n^i, a, \Phi, \Psi, \chi)n^i$, where G can be in principle a function of all the perturbations, the modulus of the momentum and the scale factor, we can find its expression exploiting the first relation of Eq. 200 [43] Indeed, inserting this parameterization of p^i into it, we can write[44]

$$p^i = \frac{p}{a}e^{\Psi}\left(1 - \frac{1}{2}\chi_{jk}n^j n^k\right)n^i \,. \tag{201}$$

Looking instead at the second relation in Eq. 200 and assuming the graviton to be massless, we can write

$$p_\mu p^\mu = g_{00}\left(p^0\right)^2 + g_{ij}p^i p^j = -m^2 = 0 \,. \tag{202}$$

This allows us to find the explicit expression for p^0:

$$\begin{aligned} g_{00}\left(p^0\right)^2 + g_{ij}p^i p^j = -a^2e^{2\Phi}\left(p^0\right)^2 + p^2 = 0 \\ \left(p^0\right)^2 = \frac{p^2}{a^2}e^{-2\Phi} \Rightarrow p^0 = \frac{p}{a}e^{-\Phi} \,. \end{aligned} \tag{203}$$

Then, we can then define the comoving momentum as $q^\mu \equiv p^\mu / a$, which is useful to write in an alternative way p^0 and p^i as [136]

$$p^0 = \frac{q}{a^2}e^{-\Phi} \quad , \quad p^i = \frac{q}{a^2}e^{\Psi}\left(1 - \frac{1}{2}\chi_{jk}n^j n^k\right)n^i \tag{204}$$

At this point we can reconstruct the full expression of Eq. 191.

- Let us start from $\frac{dx^i}{d\eta}$. We can recast it as [136]

$$\frac{dx^i}{d\eta} = \frac{p^i}{p^0} = \frac{\frac{q}{a^2}e^{\Psi}\left(1 - \frac{1}{2}\chi_{jk}n^j n^k\right)n^i}{\frac{q}{a^2}e^{-\Phi}} = e^{\Phi+\Psi}\left(1 - \frac{1}{2}\chi_{jk}n^j n^k\right)n^i \,. \tag{205}$$

  This term is multiplied by $\frac{\partial f}{\partial x^i}$, so that it depends on the distribution function on the position. However, due to our homogeneity assump-

43 The procedure used to extract the expression of the momentum, together with the explicit expression of the Boltzmann equation we are about to treat, is very similar to what is usually done for CMB photons. For example, see [3, 136].

44 Here only first order contributions are kept into the equation.

tion of the background spacetime, this term already provides a first-order contribution; hence we must keep only the term at zeroth order of the above expression of $\frac{dx^i}{d\eta}$, i. e.

$$e^{\Phi+\Psi}\left(1-\frac{1}{2}\chi_{jk}n^j n^k\right)n^i \simeq n^i \,. \tag{206}$$

Summarizing

$$\frac{\partial f}{\partial x^i}\frac{dx^i}{d\eta} \simeq \frac{\partial f}{\partial x^i}n^i \,. \tag{207}$$

This term, together with $\frac{\partial f}{\partial \eta}$, encodes the free-streaming behavior of gravitons, i. e. the propagation of perturbations on all scales [3] [45].

- The next term to be evaluated is $\propto \frac{dq}{d\eta}$. To obtain its expression, it is useful to consider the following equation [136]

$$\frac{dp^0}{d\lambda}+\Gamma^0_{\alpha\beta}p^\alpha p^\beta = 0 = \frac{dp^0}{d\lambda}\frac{d\lambda}{d\eta}+\frac{\Gamma^0_{\alpha\beta}p^\alpha p^\beta}{\frac{d\eta}{d\lambda}} = \frac{dp^0}{d\eta}+\frac{\Gamma^0_{\alpha\beta}p^\alpha p^\beta}{p^0} \,. \tag{208}$$

In fact, with some algebra and dropping higher-order contributions, one can find

$$\frac{dp^0}{d\eta} \simeq \frac{dq}{d\eta}\frac{1-\Phi}{a}-\frac{q}{a^2}\left[2\mathcal{H}(1-\Phi)+\frac{d\Phi}{d\eta}+n^i\frac{d\Phi}{dx^i}\right] \tag{209}$$

$$\frac{\Gamma^0_{\alpha\beta}p^\alpha p^\beta}{p^0} \simeq \frac{q}{a^2}\left[2\mathcal{H}(1-\Phi)+\frac{d\Phi}{d\eta}-\frac{d\Psi}{d\eta}+\frac{1}{2}\frac{d\chi_{jk}}{d\eta}n^j n^k+2\frac{d\Phi}{dx^i}n^i\right] , \tag{210}$$

which contains the term we are interested in, that is, $\frac{dq}{d\eta}$. Summing the two equations as in Eq. 208,

$$\frac{dq}{d\eta} \simeq q\left[\frac{d\Psi}{d\eta}-\frac{d\Phi}{dx^i}n^i-\frac{1}{2}\frac{d\chi_{jk}}{d\eta}n^j n^k\right] . \tag{211}$$

This contribution accounts for the redshifting of gravitons during the evolution of the Universe. We will see that this includes the SW, ISW and RS effects.

- The last term $\propto \frac{\partial f}{\partial n^i}$ does not need to be computed. In fact, $\frac{\partial f}{\partial n^i}$ is already at least of order one and $\frac{\mathrm{d}n^i}{\mathrm{d}\eta}$ account for the gravitational lensing among the propagation of the graviton, and thus it is also of at least order one.

45 At higher order this includes time delay effects due to the deviation of the geodetic when passing through distorted regions by massive objects.

Finally, we can write Eq. 191 in the first order as

$$\frac{\partial f}{\partial \eta} + \frac{\partial f}{\partial x^i} n^i + \left[\frac{d\Psi}{d\eta} - \frac{1}{2} \frac{d\chi_{jk}}{d\eta} n^j n^k - \frac{d\Phi}{dx^i} n^i \right] q \frac{\partial f}{\partial q} = 0 \,, \tag{212}$$

6.2 SOLUTIONS OF THE BOLTZMANN EQUATIONS

In order to find the solutions of the above equations and to mimic exactly the analogous CMB procedure, it is useful to decompose the gravitons distribution function into a background contribution plus a first order one [3, 49, 50]

$$f(\eta, q, x^i, n^i) \simeq \bar{f}(\eta, q) + \delta f(\eta, q, x^i, n^i) \,. \tag{213}$$

where: $\bar{f}(\eta, q)$ = solution of the zeroth order equation, giving $\frac{\partial \bar{f}(\eta, q)}{\partial \eta} = 0$ [46];

$\delta f(\eta, q, x^i, n^i)$ = solution of the first order equation.

In order to simplify the first order Boltzmann equation, it is standard habit to parametrize it with a function $\Gamma(\eta, q, x^i, n^i)$ in the following way (see [3, 138])

$$\delta f(\eta, q, x^i, n^i) \equiv -q \frac{\partial \bar{f}}{\partial q} \Gamma(\eta, q, x^i, n^i) \,. \tag{214}$$

In the case of a thermal distribution of temperature T, such as the CMB, $\Gamma = \delta T / T$, which indeed corresponds to what we will call Θ in Chap. 2. However, the difference between the two cases, i. e. CMB and CGWB, is that in the former photons were thermal, thus the continuous scatterings produced frequency-independent perturbations; whereas in the latter, being the collision term negligible, Γ generally retains a dependence $\mathcal{O}(1)$ on the frequency.

46 Also further in this Thesis, the over-line $-$ on top of a quantity will indicate that it is a background, i. e. zeroth order, one.

Going back to the Boltzmann equations, at first order holds

$$\begin{aligned}
&\frac{\partial f}{\partial \eta} + \frac{\partial f}{\partial x^i} n^i + \left[\frac{d\Psi}{d\eta} - \frac{1}{2} \frac{d\chi_{jk}}{d\eta} n^j n^k - \frac{d\Phi}{dx^i} n^i \right] q \frac{\partial f}{\partial q} \simeq \\
\simeq &\frac{\partial \bar{f}}{\partial \eta} - \frac{\partial}{\partial \eta} \left(q \frac{\partial \bar{f}}{\partial q} \Gamma \right) + \frac{\partial \bar{f}}{\partial x^i} n^i - n^i \frac{\partial}{\partial x^i} \left(q \frac{\partial \bar{f}}{\partial q} \Gamma \right) + \frac{dq}{d\eta} \frac{\partial \bar{f}}{\partial q} + \\
&- \frac{dq}{d\eta} \frac{\partial}{\partial q} \left(q \frac{\partial \bar{f}}{\partial q} \Gamma \right) \simeq \\
\simeq &- q \frac{\partial \bar{f}}{\partial q} \frac{\partial \Gamma}{\partial \eta} + n^i q \frac{\partial \bar{f}}{\partial q} \frac{\partial \Gamma}{\partial x^i} + \frac{dq}{d\eta} \frac{\partial \bar{f}}{\partial q} = -q \frac{\partial \bar{f}}{\partial q} \left[\frac{\partial \Gamma}{\partial \eta} + n^i \frac{\partial \Gamma}{\partial x^i} - \frac{1}{q} \frac{dq}{d\eta} \right] \simeq \\
\simeq &- q \frac{\partial \bar{f}}{\partial q} \left[\frac{\partial \Gamma}{\partial \eta} + n^i \frac{\partial \Gamma}{\partial x^i} - \frac{d\Psi}{d\eta} + \frac{d\Phi}{dx^i} n^i + \frac{1}{2} \frac{d\chi_{jk}}{d\eta} n^j n^k \right] = 0 \, .
\end{aligned} \tag{215}$$

At this point, we can define the source function

$$S(\eta, x^i, n^i) \equiv \frac{d\Psi}{d\eta} - \frac{d\Phi}{dx^i} n^i - \frac{1}{2} \frac{d\chi_{jk}}{d\eta} n^j n^k \, , \tag{216}$$

in order to write the first order Boltzmann equation as

$$\frac{\partial \Gamma}{\partial \eta} + n^i \frac{\partial \Gamma}{\partial x^i} = S(\eta, x^i, n^i) \, . \tag{217}$$

The source function contains the scalar and tensor perturbations, which will affect the further propagation of gravitons through the first order Boltzmann equation, providing the "anisotropies" of the distribution function[47]. It is also interesting to note that S do not depend on q, indicating that these propagation effects are q-independent, at least at first order in the perturbations.

It is convenient to go into Fourier space through

$$\Gamma \equiv \int \frac{d^3k}{(2\pi)^3} e^{i \vec{k} \vec{x}} \Gamma(\eta, \vec{k}, q, \hat{n}) \, , \tag{218}$$

$$S \equiv \int \frac{d^3k}{(2\pi)^3} e^{i \vec{k} \vec{x}} S(\eta, \vec{k}, \hat{n}) = \Psi' - ik\mu\Phi - \frac{1}{2} n^i n^j \chi'_{ij} \tag{219}$$

to recast Eq. 217 to

$$\Gamma' + ik\mu\Gamma = S(\eta, \vec{k}, \hat{n}) \, , \tag{220}$$

47 Notice that, sending the source function to 0, only the free-streaming terms survive, thus one would obtain a "smooth" distribution function. Instead, as said before, the presence of these perturbations, which contribute to the source function, will determine the generation of small anisotropies.

where $\mu \equiv \widehat{k} \cdot \widehat{n}$ is the cosine of the angle between the wavenumber of each Fourier mode and the GW direction of motion.

The formal solution of Eq. 220 is given by [49, 50] and reads [48]

$$\begin{aligned}
&\Gamma(\eta, \vec{k}, q, \widehat{n}) = \\
&= \int_{\eta_{\rm in}}^{\eta} d\eta' \mathrm{e}^{ik\mu(\eta'-\eta)} \left[\Gamma\left(\eta', \vec{k}, q, \widehat{n}\right) \delta\left(\eta' - \eta_{\rm in}\right) + S\left(\eta', \vec{k}, \widehat{n}\right)\right] = \\
&= \int_{\eta_{\rm in}}^{\eta} d\eta' \mathrm{e}^{ik\mu(\eta'-\eta)} \left[\Gamma\left(\eta', \vec{k}, q, \widehat{n}\right) \delta\left(\eta' - \eta_{\rm in}\right) + \Psi' - ik\mu\Phi - \frac{1}{2} n^i n^j \chi'_{ij}\right] .
\end{aligned} \tag{222}$$

Then, we can integrate by parts the term $\propto \Phi$ to obtain the final form of Γ

$$\begin{aligned}
&\Gamma(\eta, \vec{k}, q, \widehat{n}) = \\
&= e^{ik\mu(\eta_{\rm in}-\eta)} \Gamma\left(\eta_{\rm in}, \vec{k}, q, \widehat{n}\right) + \int_{\eta_{\rm in}}^{\eta} d\eta' \mathrm{e}^{ik\mu(\eta'-\eta)} \left[\Psi' - ik\mu\Phi - \frac{1}{2} n^i n^j \chi'_{ij}\right] \\
&= e^{ik\mu(\eta_{\rm in}-\eta)} \Gamma\left(\eta_{\rm in}, \vec{k}, q, \widehat{n}\right) - \mathrm{e}^{ik\mu(\eta'-\eta)} \Phi(\eta', \vec{k}) \Big|_{\eta_{\rm in}}^{\eta} + \\
&\quad + \int_{\eta_{\rm in}}^{\eta} d\eta' \mathrm{e}^{ik\mu(\eta'-\eta)} \left[\Psi' + \Phi' - \frac{1}{2} n^i n^j \chi'_{ij}\right] = \\
&= -\Phi(\eta, \vec{k}) + e^{ik\mu(\eta_{\rm in}-\eta)} \left[\Gamma\left(\eta_{\rm in}, \vec{k}, q, \widehat{n}\right) + \Phi(\eta_{\rm in}, \vec{k})\right] + \\
&\quad + \int_{\eta_{\rm in}}^{\eta} d\eta' \mathrm{e}^{ik\mu(\eta'-\eta)} \left[\Psi' + \Phi' - \frac{1}{2} n^i n^j \chi'_{ij}\right] .
\end{aligned} \tag{223}$$

48 Obtaining this is very straightforward. Eq. 220 is of the type $y'(x) = a(x)y(x) + b(x)$, thus can be solved using

$$y(x) = e^{A(x)} \left[C + \int e^{-A(x)} b(x)\, dx\right] \quad \text{with} \quad A(x) = \int a(x)\, dx\, . \tag{221}$$

The integration constant C can be easily fixed imposing that, at $\eta_{\rm in}$, Γ is equal to some initial value $\Gamma(\eta, \vec{k}, q, \widehat{n}) = \Gamma\left(\eta_{\rm in}, \vec{k}, q, \widehat{n}\right)$ set by the specific production mechanism.

Disregarding the first isotropic term, representing a monopole contribution to which we are not interested[49], we can write

$$\begin{aligned}\Gamma(\eta, \vec{k}, q, \hat{n}) &= \mathrm{e}^{ik\mu(\eta_{\rm in}-\eta)}\Gamma\left(\eta_{\rm in}, \vec{k}, q, \hat{n}\right) + \\ &+ \int_{\eta_{\rm in}}^{\eta} d\eta' \mathrm{e}^{ik\mu(\eta'-\eta)}\left[\Phi(\eta', \vec{k})\delta(\eta'-\eta_{\rm in}) + \frac{\partial\left(\Psi(\eta', \vec{k}) + \Phi(\eta', \vec{k})\right)}{\partial\eta'}\right] \\ &- \int_{\eta_{\rm in}}^{\eta} d\eta' \mathrm{e}^{ik\mu(\eta'-\eta)}\left[\frac{1}{2}n^i n^j \frac{\partial\chi_{ij}(\eta', \vec{k})}{\partial\eta'}\right] \\ =&\Gamma_I(\eta, \vec{k}, q, \hat{n}) + \Gamma_S(\eta, \vec{k}, \hat{n}) + \Gamma_T(\eta, \vec{k}, \hat{n}) \,.\end{aligned} \tag{224}$$

Here, we have distinguished three different contributions to Γ, indicated by the subscripts I, S, T:

- the first term represents the initial condition set by some cosmological process at $\eta_{\rm in}$.

$$\Gamma_I(\eta, \vec{k}, q, \hat{n}) \equiv e^{ik\mu(\eta_{\rm in}-\eta)}\Gamma\left(\eta_{\rm in}, \vec{k}, q, \hat{n}\right) \,. \tag{225}$$

  It carries the "memory" of the initial conditions to the following evolution of the distribution function in a completely different way w. r. t. what one observes for the CMB [94, 95]. Indeed, CMB photons were thermally coupled before the recombination epoch, thus the continuous and very efficient scatterings erased any trace of the initial conditions, leaving behind a nearly memory-less plasma [50]. Once they decoupled, they started free-streaming causing us to see the CMB. Instead, gravitons have never being thermal (at least below the Planck energy [145]).

- The second term is the scalar sourced contribution to the distribution function.

$$\begin{aligned}\Gamma_S(\eta, \vec{k}, q, \hat{n}) \equiv &\int_{\eta_{\rm in}}^{\eta} d\eta' \mathrm{e}^{ik\mu(\eta'-\eta)}\Phi(\eta', \vec{k})\delta(\eta'-\eta_{\rm in}) + \\ &+ \int_{\eta_{\rm in}}^{\eta} d\eta' \mathrm{e}^{ik\mu(\eta'-\eta)}\frac{\partial\left(\Psi(\eta', \vec{k}) + \Phi(\eta', \vec{k})\right)}{\partial\eta'} \,.\end{aligned} \tag{226}$$

  Inside it, the first term represents the SW effect, whereas an anisotropy is set by the value of the gravitational potential Φ at $\eta_{\rm in}$. The second one accounts for the propagation of gravitons from $\eta_{\rm in}$ to us today,

49 Notice that indeed Φ does not depend on $\hat{n}$, thus on the direction of observation in the sky. The only angle dependency on that term is inside the exponent of $e^{ik\mu(\eta_{\rm in}-\eta)}$, however this particular combination is still isotropic on the full-sky.

50 In other words, the mean free path of photons was very short.

including the ISW effect, i. e. propagation during radiation domination, and the RS effect, i. e. propagation during the very late Universe in dark energy domination.

- The last term is the tensor-sourced one, i. e. , generated by the GW perturbation χ_{ij} of the metric (see Eq. 198).

$$\Gamma_T(\eta, \vec{k}, q, \hat{n}) \equiv -\int_{\eta_{\rm in}}^{\eta} d\eta' \mathrm{e}^{ik\mu(\eta'-\eta)} \left[\frac{1}{2} n^i n^j \frac{\partial \chi_{ij}(\eta', \vec{k})}{\partial \eta'}\right] . \quad (227)$$

6.3 SPHERICAL HARMONICS DECOMPOSITION

At this point we already show in Chap. 2 that it is convenient to decompose these fluctuations into SHs.
After doing so, we plug into Eq. 155 the expression of the $\Gamma(\hat{n})$ shown by Eq. 224 in order to write

$$\begin{aligned}\Gamma_{\ell m} = &\int d^2n\, Y^*_{\ell m}(\hat{n}) \int \frac{d^3k}{(2\pi)^3} e^{i\vec{k}\cdot\vec{x}} \\ &\times \left[\Gamma_I(\eta, \vec{k}, q, \hat{n}) + \Gamma_S(\eta, \vec{k}, \hat{n}) + \Gamma_T(\eta, \vec{k}, \hat{n})\right] \\ =&\Gamma_{\ell m,I} + \Gamma_{\ell m,S} + \Gamma_{\ell m,T} ,\end{aligned} \quad (228)$$

where we have carried onto the SH coefficients the same notation used to identify the different contributions to Γ. Let us examine every term more deeply.

6.3.1 *Initial Condition Term*

The initial condition term reads

$$\Gamma_{\ell m,I} = \int \frac{d^3k}{(2\pi)^3} e^{i\vec{k}\cdot\vec{x}_0} \Gamma_I(\eta, \vec{k}, q, \hat{n}) \int d^2n\, Y^*_{\ell m}(\hat{n}) e^{-ik(\eta_0-\eta_{\rm in})\hat{k}\cdot\hat{n}} . \quad (229)$$

$\vec{x}_0$ is the origin of the reference frame where the observer is, which we can set to $\vec{x}_0 = 0$ without loss of generality[51] and that $\eta_{\rm in}$ represents the last time that cosmological GWs have been produced, i. e. the end of inflation.

51 In the standard isotropic and homogeneous case the exponential containing $\vec{x}_0$ gets canceled, even without choosing the specific reference frame in which $\vec{x}_0 = 0$. However, when considering modulations, it will not. The reason why involves the two-point correlation function of $\Gamma_{\ell m}$, and the stochastic variables present in it such as ζ, thus we will make a more detailed comment on this in footnote 53.

In order to make a little more explicit the initial conditions term, we can make use of a useful decomposition of the exponential as function of spherical Bessel functions, Legendre polynomial and SHs reading

$$\begin{aligned} \mathrm{e}^{-i\vec{k}\cdot\vec{y}} =& \sum_{\ell}(-i)^{\ell}(2\ell+1)j_{\ell}(ky)P_{\ell}(\widehat{k}\cdot\widehat{y}) = \\ =& 4\pi\sum_{\ell}\sum_{m=-\ell}^{\ell}(-i)^{\ell}j_{\ell}(ky)Y_{\ell m}(\widehat{k})Y^{*}_{\ell m}(\widehat{y}) \ . \end{aligned} \tag{230}$$

In our case, it yields

$$\mathrm{e}^{-ik(\eta_0-\eta_{\mathrm{in}})\widehat{k}\cdot\widehat{n}} = 4\pi\sum_{\ell'}\sum_{m'=-\ell'}^{\ell'}(-i)^{\ell'}j_{\ell'}[k(\eta_0-\eta_{\mathrm{in}})]Y_{\ell' m'}(\widehat{n})Y^{*}_{\ell' m'}(\widehat{k}) \ . \tag{231}$$

Plugging this expansion into Eq. 229 and remembering the orthogonality condition of SHs

$$\int d\widehat{k}Y^{*}_{\ell m}(\widehat{k})Y_{\ell' m'}(\widehat{k}) = \delta_{\ell\ell'}\delta_{mm'} \ , \tag{232}$$

one obtains

$$\Gamma_{\ell m,I} = 4\pi(-i)^{\ell}\int\frac{d^3k}{(2\pi)^3}\Gamma_I(\eta,\vec{k},q,\widehat{n})Y^{*}_{\ell m}(\widehat{k})j_{\ell}[k(\eta_0-\eta_{\mathrm{in}})] \ , \tag{233}$$

where we stress the presence of a dependency on the frequency q, which indicate the role of the specific physics we are considering behind the initial conditions.

6.3.2 *Scalar Sourced Term*

As aforementioned, this term accounts for anisotropies of the distribution function produced by the propagation of GWs in a perturbed Universe, specifically due to scalar perturbations.

In this context, these perturbations are typically expressed as

$$\Phi = \zeta(\vec{k}) \times \{\text{Transfer Function}(k)\} \times \{\text{Growth Function}(\eta)\} \ , \tag{234}$$

where: $\zeta(\vec{k})$ = primordial value of the curvature perturbation set during inflation;

Transfer Function(k) = evolution of perturbations through the epochs of horizon crossing and radiation/-matter transition;

Growth Function(η) = wavelength-independent growth at late times [3].

From now on, until differently specified, we will refer with the name "transfer function" to the actual product of Transfer Function(k) $\times$ Growth Function(η) of Eq. 234, in such a way that we can write

$$\Phi(\eta, \vec{k}) = T_\Phi(\eta, k)\zeta(\vec{k}) \quad , \quad \Psi(\eta, \vec{k}) = T_\Psi(\eta, k)\zeta(\vec{k}) \, . \tag{235}$$

Being in an isotropic situation and not considering any anisotropic stress, we consider for simplicity $T_\Phi = T_\Psi$.

Using the parametrization of Eq. 235 and exploiting the same expansion of the exponential shown in Eq. 231, we can write

$$\begin{aligned}\Gamma_{\ell m,S} &= 4\pi(-i)^\ell \int \frac{d^3k}{(2\pi)^3}\zeta(\vec{k})Y^*_{\ell m}(\widehat{k})\Big\{T_\Phi(\eta_{\rm in}, k)j_\ell[k(\eta_0 - \eta_{\rm in})] \\ &+ \int_{\eta_{\rm in}}^{\eta_0} d\eta' \frac{\partial\Big[\Psi(\eta', \vec{k}) + \Phi(\eta', \vec{k})\Big]}{\partial\eta'} j_\ell\big[k\big(\eta_0 - \eta'\big)\big]\Big\} \\ &= 4\pi(-i)^\ell \int \frac{d^3k}{(2\pi)^3}\zeta(\vec{k})Y^*_{\ell m}(\widehat{k})T^S_\ell(k, \eta_0, \eta_{\rm in}) \, ,\end{aligned} \tag{236}$$

where we have introduced the linear transfer function

$$\begin{aligned}T^S_\ell(k, \eta_0, \eta_{\rm in}) \equiv &T_\Phi(\eta_{\rm in}, k)j_\ell[k(\eta_0 - \eta_{\rm in})] \\ &+ \int_{\eta_{\rm in}}^{\eta_0} d\eta' \frac{\partial\Big[\Psi(\eta', \vec{k}) + \Phi(\eta', \vec{k})\Big]}{\partial\eta'} j_\ell\big[k\big(\eta_0 - \eta'\big)\big] \, ,\end{aligned} \tag{237}$$

encoding the time evolution of the graviton fluctuations originated from the primordial scalar perturbations.

6.3.3 *Tensor Sourced Term*

Finally, the last contribution coming from tensor perturbations reads

$$\Gamma_{\ell m,T} = -\int d^2n \, Y^*_{\ell m}(\widehat{n}) \int \frac{d^3k}{(2\pi)^3}\frac{n^i n^j}{2}\int_{\eta_{\rm in}}^{\eta} d\eta' e^{ik(\eta' - \eta_0)\mu}\frac{\partial\chi_{ij}(\eta', \vec{k})}{\partial\eta'} \, . \tag{238}$$

Evaluating this term require a quite lenghty algebra and we are not interested in the details in this context; for this reason, we will just state the main passages and report the final result.

Firstly, one has to decompose χ_{ij} in right/left-handed circular polarizations as (see e. g. [53])

$$\chi_{ij} = \sum_{\lambda=\pm 2} e_{ij,\lambda}(\widehat{k}) \, \chi(\eta, k) \, \xi_\lambda(k^i) \, , \tag{239}$$

where $e_{ij,\lambda}(\widehat{k})$ are the polarization operators defined from the more familiar polarization tensors relative to the $+$ and $\times$ polarizations, $\chi(\eta, k)$ is the tensor mode function and $\xi_\lambda(k^i)$ is the stochastic variable analogue of ζ for the scalar term.

Then, it will be necessary to rotate the system using a rotation matrix of the form

$$S\left(\Omega_k\right) \equiv \begin{pmatrix} \cos\theta_k \cos\phi_k & -\sin\phi_k & \sin\theta_k \cos\phi_k \\ \cos\theta_k \sin\phi_k & \cos\phi_k & \sin\theta_k \sin\phi_k \\ -\sin\theta_k & 0 & \cos\theta_k \end{pmatrix} , \tag{240}$$

which will be used to rotate the SHs following

$$Y^*_{\ell m}\left(\Omega_n\right) = \sum_{m'=-\ell}^{\ell} D^{\ell}_{mm'}\left(S\left(\Omega_k\right)\right) Y^*_{\ell m'}\left(\Omega_{k,n}\right) , \tag{241}$$

where $D^{\ell}_{mm'}\left(S\left(\Omega_k\right)\right)$ is the Wigner rotation matrix [146]

$$D^{\ell}_{ms}\left(S\left(\Omega_k\right)\right) \equiv \sqrt{\frac{4\pi}{2\ell+1}} (-1)^s {}_{-s}Y^*_{\ell m}\left(\Omega_k\right) . \tag{242}$$

The above expression make use of the spin-weighted SHs, which read[146]

$$\begin{aligned} {}_{-s}Y^*_{\ell m}\left(\Omega_k\right) \equiv & (-1)^m \sqrt{\frac{(\ell+m)!(\ell-m)!(2\ell+1)}{4\pi(\ell+s)!(\ell-s)!}} \sin^{2\ell}\left(\frac{\theta_k}{2}\right) \\ & \times \sum_{r=0}^{\ell-s} \begin{pmatrix} \ell-s \\ r \end{pmatrix} \begin{pmatrix} \ell+s \\ r+s-m \end{pmatrix} (-1)^{\ell-r-s} \\ & \times \mathrm{e}^{im\phi_k} \cot^{2r+s-m}\left(\frac{\theta_k}{2}\right) . \end{aligned} \tag{243}$$

Then, exploiting the properties of SHs and of associate Legendre polynomials, one can finally arrive at the result:

$$\begin{aligned} \Gamma_{\ell m,T} = & \pi(-i)^{\ell} \sqrt{\frac{(\ell+2)!}{(\ell-2)!}} \int \frac{d^3k}{(2\pi)^3} \mathrm{e}^{i\vec{k}\cdot\vec{x}_0} \sum_{\lambda=\pm 2} {}_{-\lambda}Y^*_{\ell m}\left(\Omega_k\right) \xi_\lambda(\vec{k}) \\ & \times \int_{\eta_{\rm in}}^{\eta_0} d\eta\, \chi'(\eta,k) \frac{j_\ell\left(k\left(\eta_0-\eta\right)\right)}{k^2\left(\eta_0-\eta\right)^2} = \\ = & 4\pi(-i)^l \int \frac{d^3k}{(2\pi)^3} \mathrm{e}^{i\vec{k}\cdot\vec{x}_0} \sum_{\lambda=\pm 2} {}_{-\lambda}Y^*_{\ell m}\left(\Omega_k\right) \xi_\lambda(\vec{k}) T^T_\ell\left(k, \eta_0, \eta_{\rm in}\right) , \end{aligned} \tag{244}$$

where we introduced again a linear transfer function for the tensor modes reading

$$T_\ell^T(k,\eta_0,\eta_{\rm in}) \equiv \frac{1}{4}\sqrt{\frac{(\ell+2)!}{(\ell-2)!}}\int_{\eta_{\rm in}}^{\eta_0} d\eta\ \chi'(\eta,k)\frac{j_\ell\left(k\left(\eta_0-\eta\right)\right)}{k^2\left(\eta_0-\eta\right)^2}\ . \quad (245)$$

6.4 CONNECTION WITH OBSERVABLES

Now, we have an explicit expression for the SH decomposition's coefficients. Thus, we can see what the observable quantities are connected to the distribution function of gravitons and to the CGWB.

6.4.1 *Energy Density*

Just like any other energy source in the Universe, GWs contribute to the overall energy density. Given that we are working with the distribution function of gravitons in a Boltzmann approach, to find the energy density of GWs it is sufficient to follow the natural route of integrating the distribution function, i. e. the average number of gravitons in a volume d^3p, multiplied by the energy contribution of the single particle:

$$\begin{aligned}
\rho_{\rm GW}\left(\eta_0,\vec{x}\right) &= \int d^3p\ pf\left(\eta_0,\vec{x},q,\hat{n}\right)\\
&= \frac{1}{a^4}\int d^3q\ qf\left(\eta_0,\vec{x},q,\hat{n}\right)\\
&= \frac{1}{a^4}\int d\ln q q^4\int d^2\hat{n} f\left(\eta_0,\vec{x},q,\hat{n}\right) \qquad (246)\\
&\equiv \rho_{\rm crit}\int d\ln q\times\frac{1}{\rho_{\rm crit}}\frac{q^4}{a^4}\int d^2\hat{n} f\left(\eta_0,\vec{x},q,\hat{n}\right)\\
&\equiv \rho_{\rm crit}\int d\ln q\times\Omega_{\rm GW}\left(\eta_0,\vec{x},q\right)\ ,
\end{aligned}$$

where: $\rho_{\rm crit} \equiv \frac{3H_0^2}{8\pi G} = 3H_0^2M_P^2$ is the critical density of a Universe perfectly flat;

$\Omega_{\rm GW} =$ spectral energy density for GWs, i. e. the logarithmic contribution to the energy density.

We can write the spectral energy density as

$$\Omega_{\rm GW}(\eta_0,\vec{x},q) = \int d^2\hat{n}\ \omega_{\rm GW}(\eta_0,\vec{x},q,\hat{n})\ , \quad (247)$$

where we have introduced the angular contribution of the spectral energy

$$\begin{aligned}\omega_{\rm GW}(\eta_0,\vec{x},q,\hat{n}) \equiv& \overline{\omega}_{\rm GW}(\eta_0,q)\left[1+\frac{\delta\omega(\eta_0,\vec{x},q,\hat{n})}{\overline{\omega}_{\rm GW}(\eta_0,q)}\right]\\ =& \frac{1}{\rho_{\rm crit}}\frac{q^4}{a^4}f(\eta,\vec{x},q,\hat{n})\,,\end{aligned} \tag{248}$$

from which we can define the quantity [49, 50]

$$\delta_{\rm GW}(\eta_0,\vec{x},q,\hat{n}) \equiv \frac{\delta\omega(\eta_0,\vec{x},q,\hat{n})}{\overline{\omega}_{\rm GW}(\eta_0,q)}\,. \tag{249}$$

Then, the zeroth order homogeneous component of $\Omega_{\rm GW}$ will be

$$\overline{\Omega}_{\rm GW}(q) = \frac{4\pi}{\rho_{\rm crit}}\left(\frac{q}{a}\right)^4\overline{f}(q) = 4\pi\overline{\omega}_{\rm GW}(q)\,. \tag{250}$$

These variables allow to write the energy density contribution of GWs as

$$\begin{aligned}\rho_{\rm GW}(\eta_0,\vec{x}) &= \rho_{\rm crit}\int d\ln q\int d^2\hat{n}\,\omega_{\rm GW}\\ &= \rho_{\rm crit}\int d\ln q\int d^2\hat{n}\,(\overline{\omega}_{\rm GW}+\delta\omega_{\rm GW}) =\\ &= \rho_{\rm crit}\int d\ln q\int d^2\hat{n}\left(\frac{q}{a}\right)^4\left(\overline{f}-q\frac{\partial\overline{f}}{\partial q}\Gamma\right) =\\ &= \rho_{\rm crit}\int d\ln q\left(\frac{q}{a}\right)^4\overline{f}\int d^2\hat{n}\left(1-\frac{\partial\ln\overline{f}}{\partial\ln q}\Gamma\right) =\\ &= \rho_{\rm crit}\int d\ln q\int d^2\hat{n}\,\overline{\omega}_{\rm GW}+\rho_{\rm crit}\int d\ln q\int d^2\hat{n}\,\overline{\omega}_{\rm GW}\delta_{\rm GW}\,.\end{aligned} \tag{251}$$

Exploiting now Eq. 250, one can find

$$\begin{aligned}\frac{\partial\ln\overline{f}}{\partial\ln q} &= \frac{q}{\overline{f}}\frac{\partial\overline{f}}{\partial q} = \frac{4\pi q^5}{\rho_{\rm crit}a^4\overline{\Omega}_{\rm GW}}\frac{\rho_{\rm crit}a^4}{4\pi}\left(\frac{\partial\overline{\Omega}_{\rm GW}}{\partial q}\frac{q}{q^5}-\frac{4}{q^5}\overline{\Omega}\right) =\\ &= \frac{q}{\overline{\Omega}}\frac{\partial\overline{\Omega}_{\rm GW}}{\partial q}-4 = \frac{\partial\ln\overline{\Omega}_{\rm GW}}{\partial\ln q}-4\,,\end{aligned} \tag{252}$$

which allows to write finally

$$\delta_{\rm GW}(\eta_0,\vec{x},q,\hat{n}) = \left[4-\frac{\partial\ln\overline{\Omega}_{\rm GW}}{\partial\ln q}\right]\Gamma(\eta_0,\vec{x},q,\hat{n})\,. \tag{253}$$

Through the presence of the Γ, all the different terms introduced before will act onto the energy density of the Universe. For example, the memory of the

production mechanisms carried by the initial condition can directly affect the GW energy density that we can observe today.

Note that in this work we implicitly assume that the only primordial source of GWs is inflation. This means that from Sec. 5.1.1 we know that

$$\frac{\partial \ln \overline{\Omega}_{\rm GW}}{\partial \ln q} = n_t \ . \tag{254}$$

However in full generality, there are many other sourced we could consider. Also, another implicit assumption is to start from adiabatic initial conditions. For a complete treatment of different production mechanisms, the reader can refer to Schulze et al. [94], Dall'Armi et al. [95] and the references therein.

6.4.2 *Correlators and Angular power Spectrum*

As previously mentioned in Sec. 4.3.3, in order to compare theoretical predictions with observations, we must study the two-point correlation function of the quantities involved. In fact, all the stochastic variables we have introduced ($\Gamma(\eta_{\rm in}, \vec{k}, q)$, $\zeta(\vec{k})$, $\xi_\lambda(\vec{k})$) find their seeds in the quantum perturbations enhanced to macroscopic scales by inflation. This causes the fact that their expectation value is null, whereas their two-point correlation functions are not.

In particular, assuming that the statistical variables have approximately a Gaussian behavior (experimentally verified for the large-scale perturbations of ζ and ξ_λ, as obtained from the CMB data [147], and assumed for the initial condition term), we can write

$$\begin{aligned}
\left\langle \Gamma(\eta_{\rm in}, \vec{k}, q)\Gamma^*(\eta_{\rm in}, \vec{k}', q) \right\rangle &= \frac{2\pi^2}{k^3} P_I(q,k)(2\pi)^3\delta(\vec{k}-\vec{k}') \ , \\
\left\langle \zeta(\vec{k})\zeta^*(\vec{k}') \right\rangle &= \frac{2\pi^2}{k^3} P_s(k)(2\pi)^3\delta(\vec{k}-\vec{k}') \ , \\
\left\langle \xi_\lambda(\vec{k})\xi^*_{\lambda'}(\vec{k}') \right\rangle &= \frac{2\pi^2}{k^3} P_t(k)\delta_{\lambda\lambda'}(2\pi)^3\delta(\vec{k}-\vec{k}') \ .
\end{aligned} \tag{255}$$

Here, P_s and P_t are the scalar and tensor adimensional power spectra defined in Chap. 4 and Chap. 5.

Assuming also statistical isotropy, which will be relaxed in Chap. 7, we can also write the angular correlators of the SH decomposition coefficients as[52]

$$\langle \Gamma_{\ell m}\Gamma^*_{\ell' m'}\rangle \equiv \delta_{\ell\ell'}\delta_{mm'}\mathcal{C}_\ell = \delta_{\ell\ell'}\delta_{mm'}[\mathcal{C}_{\ell,I}(q) + \mathcal{C}_{\ell,S} + \mathcal{C}_{\ell,T}] \ , \tag{256}$$

52 Here we have assumed that the various terms are not cross-correlated. This assumption can be relaxed as in [141], where the anisotropic distribution of the GW originated in models with primordial BHs was studied.

where we have used the usual notation to distinguish the various contributions.

As an example, let us explicitly perform the calculi for the initial condition term; the other two will be nearly identical[53]

$$\begin{aligned}
\left\langle \Gamma_{\ell m,I}\Gamma^*_{\ell' m',I}\right\rangle =&(4\pi)^2(-i)^{\ell-\ell'}\int\frac{d^3k}{(2\pi)^3}\int\frac{d^3k'}{(2\pi)^3}\left\langle \Gamma(\eta_{\rm in},\vec{k},q)\Gamma^*(\eta_{\rm in},\vec{k}',q)\right\rangle\\
&\times Y^*_{\ell m}(\widehat{k})Y_{\ell' m'}(\widehat{k}')\; j_\ell[k(\eta_0-\eta_{\rm in})]j_{\ell'}\left[k'(\eta_0-\eta_{\rm in})\right]=\\
=&(4\pi)^2(-i)^{\ell-\ell'}\int\frac{d^3k}{(2\pi)^3}\int\frac{d^3k'}{(2\pi)^3}\frac{2\pi^2}{k^3}P_I(q,k)(2\pi)^3\delta(\vec{k}-\vec{k}')\\
&\times Y^*_{\ell m}(\widehat{k})Y_{\ell' m'}(\widehat{k}')\; j_\ell[k(\eta_0-\eta_{\rm in})]j_{\ell'}\left[k'(\eta_0-\eta_{\rm in})\right]=\\
=&4\pi(-i)^{\ell-\ell'}\int d^3k\frac{1}{k^3}P_I(q,k)\; j_\ell[k(\eta_0-\eta_{\rm in})]j_{\ell'}[k(\eta_0-\eta_{\rm in})]\\
&\times Y^*_{\ell m}(\widehat{k})Y_{\ell' m'}(\widehat{k})=\\
=&4\pi(-i)^{\ell-\ell'}\int\frac{dk}{k}P_I(q,k)\; j_\ell[k(\eta_0-\eta_{\rm in})]j_{\ell'}[k(\eta_0-\eta_{\rm in})]\\
&\times\int d^2\widehat{k}Y^*_{\ell m}(\widehat{k})Y_{\ell' m'}(\widehat{k})=\\
=&\delta_{\ell\ell'}\delta_{mm'}4\pi\int\frac{dk}{k}P_I(q,k)\; j^2_\ell[k(\eta_0-\eta_{\rm in})]\\
=&\delta_{\ell\ell'}\delta_{mm'}\mathcal{C}_{\ell,I}(q)\;.
\end{aligned}\tag{257}$$

Thus, summarizing we can define

$$\begin{aligned}
\mathcal{C}_{\ell,I}&\equiv 4\pi\int\frac{dk}{k}\; j^2_\ell[k(\eta_0-\eta_{\rm in})]\; P_I(q,k)\;,\\
\mathcal{C}_{\ell,S}&\equiv 4\pi\int\frac{dk}{k}T^{(S)2}_\ell(k,\eta_0,\eta_{\rm in})\; P_s(k)\;,\\
\mathcal{C}_{\ell,T}&\equiv 4\pi\int\frac{dk}{k}T^{(T)2}_\ell(k,\eta_0,\eta_{\rm in})\sum_{\lambda=\pm2}P_t(k)\;,
\end{aligned}\tag{258}$$

where the transfer functions are defined in Eq. 237 and Eq. 245.

These functions in Eq. 258 represent the contribution to the angular power spectra of the GW energy density, relative to the different source terms, and fully describe it in the full sky.

We again stress that the fact that they are diagonal in both ℓ and m is a consequence of statistical isotropy. We will see that relaxing this assumption

53 In Eq. 229, we had a factor $\exp\left\{i\vec{k}\cdot\vec{x}_0\right\}$, which in the following expression is not present (see also footnote 51). In fact, the resulting factor $\exp\left\{i\left(\vec{k}-\vec{k'}\right)\cdot\vec{x}_0\right\}$ is equal to 1 when computing the $\delta\left(\vec{k}-\vec{k'}\right)$ coming from the two-point correlation function of ζ for example. In other words, in this case homogeneity assures that this term get canceled.

will give rise to non-diagonal couplings between different multipoles ℓ and ℓ'.

Part III

DEPARTURES FROM THE STANDARD MODEL OF COSMOLOGY

In this part, we will investigate the prospect of deviating from the conventional cosmological framework. For instance, we will explore the consequences of relaxing the assumption of statistical isotropy. This departure can be phenomenologically represented by introducing modulations in the gravitational potentials, leading to a localized break in isotropy. We will provide a concise overview of this concept in the context of the CMB, where such modulations find their phenomenological justification. Subsequently, we will extend this modulation to the framework of the CGWB, employing the same Boltzmann approach demonstrated in Chap. 6. However, our exploration of departures from the standard model does not end here. Another example we will address in this part is the lack-of-correlation anomaly observed in the CMB. This anomaly, in principle, should also manifest in the CGWB.

7

CMB POWER ASYMMETRY

We know that a crucial prediction of Big-Bang cosmology is the CMB: a relic radiation coming from the LSS of photons, which gives us the most ancient snapshot of the Universe we can observe with EM radiation. In Sec. 4.5 we briefly described its anisotropies, whose study allows us to draw a comprehensive picture of the Universe. This is not the end of the story though, since CMB hides some hints of possible departures from the standard model of Cosmology, the so-called CMB anomalies. In this chapter, we will briefly describe these features and focus on the so-called CMB "hemispherical power asymmetry" and on how people in the literature have tried to characterize it as the effect of isotropy breaking modulation of gravitational potentials.

7.1 CMB ANOMALIES

Despite the success of a spatially flat ΛCDM model, there are intriguing anomalies in the large angular scales of the CMB sky that we observe. For example, the alignment of low multipole moments [148–150], the hemispherical power asymmetry [151], the low CMB variance [152], the parity asymmetry [153–155], and the cold spot [156, 157] (see also [158–160]). Their statistical significance lies between 2-4σ, depending on which estimator is used and which anomaly is considered. Another interesting anomalous feature of the CMB is its topology [161–163]. It can be studied employing a zoology of different tests, such as Minkowski functionals [164–166] or the skeleton length [167], and have also shown a relatively high significance [10, 168–172].

7.2 CMB POWER ASYMMETRY

Since the first-year data of WMAP (see, for example, [151]), hints of a possible departure from statistical isotropy have started to show to the Cosmology community. In particular, exploiting many simulated realizations of the CMB, it was possible to show that the ratio between the power on the two ecliptic hemispheres in the sky we observe is generally higher than the one obtained in the vast majority of simulations ($\approx 99\%$) [151]. Over the subsequent years, this signature has been reassessed, for example, using five-year data from WMAP, showing that only the $\approx 0.3\%$ of the simulated data achieved a similar level of asymmetry [173], or even the most recent Planck data [54, 174], where the role of the statistics "a posteriori" was also emphasized.
All these "evidences" of some possible new physics lurking behind this anomaly have obviously drawn a lot of attention in the scientific community; thus various proposal solutions were studied.

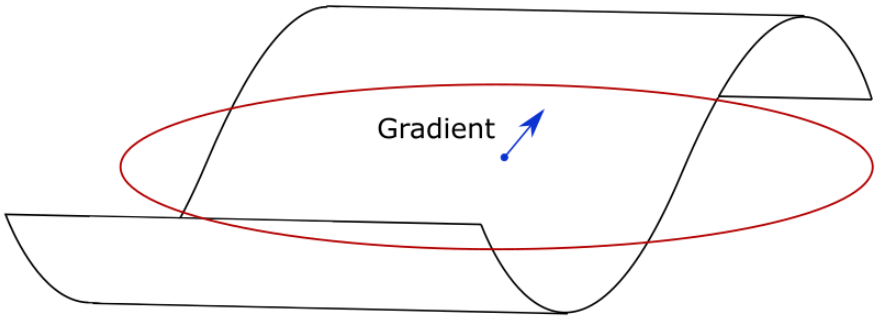

Figure 11: Intuitive idea of how a modulating field can break the local isotropy. Here the modulating field is represented as a plain wave, our Hubble volume is the red circle and the gradient of the modulating field is the blue arrow, which will naturally pick a direction in the Hubble volume, following the characteristics of the mode.

Such a power asymmetry could arise in the presence of some non-Gaussianity, typically in the context of multiple-field inflationary scenarios [175–180]. These fields generate a local break of statistical isotropy through their gradient and act on the CMB [181], leaving as a relic the asymmetry we observe; all this without flawing the hypothesis of an underlying global isotropy of the Universe, since the modulation gets averaged over many Hubble volumes.

7.3 MODULATION OF GRAVITATIONAL POTENTIAL

People have tried to describe the CMB power asymmetry by introducing in the model a super-horizon scale modulation of the gravitational potential, which will cause the temperature field to seem anisotropic on a local basis. To see this in an intuitive way it is sufficient to imagine our Hubble volume as a circle of radius R (see Fig. 11): any small-scale fluctuating field will have a wavelength much smaller than R, thus they cannot contribute to a departure from isotropy and will determine the "standard" characteristics we see in the CMB. However, if we consider a modulating field that has a wavelength larger than R, it will generate a local break of isotropy through its gradient. Considering now many Hubble volumes, the modulating field would still average to 0, reestablishing the isotropy. To translate this in a more quantitative way, we can assume that the gravitational potential $\Phi(\vec{x})$, introduced in Chap. 4 as one of the scalar perturbations of the metric, actually depends on two fields $g(\vec{x})$ and $h(\vec{x})$, where the latter is only related to super-horizon scales fluctuations and the former to sub-horizon ones [181]. h will assume a deterministic value in our Hubble volume, whereas g will look like a standard stochastic fluctuation. As mentioned above, within the Hubble volume an observer will see broken statistical isotropy as an effect of the slow modulation of h, while its local gradient and curvature will pick a preferred direction, breaking statistical isotropy. Specifically, we write

$$\Phi(\vec{x}) = g_1(\vec{x})[1 + h(\vec{x})] + g_2(\vec{x}) \,, \tag{259}$$

where: $g_1(\vec{x})$ = Gaussian random field accounting for fluctuations around the horizon scales;
$g_2(\vec{x})$ = Gaussian random field accounting for fluctuations on well-sub-horizon scales, which makes our considerations compatible with the observed statistical homogeneity and isotropy on small scales;
$h(\vec{x})$ = modulating field breaking isotropy.

Going into Fourier space, the product of g_1 and h in real space becomes naturally a convolution, thus Φ gets recast to

$$\Phi(\vec{k}) = g_1(\vec{k}) + \int \frac{d^3k'}{(2\pi)^3} g_1(\vec{k}')h(\vec{k} - \vec{k}') + g_2(\vec{k}) \,. \tag{260}$$

Given the Gaussian assumption we have made for the g fields, we can write their power spectra as

$$\left\langle g_i^*(\vec{k}) g_i(\vec{k}') \right\rangle = (2\pi^3)\delta(\vec{k} - \vec{k}') P_{g_i}(k) \quad \text{with} \quad i = 1, 2 \,, \tag{261}$$

which obviously do not couple any mode of different $\vec{k}$ thanks to the Dirac's delta.
We must now stress that we are doing ensemble averages only on one Hubble volume, thus only the g_i fields will get averaged, while h keeps its "deterministic" value. This allows us to write the 2-point correlation function of Φ as

$$\begin{aligned} \left\langle \Phi^*(\vec{k}) \Phi(\vec{k}') \right\rangle =& (2\pi)^3 \delta(\vec{k} - \vec{k}') \left[P_{g_1}(k) + P_{g_2}(k) \right] \\ &+ \left[P_{g_1}(k) + P_{g_1}(k') \right] h(\vec{k}' - \vec{k}) \\ &+ \int \frac{d^3\widetilde{k}}{(2\pi)^3} P_{g_1}(\widetilde{k}) h^*(\vec{k} - \widetilde{\vec{k}}) h(\vec{k}' - \widetilde{\vec{k}}) \,. \end{aligned} \tag{262}$$

Already now, we can notice some peculiarity: in spite of what we have just told for the 2-points correlation functions of g_i, through the presence of $h(\vec{k}' - \vec{k})$ modes with different wavenumber get correlated, assuming that they are separated by less than the wavenumber of the modulating field h.
This already gives us some information to work on, however what we observe in the sky is the temperature of CMB photons, thus we must relate Φ with that, exploiting [181]

$$\Theta(\vec{x}) = -\frac{1}{3}\Phi(\vec{x}) \,, \tag{263}$$

which can be decomposed in SHs as in Eq. 155. In this case

$$\Theta(\hat{n}) = \sum_{\ell} \sum_{m=-\ell}^{\ell} a_{\ell m} Y_{\ell m}(\hat{n}) \,, \tag{264}$$

inverted by

$$\begin{aligned} a_{\ell m} &= \int \frac{d^3k}{(2\pi)^3}\Theta(\hat{n})4\pi i^\ell j_\ell\left(kD_{\rm rec}\right)Y^*_{\ell m}(\hat{k}) \\ &= -\frac{1}{3}\int \frac{d^3k}{(2\pi)^3}\Phi(\vec{x})4\pi i^\ell j_\ell\left(kD_{\rm rec}\right)Y^*_{\ell m}(\hat{k})\ , \end{aligned} \tag{265}$$

where: $j_\ell(x) =$ spherical Bessel functions;
$D_{\rm rec}$ = distance to the recombination surface, i. e. the LSS.

The Spherical Bessel Functions (SBFs) are one of the two solutions of the Helmholtz equation

$$x^2\frac{d^2y}{dx^2} + 2x\frac{dy}{dx} + \Big(x^2 - n(n+1)\Big)\,y = 0\ . \tag{266}$$

They are defined from the "ordinary" Bessel functions as

$$j_\ell(x) \equiv \sqrt{\frac{\pi}{2x}}J_{\ell+\frac{1}{2}}(x)\ , \tag{267}$$

which can be written as

$$J_\ell(x) = \sum_{m=0}^{\infty}\frac{(-1)^m}{m!\Gamma(m+\ell+1)}\Big(\frac{x}{2}\Big)^{2m+\ell}\ . \tag{268}$$

As expected, in the isotropic and homogeneous case the temperature fields will obey to

$$\langle a^*_{\ell' m'}a_{\ell m}\rangle = \mathcal{C}_\ell^{TT}\delta_{\ell\ell'}\delta_{mm'}\ , \tag{269}$$

where $\mathcal{C}_\ell^{TT}$ is the angular power spectrum. Here, the very presence of $\delta_{\ell\ell'}$ is a direct consequence of having assumed statistical isotropy. However, in the presence of a modulating field, things change due to the modified expression of the two-point correlation function of Φ.
For simplicity, we will consider a modulation of the following form

$$\Phi(\vec{x}) = g(\vec{x})[1 + h(\vec{x})]\ , \tag{270}$$

so that we only compute the interesting modulated component, without bothering to carry on also the standard isotropic results that $g_2(\vec{x})$ would have given (one can obtain the full result by adding the non-modulated one). Hence, in Fourier space

$$\Phi(\vec{k}) = g(\vec{k}) + \int \frac{d^3k'}{(2\pi)^3}g(\vec{k}')h(\vec{k} - \vec{k}')\ , \tag{271}$$

$$\begin{aligned}\left\langle \Phi^*(\vec{k})\Phi(\vec{k}')\right\rangle =&(2\pi)^3\delta(\vec{k}-\vec{k}')P_g(k)\\ &+\left[P_g(k)+P_g(k')\right]h(\vec{k}-\vec{k}')\\ &+\int\frac{d^3\widetilde{k}}{(2\pi)^3}P_g(\widetilde{k})h^*(\vec{k}-\widetilde{\vec{k}})h(\vec{k}'-\widetilde{\vec{k}})\,.\end{aligned} \tag{272}$$

Now, we can write the correlation function for the SH coefficients at different ℓ and m as

$$\begin{aligned}\langle a^*_{\ell m}a_{\ell' m'}\rangle =&\frac{1}{9}\int\frac{d^3k}{(2\pi)^3}\int\frac{d^3k'}{(2\pi)^3}\left\langle\Phi^*(\vec{k})\Phi\left(\vec{k}'\right)\right\rangle\\ &\times(4\pi)^2 i^{\ell'-\ell}j_\ell\left(kD_{\rm rec}\right)j_{\ell'}\left(k'D_{\rm rec}\right)\\ &\times Y_{\ell m}(\widehat{k})Y^*_{\ell' m'}\left(\widehat{k}'\right)\,.\end{aligned} \tag{273}$$

To proceed further we need to plug here Eq. 272, which requires us to specify the expression for the modulating field.
There is no right or wrong choice for the modulation, but it all depends on what we want to obtain. In our case, we want to reproduce an excess power in one of the two hemispheres of the CMB, thus the most natural and simple choice is to go for a dipole modulation, such as [181]

$$h(\vec{x}) = w_1\sqrt{\frac{3}{4\pi}}\frac{1}{k_0 D_{\rm rec}}\sin\vec{k}_0\cdot\vec{x}\,, \tag{274}$$

$$h(\vec{k}) = \frac{w_1}{2i}\sqrt{\frac{3}{4\pi}}\frac{(2\pi)^3}{k_0 D_{\rm rec}}\left[\delta\left(\vec{k}-\vec{k}_0\right)-\delta\left(\vec{k}+\vec{k}_0\right)\right]\,. \tag{275}$$

where: $\vec{k}_0$ = wavenumber of the modulating field fluctuation;
w_1 = amplitude of the modulation;
1 = the subscript on the amplitude will remind us that we are considering a dipole modulation.

In first approximation, we can think of this modulation as $\propto Y_{10}$ (dipole), but again, one could have considered something different. For example, Dvorkin, Peiris, and Hu [181] also considers a quadrupolar modulation $\propto Y_{20}$ to explain another CMB anomaly, the alignment of the quadrupole and octopole.
Without entering into the details of the subsequent calculations that bring us to the final angular power spectrum, which we will profusely explore in Chap. 8 for the CGWB case, we report only the final results, so that we can compare them in the end. Just be aware that in [181] the ISW effect was ignored.

Firstly, the apex $^{(i)}$ will indicate a term at i-order in powers of h, i. e. the modulating field; thus, at zeroth order in the modulation we obtain [54]

$$\langle a^*_{\ell m} a_{\ell' m'} \rangle^{(0)} = \delta_{\ell \ell'} \delta_{m m'} C_\ell^{TT} \,, \tag{276}$$

where the angular power spectrum reads

$$C_\ell^{TT} \equiv \frac{4\pi}{9} \int \frac{dk}{k} \frac{k^3 P_g(k)}{2\pi^2} j_\ell^2(k\eta_{\rm rec}) \,. \tag{277}$$

For what regard the first order term (in the modulating field), one finds

$$\langle a^*_{\ell m} a_{\ell' m'} \rangle^{(1)} = \delta_{m m'} w_1 \left[R^{1,\ell}_{\ell' m} C_\ell^{TT} + R^{1,\ell'}_{\ell m} C_{\ell'}^{TT} \right] , \tag{278}$$

where

$$\begin{aligned} R^{\ell_1,\ell_2}_{\ell m} \equiv & (-1)^m \sqrt{\frac{(2\ell+1)\,(2\ell_1+1)\,(2\ell_2+1)}{4\pi}} \\ & \times \begin{pmatrix} \ell_1 & \ell_2 & \ell \\ 0 & 0 & 0 \end{pmatrix} \begin{pmatrix} \ell_1 & \ell_2 & \ell \\ 0 & m & -m \end{pmatrix} \end{aligned} \tag{279}$$

is a coupling matrix, which in our case (for example $\ell_1 = 1$ and $\ell_2 = \ell'$) couples modes with ℓ to $\ell \pm 1$ through the triangle rule of the $3-j$ Wigner's symbols [146].
Finally, without reporting the calculus, the second order term (in the modulating field) is given by [181] and reads

$$\langle a^*_{\ell m} a_{\ell' m'} \rangle^{(2)} = \delta_{m m'} w_1^2 \left[\sum_j R^{1,j}_{\ell m} R^{1,j}_{\ell' m} C_j^{TT} \right] , \tag{280}$$

which instead couples ℓ to $\ell \pm 2$.
The first thing we notice is that every term preserves the proportionality to $\delta_{m m'}$, which means that only coefficients with the same m are correlated. Indeed, this delta is a consequence of having used the approximation of Eq. 293, which assumes $k_0 \ll k$ and allows us to exploit the orthogonality property of SHs.
However, there is also another way to obtain this delta without assuming $k_0 \ll k$. In fact, if $\vec{k}_0$ is taken parallel to the z-axis, adding it to $\vec{k}$ will only affect its azimuthal angle θ (and its modulus clearly). In other words, the integral over the solid angle of $Y_{\ell m}(\widehat{k}) Y^*_{\ell' m'} \left(\frac{\vec{k} \pm \vec{k}_0}{|\vec{k} \pm \vec{k}_0|} \right)$ will still give a $\delta_{m m'}$.
On the other hand, the overall correlation between $a_{\ell m}$ will not be diagonal in ℓ, but there will be some non-diagonal terms correlating the first ($\ell \pm 1$) and second adjacent ($\ell \pm 2$) terms.

54 The apex ^{TT} just indicates that we are considering the self-correlation of the temperature field. In a more general context where one introduces other fields, such as the polarization ones E and B, it is possible to look also at the cross-correlations.

8

POWER ASYMMETRY WITH THE CGWB: THE THEORETICAL FOUNDATIONS

We have briefly seen in Chap. 7 what consequences a dipole modulation carries onto the CMB temperature field, but now we will plug the same dipole modulation into the framework introduced in Chap. 6.
This time we will perform all the calculations in an explicit way so that all the passages are clear to the reader. We will see that some similarity with the CMB case will pop up, together with some difference. Anyway, the same passages we are about to present can be used to obtain the final expressions of Chap. 7 for the contributions to $\left\langle \Theta_{\ell m}\Theta^{*}_{\ell' m'} \right\rangle$.
This chapter is based on Galloni et al. [182].

8.1 SCALAR CONTRIBUTION OF THE ANGULAR POWER SPECTRUM OF THE CGWB

In Chap. 6, we have seen that the gravitational potentials act on the CGWB through the SW and ISW effects. These two are part of the scalar contribution to the angular power spectrum of the CGWB, thus let us remind few expressions found in Chap. 6 and Chap. 7, which are very important to have clear. The scalar sourced term of Γ, defined in Eq. 226, reads:

$$\begin{aligned}\Gamma_S\left(\eta_0, \vec{k}, \widehat{n}\right) &= \int_{\eta_{\rm in}}^{\eta_0} d\eta' \mathrm{e}^{ik\mu(\eta'-\eta_0)} \left[T_\Phi(\eta', k)\delta(\eta'-\eta_{\rm in}) \right. \\ &\left. + \frac{\partial\left[T_\Psi\left(\eta', k\right) + T_\Phi(\eta', k)\right]}{\partial\eta'}\right] \zeta(\vec{k}) \\ &\equiv \int_{\eta_{\rm in}}^{\eta_0} d\eta' \mathrm{e}^{-ik\mu(\eta_0-\eta')} T_S\left(\eta', k\right)\zeta(\vec{k})\,.\end{aligned} \tag{281}$$

We can then decompose it in SH using Eq. 155. The coefficients of such decomposition are equal to

$$\begin{aligned}\Gamma_{\ell m,S} &= 4\pi(-i)^l \int \frac{d^3k}{(2\pi)^3} \mathrm{e}^{i\vec{k}\cdot\vec{x}_0}\zeta(\vec{k})Y^*_{\ell m}(\widehat{k})\left\{T_\Phi\left(\eta_{\rm in}\,, k\right) j_\ell\left(k\left(\eta_0-\eta_{\rm in}\right)\right)\right. \\ &\left. + \int_{\eta_{\rm in}}^{\eta_0} d\eta' \frac{\partial\left[T_\Psi\left(\eta', k\right) + T_\Phi\left(\eta', k\right)\right]}{\partial\eta'} j_\ell\left(k\left(\eta_0-\eta'\right)\right)\right\} \\ &= 4\pi(-i)^l \int \frac{d^3k}{(2\pi)^3} \mathrm{e}^{i\vec{k}\cdot\vec{x}_0}\zeta(\vec{k})Y^*_{\ell m}(\widehat{k}) T^S_\ell\left(k, \eta_0, \eta_{\rm in}\right)\,,\end{aligned} \tag{282}$$

where we have introduced the transfer function

$$T_\ell^S(k,\eta_0,\eta_{\rm in}) \equiv T_\Phi\left(\eta_{\rm in}\,,k\right) j_\ell\left(k\left(\eta_0-\eta_{\rm in}\right)\right) + \int_{\eta_{\rm in}}^{\eta_0} d\eta' \frac{\partial\left[T_\Psi\left(\eta',k\right)+T_\Phi\left(\eta',k\right)\right]}{\partial\eta'} j_\ell\left(k\left(\eta_0-\eta'\right)\right)\ . \tag{283}$$

As aforementioned, instead of the stochastic variable $\zeta(k)$ used in Chap. 4, we can plug the modulation of the gravitational potential of Eq. 271 in Eq. 282, introducing a Gaussian random field $g(k)$, having power near the horizon scale, and the modulation field $h(k)$, called "modulating field" and accounting for the symmetry breaking long-wavelength mode. This also allows us to carry on in the calculations the transfer function T_Φ, maintaining a general approach. In fact, we will specify its explicit expression only after having obtained the general expressions of the angular power spectrum of the CGWB.
Thus, we write ζ as

$$\zeta(\vec{k}) = g(\vec{k}) + \int \frac{d^3k'}{(2\pi)^3} g(\vec{k}')h(\vec{k}-\vec{k}')\ . \tag{284}$$

Hence, the correlation function becomes

$$\begin{aligned}\left\langle \zeta(\vec{k})\zeta^*\left(\vec{k}'\right)\right\rangle =& (2\pi)^3\delta\left(\vec{k}-\vec{k}'\right)P_g(k) \\ &+ \left[P_g(k)+P_g\left(k'\right)\right]h\left(\vec{k}-\vec{k}'\right) \\ &+ \int \frac{d^3\widetilde{k}}{(2\pi)^3} P_g(\widetilde{k})h(\vec{k}-\widetilde{\vec{k}})h^*\left(\vec{k}'-\widetilde{\vec{k}}\right)\ ,\end{aligned} \tag{285}$$

which can be plugged into

$$\begin{aligned}\left\langle \Gamma_{\ell m,S}\Gamma^*_{\ell' m',S}\right\rangle =& (4\pi)^2(-i)^{\ell-\ell'}\int\frac{d^3k}{(2\pi)^3}e^{i\vec{k}\cdot\vec{x}_0}\int\frac{d^3k'}{(2\pi)^3}e^{-i\vec{k}'\cdot\vec{x}_0}\left\langle\zeta(\vec{k})\zeta^*\left(\vec{k}'\right)\right\rangle \\ &\times Y^*_{\ell m}(\widehat{k})Y_{\ell' m'}\left(\widehat{k}'\right)\times T^S_\ell\left(k,\eta_0,\eta_{\rm in}\right)T^S_{\ell'}\left(k',\eta_0,\eta_{\rm in}\right)\ .\end{aligned} \tag{286}$$

Identifying the terms of Eq. 285 based on their order in $h(\vec{k})$, we can write the different contributions to the correlation of the Γ_S.

8.1.1 *Zeroth Order Term in the Modulating Field*

Starting from the zeroth order term (in the modulating field), it is easy to find

$$\begin{aligned}
&\left\langle \Gamma_{\ell m,S}\Gamma^{*}_{\ell' m',S}\right\rangle^{(0)} = \\
=&(4\pi)^2(-i)^{\ell-\ell'}\int\frac{d^3k}{(2\pi)^3}\mathrm{e}^{i\vec{k}\cdot\vec{x}_0}\int\frac{d^3k'}{(2\pi)^3}\mathrm{e}^{-i\vec{k}'\cdot\vec{x}_0}\times(2\pi)^3\delta\left(\vec{k}-\vec{k}'\right)P_g(k) \\
&\times Y^{*}_{\ell m}(\widehat{k})Y_{\ell' m'}\left(\widehat{k}'\right)\times T^{S}_{\ell}\left(k,\eta_0,\eta_{\rm in}\right)T^{S}_{\ell'}\left(k',\eta_0,\eta_{\rm in}\right) = \\
=&(4\pi)^2(-i)^{\ell-\ell'}\int\frac{d^3k}{(2\pi)^3}P_g(k)\times Y^{*}_{\ell m}(\widehat{k})Y_{\ell' m'}\left(\widehat{k}\right)\times T^{S}_{\ell}\left(k,\eta_0,\eta_{\rm in}\right)T^{S}_{\ell'}\left(k,\eta_0,\eta_{\rm in}\right) = \\
=&(4\pi)^2\int\frac{dk}{k(2\pi)^3}k^3P_g(k)\delta_{mm'}\delta_{\ell\ell'}T^{(S)2}_{\ell}\left(k,\eta_0,\eta_{\rm in}\right) = \\
=&4\pi\int\frac{dk}{k}\Delta_g(k)\delta_{mm'}\delta_{\ell\ell'}T^{(S)2}_{\ell}\left(k,\eta_0,\eta_{\rm in}\right) = \\
=&\delta_{\ell\ell'}\delta_{mm'}\mathcal{C}^{(0)}_{\ell}\ ,
\end{aligned} \tag{287}$$

where $\Delta_g \equiv \frac{k^3}{2\pi^2}P_g$. Here, we have used the orthogonality condition of SHs and the fact that the observer is positioned in $\vec{x}_0 = 0$ [55]. As one can expect by sending the modulating field to zero, this term gives the isotropic term found in Chap. 6, where one have to substitute $\Delta_g \leftrightarrow P_s$[56].

8.1.2 *First Order Term in the Modulating Field*

For what regard the first order term (in the modulating field), we must fix an explicit expression of $h(\vec{k})$. In order to mimic what we have done in Chap. 7, following [181], we assume a dipole modulation, thus we can write

$$h(\vec{k}) = \frac{w_1}{2i}\sqrt{\frac{3}{4\pi}}\frac{(2\pi)^3}{k_0\left(\eta_0-\eta_{\rm in}\right)}\left[\delta\left(\vec{k}-\vec{k}_0\right)-\delta\left(\vec{k}+\vec{k}_0\right)\right]\ . \tag{288}$$

We stress again that this choice of the modulating field is not mandatory, but instead represents the most simple example we could use to study a departure from isotropy. For now, we stick to this parametrization, but in the future it would be interesting to explore more general choices.

55 See footnotes 51 and 53 for further details on the choice for the origin of the reference frame $\vec{x}_0 = 0$.

56 Once have defined which is the power spectrum and its adimensional counterpart, the two expression are completely equivalent as one would expect.

To go on with our calculation we need to make explicit h in $\vec{k}' - \vec{k}$, thus using the expression above in Fourier space

$$h(\vec{k}' - \vec{k}) = \frac{w_1}{2i}\sqrt{\frac{3}{4\pi}}\frac{(2\pi)^3}{k_0\,(\eta_0 - \eta_{\rm in}\,)}\left[\delta\left(\vec{k}' - \vec{k} - \vec{k}_0\right) - \delta\left(\vec{k}' - \vec{k} + \vec{k}_0\right)\right], \tag{289}$$

which allows to find

$$\begin{aligned}
&\left\langle \Gamma_{\ell m,S}\Gamma^*_{\ell' m',S}\right\rangle^{(1)} = \\
&(4\pi)^2(-i)^{\ell-\ell'}\int\frac{d^3k}{(2\pi)^3}e^{i\vec{k}\cdot\vec{x}_0}\int\frac{d^3k'}{(2\pi)^3}e^{-i\vec{k}'\cdot\vec{x}_0}\times\left[P_g(k) + P_g\left(k'\right)\right]h\left(\vec{k}' - \vec{k}\right) \\
&\times Y^*_{\ell m}(\widehat{k})Y_{\ell' m'}\left(\widehat{k}'\right)\times T^S_\ell\left(k,\eta_0,\eta_{\rm in}\right)T^S_{\ell'}\left(k',\eta_0,\eta_{\rm in}\right) \\
=&(4\pi)^2(-i)^{\ell-\ell'}\int\frac{d^3k}{(2\pi)^3}e^{i\vec{k}\cdot\vec{x}_0}\int\frac{d^3k'}{(2\pi)^3}e^{-i\vec{k}'\cdot\vec{x}_0}\times\left[P_g(k) + P_g\left(k'\right)\right] \\
&\times Y^*_{\ell m}(\widehat{k})Y_{\ell' m'}\left(\widehat{k}'\right)\times T^S_\ell\left(k,\eta_0,\eta_{\rm in}\right)T^S_{\ell'}\left(k',\eta_0,\eta_{\rm in}\right) \\
&\times\frac{w_1}{2i}\sqrt{\frac{3}{4\pi}}\frac{(2\pi)^3}{k_0\,(\eta_0 - \eta_{\rm in}\,)}\left[\delta\left(\vec{k}' - \vec{k} - \vec{k}_0\right) - \delta\left(\vec{k}' - \vec{k} + \vec{k}_0\right)\right].
\end{aligned} \tag{290}$$

Let us consider the first of the two Dirac deltas and solve that term. Again, assuming the origin in $x_0 = 0$ [57] we can get rid of the exponentials and, integrating the delta, we get

$$\begin{aligned}
&\left\langle \Gamma_{\ell m,S}\Gamma^*_{\ell' m',S}\right\rangle^{(1)}_{1st} = \\
=&(4\pi)^2(-i)^{\ell-\ell'}\int\frac{d^3k}{(2\pi)^3}\int\frac{d^3k'}{(2\pi)^3}\times\left[P_g(k) + P_g\left(k'\right)\right] \\
&\times Y^*_{\ell m}(\widehat{k})Y_{\ell' m'}\left(\widehat{k}'\right)\times T^S_\ell\left(k,\eta_0,\eta_{\rm in}\right)T^S_{\ell'}\left(k',\eta_0,\eta_{\rm in}\right) \\
&\times\frac{w_1}{2i}\sqrt{\frac{3}{4\pi}}\frac{(2\pi)^3}{k_0\,(\eta_0 - \eta_{\rm in}\,)}\delta\left(\vec{k}' - \vec{k} - \vec{k}_0\right) \\
=&\frac{(4\pi)^2}{(2\pi)^3}(-i)^{\ell-\ell'}\int d^3k\left[P_g(k) + P_g\left(\left|\vec{k} + \vec{k}_0\right|\right)\right] \\
&\times Y^*_{\ell m}(\widehat{k})Y_{\ell' m'}\left(\frac{\vec{k} + \vec{k}_0}{\left|\vec{k} + \vec{k}_0\right|}\right)\times T^S_\ell\left(k,\eta_0,\eta_{\rm in}\right)T^S_{\ell'}\left(\left|\vec{k} + \vec{k}_0\right|,\eta_0,\eta_{\rm in}\right) \\
&\times\frac{w_1}{2i}\sqrt{\frac{3}{4\pi}}\frac{1}{k_0\,(\eta_0 - \eta_{\rm in})}\,.
\end{aligned}$$

57 See footnotes 51 and 53 for further details on the choice for the origin of the reference frame $\vec{x}_0 = 0$.

(291)

Now, we can make explicit the product of the transfer function and the SHs evaluated in $|\vec{k}+\vec{k}_0|$, where we can identify the SW (second line) and the ISW (third line) effects for the CGWB

$$\begin{aligned}
&\frac{1}{k_0\left(\eta_0-\eta_{\rm in}\right)}\sqrt{\frac{3}{4\pi}}T^S_{\ell'}\left(|\vec{k}+\vec{k}_0|,\eta_0,\eta_{\rm in}\right)Y_{\ell'm'}\left(\frac{\vec{k}+\vec{k}_0}{|\vec{k}+\vec{k}_0|}\right)= \\
&\frac{1}{k_0\left(\eta_0-\eta_{\rm in}\right)}\sqrt{\frac{3}{4\pi}}\Bigg[T_\Phi\left(\eta_{\rm in},|\vec{k}+\vec{k}_0|\right)j_{\ell'}\left[|\vec{k}+\vec{k}_0|\,\left(\eta_0-\eta_{\rm in}\right)\right] \\
&+\int_{\eta_{\rm in}}^{\eta_0}d\eta'\frac{\partial\left[T_\Psi(\eta',|\vec{k}+\vec{k}_0|)+T_\Phi(\eta',|\vec{k}+\vec{k}_0|)\right]}{\partial\eta'}j_{\ell'}\left[|\vec{k}+\vec{k}_0|\,\left(\eta_0-\eta'\right)\right]\Bigg] \\
&\times Y_{\ell'm'}\left(\frac{\vec{k}+\vec{k}_0}{|\vec{k}+\vec{k}_0|}\right)\,.
\end{aligned} \tag{292}$$

Now, we can introduce an approximation to expand the product of a SBF and a SH in the previous expression for $k_0 \ll k$. Specifically, one can show that [181]

$$\begin{aligned}
&\tfrac{1}{k_0(\eta_0-\eta_{\rm in})}\sqrt{\tfrac{3}{4\pi}}j_\ell\left(\left|\vec{k}+\alpha\vec{k}_0\right|\left(\eta_0-\eta_{\rm in}\right)\right)Y_{\ell m}\left(\tfrac{\vec{k}+\alpha\vec{k}_0}{|\vec{k}+\alpha\vec{k}_0|}\right) \\
&\approx \tfrac{1}{k_0(\eta_0-\eta_{\rm in})}\sqrt{\tfrac{3}{4\pi}}j_\ell(k\left(\eta_0-\eta_{\rm in}\right))Y_{\ell m}(\widehat{k}) \\
&\quad-\tfrac{\alpha}{2}R^{1,\ell+1}_{\ell m}j_{\ell+1}(k\left(\eta_0-\eta_{\rm in}\right))Y_{\ell+1,m}(\widehat{k}) \\
&\quad+\tfrac{\alpha}{2}R^{1,\ell-1}_{\ell m}j_{\ell-1}(k\left(\eta_0-\eta_{\rm in}\right))Y_{\ell-1,m}(\widehat{k})\,,
\end{aligned} \tag{293}$$

where

$$\begin{aligned}
R^{\ell_1,\ell_2}_{\ell m}\equiv&(-1)^m\sqrt{\frac{\left(2\ell+1\right)\left(2\ell_1+1\right)\left(2\ell_2+1\right)}{4\pi}} \\
&\times\begin{pmatrix}\ell_1&\ell_2&\ell\\0&0&0\end{pmatrix}\begin{pmatrix}\ell_1&\ell_2&\ell\\0&m&-m\end{pmatrix}\,.
\end{aligned} \tag{294}$$

In our case we have $\alpha = 1$ and $\ell \to \ell'$, $m \to m'$, thus [58]

$$\begin{aligned}
&\tfrac{1}{k_0(\eta_0-\eta_{\rm in})}\sqrt{\tfrac{3}{4\pi}} j_{\ell'}\left(\left|\vec{k}+\vec{k}_0\right|(\eta_0-\eta_{\rm in})\right) Y_{\ell' m'}\left(\tfrac{\vec{k}+\vec{k}_0}{|\vec{k}+\vec{k}_0|}\right)\\
&\approx \tfrac{1}{k_0(\eta_0-\eta_{\rm in})}\sqrt{\tfrac{3}{4\pi}} j_{\ell'}(k(\eta_0-\eta_{\rm in}))Y_{\ell' m'}(\widehat{k})\\
&\quad -\tfrac{1}{2}R^{1,\ell'+1}_{\ell' m'} j_{\ell'+1}(k(\eta_0-\eta_{\rm in}))Y_{\ell'+1,m'}(\widehat{k})\\
&\quad +\tfrac{1}{2}R^{1,\ell'-1}_{\ell' m'} j_{\ell'-1}(k(\eta_0-\eta_{\rm in}))Y_{\ell'-1,m'}(\widehat{k})\,.
\end{aligned} \tag{296}$$

With this approximation, we can write for the SW effect (second line of Eq. 292)

$$\begin{aligned}
&\frac{1}{k_0(\eta_0-\eta_{\rm in})}\sqrt{\frac{3}{4\pi}} T_\Phi\left(\eta_{\rm in}, |\vec{k}+\vec{k}_0|\right) j_{\ell'}\left[|\vec{k}+\vec{k}_0|\,(\eta_0-\eta_{\rm in})\right]\\
&\times Y_{\ell' m'}\left(\frac{\vec{k}+\vec{k}_0}{|\vec{k}+\vec{k}_0|}\right) =\\
&\approx \frac{1}{k_0(\eta_0-\eta_{\rm in})}\sqrt{\frac{3}{4\pi}} T_\Phi\left(\eta_{\rm in}, |\vec{k}+\vec{k}_0|\right) j_{\ell'}(k(\eta_0-\eta_{\rm in}))Y_{\ell' m'}(\widehat{k})\\
&-\frac{1}{2}R^{1,\ell'+1}_{\ell' m'} T_\Phi\left(\eta_{\rm in}, |\vec{k}+\vec{k}_0|\right) j_{\ell'+1}(k(\eta_0-\eta_{\rm in}))Y_{\ell'+1,m'}(\widehat{k})\\
&+\frac{1}{2}R^{1,\ell'-1}_{\ell' m'} T_\Phi\left(\eta_{\rm in}, |\vec{k}+\vec{k}_0|\right) j_{\ell'-1}(k(\eta_0-\eta_{\rm in}))Y_{\ell'-1,m'}(\widehat{k}) =\\
&= \frac{1}{k_0(\eta_0-\eta_{\rm in})}\sqrt{\frac{3}{4\pi}} T^{SW}_{\ell'}\left(|\vec{k}+\vec{k}_0|\right) Y_{\ell' m'}(\widehat{k})\\
&-\frac{1}{2}R^{1,\ell'+1}_{\ell' m'} T^{SW}_{\ell'+1}\left(|\vec{k}+\vec{k}_0|\right) Y_{\ell'+1,m'}(\widehat{k})\\
&+\frac{1}{2}R^{1,\ell'-1}_{\ell' m'} T^{SW}_{\ell'-1}\left(|\vec{k}+\vec{k}_0|\right) Y_{\ell'-1,m'}(\widehat{k})\,,
\end{aligned} \tag{297}$$

where we have defined the following quantity

$$T^{SW}_{\ell}\left(|\vec{k}+\vec{k}_0|\right) \equiv T_\Phi\left(\eta_{\rm in}, |\vec{k}+\vec{k}_0|\right) j_\ell(k(\eta_0-\eta_{\rm in}))\,. \tag{298}$$

58 In spite of what is reported in [181], in Eq. 293 we presented an extra 1/2 factor in front of the first order terms in the expansion. This factors is due to the known relation of the derivative of Bessel functions [31]

$$\frac{\mathrm{d}J_\ell(z)}{\mathrm{d}z} = \boxed{\frac{1}{2}}[J_{\ell-1}(z) - J_{\ell+1}(z)]\,. \tag{295}$$

Even if this does not seem the case at first sight, this factor is indeed crucial to reconcile our results with the ones of [181] (we will come back on this later on in this Thesis).

We stress that this transfer function is different from the SW contribution of Eq. 283 because here T_Φ is evaluated in $|\vec{k}+\vec{k}_0|$ and not in $\vec{k}$.
Looking now at the ISW effect (third line of Eq. 292), we can write similarly

$$
\begin{aligned}
&\frac{1}{k_0\left(\eta_0-\eta_{\rm in}\right)}\sqrt{\frac{3}{4\pi}}\int_{\eta_{\rm in}}^{\eta_0}d\eta'\frac{\partial\left[T_\Psi(\eta',|\vec{k}+\vec{k}_0|)+T_\Phi(\eta',|\vec{k}+\vec{k}_0|)\right]}{\partial\eta'}\\
&\times j_{\ell'}\left[|\vec{k}+\vec{k}_0|\ \left(\eta_0-\eta'\right)\right]Y_{\ell'm'}\left(\frac{\vec{k}+\vec{k}_0}{|\vec{k}+\vec{k}_0|}\right)=\\
&\approx\frac{1}{k_0\left(\eta_0-\eta_{\rm in}\right)}\sqrt{\frac{3}{4\pi}}\int_{\eta_{\rm in}}^{\eta_0}d\eta'\frac{\partial\left[T_\Psi(\eta',|\vec{k}+\vec{k}_0|)+T_\Phi(\eta',|\vec{k}+\vec{k}_0|)\right]}{\partial\eta'}\\
&\times j_{\ell'}\left(k\left(\eta_0-\eta'\right)\right)Y_{\ell'm'}\left(\widehat{k}\right)+\\
&-\frac{1}{2}R^{1,\ell'+1}_{\ell'm'}\int_{\eta_{\rm in}}^{\eta_0}d\eta'\frac{\eta_0-\eta'}{\eta_0-\eta_{\rm in}}\frac{\partial\left[T_\Psi(\eta',|\vec{k}+\vec{k}_0|)+T_\Phi(\eta',|\vec{k}+\vec{k}_0|)\right]}{\partial\eta'}\\
&\times j_{\ell'+1}\left(k\left(\eta_0-\eta'\right)\right)Y_{\ell'+1,m'}\left(\widehat{k}\right)+\\
&+\frac{1}{2}R^{1,\ell'-1}_{\ell'm'}\int_{\eta_{\rm in}}^{\eta_0}d\eta'\frac{\eta_0-\eta'}{\eta_0-\eta_{\rm in}}\frac{\partial\left[T_\Psi(\eta',|\vec{k}+\vec{k}_0|)+T_\Phi(\eta',|\vec{k}+\vec{k}_0|)\right]}{\partial\eta'}\\
&\times j_{\ell'-1}\left(k\left(\eta_0-\eta'\right)\right)Y_{\ell'-1,m'}\left(\widehat{k}\right)=\\
&=\frac{1}{k_0\left(\eta_0-\eta_{\rm in}\right)}\sqrt{\frac{3}{4\pi}}T^{ISW}_{\ell'}\Big(|\vec{k}+\vec{k}_0|\Big)Y_{\ell'm'}(\widehat{k})\\
&-\frac{1}{2}R^{1,\ell'+1}_{\ell'm'}T^{ISW\star}_{\ell'+1}\Big(|\vec{k}+\vec{k}_0|\Big)Y_{\ell'+1,m'}(\widehat{k})\\
&+\frac{1}{2}R^{1,\ell'-1}_{\ell'm'}T^{ISW\star}_{\ell'-1}\Big(|\vec{k}+\vec{k}_0|\Big)Y_{\ell'-1,m'}(\widehat{k})\ .
\end{aligned}
\tag{299}
$$

This time the approximation of Eq. 293 gives us a new extra factor inside the integral.
Indeed, when computing the first order term of the expansion, one has to evaluate

$$
\frac{\mathrm{d}j_\ell(z(\alpha))}{\mathrm{d}\alpha}=\frac{\mathrm{d}j_\ell(z)}{\mathrm{d}z}\frac{\mathrm{d}z(\alpha)}{\mathrm{d}\alpha}\ , \tag{300}
$$

where: $z(\alpha)\ \equiv\ |\vec{k}+\alpha\vec{k}_0|\left(\eta_0-\eta'\right)$;
$\alpha\ll1\rightarrow$ this allows to realize $\alpha k_0\ll k$.

Then, looking at the derivative of z w. r. t. α

$$\begin{aligned}\frac{\mathrm{d}z(\alpha)}{\mathrm{d}\alpha} =&(\eta_0-\eta')\frac{\mathrm{d}}{\mathrm{d}\alpha}\left(\sqrt{k^2+\alpha^2k_0^2+2\alpha\cos(\theta)kk_0}\right)\\ \simeq&(\eta_0-\eta')\frac{\mathrm{d}}{\mathrm{d}\alpha}\left(\sqrt{k^2+2\alpha\cos(\theta)kk_0}\right)\\ =&(\eta_0-\eta')\frac{1}{2}\frac{2\cos(\theta)kk_0}{\sqrt{k^2+2\alpha\cos(\theta)kk_0}}\simeq(\eta_0-\eta')\frac{\cos(\theta)kk_0}{k}\\ \simeq&(\eta_0-\eta')\cos(\theta)k_0\simeq k_0(\eta_0-\eta')\,,\end{aligned} \tag{301}$$

where we approximated the cosine to 1 as done for Eq. 293. We can see that now the derivative just obtained does not cancel out the front factor present in Eq. 299, giving instead an extra factor

$$\frac{\eta_0-\eta'}{\eta_0-\eta_{\rm in}}\neq 1\,. \tag{302}$$

For this reason in Eq. 299, we have defined two different transfer functions, distinguished by a $\star$

$$\begin{aligned}T_\ell^{ISW}\left(|\vec{k}+\vec{k}_0|\right)\equiv&\int_{\eta_{\rm in}}^{\eta_0}d\eta'\frac{\partial\left[T_\Psi(\eta',|\vec{k}+\vec{k}_0|)+T_\Phi(\eta',|\vec{k}+\vec{k}_0|)\right]}{\partial\eta'}\\ &\times j_\ell\left(k\left(\eta_0-\eta'\right)\right)\,,\\ T_\ell^{ISW\star}\left(|\vec{k}+\vec{k}_0|\right)\equiv&\int_{\eta_{\rm in}}^{\eta_0}d\eta'\frac{\partial\left[T_\Psi(\eta',|\vec{k}+\vec{k}_0|)+T_\Phi(\eta',|\vec{k}+\vec{k}_0|)\right]}{\partial\eta'}\\ &\times\frac{\eta_0-\eta'}{\eta_0-\eta_{\rm in}}j_\ell\left(k\left(\eta_0-\eta'\right)\right)\,.\end{aligned} \tag{303}$$

We stress again that this transfer function is in general different from the ISW contribution of T_ℓ^S (see Eq. 283) because here T_Φ and T_Ψ are evaluated in $|\vec{k}+\vec{k}_0|$ and not in $\vec{k}$.
In addition, the presence of the extra factor, induced by the modulation, represents a signature of the departure from isotropy of the CGWB, given

that it is not present in the isotropic computations.
Neglecting for the moment the ISW effect, Eq. 291 becomes

$$\begin{aligned}
&\left\langle \Gamma_{\ell m,S}\Gamma^{*}_{\ell' m',S}\right\rangle^{(1)}_{1st} = \\
=&\frac{(4\pi)^2}{(2\pi)^3}(-i)^{\ell-\ell'}\frac{w_1}{2i}\int dk k^2\left[P_g(k)+P_g\left(|\vec{k}+\vec{k}_0|\right)\right]T^S_\ell\left(k,\eta_0,\eta_{\rm in}\right)\\
&\times\int d\widehat{k}Y^*_{\ell m}(\widehat{k})\Big[\frac{1}{k_0\left(\eta_0-\eta_{\rm in}\right)}\sqrt{\frac{3}{4\pi}}T^{SW}_{\ell'}\left(|\vec{k}+\vec{k}_0|\right)Y_{\ell' m'}(\widehat{k})\\
&-\frac{1}{2}R^{1,\ell'+1}_{\ell' m'}T^{SW}_{\ell'+1}\left(|\vec{k}+\vec{k}_0|\right)Y_{\ell'+1,m'}(\widehat{k})+\frac{1}{2}R^{1,\ell'-1}_{\ell' m'}T^{SW}_{\ell'-1}\left(|\vec{k}+\vec{k}_0|\right)Y_{\ell'-1,m'}(\widehat{k})\Big],
\end{aligned}\tag{304}$$

which, computing individually the three resulting terms, becomes

$$\begin{aligned}
&\left\langle \Gamma_{\ell m,S}\Gamma^{*}_{\ell' m',S}\right\rangle^{(1)}_{1st} = \\
=&\frac{(4\pi)^2}{(2\pi)^3}(-i)^{\ell-\ell'}\frac{w_1}{2i}\int dk k^2\left[P_g(k)+P_g\left(|\vec{k}+\vec{k}_0|\right)\right]T^S_\ell\left(k,\eta_0,\eta_{\rm in}\right)T^{SW}_{\ell'}\left(|\vec{k}+\vec{k}_0|\right)\\
&\times\frac{1}{k_0\left(\eta_0-\eta_{\rm in}\right)}\sqrt{\frac{3}{4\pi}}\times\int d\widehat{k}Y^*_{\ell m}(\widehat{k})Y_{\ell' m'}(\widehat{k})+\\
&-\frac{(4\pi)^2}{(2\pi)^3}(-i)^{\ell-\ell'}\frac{w_1}{2i}\int dk k^2\left[P_g(k)+P_g\left(|\vec{k}+\vec{k}_0|\right)\right]T^S_\ell\left(k,\eta_0,\eta_{\rm in}\right)T^{SW}_{\ell'+1}\left(|\vec{k}+\vec{k}_0|\right)\\
&\times\frac{1}{2}R^{1,\ell'+1}_{\ell' m'}\int d\widehat{k}Y^*_{\ell m}(\widehat{k})Y_{\ell'+1,m'}(\widehat{k})+\\
&+\frac{(4\pi)^2}{(2\pi)^3}(-i)^{\ell-\ell'}\frac{w_1}{2i}\int dk k^2\left[P_g(k)+P_g\left(|\vec{k}+\vec{k}_0|\right)\right]T^S_\ell\left(k,\eta_0,\eta_{\rm in}\right)T^{SW}_{\ell'-1}\left(|\vec{k}+\vec{k}_0|\right)\\
&\times\frac{1}{2}R^{1,\ell'-1}_{\ell' m'}\int d\widehat{k}Y^*_{\ell m}(\widehat{k})Y_{\ell'-1,m'}(\widehat{k})= \\
=&\frac{(4\pi)^2}{(2\pi)^3}\frac{w_1}{2i}\int dk k^2\left[P_g(k)+P_g\left(|\vec{k}+\vec{k}_0|\right)\right]T^S_\ell\left(k,\eta_0,\eta_{\rm in}\right)T^{SW}_{\ell}\left(|\vec{k}+\vec{k}_0|\right)\\
&\times\frac{1}{k_0\left(\eta_0-\eta_{\rm in}\right)}\sqrt{\frac{3}{4\pi}}\times\delta_{\ell\ell'}\delta_{mm'}+\\
&-\frac{(4\pi)^2}{(2\pi)^3}(-i)\frac{w_1}{2i}\int dk k^2\left[P_g(k)+P_g\left(|\vec{k}+\vec{k}_0|\right)\right]T^S_\ell\left(k,\eta_0,\eta_{\rm in}\right)T^{SW}_{\ell}\left(|\vec{k}+\vec{k}_0|\right)\\
&\times\frac{1}{2}R^{1,\ell}_{\ell' m}\delta_{mm'}+\\
&+\frac{(4\pi)^2}{(2\pi)^3}(-i)^{-1}\frac{w_1}{2i}\int dk k^2\left[P_g(k)+P_g\left(|\vec{k}+\vec{k}_0|\right)\right]T^S_\ell\left(k,\eta_0,\eta_{\rm in}\right)T^{SW}_{\ell}\left(|\vec{k}+\vec{k}_0|\right)\\
&\times\frac{1}{2}R^{1,\ell}_{\ell' m}\delta_{mm'}=
\end{aligned}$$

$$
\begin{aligned}
=&\frac{(4\pi)^2}{(2\pi)^3}\frac{w_1}{2i}\int dk k^2\left[P_g(k)+P_g\left(|\vec{k}+\vec{k}_0|\right)\right]T_\ell^S\left(k,\eta_0,\eta_{\rm in}\right)T_\ell^{SW}\left(|\vec{k}+\vec{k}_0|\right)\\
&\times\frac{1}{k_0\left(\eta_0-\eta_{\rm in}\right)}\sqrt{\frac{3}{4\pi}}\times\delta_{\ell\ell'}\delta_{mm'}+\\
&+\frac{(4\pi)^2}{(2\pi)^3}\frac{w_1}{2}R^{1,\ell}_{\ell' m}\delta_{mm'}\int dk k^2\left[P_g(k)+P_g\left(|\vec{k}+\vec{k}_0|\right)\right]\\
&\times T_\ell^S\left(k,\eta_0,\eta_{\rm in}\right)T_\ell^{SW}\left(|\vec{k}+\vec{k}_0|\right).
\end{aligned}
\tag{305}
$$

In other words, we get an isotropic contribution ($\propto \delta_{\ell\ell'}$) and one that couples $\ell\pm1$ to ℓ through the 3-j symbols in the definition of R. Indeed the triangle inequality[59] applied to the $3-j$ symbols gives the only non-null contribution when $\ell'=\ell\pm1$.

We have just computed the first contribution to Eq. 290, so we must compute the other one, coming from the other Dirac delta. However we can exploit a simple trick to fasten the procedure: if we integrate the delta in k (instead of k'), the delta sends $k\to k'+k_0$ and the procedure becomes exactly the same as in the previous case, at the cost of inverting the primes. One can show that in the end the contribution reads[60]

$$
\begin{aligned}
&\left\langle\Gamma_{\ell m,S}\Gamma^*_{\ell' m',S}\right\rangle^{(1)}_{2nd}=\\
=&-\frac{(4\pi)^2}{(2\pi)^3}\frac{w_1}{2i}\int dk k^2\left[P_g(k)+P_g\left(|\vec{k}+\vec{k}_0|\right)\right]T_\ell^S\left(k,\eta_0,\eta_{\rm in}\right)T_\ell^{SW}\left(|\vec{k}+\vec{k}_0|\right)\\
&\times\frac{1}{k_0\left(\eta_0-\eta_{\rm in}\right)}\sqrt{\frac{3}{4\pi}}\times\delta_{\ell\ell'}\delta_{mm'}+\\
&+\frac{(4\pi)^2}{(2\pi)^3}\frac{w_1}{2}R^{1,\ell'}_{\ell m}\delta_{mm'}\int dk' k'^2\left[P_g(k')+P_g\left(k'+k_0\right)\right]\\
&\times T_{\ell'}^S\left(k',\eta_0,\eta_{\rm in}\right)T_{\ell'}^{SW}(k'+k_0).
\end{aligned}
\tag{307}
$$

59 For a symbol of the type

$$
\begin{pmatrix}\ell_1 & \ell_2 & \ell\\ 0 & m & -m\end{pmatrix}
\tag{306}
$$

the following has to hold: $|\ell_1-\ell_2|\leq\ell\leq\ell_1+\ell_2$. In our case this becomes $|\ell-1|\leq\ell'\leq\ell+1$, however these are all integer quantities, thus ℓ' is fixed to $\ell\pm1$ (see [146]).

60 We included the minus sign in front of the delta in such a way that the two contributions have to be summed.

Notice that the isotropic term is the same in the two contributions, exception made for a minus sign in the latter expression, thus the final expression will be

$$\begin{aligned}
&\left\langle \Gamma_{\ell m,S}\Gamma^{*}_{\ell' m',S}\right\rangle^{(1)}_{SW} = \left\langle \Gamma_{\ell m,S}\Gamma^{*}_{\ell' m',S}\right\rangle^{(1)}_{1st} + \left\langle \Gamma_{\ell m,S}\Gamma^{*}_{\ell' m',S}\right\rangle^{(1)}_{2nd} = \\
=&\frac{(4\pi)^2}{(2\pi)^3}\frac{w_1}{2}R^{1,\ell}_{\ell' m}\delta_{mm'}\int dk k^2\left[P_g(k)+P_g\left(|\vec{k}+\vec{k}_0|\right)\right]T^{S}_{\ell}\left(k,\eta_0,\eta_{\rm in}\right)T^{SW}_{\ell}\left(|\vec{k}+\vec{k}_0|\right) \\
&+\frac{(4\pi)^2}{(2\pi)^3}\frac{w_1}{2}R^{1,\ell'}_{\ell m}\delta_{mm'}\int dk' k'^2\left[P_g(k')+P_g\left(k'+k_0\right)\right]T^{S}_{\ell'}\left(k',\eta_0,\eta_{\rm in}\right)T^{SW}_{\ell'}(k'+k_0) = \\
=&4\pi\frac{w_1}{2}R^{1,\ell}_{\ell' m}\delta_{mm'}\int \frac{dk}{k}\frac{k^3}{2\pi^2}\left[P_g(k)+P_g\left(|\vec{k}+\vec{k}_0|\right)\right]T^{S}_{\ell}\left(k,\eta_0,\eta_{\rm in}\right)T^{SW}_{\ell}\left(|\vec{k}+\vec{k}_0|\right) \\
&+4\pi\frac{w_1}{2}R^{1,\ell'}_{\ell m}\delta_{mm'}\int \frac{dk'}{k'}\frac{k'^3}{2\pi^2}\left[P_g(k')+P_g\left(k'+k_0\right)\right]T^{S}_{\ell'}\left(k',\eta_0,\eta_{\rm in}\right)T^{SW}_{\ell'}(k'+k_0) = \\
=&\frac{w_1}{2}\delta_{mm'}\left[R^{1,\ell}_{\ell' m}\mathcal{C}^{SW}_{\ell}+R^{1,\ell'}_{\ell m}\mathcal{C}^{SW}_{\ell'}\right],
\end{aligned} \tag{308}$$

where we defined the angular power spectrum (of the CGWB) relative to this contribution as

$$\mathcal{C}^{SW}_{\ell} \equiv 4\pi\int\frac{dk}{k}\frac{k^3}{2\pi^2}\left[P_g(k)+P_g\left(|\vec{k}+\vec{k}_0|\right)\right]T^{S}_{\ell}\left(k,\eta_0,\eta_{\rm in}\right)T^{SW}_{\ell}\left(|\vec{k}+\vec{k}_0|\right). \tag{309}$$

In order to simplify our computation, until now we had temporarily neglected the ISW effect contribution, leaving only the easier-to-treat SW one. However, in spite of the different explicit expressions of the two effects, they can be treated in the same way; just pay attention to the presence of the modified transfer functions that characterize the ISW effect. In other words, without reporting the same passages done for the SW case, we can write for its integrated counterpart

$$\left\langle \Gamma_{\ell m,S}\Gamma^{*}_{\ell' m',S}\right\rangle^{(1)}_{ISW} = \frac{w_1}{2}\delta_{mm'}\left[R^{1,\ell}_{\ell' m}\mathcal{C}^{ISW}_{\ell}+R^{1,\ell'}_{\ell m}\mathcal{C}^{ISW}_{\ell'}\right], \tag{310}$$

where now

$$\mathcal{C}^{ISW}_{\ell} \equiv 4\pi\int\frac{dk}{k}\frac{k^3}{2\pi^2}\left[P_g(k)+P_g\left(|\vec{k}+\vec{k}_0|\right)\right]T^{S}_{\ell}\left(k,\eta_0,\eta_{\rm in}\right)T^{ISW\star}_{\ell}\left(|\vec{k}+\vec{k}_0|\right). \tag{311}$$

To obtain the full first order contribution to the correlation of the SH coefficients, we can then sum Eq. 308 and Eq. 310 to obtain

$$\left\langle \Gamma_{\ell m,S}\Gamma^{*}_{\ell' m',S}\right\rangle^{(1)} = \frac{w_1}{2}\delta_{mm'}\left[R^{1,\ell}_{\ell' m}\mathcal{C}^{(1)}_{\ell}+R^{1,\ell'}_{\ell m}\mathcal{C}^{(1)}_{\ell'}\right], \tag{312}$$

where

$$\begin{aligned}\mathcal{C}_\ell^{(1)} \equiv & 4\pi \int \frac{dk}{k} \frac{k^3}{2\pi^2} \left[P_g(k) + P_g\left(|\vec{k} + \vec{k}_0|\right)\right] T_\ell^S\left(k, \eta_0, \eta_{\rm in}\right) \\ & \times \left[T_\ell^{SW}\left(|\vec{k} + \vec{k}_0|\right) + T_\ell^{ISW\star}\left(|\vec{k} + \vec{k}_0|\right)\right] \\ = & 4\pi \int \frac{dk}{k} \frac{k^3}{2\pi^2} \left[P_g(k) + P_g\left(|\vec{k} + \vec{k}_0|\right)\right] T_\ell^S\left(k, \eta_0, \eta_{\rm in}\right) \times U_\ell^\star\left(|\vec{k} + \vec{k}_0|\right) .\end{aligned} \tag{313}$$

Here, we defined a new transfer function

$$U_\ell^\star\left(|\vec{k} + \vec{k}_0|\right) \equiv T_\ell^{SW}\left(|\vec{k} + \vec{k}_0|\right) + T_\ell^{ISW\star}\left(|\vec{k} + \vec{k}_0|\right) , \tag{314}$$

which is different from the "regular" $T_\ell^S\left(k, \eta_0, \eta_{\rm in}\right)$ of Eq. 283 since T_Φ, T_Ψ are evaluated in $|\vec{k} + \vec{k}_0|$ and the ISW term contains the extra factor $\frac{\eta_0 - \eta'}{\eta_0 - \eta_{\rm in}}$ (see Eq. 303 for the full expression of the transfer functions containing this term).

8.1.3 *Second Order Term in the Modulating Field*

We now compute the term $\left\langle \Gamma^*_{\ell m,S}(q)\Gamma_{\ell' m',S}(q)\right\rangle^{(2)}$, which however requires a longer calculation to be carried out.
Reminding the expression of $h(\vec{k}-\vec{k}')$ of Eq. 289, we can write

$$
\begin{aligned}
&\left\langle \Gamma_{\ell m,S}\Gamma^*_{\ell' m',S}\right\rangle^{(2)} = \\
&(4\pi)^2(-i)^{\ell-\ell'}\int\frac{d^3k}{(2\pi)^3}\int\frac{d^3k'}{(2\pi)^3}\times\int\frac{d^3\widetilde{k}}{(2\pi)^3}P_g(\widetilde{k})h^*(\vec{k}-\widetilde{\vec{k}})h\left(\vec{k}'-\widetilde{\vec{k}}\right)\\
&\times Y^*_{\ell m}(\widehat{k})Y_{\ell' m'}\left(\widehat{k}'\right)\times T^S_\ell\left(k,\eta_0,\eta_{\rm in}\right)T^S_{\ell'}\left(k',\eta_0,\eta_{\rm in}\right) = \\
=&(4\pi)^2(-i)^{\ell-\ell'}\int\frac{d^3k}{(2\pi)^3}\int\frac{d^3k'}{(2\pi)^3}\int\frac{d^3\widetilde{k}}{(2\pi)^3}P_g(\widetilde{k})\\
&\times Y^*_{\ell m}(\widehat{k})Y_{\ell' m'}\left(\widehat{k}'\right)\times T^S_\ell\left(k,\eta_0,\eta_{\rm in}\right)T^S_{\ell'}\left(k',\eta_0,\eta_{\rm in}\right)\\
&\times\frac{w_1^2}{4}\frac{3}{4\pi}\frac{(2\pi)^6}{k_0^2(\eta_0-\eta_{\rm in})^2}\left[\delta(\vec{k}-\widetilde{\vec{k}}-\vec{k}_0)-\delta(\vec{k}-\widetilde{\vec{k}}+\vec{k}_0)\right]\\
&\times\left[\delta(\vec{k}'-\widetilde{\vec{k}}-\vec{k}_0)-\delta(\vec{k}'-\widetilde{\vec{k}}+\vec{k}_0)\right] = \\
=&\frac{4\pi}{2\pi^2}\frac{w_1^2}{4}(-i)^{\ell-\ell'}\int d^3k\int d^3k'\int d^3\widetilde{k}\,P_g(\widetilde{k})\\
&\times Y^*_{\ell m}(\widehat{k})Y_{\ell' m'}\left(\widehat{k}'\right)\times T^S_\ell\left(k,\eta_0,\eta_{\rm in}\right)T^S_{\ell'}\left(k',\eta_0,\eta_{\rm in}\right)\\
&\times\frac{3}{4\pi}\frac{1}{k_0^2(\eta_0-\eta_{\rm in})^2}\Big[\delta(\vec{k}-\widetilde{\vec{k}}-\vec{k}_0)\delta(\vec{k}'-\widetilde{\vec{k}}-\vec{k}_0)\\
&-\delta(\vec{k}-\widetilde{\vec{k}}-\vec{k}_0)\delta(\vec{k}'-\widetilde{\vec{k}}+\vec{k}_0)+\delta(\vec{k}-\widetilde{\vec{k}}+\vec{k}_0)\delta(\vec{k}'-\widetilde{\vec{k}}+\vec{k}_0)\\
&-\delta(\vec{k}-\widetilde{\vec{k}}+\vec{k}_0)\delta(\vec{k}'-\widetilde{\vec{k}}-\vec{k}_0)\Big]\,.
\end{aligned}
\tag{315}
$$

Following the same idea of the first order term (in the modulating field), we calculate one contribution at a time, however in this case every term contains a couple of deltas, instead of a single one. For all of them, the "secret" to obtain a fairly simple calculation is to integrate $\vec{k}$ and $\vec{k}'$, leaving behind

$\vec{\widetilde{k}}$.

Naturally, we start from the first one, which gives the following expression

$$\begin{aligned}
&\left\langle \Gamma_{\ell m,S}\Gamma^{*}_{\ell' m',S}\right\rangle^{(2)}_{1st} = \\
=&\frac{4\pi}{2\pi^2}\frac{w_1^2}{4}(-i)^{\ell-\ell'}\int d^3k\int d^3k'\int d^3\widetilde{k}\, P_g(\widetilde{k}) \\
&\times Y^{*}_{\ell m}(\widehat{k})Y_{\ell' m'}\left(\widehat{k}'\right)\times T^S_{\ell}\left(k,\eta_0,\eta_{\rm in}\right)T^S_{\ell'}\left(k',\eta_0,\eta_{\rm in}\right) \\
&\times\frac{3}{4\pi}\frac{1}{k_0^2(\eta_0-\eta_{\rm in})^2}\delta(\vec{k}-\vec{\widetilde{k}}-\vec{k}_0)\delta(\vec{k}'-\vec{\widetilde{k}}-\vec{k}_0) = \\
=&\frac{4\pi}{2\pi^2}\frac{w_1^2}{4}(-i)^{\ell-\ell'}\int d^3\widetilde{k}\, P_g(\widetilde{k}) \\
&\times\sqrt{\frac{3}{4\pi}}\frac{1}{k_0(\eta_0-\eta_{\rm in})}Y^{*}_{\ell m}\left(\frac{\vec{\widetilde{k}}+\vec{k}_0}{|\vec{\widetilde{k}}+\vec{k}_0|}\right)T^S_{\ell}\left(|\vec{\widetilde{k}}+\vec{k}_0|,\eta_0,\eta_{\rm in}\right) \\
&\times\sqrt{\frac{3}{4\pi}}\frac{1}{k_0(\eta_0-\eta_{\rm in})}Y_{\ell' m'}\left(\frac{\vec{\widetilde{k}}+\vec{k}_0}{|\vec{\widetilde{k}}+\vec{k}_0|}\right)T^S_{\ell'}\left(|\vec{\widetilde{k}}+\vec{k}_0|,\eta_0,\eta_{\rm in}\right)\,.
\end{aligned} \tag{316}$$

We can then apply again Eq. 293 for each of the product of transfer function and SH [61]. Reminding that the transfer function can be divided in a SW and a ISW contribution, where we must keep track of the starred components, we can write

$$\begin{aligned}
&\left\langle \Gamma_{\ell m,S}\Gamma^{*}_{\ell' m',S}\right\rangle^{(2)}_{1st} = \\
=&\frac{4\pi}{2\pi^2}\frac{w_1^2}{4}(-i)^{\ell-\ell'}\int d^3\widetilde{k}\, P_g(\widetilde{k}) \\
&\times\Big[\frac{1}{k_0\left(\eta_0-\eta_{\rm in}\right)}\sqrt{\frac{3}{4\pi}}U_{\ell}\left(|\vec{\widetilde{k}}+\vec{k}_0|\right)Y^{*}_{\ell m}(\widehat{\widetilde{k}}) \\
&-\frac{1}{2}R^{1,\ell+1}_{\ell m}U^{\star}_{\ell+1}\left(|\vec{\widetilde{k}}+\vec{k}_0|\right)Y^{*}_{\ell+1,m}(\widehat{\widetilde{k}}) \\
&+\frac{1}{2}R^{1,\ell-1}_{\ell m}U^{\star}_{\ell-1}\left(|\vec{\widetilde{k}}+\vec{k}_0|\right)Y^{*}_{\ell-1,m}(\widehat{\widetilde{k}})\Big] \\
&\times\Big[\frac{1}{k_0\left(\eta_0-\eta_{\rm in}\right)}\sqrt{\frac{3}{4\pi}}U_{\ell'}\left(|\vec{\widetilde{k}}+\vec{k}_0|\right)Y_{\ell' m'}(\widehat{\widetilde{k}}) \\
&-\frac{1}{2}R^{1,\ell'+1}_{\ell' m'}U^{\star}_{\ell'+1}\left(|\vec{\widetilde{k}}+\vec{k}_0|\right)Y_{\ell'+1,m'}(\widehat{\widetilde{k}}) \\
&+\frac{1}{2}R^{1,\ell'-1}_{\ell' m'}U^{\star}_{\ell'-1}\left(|\vec{\widetilde{k}}+\vec{k}_0|\right)Y_{\ell'-1,m'}(\widehat{\widetilde{k}})\Big]\,,
\end{aligned} \tag{317}$$

61 See also footnote 58.

where we defined

$$U_\ell\left(|\widetilde{\vec{k}}+\vec{k}_0|\right)\equiv T_\ell^{SW}\left(|\widetilde{\vec{k}}+\vec{k}_0|\right)+T_\ell^{ISW}\left(|\widetilde{\vec{k}}+\vec{k}_0|\right). \tag{318}$$

Let us now compute the product of the square brackets, multiplied by $(-i)^{\ell-\ell'}$ (all the spherical harmonics will depend on $\widehat{\widetilde{k}}$ and the transfer functions on $\left(|\widetilde{\vec{k}}+\vec{k}_0|\right)$, so we drop dependencies for the sake of notation):

$$\begin{aligned}
&(-i)^{\ell-\ell'}\Big[\frac{3}{4\pi}\frac{1}{k_0^2(\eta_0-\eta_{\rm in})^2}U_\ell U_{\ell'}Y_{\ell' m'}Y^*_{\ell m}+\\
&-\frac{1}{2k_0\,(\eta_0-\eta_{\rm in})}\sqrt{\frac{3}{4\pi}}R^{1,\ell'+1}_{\ell' m'}U_\ell U^\star_{\ell'+1}Y^*_{\ell m}Y_{\ell'+1,m'}+\\
&+\frac{1}{2k_0\,(\eta_0-\eta_{\rm in})}\sqrt{\frac{3}{4\pi}}R^{1,\ell'-1}_{\ell' m'}U_\ell U^\star_{\ell'-1}Y^*_{\ell m}Y_{\ell'-1,m'}+\\
&-\frac{1}{2k_0\,(\eta_0-\eta_{\rm in})}\sqrt{\frac{3}{4\pi}}R^{1,\ell+1}_{\ell m}U^\star_{\ell+1}U_{\ell'}Y^*_{\ell+1,m}Y_{\ell' m'}+\\
&+\frac{1}{2k_0\,(\eta_0-\eta_{\rm in})}\sqrt{\frac{3}{4\pi}}R^{1,\ell-1}_{\ell m}U^\star_{\ell-1}U_{\ell'}Y^*_{\ell-1,m}Y_{\ell' m'}+\\
&-\frac{1}{4}R^{1,\ell+1}_{\ell m}R^{1,\ell'-1}_{\ell' m'}U^\star_{\ell+1}U^\star_{\ell'-1}Y^*_{\ell+1,m}Y_{\ell'-1,m'}+\\
&+\frac{1}{4}R^{1,\ell+1}_{\ell m}R^{1,\ell'+1}_{\ell' m'}U^\star_{\ell+1}U^\star_{\ell'+1}Y^*_{\ell+1,m}Y_{\ell'+1,m'}+\\
&-\frac{1}{4}R^{1,\ell-1}_{\ell m}R^{1,\ell'+1}_{\ell' m'}U^\star_{\ell-1}U^\star_{\ell'+1}Y^*_{\ell-1,m}Y_{\ell'+1,m'}+\\
&+\frac{1}{4}R^{1,\ell-1}_{\ell m}R^{1,\ell'-1}_{\ell' m'}U^\star_{\ell-1}U^\star_{\ell'-1}Y^*_{\ell-1,m}Y_{\ell'-1,m'}\Big].
\end{aligned} \tag{319}$$

Integrating in $\int d\widehat{\widetilde{k}}$ the products of spherical harmonics will provide several different Kronecker deltas, which will then make explicit also the power of $-i$ for each term:

$$\begin{aligned}
&\frac{3}{4\pi}\frac{1}{k_0^2(\eta_0-\eta_{\rm in})^2}U_\ell U_\ell \delta_{\ell\ell'}\delta_{mm'}(-i)^0+\\
&-\frac{1}{2k_0\,(\eta_0-\eta_{\rm in})}\sqrt{\frac{3}{4\pi}}R^{1,\ell}_{\ell' m}U_\ell U^\star_\ell \delta_{mm'}(-i)^1+\\
&+\frac{1}{2k_0\,(\eta_0-\eta_{\rm in})}\sqrt{\frac{3}{4\pi}}R^{1,\ell}_{\ell' m}U_\ell U^\star_\ell \delta_{mm'}(-i)^{-1}+\\
&-\frac{1}{2k_0\,(\eta_0-\eta_{\rm in})}\sqrt{\frac{3}{4\pi}}R^{1,\ell'}_{\ell m}U^\star_{\ell'} U_{\ell'} \delta_{mm'}(-i)^{-1}+\\
&+\frac{1}{2k_0\,(\eta_0-\eta_{\rm in})}\sqrt{\frac{3}{4\pi}}R^{1,\ell'}_{\ell m}U^\star_{\ell'} U_{\ell'} \delta_{mm'}(-i)^{1}+\\
&-\frac{1}{4}\sum_j R^{1,j}_{\ell m}R^{1,j}_{\ell' m}U^\star_j U^\star_j \delta_{mm'}(-i)^{-2}+\\
&+\frac{1}{4}\sum_j R^{1,j}_{\ell m}R^{1,j}_{\ell' m}U^\star_j U^\star_j \delta_{mm'}(-i)^{0}+\\
&-\frac{1}{4}\sum_j R^{1,j}_{\ell m}R^{1,j}_{\ell' m}U^\star_j U^\star_j \delta_{mm'}(-i)^{2}+\\
&+\frac{1}{4}\sum_j R^{1,j}_{\ell m}R^{1,j}_{\ell' m}U^\star_j U^\star_j \delta_{mm'}(-i)^{0}\,.
\end{aligned} \tag{320}$$

Thus, summing the various terms one ends up with

$$\begin{aligned}
&\left\langle \Gamma_{\ell m,S}\Gamma^*_{\ell' m',S}\right\rangle^{(2)}_{1st}=\\
=&\frac{4\pi}{2\pi^2}\frac{w_1^2}{4}\int d\widetilde{k}\;P_g(\widetilde{k})\Big[\frac{3}{4\pi}\frac{1}{k_0^2(\eta_0-\eta_{\rm in})^2}U_\ell U_\ell \delta_{\ell\ell'}\delta_{mm'}+\\
&+\frac{i}{k_0\,(\eta_0-\eta_{\rm in})}\sqrt{\frac{3}{4\pi}}R^{1,\ell}_{\ell' m}U_\ell U^\star_\ell \delta_{mm'}-\frac{i}{k_0\,(\eta_0-\eta_{\rm in})}\sqrt{\frac{3}{4\pi}}R^{1,\ell'}_{\ell m}U^\star_{\ell'} U_{\ell'} \delta_{mm'}+\\
&+\sum_j R^{1,j}_{\ell m}R^{1,j}_{\ell' m}U^\star_j U^\star_j \delta_{mm'}\Big]\,.
\end{aligned} \tag{321}$$

At this point, one would have to compute the other three terms coming from the other couples of Dirac deltas of Eq. 315, however one can exploit the following shortcut to reach the final solution:

- the sign in front of the isotropic term ($\propto \delta_{\ell\ell'}$) is exclusively defined by the sign in front of the couple of Dirac deltas (see the first term of Eq. 321 for example);

- the Dirac delta imposing $k = \widetilde{k} \pm k_0$ translates into a final term $\propto \mp R^{1,\ell'}_{\ell m}$ (see the third term of Eq. 321 for example);
- the Dirac delta imposing $k' = \widetilde{k} \pm k_0$ translates into a final term $\propto \pm R^{1,\ell}_{\ell' m}$ (see the second term of Eq. 321 for example);
- if the two deltas has agreeing signs in front of k_0, one ends up with a plus in front of the term with the sum over j, otherwise one gets a minus sign (see the fourth term of Eq. 321 for example).

Applying these rules, one can show that the only surviving term is the one proportional to the sum over j [62]:

$$\begin{aligned}
&\left\langle \Gamma_{\ell m,S}\Gamma^{*}_{\ell' m',S}\right\rangle^{(2)} \\
=&\frac{4\pi}{2\pi^2}\frac{w_1^2}{4}\int d\widetilde{k}\; P_g(\widetilde{k}) 4 \sum_j R^{1,j}_{\ell m} R^{1,j}_{\ell' m} U^{\star}_j U^{\star}_j \delta_{mm'} \\
=&w_1^2 \delta_{mm'} 4\pi \int \frac{d^3\widetilde{k}}{\widetilde{k}}\frac{\widetilde{k}^3}{2\pi^2} P_g(\widetilde{k}) \sum_j R^{1,j}_{\ell m} R^{1,j}_{\ell' m} U^{\star}_j U^{\star}_j \\
=&w_1^2 \delta_{mm'} \sum_j R^{1,j}_{\ell m} R^{1,j}_{\ell' m} \mathcal{C}^{(2)}_j \;,
\end{aligned} \tag{322}$$

where

$$\mathcal{C}^{(2)}_{\ell} \equiv 4\pi \int \frac{dk}{k}\frac{k^3}{2\pi^2} P_g(k) U^{\star}_{\ell}(k) U^{\star}_{\ell}(k) \;. \tag{323}$$

8.1.4 *Full Expression of the Correlator*

Finally we are able to write the full expression for $\left\langle \Gamma_{\ell m,S}\Gamma^{*}_{\ell' m',S}\right\rangle$, which will contain the zeroth, first and second order contributions (in the modulating field) just derived (this subsection is intended to be a summary of the previously obtained expressions). It reads

$$\begin{aligned}
&\left\langle \Gamma_{\ell m,S}\Gamma^{*}_{\ell' m',S}\right\rangle = \delta_{\ell\ell'}\delta_{mm'}\mathcal{C}^{(0)}_{\ell} + \frac{w_1}{2}\delta_{mm'}\left[R^{1,\ell}_{\ell' m}\mathcal{C}^{(1)}_{\ell} + R^{1,\ell'}_{\ell m}\mathcal{C}^{(1)}_{\ell'}\right] + \\
&+ w_1^2 \delta_{mm'} \sum_j R^{1,j}_{\ell m} R^{1,j}_{\ell' m} \mathcal{C}^{(2)}_j \;,
\end{aligned} \tag{324}$$

62 We implicitly assume here that the transfer function in $\widetilde{k} \pm k_0$ is approximately equal to the one evaluated in $\widetilde{k}$. Having done differently would have not allowed to cancel the various term disappearing in this following passage.

where

$$\begin{aligned}
\mathcal{C}_\ell^{(0)} \equiv & 4\pi \int \frac{dk}{k} \frac{k^3}{2\pi^2} P_g(k) T_\ell^{(S)2}(k) \ , \\
\mathcal{C}_\ell^{(1)} \equiv & 4\pi \int \frac{dk}{k} \frac{k^3}{2\pi^2} \left[P_g(k) + P_g\left(|\vec{k} + \vec{k}_0| \right) \right] T_\ell^S(k) \, U_\ell^\star\left(|\vec{k} + \vec{k}_0| \right) \ , \\
\mathcal{C}_\ell^{(2)} \equiv & 4\pi \int \frac{dk}{k} \frac{k^3}{2\pi^2} P_g(k) U_\ell^\star(k) U_\ell^\star(k) \ .
\end{aligned} \tag{325}$$

We also remind the expression of the transfer functions

$$\begin{aligned}
T_\ell^S(k, \eta_0, \eta_{\rm in}) \equiv & T_\Phi(\eta_{\rm in}, k) \, j_\ell(k(\eta_0 - \eta_{\rm in})) \\
& + \int_{\eta_{\rm in}}^{\eta_0} d\eta' \frac{\partial [T_\Psi(\eta', k) + T_\Phi(\eta', k)]}{\partial \eta'} j_\ell(k(\eta_0 - \eta')) \ , \\
U_\ell^\star\left(|\vec{k} + \vec{k}_0| \right) \equiv & T_\ell^{SW}\left(|\vec{k} + \vec{k}_0| \right) + T_\ell^{ISW\star}\left(|\vec{k} + \vec{k}_0| \right) , \\
U_\ell\left(|\vec{k} + \vec{k}_0| \right) \equiv & T_\ell^{SW}\left(|\vec{k} + \vec{k}_0| \right) + T_\ell^{ISW}\left(|\vec{k} + \vec{k}_0| \right) , \\
T_\ell^{SW}\left(|\vec{k} + \vec{k}_0| \right) \equiv & T_\Phi\left(\eta_{\rm in}, |\vec{k} + \vec{k}_0| \right) j_\ell(k(\eta_0 - \eta_{\rm in})) \ , \\
T_\ell^{ISW}\left(|\vec{k} + \vec{k}_0| \right) \equiv & \int_{\eta_{\rm in}}^{\eta_0} d\eta' \frac{\partial \left[T_\Psi\left(\eta', |\vec{k} + \vec{k}_0| \right) + T_\Phi\left(\eta', |\vec{k} + \vec{k}_0| \right) \right]}{\partial \eta'} \\
& \times j_\ell(k(\eta_0 - \eta')) \ , \\
T_\ell^{ISW\star}\left(|\vec{k} + \vec{k}_0| \right) \equiv & \int_{\eta_{\rm in}}^{\eta_0} d\eta' \frac{\partial \left[T_\Psi\left(\eta', |\vec{k} + \vec{k}_0| \right) + T_\Phi\left(\eta', |\vec{k} + \vec{k}_0| \right) \right]}{\partial \eta'} \\
& \times \frac{\eta_0 - \eta'}{\eta_0 - \eta_{\rm in}} j_\ell(k(\eta_0 - \eta')) \ .
\end{aligned} \tag{326}$$

Firstly, we notice that approximating these results for $\vec{k} + \vec{k}_0 \approx \vec{k}$ and neglecting the ISW effect, we get $U_\ell = U_\ell^\star = T_\ell^S$, thus $\mathcal{C}_\ell^{(0)} = \mathcal{C}_\ell^{(1)} = \mathcal{C}_\ell^{(2)}$. In other words, the results obtained in [181] are reproduced by our computation, considering that they used $T_\Phi = -\frac{1}{3}$.
The more careful readers would have noticed that, in the case of the second-order term in the modulating field, the presence of the factor $1/2$ in Eq. 293 (see footnote 58) has indeed allowed us to obtain the same contribution of [181] reported in Eq. 280 (canceling out a 4, which would have come from the sum performed to obtain Eq. 322). On the other hand, the same factor seems to have made us fail in reproducing [181] for what concerns the first-order term in the modulating field (see Eq. 278). This problem is solved by looking closely at $\mathcal{C}_\ell^{(1)}$, where there is a sum of power spectra, which can

be assumed to be equal at first-order in k/k_0[63]. This provides a factor 2, canceling out the $1/2$ we have here.

63 This reduces to show that

$$\frac{k^3}{2\pi^2}P_g\left(|\vec{k}+\vec{k}_0|\right)=\Delta_0\left(\frac{|\vec{k}+\vec{k}_0|}{k_0}\right)^{n_s-1}=\Delta_0\left(\frac{\sqrt{k^2+k_0^2+2k\cdot k_0\cos(\theta)}}{k_0}\right)^{n_s-1}, \quad (327)$$

which for $k_0 \ll k$ can be approximated as

$$\begin{aligned}&\Delta_0\left[\sqrt{\left(\frac{k}{k_0}\right)^2+1+2\frac{k}{k_0}\cos(\theta)}\right]^{n_s-1}\\ \simeq&\Delta_0\left(\frac{k}{k_0}\right)^{n_s-1}=\frac{k^3}{2\pi^2}P_g(k)\,.\end{aligned} \quad (328)$$

9

POWER ASYMMETRY WITH THE CGWB: RESULTS AND FORECASTS

In the previous chapter, we laid the theoretical foundations to describe a modulation of the gravitational potentials in the context of the CGWB. Here, we focus on the analysis that can lead to some predictions on the significance of this anomaly assuming to observe the GW background with some interferometer.
This chapter is based on Galloni et al. [182].

9.1 STATISTICS IN THE PRESENCE OF A DIPOLAR MODULATION

In order to compute the contributions $\mathcal{C}_\ell^{(i)}$ of Eq. 325 we modified the publicly available Boltzmann code `Cosmic Linear Anisotropy Solving System (CLASS)` [183, 184], both for the CGWB and the CMB. We add the CGWB in the code similarly to [104] by mimicking the CMB procedures, while modifying the source functions as in Eq. 226. Furthermore, the tensor-induced contribution is reproduced by mimicking the CMB procedure and exploiting the equations of [49, 50]. Then, we modify the vector of values of the mode k where the gravitational potential transfer functions are evaluated throughout the code to shift them to $k + k_0$ (recall Eq. 326). Furthermore, we calculate the cross-correlation between the CMB and the CGWB, which will be crucial in comparing the two observables [185–188] [64].

Recall that in [181] the ISW term was neglected, whereas in our modification of CLASS we implement it. Furthermore, in our computation, we keep the expression of the full transfer function encoded in CLASS, without assuming any approximation. Also, remember that we assumed $k \ll k_0$ to obtain the expression of $\mathcal{C}_\ell^{(1)}$ and $\mathcal{C}_\ell^{(2)}$, therefore the results should only be trusted when that condition is satisfied.

Before looking at the effects of the modulation, it is worth exploring how the tensor spectral tilt affects the theoretical angular power spectrum of the CGWB following Eq. 226. Fig. 12 shows respectively the CGWB angular power spectrum (left) and its cross-correlation spectrum with CMB temperature anisotropy (right) (in Sec. A.1 we distinguish the scalar and tensor contributions to the spectra). These two figures need further clarification: when we look at the CGWB, the actual observable we can measure with interferometers is the GWs energy density and its anisotropies, i. e. the energy contrast as a function of the direction in the sky. As mentioned above, this

64 At the time [182] was written, the work of Schulze et al. [94] was not available, so we independently coded the CGWB in CLASS. Now, one can find an official release of CLASS that natively provides these computations.

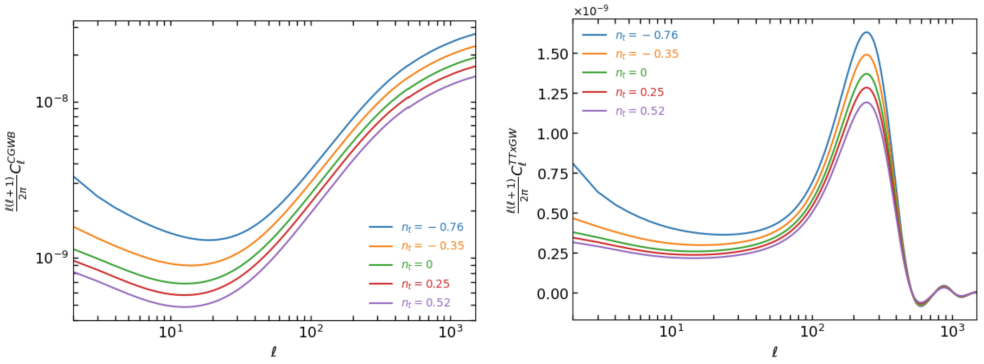

Figure 12: CGWB angular power spectrum (left) and cross-correlation angular power spectrum between CMB temperature and CGWB (right) when we assume different values for the tensor spectral tilt n_t and we do not consider any effect due to the modulation ($\omega_1 = 0$).

is related to the anisotropies of Γ through Eq. 253. Thus, be aware that from this point on we will work with the angular power spectrum of the density contrast, gaining extra $(4 - n_t)$ factors when we compute the CGWB, or its cross-correlation with the CMB temperature. For this reason, these two will depend on the spectral tilt n_t through both the $\Gamma \to \delta_{GW}$ conversion factor and the presence of Γ_I in Eq. 226. However, this is not all: Eq. 217 shows that there is another term that contributes to the CGWB anisotropies induced by the presence of tensor perturbations of the metric χ_{ij} in Eq. 198. The transfer function of this term is proportional to the time derivative of the tensor mode function when decomposing the perturbation in circular polarizations (see e. g. [53]), i. e. $\propto -\chi'(\eta, k)$. Then, the angular power spectrum will depend on the power-law description of the primordial tensor power spectrum [49]. In the case of CMB [189], the transfer function relative to tensor perturbations is also $\propto -\chi'$, thus red-tilted spectra are expected not only to enhance both the tensor contributions of the angular power spectra of CGWB and TT CMB at large scales, but also their cross-correlation (see Sec. A.1 for some further detail).

To fully explore the dependence on n_t, we choose some values for the tilt that span the limits provided by [54] when including the data from LIGO-Virgo, i. e. $-0.76 < n_t < 0.52$. Specifically, we choose $n_t = -0.76$, -0.35, 0, 0.25 or 0.52. It should be emphasized once again that we are assuming a power-law description of the tensor power spectrum in an inflationary context. Furthermore, from this point on, all six ΛCDM parameters are set to the best fit of [190], whereas the tensor-to-scalar ratio is chosen to saturate the bound provided by [54] when including the data from LIGO-Virgo, that is, $r = 0.066$ at 0.01 Mpc^{-1} [65].

Going back to the CGWB angular power spectrum, the left panel of Fig. 12 shows how the spectrum changes when we assume different values of n_t. Recalling Eq. 226 and reminding the presence of the tensor-sourced contribution, one can see that the higher the tilt, the more the anisotropies will be suppressed. This same effect is brought to the cross-spectrum, as shown in the right panel of Fig. 12. Interestingly, one can notice that for very red-tilted spectra, the total cross-spectrum at large scales tends to increase significantly

65 The updated bounds on r and n_t will be discussed in Chap. 13, which of course was not available at the time [182] was written.

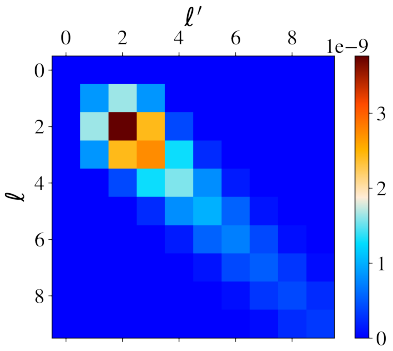

Figure 13: Covariance matrix between ℓ and ℓ' for $m = 0$ for the first 10 multipoles of the CGWB. Here the generated variance on the dipole is clearly visible.

due to tensor contribution, as expected from the previous discussion of the tensor sourced contribution (see also Sec. A.1).

9.1.1 *Contributions to the correlators*

Let us recall that $\mathcal{C}_\ell^{(1)}$ and $\mathcal{C}_\ell^{(2)}$ are just a part of the whole expression of the two novel contributions to the correlators (see Eq. 325), and thus more work has to be done to include the proportionality coefficients. The next step to simplify the computation would be to fix the value of m, given that the correlators are "diagonal" in m, and compute Eq. 325. Using HEALPix [191], we are able to compute a realization of $\Theta_{\ell m}$ once the angular power spectrum is specified. In the standard case the $\Theta_{\ell m}$ are distributed around a Gaussian with zero mean and a variance given by the angular power spectrum [66]. So, we modified some of the routines of HEALPix in order to account for the correlation between multipoles introduced by the modulation but, most importantly, for the fact that now the results will depend on m (i. e. broken statistical isotropy).

As an example, in Fig. 13 the correlation matrix between ℓ and ℓ' for the first 10 multiples for $m = 0$ of the CGWB when we assumed $\omega_1 = 4$. One can notice that indeed there is a small contribution to the "pure" dipole coming from the second order term in the modulating field and a much bigger one coming from the cross-correlation between the quadrupole and the dipole ($(\ell, \ell') = (1, 2)$ or vice versa). Setting again the modulating amplitude to $\omega_1 = 4$ just for illustrative purposes, we obtain the Fig. 14 for the modulated case of the CGWB. Now, we compute the cross-correlation coefficient between the CGWB and CMB, defined as $\mathcal{C}_\ell^{CMB\times CGWB} / \sqrt{\mathcal{C}_\ell^{CMB} \times \mathcal{C}_\ell^{CGWB}}$. This coefficient will clearly depend on the value of the spectral tilt n_t, thus it is worth showing its variation for different values of the tilt. Once again, we choose $n_t = \{-0.76,\ -0.35,\ 0,\ 0.25,\ 0.52\}$. Fig. 15 shows that there are two main regions where the CMB and the CGWB are correlated, namely the largest scales $\ell < 100$ and around $\ell = 200$. Indeed, the SW effect of GWs and CMB photons are generated respectively at η_{in} and η_{rec} (respectively, through

66 In the standard case there is no correlation between multipoles, thus the variance of the $\Theta_{\ell m}$ is the same for every m once you fix ℓ and is solely controlled by the value of $\mathcal{C}_\ell$.

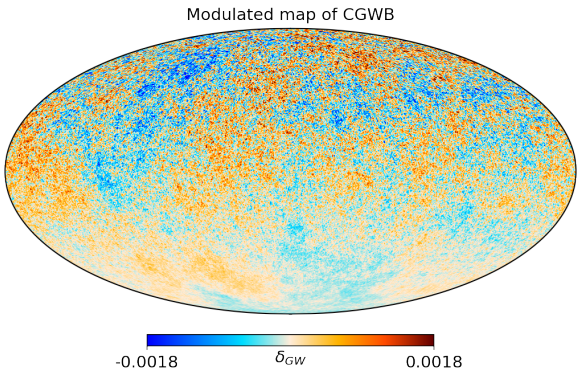

Figure 14: Modulated CGWB map with $\ell_{max} = 400$ with a very high modulation amplitude to enhance its effect.

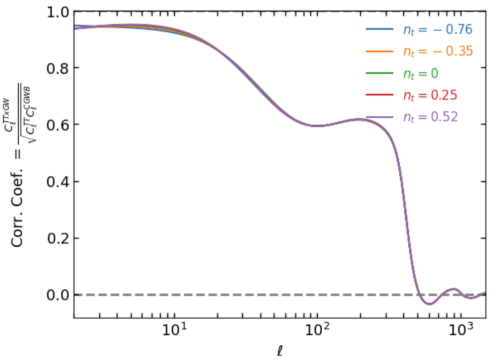

Figure 15: Correlation coefficient between the CMB and CGWB when we assume different values of the tensor spectral tilt n_t.

the convolution with a Dirac delta and the visibility function). However, the spatial separation of the events is much smaller than the scale of the perturbation considered on those multipoles, so the cross-correlation is still high[67]. Instead, the other region is due to the correlation between the first acoustic peak of CMB and the ISW effect on GWs [187].

9.1.2 *Correlation CMB vs CGWB*

To fully exploit the cross-correlation between CMB and CGWB and the available data for the temperature field, we generate constrained realizations of the CGWB [187, 192]. In fact, looking again at Fig. 15, one can notice that on multipoles lower than ≈ 50 the realization of the CGWB should be nearly deterministically fixed by our observation of CMB, because the correlation coefficient is nearly 1. However, in our case we have to emphasize a peculiarity: a constrained realization of the CGWB ($\Gamma_{\ell m}$) given a realization of the CMB temperature field ($a_{\ell m}$) is customarily given by [193]

$$\Gamma_{\ell m} = \frac{C_\ell^{CMB\times CGWB}}{C_\ell^{CMB}} a_{\ell m} + \xi_{\ell m} \sqrt{C_\ell^{CGWB} - \frac{\left(C_\ell^{CMB\times CGWB}\right)^2}{C_\ell^{CMB}}}\,, \quad (329)$$

67 In fact, the more you go towards small scales, the more that contribution fades away, given that the spatial separation gets too large w. r. t. the scale of the perturbation.

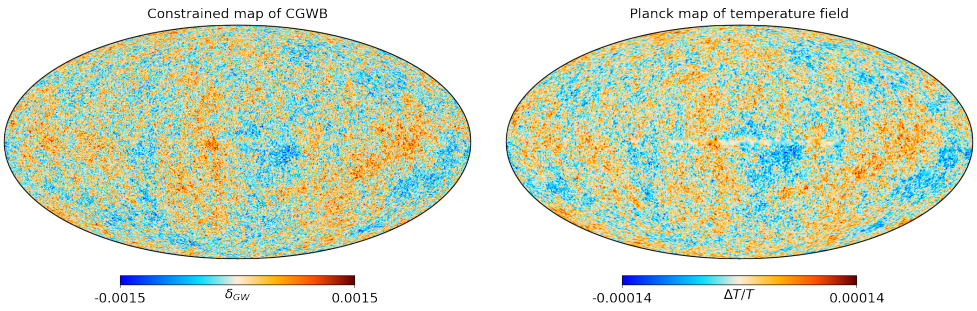

Figure 16: Constrained realization of the CGWB with $\ell_{max} = 400$ (left) and Planck CMB map, whose spherical harmonics coefficients with $\ell > \ell_{max} = 400$ are filtered out (right). It is clear that the large-scale features of Planck's map are faithfully reproduced here, whereas the two observables drift apart on smaller scales.

where $\xi_{\ell m}$ is a Gaussian random field with mean 0 and unitary variance. In other words, for multipoles where the cross-spectrum is high, the realization of the CGWB acquires a mean similar to the CMB one and will have a suppressed variance around that. Vice versa, when the cross-spectrum is low, the CGWB realizations will go back to the standard case, i. e. it will have a null mean and a variance equal to the square root of the angular power spectrum. In spite of this, we know that the dipolar modulation model we adopted to describe the power asymmetry introduces a coupling between different multipoles, which is not accounted for in Eq. 329. For this reason, we need to generalize this equation to a case with non-zero contributions in the off-diagonal elements of the covariance matrices. This is done by considering the known formulas of the mean and variance of a conditioned multivariate Gaussian, which recast Eq. 329 to [194, 195]

$$\vec{\Gamma}_m = Cov_m^{CMB\times CGWB}\left(Cov_m^{CMB}\right)^{-1}\vec{a}_m + \vec{\xi}_m \times Chol.[M_m]\,, \quad (330)$$

$$M_m = Cov_m^{CGWB} - Cov_m^{CMB\times CGWB}\left(Cov_m^{CMB}\right)^{-1}\left(Cov_m^{CMB\times CGWB}\right)^{T}. \quad (331)$$

In Eq. 330 we are fixing the index m and for each we define $\vec{a}_m$, $\vec{\xi}_m$ and $\vec{\Gamma}_m$, which are vectors long $\ell_{max} - m$. Indeed, $\Gamma_{\ell m}, a_{\ell m}, \xi_{\ell m}$ in Eq. 329 are the elements of these vectors: $\vec{a}_m$ is extracted from the complete vector of the CMB realization fixing m, while $\vec{\xi}_m$ is a multivariate Gaussian vector with 0 mean and unit variance ($\mathbb{I}_{\ell_{max}-m}$). Finally, $\vec{\Gamma}_m$ is built using the covariance matrices between ℓ, ℓ' (Eq. 324 shows the CGWB case, represented graphically in Fig. 13). In addition, *Chol.* indicates that we are taking the Cholesky decomposition of matrices M_m to obtain the correct covariance. Thus, since we want to assess the significance of a certain modulating amplitude using these constrained realizations, we will plug in the expression of the covariance matrices the estimated value of the amplitude we can get from our CMB observation (see Sec. 9.2 for further details). Furthermore, one can easily show that in the case of diagonal matrices (i. e. without modulation), Eq. 330 is equivalent to Eq. 329.

Comparing the left and right panels of Fig. 16, the latter being Planck's temperature map downgraded to $\ell_{max} = 400$, one can notice that the large-scale features present in the CMB are faithfully reproduced in our realization of the CGWB, given that the cross-correlation is high on those scales. Let us recall that to pass to an energy-contrast description of the CGWB, we multiply Eq. 330 by $(4 - n_t)$.

9.2 THE ROLE OF GW IN ASSESSING THE ANOMALY

9.2.1 *Estimator of the modulating amplitude*

We apply the estimator defined in [181] to assess the amplitude of the modulating field from a sky map realization. For every couple of sky-realizations $X^*_{\ell m} Y_{\ell+1,m}$, where $XY = \{TT,\ GWGW,\ TGW,\ GWT\}$, they define the estimator for ω_1 as

$$\widehat{\omega}^{XY}_{1,\ell m} = \frac{X^*_{\ell m} Y_{\ell+1,m}}{f^{XY}_\ell R^{1\ell}_{\ell+1,m}} \,. \tag{332}$$

The coefficients f^{XY}_ℓ are given by

$$\langle X^*_{\ell m} Y_{\ell+1,m} \rangle = \omega_1 f^{XY}_\ell R^{1\ell}_{\ell+1,m} \,, \tag{333}$$

so that $\left\langle \widehat{\omega}^{XY}_{1,\ell m} \right\rangle = \omega_1$. In our case, the expression of these coefficients is fairly simple:

$$f^{XY}_\ell = C^{XY}_\ell + C^{XY}_{\ell+1} \,, \tag{334}$$

with $f^{TGW}_\ell = f^{GWT}_\ell$.

The estimators are combined to form a joint estimator defined as

$$\widehat{\omega}_1 = \sum_{XY} \sum_{\ell m} A^{XY}_{\ell m} \widehat{\omega}^{XY}_{1,\ell m} \,, \tag{335}$$

where $A^{XY}_{\ell m}$ are weights which satisfy

$$\sum_{XY} \sum_{\ell m} A^{XY}_{\ell m} = 1 \tag{336}$$

and minimize the variance of the joint estimator. Their definition is as follows

$$A^{XY}_{\ell m} = \frac{\sum_{X'Y'} \left[\mathcal{D}^{(\ell)}\right]^{-1}_{XY,X'Y'} \left(R^{1\ell}_{\ell+1,m}\right)^2}{\sum_{XY,X'Y'} \sum_{\ell m} \left[\mathcal{D}^{(\ell)}\right]^{-1}_{XY,X'Y'} \left(R^{1\ell}_{\ell+1,m}\right)^2} \,, \tag{337}$$

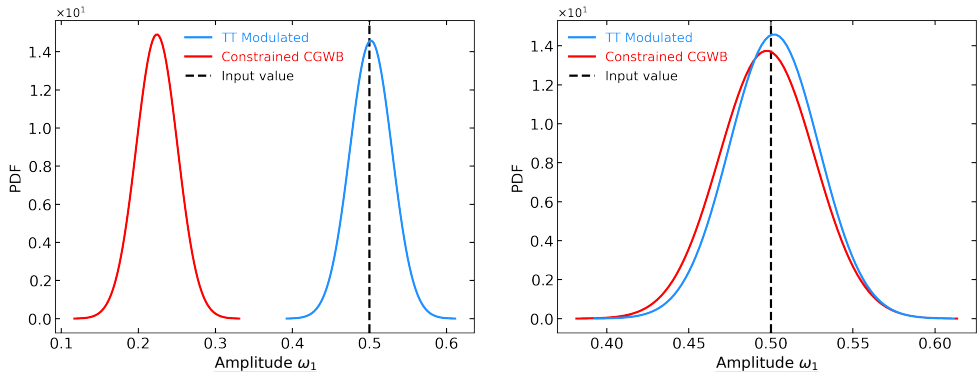

Figure 17: Estimated modulating amplitude for a set of 1000 realizations, assuming $\ell_{max} = 100$, $n_t = 0$. The dashed black line indicates the input value of the modulating amplitude. The solid blue curve represents the CMB modulated realizations, whereas the solid red one the constrained CGWB realizations. On the left, we exploited Eq. 329, whereas on the right its generalized counterpart, Eq. 330.

where

$$\mathcal{D}^{(\ell)}_{XY,X'Y'} = \frac{\mathcal{C}_\ell^{XX'}\mathcal{C}_{\ell+1}^{YY'}}{f_\ell^{XY} f_\ell^{X'Y'}} \,. \tag{338}$$

As a validating step of this estimator and our machinery, we generate a set of $N = 1000$ realizations of the CMB and CGWB. We modulate each CMB realization with $\omega_1 = 0.5$ and from each of them we generate a constrained realization of the CGWB. This is the perfect place to emphasize the difference between using Eq. 329 or Eq. 330 to produce the constrained realizations of the CGWB. The left panel of Fig. 17 shows that indeed the estimated amplitudes in the case of the CMB are correctly distributed around the input value, with some dispersion given by cosmic variance. The distribution for the CGWB is however centered around a lower value than the CMB one. Indeed, this is not surprising, because we obtain these realizations as constrained ones from the CMB set using Eq. 329. Since the "signal" of the modulation is transferred to the CGWB by $a_{\ell m}$ mainly through the first ≈ 50 multipoles, where the correlation is high, and given that the realizations we produce have $\ell_{max} = 100$, the estimate on GWs is dragged to 0. However, we underline that this effect is due solely to our procedure. Indeed, in the right panel of Fig. 17 one can see that also the GW estimates are distributed around our input value for the CMB modulated set with a similar variance. This is due to the fact that in this case we use Eq. 330, thus even in low correlation regions, the covariance of the CGWB realization retains the coupling between multipoles induced by the presence of the modulation, which carries the modulation-amplitude-information in all multipoles.

In any case, from this point on, we will set $\ell_{max} = 20$, since the power asymmetry affects only large scales [174]. Furthermore, we will be using the generalized expression of the constrained realizations, i. e. Eq. 330, since it best represents our model predictions.

9.2.2 *Cosmic variance distribution*

We can now study what the Cosmic Variance (CV) distribution looks like when we add GWs using the joint estimator defined from Eq. 332 to Eq. 338.

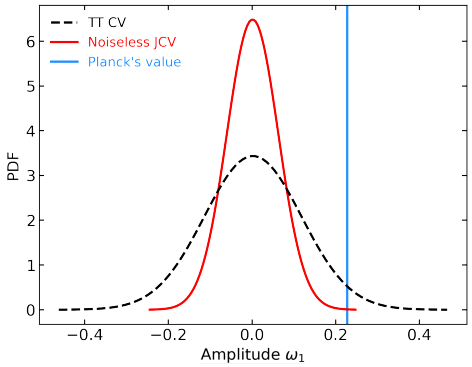

Figure 18: Estimated dispersion due to cosmic variance with a set of 1000 realizations, assuming $\ell_{max} = 20$, $n_t = 0$. The dashed black curve is the dispersion of the temperature realizations, whereas the solid red line indicates the dispersion of the joint estimation using both GWs and CMB. This time, the GWs realizations are obtained independently from the CMB ones. The solid blue line is the value inferred by Planck's SMICA map.

This will allow us to find our null hypothesis to assess the significance of CMB power asymmetry when adding a GWs observation. In this case, we must use unconstrained realizations of the CGWB since we want both fields to fluctuate freely [193]. The expression for unconstrained realizations can be obtained from Eq. 330 setting $Cov_m^{CMB\times CGWB} = 0$ [68]. For this analysis, we assume a scale-invariant power spectrum, thus $n_t = 0$. However, a clarification is due: given that we have to study how CV can simulate the presence of a modulation, we are assuming a cosmological model without any modulating field. For this reason, the $\mathcal{C}_\ell^{XX'}$ we used for the estimator are the standard ones (e. g. first row of Eq. 325 multiplied by the proper $\Gamma \to \delta_{GW}$ conversion factor). Fig. 18 shows that the cosmic variance dispersion decreases noticeably compared to the TT CV case. From this point on, we will call Joint Cosmic Variance (JCV) the shrunken distribution obtained when the CGWB is considered together with CMB temperature. The value we estimate from Planck's SMICA map $\omega_1 = 0.23$ passes from 1.95σ in the TT-only case to 3.70σ when we consider the JCV, prominently favoring this modulation model w. r. t. some unknown systematic effect.

However, notice that we have yet to introduce any instrumental noise for the GWs part, which is expected to have an impact on the result. Indeed, when we consider this extra source of noise Eq. 338 is recast to

$$\mathcal{D}^{(\ell)}_{XY,X'Y'} = \frac{\left(\mathcal{C}_\ell^{XX'} + N_\ell^{XX'}\right)\left(\mathcal{C}_{\ell+1}^{YY'} + N_{\ell+1}^{YY'}\right)}{f_\ell^{XY} f_\ell^{X'Y'}} \tag{339}$$

and we add a realization of the noise to the realization of the CGWB.

The inverse of Eq. 339, which is the one entering the equations for the estimator, will tend to zero for noise-dominated cases. In other words, when the noise of an experiment is too large, the JCV will be completely disrupted and will become much larger than the TT CV, since the GWs part will contribute to largely enhance the dispersion of the simulations. Here, we will consider Laser Interferometer Space Antenna (LISA) and Big Bang Observer (BBO) as our testing frameworks, whose instrumental noise is obtained through the

68 So equivalently, one can obtain the correct expression from Eq. 329 while imposing $\mathcal{C}_\ell^{CMB\times CGWB} = 0$.

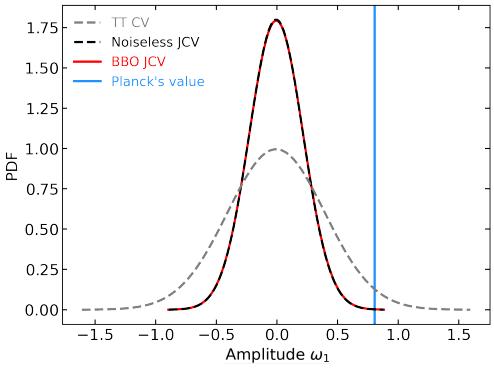

Figure 19: JCV when we include the instrumental noise coming from BBO. The red curve is obtained by assuming $\ell_{max} = 6$, $n_t = 0.52$, whereas the blue vertical line indicates the value estimated from Planck's temperature map. The dashed gray and black lines represent respectively the CV when using only CMB temperature realizations and the noiseless JCV, thus when we include also the CGWB.

publicly available code schNell [187, 196]. The noise spectrum of these instruments will depend on the value we assume for n_t. In fact, the expected noise levels N_ℓ of LISA and BBO are related to the angular noise spectrum of density contrast through $N_\ell^{CGWB} = N_\ell / \overline{\Omega}_{GW}^2$. In our case, having assumed a power-law description of the primordial power spectrum, we compute the average energy density at some frequency[69] as [54]:

$$\overline{\Omega}_{GW}(f) = \frac{r A_s}{24 z_{eq}} \left(\frac{f}{f_{pivot}} \right)^{n_t} , \tag{340}$$

where r is the tensor-to-scalar ratio at $f_{pivot} \approx 1.55 \times 10^{-17}$ Hz, corresponding to $k = 0.01$ Mpc^{-1}, and $z_{eq} \approx 3400$ is the redshift of matter-radiation equality (calculated by the Boltzmann code)[70]. In this way, the more blue tilted the spectral index is, the higher will be $\overline{\Omega}_{GW}$ at the reference frequencies of both BBO and LISA.

The resolution of GW interferometers is typically quite low and limited to the first 10-20 multipoles [197], so the JCV we obtain will improve the TT CV in just few cases. Here we report the case of BBO when we assume $n_t = 0.52$. Indeed, even if choosing a higher tilt decreases the GW signal (see Fig. 12), its effect on how much power reaches the typical scales of interferometers is far more dominant. Thus, we choose to maximize the value in the allowed range of [54]. To obtain Fig. 19, we limit our analysis to the first six multipoles, given that the noise for $\ell > 6$ is too large. The figure shows that despite the noise the GW signal is strong enough to allow BBO to be signal dominated and to recover identically the noiseless JCV. Notice that the Planck estimated value we report here is different from the one shown in Fig. 18 because we changed the range of multipoles. Here, the value of the modulating amplitude obtained for Planck's SMICA map is $\omega_1 = 0.80$.

69 The reference frequency of LISA is 10^{-2} Hz, instead for BBO 1 Hz.
70 It can be shown that this expression is an approximation to Eq. 188.

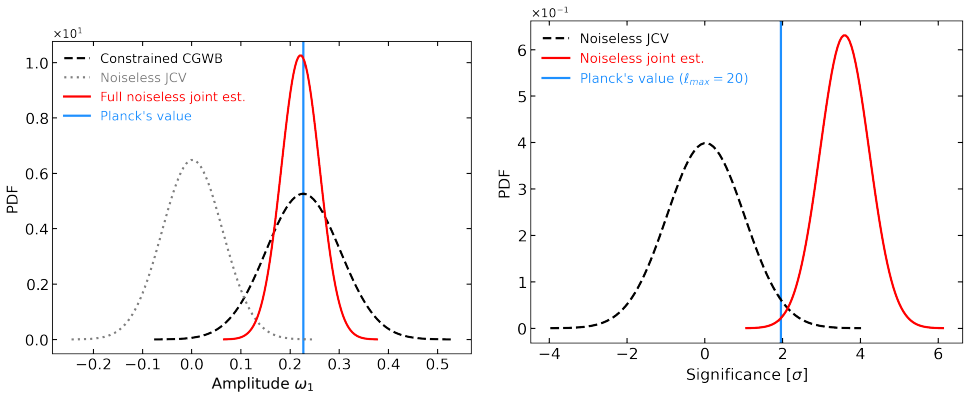

Figure 20: *Left:* Estimated modulating amplitude for a set of 1000 realizations constrained on the Planck's map, assuming $\ell_{max} = 20$, $n_t = 0$. The dashed black curve is the dispersion for the CGWB realizations constrained to the Planck's map, whose value is represented as a solid vertical blue line. The solid red curve indicates the dispersion of the joint estimation using both the realizations of the CGWB and Planck's map. Finally, the dotted gray line represents the JCV dispersion. *Right:* Estimated significance for the joint estimator of the modulating amplitude using a set of 1000 CGWB realizations constrained on the Planck map, assuming $\ell_{max} = 20$, $n_t = 0$. The dashed black curve indicates the significance of JCV (red curve of Fig. 18). The Planck map significance without GWs is represented as a solid vertical blue line, whereas the solid red curve indicates the dispersion of the joint estimation.

9.2.3 *Forecasts for future observations*

Finally, we can forecast what we can expect to see with a future observation of GWs. Once again we start with the noiseless case and we generate a set of 1000 realizations of the CGWB constrained on the Planck SMICA map, assuming that a modulation is already present in this map. Also, here a clarification is due: given the assumption we make for Planck's SMICA map, the modulating information is passed to the GW background through the fact that the CGWB realizations are constrained on the CMB one. Thus, we assume that the model describing the anisotropies of both CMB and CGWB is a modulated one. So, the $\mathcal{C}_\ell^{XX'}$ we use in the estimator definitions are the $\mathcal{C}_\ell^{(1)}$ mentioned in Chap. 8 (e. g. see Eq. 313 for the CGWB equation). This is indeed a difference w. r. t. [181], where $\mathcal{C}_\ell^{(0)} = \mathcal{C}_\ell^{(1)} = \mathcal{C}_\ell^{(2)}$. In spite of this, having assumed $\mathcal{C}_\ell^{(1)}$ is crucial to fully capture the modulation amplitude, given that we do not neglect the ISW effect, of which we find a modified expression w. r. t. the standard one in Eq. 326, and we do not assume any approximation for the gravitational potential transfer functions.

The left panel of Fig. 20 shows that if a modulation is indeed there, the CGWB will distribute as a normal with $\{\mu, \sigma\} = \{0.23, 0.08\}$, whereas the joint estimator with $\{\mu, \sigma\} = \{0.22, 0.04\}$.

For the sake of clarity, we compute the significance of the joint estimator w. r. t. the JCV. The right panel of Fig. 20 clearly shows the increase in significance that we can expect from a signal-dominated detection of the CGWB. The significance of the joint estimator is distributed as a normal distribution with $\{\mu, \sigma\} = \{3.60, 0.63\}$; specifically, 83.4% of the simulations shown in the right panel of Fig. 20 below the red curve has significance $\geq 3\sigma$ and all improve the significance w. r. t. the Planck value of the SMICA map when assuming $\ell_{max} = 20$, i. e. 1.95σ (solid blue line).

At this point, we repeat the same analysis including the instrumental noise from either LISA or BBO. As we have previously mentioned, the CGWB anisotropies are very hard to observe, thus we report here only the results for BBO when assuming $n_t = 0.52$. As it turns out, all other cases present a large noise, which quickly dominates the measurement for multipoles $\ell > 4$.

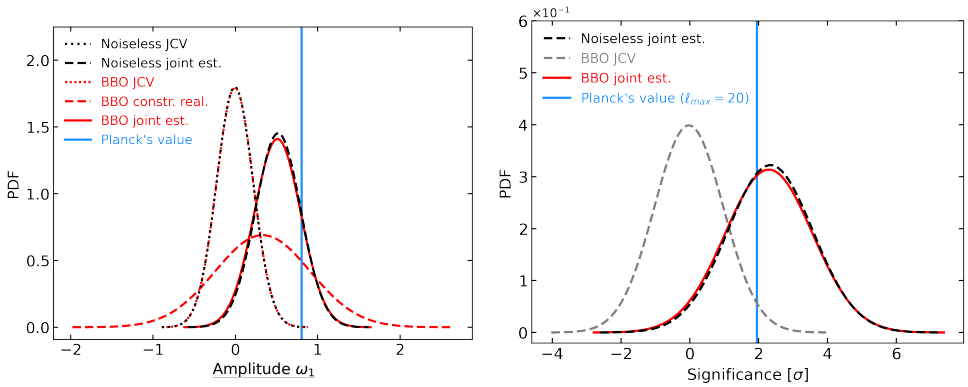

Figure 21: *Left:* Joint estimation of the modulating amplitude when we include the instrumental noise of BBO, assuming $\ell_{max} = 6$, $n_t = 0.52$. The black and red dotted lines are, respectively, obtained including or not the BBO instrumental noise. The dashed black line indicates the noiseless joint estimation from the constrained realizations on the Planck SMICA map, whereas the dashed red line represents the CGWB constrained realizations. Finally, the red solid line is the joint estimation when we include the BBO instrumental noise. *Right:* Estimated significance for the joint estimator of the modulating amplitude using a set of 1000 CGWB realizations constrained on the Planck map and including the instrumental noise of BBO, assuming $\ell_{max} = 6$, $n_t = 0.52$ (solid red line). The dashed gray curve is the dispersion of the BBO JCV we show in Fig. 19. The significance of Planck's map without GWs is represented as a solid vertical blue line. The black dashed line is the noiseless case.

The left panel of Fig. 21 shows the results: once again we limit our analysis to the first six multipoles. This allows BBO to recover very well the modulation inherited by the Planck map with the same precision as the noiseless case (compare the solid red curve with the dashed black one). As before, we recast the BBO JCV and joint estimation in terms of significance in the right panel of Fig. 21.

This shows once again the increment in significance that we can expect from a detection of the CGWB. The significance of the BBO joint estimator is distributed as a normal distribution with $\{\mu, \sigma\} = \{2.3, 1.3\}$; this time, the 27.9% of the simulations shown in the right panel of Fig. 21 below the red curve has a significance $\geq 3\sigma$. This degradation is mainly due to the fact that we had to limit $\ell_{max} = 6$. Indeed, in the noiseless case (black dashed line), about the same percentage (within 1%) of the simulations has a significance $\geq 3\sigma$. Also, the 60.1% of the BBO simulations improves the significance w. r. t. the Planck value of 1.95σ.

So, in spite of this degradation, it is notable that BBO has indeed the potential to shed light on the significance of the CMB power asymmetry.

9.3 SUMMARY AND CONCLUSIONS

In this chapter and in Chap. 8, we have computed the effect on the two-point correlation functions of both the CMB temperature field and the CGWB in the case of a dipolar modulation of the gravitational potentials, which can potentially reproduce this power asymmetry. This modulation breaks the statistical isotropy on our Hubble volume without flawing the Universe's global isotropy and homogeneity.

These kinds of model generate a coupling between multipoles ℓ, $\ell \pm 1$ and $\ell \pm 2$ in all observables, which can then be tested through the statistical tools developed in [181]. GWs behaves nearly identically to CMB temperature, thus we exploited constrained realizations of the CGWB to perform our joint analysis with the SMICA Planck temperature map and unconstrained realizations of both the CMB and the CGWB to assess the cosmic variance associated with a model without modulation.

In Chap. 8, we present the main theoretical results of [182]: the analytic expression of CMB and CGWB anisotropies in the presence of a dipolar modulation of gravitational potentials. In particular, we include SW and ISW for both observables. In Sec. 9.1, we explore the dependence of the CGWB angular power spectrum on the tensor spectral tilt n_t (also, in Sec. A.1 we explore this dependency distinguishing between the contributions of the scalar and the tensor to the anisotropies). This is done in a similar fashion to [104] for other parameters as N_{eff} (see also [198]). In Sec. 9.2, we study the role of GWs in assessing the significance of the CMB power asymmetry. We show that in the noiseless case, the significance is severely increased as shown in figure 20. Specifically, 83.4% of the simulations has a significance $\geq 3\sigma$ and all of them improve the value from Planck's map of 1.95σ. Also, we study the capabilities of both LISA and BBO to observe this kind of anomaly. In the case of a blue tilted spectrum ($r = 0.066$ at 0.01 Mpc^{-1} and $n_t = 0.52$, which saturates the upper bounds of [54]), useful for providing enough energy density of GWs at the scales of the considered interferometers, we show that BBO has the ability to fully reproduce the noiseless case, since it is signal-dominated. Indeed, when limiting to the first six multipoles, the 60.1% of the simulations improves the significance we obtain for the Planck's temperature map, i.e. 1.95σ, and the 27.9% reaches a significance greater than 3σ. This suggests that future observation of the CGWB could be the keystone in assessing finally the physical origin of the CMB power asymmetry.

It should be emphasized that we performed our analysis assuming a standard power-law characterization of the tensor power spectrum (Eq. 398). This conservative perspective quite drastically limits the range of possibilities we could explore, especially for the values of n_t and so the average energy density of GWs we obtained at the typical frequencies of LISA and BBO. In a more general context, one could study other inflationary models that bring much more power to interferometric scales, thus enhancing the possibility of measuring the anisotropies of the CGWB (see, for example, Chap. 5). Furthermore, there are a plethora of other cosmological phenomena that could produce a CGWB that we did not even mention, such as phase transitions, cosmic strings, or reheating. All of these would contribute to a set of new features, which could potentially enhance the detection of GWs anisotropies [94, 95]. Last but not least, in principle also the AGWB is affected by the presence of a modulation of the gravitational potentials, opening another window on the exploration of this anomaly. In the same line of reasoning, we could also investigate possible connections with large-scale structures and tracers [199, 200].

10

LACK-OF-CORRELATION WITH THE CGWB

In Chap. 7 we mentioned the presence of the so-called anomalies on the observed CMB sky, while in Chap. 8 and Chap. 9, we showed the theoretical and observational consequences of a modulating field that accounts for the hemispherical power asymmetry. Here, we move to another anomaly, i. e. the lack-of-correlation.
This chapter is based on Galloni et al. [201].

10.1 THE ANOMALY

Unlike what was expected, we observed a strange feature in the so-called two-point angular correlation of the CMB temperature anisotropies $C(\theta)$: it is almost zero when evaluated on large angular scales (see Sec. 10.2.3 below). For this reason, this was named "lack-of-correlation" anomaly [122, 202–206]. This characteristic of $C(\theta)$ was able to survive the test of time, since it was first observed by COBE [32, 202, 207], then reassessed with WMAP [152, 208, 209], and further confirmed by Planck [174, 210, 211], suggesting that it is not the consequence of some unknown systematic effect.

In order to assess the significance of these anomalies, a number of different techniques have been used. These can be based on some two-point statistic (such as the angular power spectrum), or on peak statistics, and N-point correlation functions (see [174] and the references therein). Independently from the analysis, the fundamental question one tries to answer is: are these features the consequence of a rare realization of the standard ΛCDM model, or do we need to abandon it in favor of a more complex one? One of the obstacles that this question poses is where to search for new information on the anomalies. In fact, CMB temperature has been observed in a cosmic variance-limited fashion on low and intermediate multipole scales; thus, we cannot unveil any new information from the temperature alone. To determine whether these are the consequence of a physical phenomenon, we must exploit other observables, correlated with the CMB temperature, such as the CMB polarization [181, 193, 212–215].

Another non-trivial limitation in assessing the physical nature of the CMB anomalies is the fact that one typically uses "a posteriori" statistics. In fact, estimators are often designed to maximize the significance of a certain anomaly under some a posteriori assumption on the data. Thus, one has to face the following antithesis: neglecting the assumption made on the data, is the evidence of the anomaly still significant? This is often called the "look-elsewhere effect" [174]. Here, we will take care of this aspect of the lack-of-correlation anomaly.

10.2 DATASETS AND METHODOLOGY

As mentioned before, we want to study and build an estimator which is able to reject the fluke hypothesis of the lack of correlation anomaly. Therefore, we investigate the idea that what we observe in the CMB sky is just a rare realization of the standard ΛCDM model. In particular, we want to use the CGWB and try to predict its ability to shed some light on the physical origin of the anomaly.

Before presenting the results, we describe the datasets used for our analysis (see Sec. 10.2.1). In addition, we provide more information on our methodology, with a focus on specific key aspects. This includes developing a procedure to simulate the CGWB sky (as outlined in Sec. 10.2.2), gaining a deeper understanding of the crucial quantity that results in the lack of correlation in our data (as described in Sec. 10.2.3), defining an estimator that measures the anomaly (outlined in Sec. 10.2.4), and specifying the analysis that we performed in this study (as presented in Sec. 10.2.5 and Sec. 10.2.6). Indeed, the final goal of this analysis is to be able to associate a value with the lack of correlation anomaly; for each value, we want to be able to conclude whether it is compatible or not with the fluke hypothesis.

10.2.1 *Datasets*

We use the Planck SMICA temperature map as our observation for CMB [216][71]. It comes at a resolution of ≈ 5 arcmin, which corresponds to a pixelization of the sky in $\approx 5 \times 10^7$ equal-area pixels[72]. Furthermore, masking the galactic plane enhances the discrepancy between the data and the ΛCDM predictions [174, 209, 217, 218], therefore, it is important to treat the cut-sky case. To capture this feature, we will consider the full-sky SMICA map and a masked version, where we use the Planck common mask for intensity[73]. In the latter case (and whenever a mask is involved in the computations), we use the pseudo-$\mathcal{C}_\ell$ formalism to recover the unbiased angular power spectra (`NaMaster` [219])[74].

Regarding the CGWB, we obtain the theoretical angular power spectrum with a modified version of `CLASS` [183, 184][75]. Specifically, we use the expressions shown in [187] and set the ΛCDM parameters to their best-fit values provided by Planck 2018 (see Tab. 1). We consider only the scalar contribution to the anisotropies, neglecting any tensorial contribution [49, 141].

Soon, detectors like LISA [220–224], DECi-hertz Interferometer Gravitational wave Observatory (DECIGO) [225], Einstein Telescope (ET) [226, 227] and Cosmic Explorer (CE) [228] will provide the possibility to observe the CGWB, providing fundamental knowledge on the physics of the early Uni-

71 http://pla.esac.esa.int/pla/#maps.
72 This is usually expressed in terms of the N_{side} parameter of `Healpy`, which define the sky partition. In this case, $N_{\text{side}} = 2048$.
73 http://pla.esac.esa.int/pla/#maps.
74 https://github.com/LSSTDESC/NaMaster.
75 https://github.com/lesgourg/class_public.

Parameter	Best-fit value
$A_s \times 10^9$	2.100549
n_s	0.9660499
$\Omega_b h^2$	0.0223828
$\Omega_{cdm} h^2$	0.1201075
τ_{reio}	0.05430842
H_0	67.32117 $\left[\text{km s}^{-1}\text{ Mpc}^{-1}\right]$
Y_{He}	0.2454006
T_0	2.7255 [K]
$\sum m_\nu$	0.06 [eV]

Table 1: Assumed values of the 6 ΛCDM parameters and other important ones. The quantities A_s and n_s represent the amplitude and tilt of the primordial scalar perturbations. The energy densities of baryons and cold dark matter are denoted by Ω_b and Ω_{cdm}, respectively. H_0 is the Hubble constant expressed in km s^{-1} Mpc^{-1}, which is divided by 100 to obtain $h \equiv H_0/100$. τ_{reio} represents the optical depth of reionization. Then, Y_{He} is the fraction of helium, T_0 is the average temperature of the CMB in Kelvin, and $\sum m_\nu$ is the mass of neutrinos, assuming that 1 is massive and the other 2 are massless.

verse. In fact, these could not only measure the average contribution to energy density brought by GWs, but they could also detect its fluctuations on the celestial sphere. This possibility depends on the actual monopole radiation at the frequencies of the various detectors; the higher the better. To cover the possible performance of these experiments, we will consider 3 maximum multipoles to perform our analysis: $\ell_{max} = 4, 6, 10$. These are the multipoles that one may be able to recover in a signal-dominated way in the next future, exploiting one of the experiments mentioned or a combination of them. To be consistent with this choice, we will also assume $\ell_{max} = 4, 6, 10$ for the temperature part of the analysis. Also, to reduce the computational cost of working at Planck's full-resolution, the CMB map is also degraded to $N_{side} = 64$[76]. Before degrading it, we smooth it with a Gaussian beam with Full Width Half Maximum (FWHM) equal to 2°. Note that the scale corresponding to $N_{side} = 64$ is $\approx 0.92^\circ$, but we follow the general principle of applying a smoothing approximately two or three times bigger than the grid scale to avoid pixelization effects [217]. Regarding the mask, we also degrade it to $N_{side} = 64$ to match the CMB map. The mask is then thresholded by setting to zero the pixels in which the value is less than 0.9; the others are set to unity [174].

Furthermore, since we also want to exploit the cross-correlation of these two fields as an observable, we also produce the cross-maps from our realiza-

76 Although $N_{side} = 64$ allows to describe $3N_{side} - 1$ multipoles (thus much more than what is used for this analysis), in our case no significant computational advantage was found in reducing N_{side} below 64.

tions of TT and CGWB[77]. Although GWs are indeed very difficult to observe, it could be possible in the next future to obtain a relevant signal-to-noise ratio from their cross-correlation with CMB temperature without the need to measure the GW autospectrum. In fact, cross-correlation is often used in the literature to extract information from a noise-dominated context, since it provides unbiased information on the two correlated probes (see, e. g. [187, 190, 229, 230]).

For the sake of brevity, we will use the expression "masked GWGW" in the case where we apply a mask on TT (the CGWB is always evaluated full-sky). Instead, when TT is also full-sky, we will simply use GWGW. For cross-correlation, we will use TGW.

In conclusion, we produce $N = 10,000$ realizations of unconstrained CGWB and TT (full sky and masked). Using both sets of full-sky and masked TT, we also compute the corresponding constrained CGWB realizations, using Planck SMICA as our CMB observation. In addition, we also compute the cross-correlation maps between unconstrained and constrained GWGW and TT (full sky and masked).

10.2.2 *Constrained realizations of masked sky*

Let us consider a generic example with two observables X and Y, which share a certain degree of correlation (in our case, they will be, respectively, the CMB temperature and the CGWB).

In the full-sky case, we already know that a random Gaussian realization of $a_{\ell m}^{XX}$ of X can be obtained by its angular power spectrum C_ℓ^{XX}, which encodes the variance of the coefficients of the spherical harmonics (see Chap. 4). In a more mathematical fashion, we can write

$$a_{\ell m}^{XX} = \xi_{\ell m} \sqrt{C_\ell^{XX}} \,, \tag{341}$$

where $\xi_{\ell m}$ is a random Gaussian field with null mean and unitary variance. Once $a_{\ell m}^{XX}$ have been measured, we can generate $a_{\ell m}^{YY}$ realizations consistent with these, namely constrained realizations, as we have shown in Sec. 9.1.2. In fact, to condition the random realizations of Y on the information already available on X, one can use the same Gaussian seed $\xi_{\ell m}$ to write

$$a_{\ell m}^{YY} = \frac{C_\ell^{XY}}{\sqrt{C_\ell^{XX}}} \xi_{\ell m} + \xi'_{\ell m} \sqrt{C_\ell^{YY} - \frac{\left(C_\ell^{XY}\right)^2}{C_\ell^{XX}}} \,. \tag{342}$$

where C_ℓ^{XY} is the cross-correlation spectrum of the two observables and $\xi'_{\ell m}$ is another random Gaussian field ($\langle \xi_{\ell m} \xi'^{*}_{\ell m} \rangle = 0$). Recasting this in terms of $a_{\ell m}^{XX}$, this expression becomes essentially Eq. 329.

77 To be consistent with what is customarily done for CMB temperature, we will indicate the auto-spectra of the CGWB with GWGW.

In Eq. 329, the first term on the right side is extracting the Gaussian seed of X, i. e. $\xi_{\ell m}$, and translating it into a deterministic part of the realization Y. Note that Eq. 329 depends on the underlying assumptions of Gaussianity and statistical isotropy of the coefficients of the spherical harmonics (a generalization is Eq. 330). Furthermore, the specific shape of $\mathcal{C}_\ell^{XX}, \mathcal{C}_\ell^{XY}, \mathcal{C}_\ell^{YY}$ will depend on the assumed cosmological model, which in our case is the ΛCDM model.

Eq. 329 can be generalized to the case of masked skies. To do so, we must recall the definition of $a_{\ell m}^{XX}$ as the coefficients of the decomposition of spherical harmonics of the X field on the 2D sphere. In particular, starting from the full-sky (FS) case, we can write (we drop the apex XX for the sake of notation) [231, 232]

$$a_{\ell m}^{\rm FS} \equiv \int_{\rm full-sky} Y_{\ell m}^*(\theta, \phi) X(\theta, \phi)\, {\rm d}(\cos\theta)\, {\rm d}\phi \,, \tag{343}$$

where $Y_{\ell m}$ are the spherical harmonics and θ, ϕ are the angles on the celestial sphere. These $a_{\ell m}^{\rm FS}$ (Full-Sky (FS)) are predicted to be statistically isotropic Gaussian realizations with a null mean and a variance defined as

$$\left\langle a_{\ell m}^{*,{\rm FS}} a_{\ell m}^{\rm FS} \right\rangle = \delta_{\ell\ell'}\delta_{mm'}\mathcal{C}_\ell \,, \tag{344}$$

where $\mathcal{C}_\ell$ is the angular power spectrum of X. From a full-sky observation, one can estimate the angular power spectrum as

$$\widehat{\mathcal{C}}_\ell = \frac{1}{2\ell+1} \sum_{m=-\ell}^{\ell} \left| a_{\ell m}^{\rm FS} \right|^2 . \tag{345}$$

In the presence of a mask, Eq. 343 gets slightly modified in order to consider that the integration is performed on the unmasked patch of the sphere. Thus, the spherical harmonics do not constitute an orthogonal basis and the $a_{\ell m}$ coefficients measured on the Cut-Sky (CS) have couplings between multipoles. Despite this, it is possible to recover the corresponding full-sky values knowing the geometrical couplings introduced by the mask (see Sec. B.1) [231, 232]. In particular, they are related by (the sum over repeated indexes is understood)

$$a_{\ell m}^{\rm CS} = a_{\ell' m'}^{\rm FS} \times W_{\ell m}^{\ell' m'} \,, \tag{346}$$

where $W_{\ell m}^{\ell' m'}$ is the window function of the mask considered.

Thus, Eq. 329 must be modified to account for this since it assumes the full-sky condition. In particular, when we consider the coefficients of the cut-sky, that is, $a_{\ell m}^{\rm CS}$, we must recast the first factor on the right-hand side as

$$\frac{\mathcal{C}_\ell^{XY}}{\mathcal{C}_\ell^{XX}} \times a_{\ell m}^{\rm CS} \Longrightarrow \frac{\mathcal{C}_\ell^{XY}}{\mathcal{C}_\ell^{XX}} \times a_{\ell' m'}^{\rm CS} \left(W_{\ell m}^{\ell' m'} \right)^{-1} = \frac{\mathcal{C}_\ell^{XY}}{\mathcal{C}_\ell^{XX}} \times \widehat{a}_{\ell m}^{\rm FS} \,. \tag{347}$$

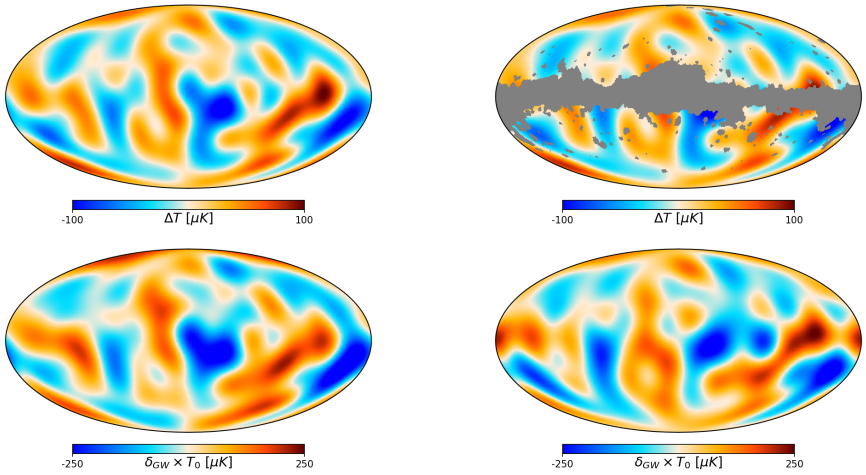

Figure 22: The two upper panels in the upper part show the SMICA map downgraded to $N_{\rm side} = 64$ and filtered to remove the multipoles above $\ell > 10$ for the full-sky and masked case. In the lower panels, we show one of the corresponding constrained realizations of the CGWB.

In this way, the cut-sky coefficients are remapped to the full-sky ones and the rest of the formula can remain the same. Note that we indicated the full-sky coefficients on the right-hand side as $\widehat{a}^{\rm FS}_{\ell m}$ to remark that we are not obtaining their true values, but rather an estimate of them. In other words, following this procedure, we get an estimator of the full-sky coefficients from a partial-sky observation. Note that this becomes unfeasible as the window function becomes singular for aggressive masks. For the full-sky case, the window function goes to $W^{\ell' m'}_{\ell m} = \delta_{\ell\ell'}\delta_{mm'}$ (see Sec. B.1), recovering the usual expressions. Accounting for the complete expression of this matrix allows us to correctly obtain the full-sky coefficients for X, which are then converted in terms of Y by the factor $\mathcal{C}^{XY}_\ell / \mathcal{C}^{XX}_\ell$. Note that another underlying assumption of this generalized procedure is that Y is full-sky; otherwise, one has to take care again of the couplings between multipoles of the Y realization.

As an example, in Fig. 22 we show different sky realizations of the CGWB. In the upper part of the figure, we plot the downgraded SMICA map, for which we filter out the multipoles with $\ell > 10$. Respectively, we show the full-sky and masked ones in the left and right panels. Instead, in the lower part of the figure, we show two constrained CGWB realizations based on the map above (thus full-sky or masked). Thus, the one on the left is obtained with Eq. 329 and the other is responsible for the generalization discussed in this section.

As is customarily done in the literature, we normalize the CMB anisotropies to the monopole radiation of the CMB, $T_0 = 2.7255 \times 10^6\ \mu K$ [23], so that we show the maps in units of μK. Usually in the case of the CGWB one plots the energy density contrast as defined in [49]. However, to be consistent with the choice for CMB and to be visually clear, we also normalize the CGWB anisotropies to the same quantity. Thus, the energy density will also be expressed in units of μK.

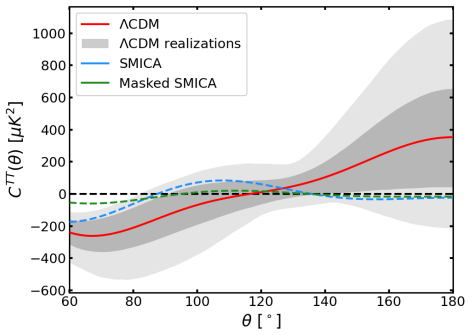

Figure 23: Two-points angular correlation function of CMB temperature. Here, we assume $\ell_{\max} = 4$. The red line is the mean of the ΛCDM realizations and the gray bands are the 1 and 2 σ around that.

10.2.3 *Angular correlation function*

Having defined the datasets and how to obtain constrained realizations in the masked case, we briefly explore the actual quantity presenting the lack-of-correlation in current data. Indeed, we know that the fluctuations ΔT in the photon temperature T that we observe are very well described by their spherical harmonic coefficients defined in Eq. 343. For T, it is recast to [34]

$$a_{\ell m} \equiv \int Y^*_{\ell m}(\theta, \phi) \frac{\Delta T}{T_0}(\theta, \phi)\, \mathrm{d}(\cos\theta)\, \mathrm{d}\phi \,, \tag{348}$$

where T_0 is the average temperature, i. e. , the monopole radiation. Then, from a full-sky CMB observation, one can estimate the angular power spectrum using Eq. 345. This quantity plays a key role in almost every estimation of cosmological parameters, given that it is a very efficient summary statistic to study the properties of $a_{\ell m}$ (at least assuming Gaussianity [147]).

An alternative and equivalent way to convey the same information is the two-point angular correlation function, defined as [159]

$$C(\theta) \equiv \left\langle \frac{\Delta T}{T_0}(\hat{n}_1) \frac{\Delta T}{T_0}(\hat{n}_2) \right\rangle \Bigg|_{\hat{n}_1 \cdot \hat{n}_2 = \cos\theta} = \sum_{\ell=0}^{\infty} \frac{2\ell + 1}{4\pi} \mathcal{C}_\ell P_\ell(\cos\theta) \,, \tag{349}$$

where P_ℓ are the Legendre polynomials. In other words, $C(\theta)$ and $\mathcal{C}_\ell$ are related by a series of P_ℓ, thus the former allows us to better appreciate the large-scale behavior and the latter the small-scale one. Also, in the assumption of Gaussian fluctuations, all the available information is encoded in $\mathcal{C}_\ell$, thus the same holds for $C(\theta)$.

Thus, at this point, we can compute $C^{\mathrm{TT}}(\theta)$ from the SMICA map to understand the actual anomaly. Fig. 23 shows the result. One can see that the SMICA map, especially the masked one, has a low correlation for scales larger than $\sim 60°$. Also, note that the curves shown in Fig. 23 are not equal to those shown in [159]. Indeed, assuming $\ell_{\max} = 4$ means that Fig. 23 shows only the angular correlation given by the first four multipoles of the expansion.

Let us now look at the CGWB realizations. The top panels of Fig. 24 show both the full-sky and masked realizations. Here, we can appreciate the fact

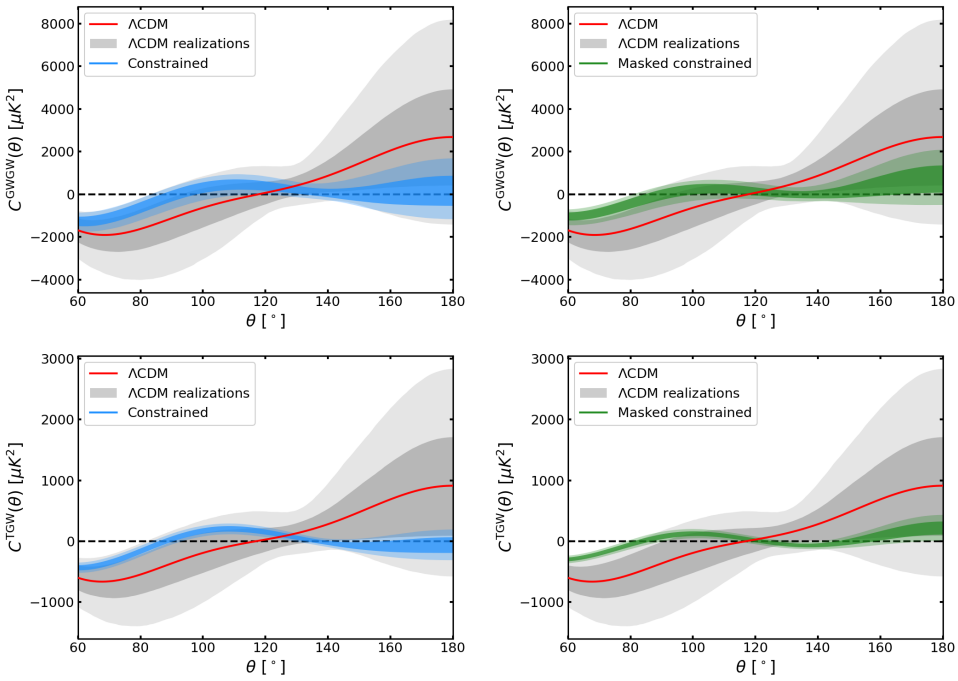

Figure 24: In the top panels, this figure shows the two-points angular correlation function of the CGWB, while the bottom ones the correlation function of TGW. The left and right panels refer respectively to the full-sky and masked cases. Here, we assume $\ell_{max} = 4$. The red line is the mean of the ΛCDM realizations and the gray bands are the 1 and 2 σ around that.

that the very high correlation existing between TT and GWGW contributes to severely shrinking the dispersion of the CGWB realizations. Furthermore, the TT mask makes them very consistent with zero on almost all the scales considered ($> 80°$). These two features already show that GWs could be a pristine probe to test the fluke hypothesis.

Finally, the bottom panels of Fig. 24 shows the angular correlation functions of TGW. It shows that the dispersion of the constrained realizations of TGW is even smaller than that of the CGWB. This suggests that TGW could also be a very interesting probe for this analysis of the fluke hypothesis. In Sec. B.2, we show the angular correlation functions of GWGW and TGW assuming $\ell_{max} = 2000$ to appreciate the difference w. r. t. CMB temperature, while neglecting the expected performance of future interferometers.

10.2.4 *S-statistic for auto- and cross-correlations*

To quantify this lack of temperature correlation, Spergel et al. [203] introduced the quantity

$$S_{1/2} = \int_{-1}^{1/2} [C(\theta)]^2 \mathrm{d}(\cos\theta) \,, \tag{350}$$

which integrates the squared correlation on scales larger than $60°$. Clearly, this naturally captures the total distance between the angular correlation and zero in that angular range, regardless of its sign.

Copi et al. [212] introduced a way to find the optimal angular range in which an additional observable can provide most of the information. Thus,

by varying the minimum and maximum angles, the estimator $S_{1/2}$ is recast to

$$S_{\theta_{\rm min},\theta_{\rm max}} = \int_{\theta_{\rm min}}^{\theta_{\rm max}} [C(\theta)]^2 {\rm d}(\cos\theta) = \sum_{\ell=2}^{\ell_{\rm max}} \sum_{\ell'=2}^{\ell_{\rm max}} \frac{(2\ell+1)}{4\pi} \frac{(2\ell'+1)}{4\pi} \mathcal{C}_\ell^{XX} I_{\ell\ell'}^{\theta_{\rm min},\theta_{\rm max}} \mathcal{C}_{\ell'}^{XX} \,, \tag{351}$$

with

$$I_{\ell\ell'}^{\theta_{\rm min},\theta_{\rm max}} = \int_{\theta_{\rm min}}^{\theta_{\rm max}} P_\ell(x) P_{\ell'}(x) {\rm d}x \,. \tag{352}$$

Here, we have introduced $\ell_{\rm max} \neq \infty$ since we must account for the fact that a realistic observation depends on the angular resolution of the experiments considered. In fact, above a certain multipole, we know that noise will dominate the measurement. The same treatment was adopted in [193], where the multipole cut was made when the signal-to-noise ratio of the E-mode polarization was essentially saturated. It should be underlined that $\ell_{\rm max}$ affects the calculation of $I_{\ell\ell'}^{\theta_{\rm min},\theta_{\rm max}}$. In fact, multipoles up to $\ell_{\rm max}$ will describe scales larger than approximately $180^\circ/\ell_{\rm max}$. Instead, the behavior on smaller scales will be determined by noise or by interference of the Legendre modes considered. To be conservative on which scales we consider well described by the available multipoles, we will impose a lower bound on $\theta_{\rm min}$ and $\theta_{\rm max}$ of

$$\theta_{\rm cut} = \frac{180^\circ}{\ell_{\rm max} - 1} \,, \tag{353}$$

so that $\theta_{\rm min}, \theta_{\rm max} \geq \theta_{\rm cut}$. In this way, we can also avoid "border effects" when approaching $180^\circ/\ell_{\rm max}$.

We can apply the estimator defined in Eq. 351 to the three angular power spectra by substituting $\mathcal{C}_\ell^{\rm TT}$, $\mathcal{C}_\ell^{\rm GWGW}$, or $\mathcal{C}_\ell^{\rm TGW}$ into the above definitions. This provides us with three quantities: $S_{\theta_{\rm min},\theta_{\rm max}}^{\rm TT}$, $S_{\theta_{\rm min},\theta_{\rm max}}^{\rm GWGW}$, and $S_{\theta_{\rm min},\theta_{\rm max}}^{\rm TGW}$.

In addition to the three $S_{\theta_{\rm min},\theta_{\rm max}}$ estimators, we study the joint estimator following the definition introduced in Chiocchetta et al. [193], which yields

$$S_{\theta_{\rm min},\theta_{\rm max}}^{\rm TT,Z} = \sqrt{\left(\frac{S_{\theta_{\rm min},\theta_{\rm max}}^{\rm TT}}{\left\langle S_{\theta_{\rm min},\theta_{\rm max}}^{\rm TT} \right\rangle}\right)^2 + \left(\frac{S_{\theta_{\rm min},\theta_{\rm max}}^{\rm Z}}{\left\langle S_{\theta_{\rm min},\theta_{\rm max}}^{\rm Z} \right\rangle}\right)^2} \,, \tag{354}$$

where $Z = \{\mathrm{TGW}, \mathrm{GWGW}\}$. We can also define the combination of all the available estimators as follows

$$S^{\mathrm{TT,TGW,GWGW}}_{\theta_{\mathrm{min}},\theta_{\mathrm{max}}} = \sqrt{\left(\frac{S^{\mathrm{TT}}_{\theta_{\mathrm{min}},\theta_{\mathrm{max}}}}{\left\langle S^{\mathrm{TT}}_{\theta_{\mathrm{min}},\theta_{\mathrm{max}}}\right\rangle}\right)^2 + \left(\frac{S^{\mathrm{TGW}}_{\theta_{\mathrm{min}},\theta_{\mathrm{max}}}}{\left\langle S^{\mathrm{TGW}}_{\theta_{\mathrm{min}},\theta_{\mathrm{max}}}\right\rangle}\right)^2 + \left(\frac{S^{\mathrm{GWGW}}_{\theta_{\mathrm{min}},\theta_{\mathrm{max}}}}{\left\langle S^{\mathrm{GWGW}}_{\theta_{\mathrm{min}},\theta_{\mathrm{max}}}\right\rangle}\right)^2}. \tag{355}$$

When we consider constrained realizations of GWGW or TGW, $S^{\mathrm{TT}}_{\theta_{\mathrm{min}},\theta_{\mathrm{max}}}$ will be replaced with SMICA data, that is, $S^{\mathrm{SMICA}}_{\theta_{\mathrm{min}},\theta_{\mathrm{max}}}$. Still, both of them, GWGW and SMICA, will be normalized by their unconstrained counterparts.

Essentially, this joint estimator is a sum in quadrature of the two normalized estimators. When this estimator departs from 1, it means that both TT and GWGW are doing so. Note that in the constrained case, $S^{\mathrm{TT,GWGW}}_{\theta_{\mathrm{min}},\theta_{\mathrm{max}}}$ cannot be lower than $S^{\mathrm{SMICA}}_{\theta_{\mathrm{min}},\theta_{\mathrm{max}}} / \left\langle S^{\mathrm{TT}}_{\theta_{\mathrm{min}},\theta_{\mathrm{max}}}\right\rangle$. The same applies to $S^{\mathrm{TT,TGW}}_{\theta_{\mathrm{min}},\theta_{\mathrm{max}}}$ and $S^{\mathrm{TT,TGW,GWGW}}_{\theta_{\mathrm{min}},\theta_{\mathrm{max}}}$.

In Sec. 10.2.2 we mentioned that we normalize the CMB anisotropies to T_0, so the estimator $S^{\mathrm{TT}}_{\theta_{\mathrm{min}},\theta_{\mathrm{max}}}$ will be expressed in units of μK^4. Since we also use this normalization for the CGWB, the same is true for $S^{\mathrm{TGW}}_{\theta_{\mathrm{min}},\theta_{\mathrm{max}}}$ and $S^{\mathrm{GWGW}}_{\theta_{\mathrm{min}},\theta_{\mathrm{max}}}$.

10.2.5 *Optimal angular range*

In order to select the optimal range of angles for the estimator $S_{\theta_{\mathrm{min}},\theta_{\mathrm{max}}}$ (see Eq. 351), we apply the procedure introduced in [212] both to the case of single estimators and to the joint case. Given an observation of the CMB temperature, the optimal range of angles is issued by θ_{min} and θ_{max} that maximize the displacement between the values of $S_{\theta_{\mathrm{min}},\theta_{\mathrm{max}}}$ obtained through constrained and unconstrained realizations of the CGWB. This somehow tells us in what angular range the CGWB is most sensitive to the signal we observe in TT, in terms of lack-of-correlation. To quantify this displacement, we proceed as follows:

1. we first grid the values of θ_{min} and θ_{max} and at each node of the grid we compute the constrained and unconstrained estimators $S^{\mathrm{GWGW}}_{\theta_{\mathrm{min}},\theta_{\mathrm{max}}}$;
2. then, for each node, we compute the 99th percentile of the values given by the constrained realizations, and we count how many unconstrained realizations give a higher value of $S_{\theta_{\mathrm{min}},\theta_{\mathrm{max}}}$. Translating this in terms of a percentage, we call this quantity Percentage Displacement (PD);
3. finally, by studying the results on the grid, we can identify which regions give higher PDs. When searching for which specific configuration gives the optimal angular range, we have to keep in mind

what our statistical error is in evaluating PDs. We can define it as $\sigma_{\rm PD} = 1/N \simeq 0.01\%$. Thus, we round the obtained PDs to the second decimal figure;

4. then, if two or more configurations have the same PD, we privilege the one where $\Delta\theta = \theta_{\rm max} - \theta_{\rm min}$ is maximal. In this way, we are choosing the case where we integrate over the most scales.

We repeat the same analysis for $S^{\rm TGW}_{\theta_{\rm min},\theta_{\rm max}}$, $S^{\rm TT,GWGW}_{\theta_{\rm min},\theta_{\rm max}}$, $S^{\rm TT,TGW}_{\theta_{\rm min},\theta_{\rm max}}$ and $S^{\rm TT,TGW,GWGW}_{\theta_{\rm min},\theta_{\rm max}}$. In the joint cases, we find the optimal angular range to assess the fluke hypothesis simultaneously exploiting more than one field.

10.2.6 *Significance accounting for the look-elsewhere effect*

Until now, we have only mentioned the fluke hypothesis, explaining the methodology we want to use to find out whether GWs can help to reject at least some of the assumptions of the ΛCDM model. Despite this, we cannot say anything about the significance of the anomaly using the optimal angles analysis.

Indeed, could we say that the significance of the anomaly is the distance of a certain data point (i. e. a specific value of $S_{\theta_{\rm min},\theta_{\rm max}}$ of a realization) from the unconstrained ΛCDM simulations (in terms of sigma or p-value)? The answer is not that straightforward, and the reason is called the "look-elsewhere" effect [174]. Indeed, a certain realization would have a significance in each angular range, and by choosing the optimal angular range, we would a posteriori choose the configuration that maximizes that number. In other words, we design the analysis to provide the best possible solution. In a different angular range, the data may agree completely with the prediction of ΛCDM.

A well-known strategy to account for the look-elsewhere effect is to study the PD of the realizations irrespective of their angular range: one searches for the maximum PD for each realization without caring about the angular range. Then, the fraction of these probabilities that are found to be lower than the maximum PD yielded by the data is a global p-value [174].

Despite this, in this work we choose to follow a novel procedure to account for the look-elsewhere effect. We define a new estimator for the lack of correlation as the sum of all configurations in the angular range of $S_{\theta_{\rm min},\theta_{\rm max}}$. For a generic observable X, it reads

$$S^{\rm XX} \equiv \sum_{\{\theta_{\rm min},\theta_{\rm max}\}} \frac{S^{\rm XX}_{\theta_{\rm min},\theta_{\rm max}}}{\left\langle S^{\rm XX}_{\theta_{\rm min},\theta_{\rm max}} \right\rangle} \,. \tag{356}$$

This may be regarded as a marginalization of $S^{\rm XX}_{\theta_{\rm min},\theta_{\rm max}}$ over angular information. Now, $S^{\rm XX}$ tells us whether a simulation of X has an anomalously low covariance, regardless of the angular range considered. This reasoning can be applied to each field that we considered in the previous analysis; thus, TT, TGW, GWGW, and their combinations. Note that we also normalize the

values entering the sum by the mean of the unconstrained realizations, as done in Eq. 354 and Eq. 355. This is because we do not want our results to be driven by the eventual presence of a high $S_{\theta_{\min},\theta_{\max}}$ region, which would dominate the sum over angular ranges.

Using this new estimator, we can study the significance of the lack-of-correlation anomaly taking into account the look-elsewhere effect. In fact, comparing the resulting values of S with those obtained from the CMB data or from the constrained realizations of the CGWB, we compute the significance in terms of sigma. In other words, with this approach, we can still affirm that a future observation of the CGWB falling outside the constrained curve indicates that we must revise our assumptions. However, we can also associate significance to data points that fall within the predicted curve. In this way, we can study the effects of the inclusion of GWs on the actual assessment of the physical origin of the anomaly.

Finally, to quantify the significance we first compute the p-value of each realization (so the probability of getting an unconstrained realization with a lower value than the considered one), and then we translate the p-value in terms of a σ-distance w. r. t. a normal Gaussian. Given that we have a finite number of realizations, there may be cases in which no unconstrained realizations are found below a certain constrained value of S. In this case, we recall that each percentage we obtain has an error of 0.01%, thus we associate with null p-value realizations a probability of 0.01%. This may underestimate the significance of the furthest values of S w. r. t. the unconstrained realizations.

Before reporting the results of this analysis, we mention that the complete code to reproduce them is publicly available [78].

10.3 RESULTS

In the following, we show the results assuming the most pessimistic case analyzed of $\ell_{\max} = 4$. Finally, in Sec. B.4 we show the other two cases of $\ell_{\max} = 6$ and 10.

10.3.1 *Optimal angles*

We begin studying the optimal range of angles for each estimator as described in Sec. 10.2.5. We show the results for $S^{\mathrm{GWGW}}_{\theta_{\min},\theta_{\max}}$ and $S^{\mathrm{TGW}}_{\theta_{\min},\theta_{\max}}$ in the top and bottom panels of Fig. 25. The left and right panels show the results for the full-sky and masked analyses, respectively. Note that every optimal angle plot we show from now on is symmetric by construction; however, we add a gray-shaded region to emphasize that $\theta_{\min}$ cannot be greater than $\theta_{\max}$.

The PDs of both GWGW and TGW change when passing from the full sky to masked analysis, showing that masking the galactic plane enhances the lack of correlation [174, 209, 217, 218]. Comparing this result with [212],

78 https://github.com/ggalloni/lack_of_correlation_with_GWs.

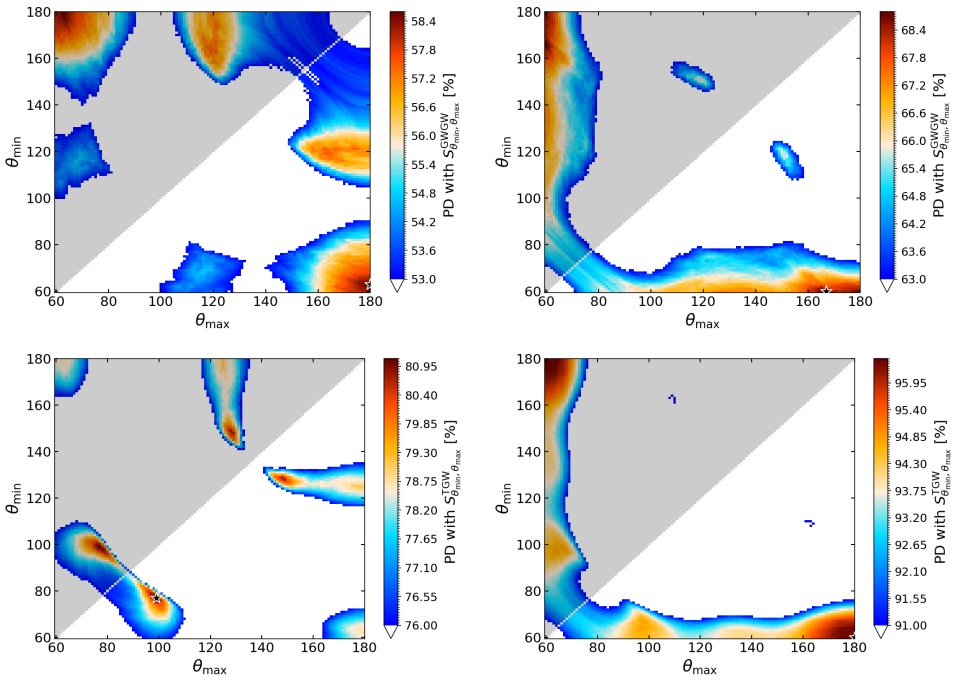

Figure 25: *Top:* optimal angles for GWGW. *Bottom:* optimal angles for TGW. The left and right panels show respectively the results when we assume either full-sky or masked SMICA as our CMB observation. The star shows the best angular range. Here, we assume $\ell_{max} = 4$.

who performed the same analysis using the CMB E-mode polarization, we can appreciate how powerful GWs are in testing the fluke hypothesis. In fact, having a $\sim 90\%$ PD means that the distribution that TGW must follow if ΛCDM is correct is extremely peaked and localized. This maximizes the possibility of rejecting it in the event that a future observation happens to be outside that distribution, with the corresponding level of significance.

We repeat the same analysis for $S^{TT,GWGW}_{\theta_{min},\theta_{max}}$, $S^{TT,TGW}_{\theta_{min},\theta_{max}}$ and $S^{TT,TGW,GWGW}_{\theta_{min},\theta_{max}}$; see Fig. 26. Once again, the left and right panels show the full-sky and masked cases. Note that in all cases there is a high-PD region near the range $[60°, 180°]$, i. e. the range of the original estimator $S_{1/2}$ introduced by Spergel et al. [203].

In this context, the PD reaches values well above 90%, especially for the masked case of $S^{TT,TGW}_{\theta_{min},\theta_{max}}$, where the optimal region reaches $\sim 98\%$. This shows that GWs may be crucial to test the fluke hypothesis and eventually reject the ΛCDM model. Interestingly, the best results are obtained by combining the CMB temperature with its cross-correlation with the CGWB. Instead, including the GWGW spectrum seems to reduce the ability to test the fluke hypothesis. All the results on the optimal angles are summarized in Tab. 2.

Assuming that we choose the optimal angular range for the full-sky and masked case, the top panels of Fig. 27 show the correspondent distributions of $S^{GWGW}_{\theta_{min},\theta_{max}}$. Doing the same for TGW, we instead obtain the bottom panels of Fig. 27. Note that TGW gives PDs consistently higher than the ones from GWGW. This suggests that TGW is a better probe to test the fluke hypothesis. In fact, even without combining more than one probe (see the following paragraphs), TGW achieves a PD of 96.41% under the most pessimistic assumption of $\ell_{max=4}$.

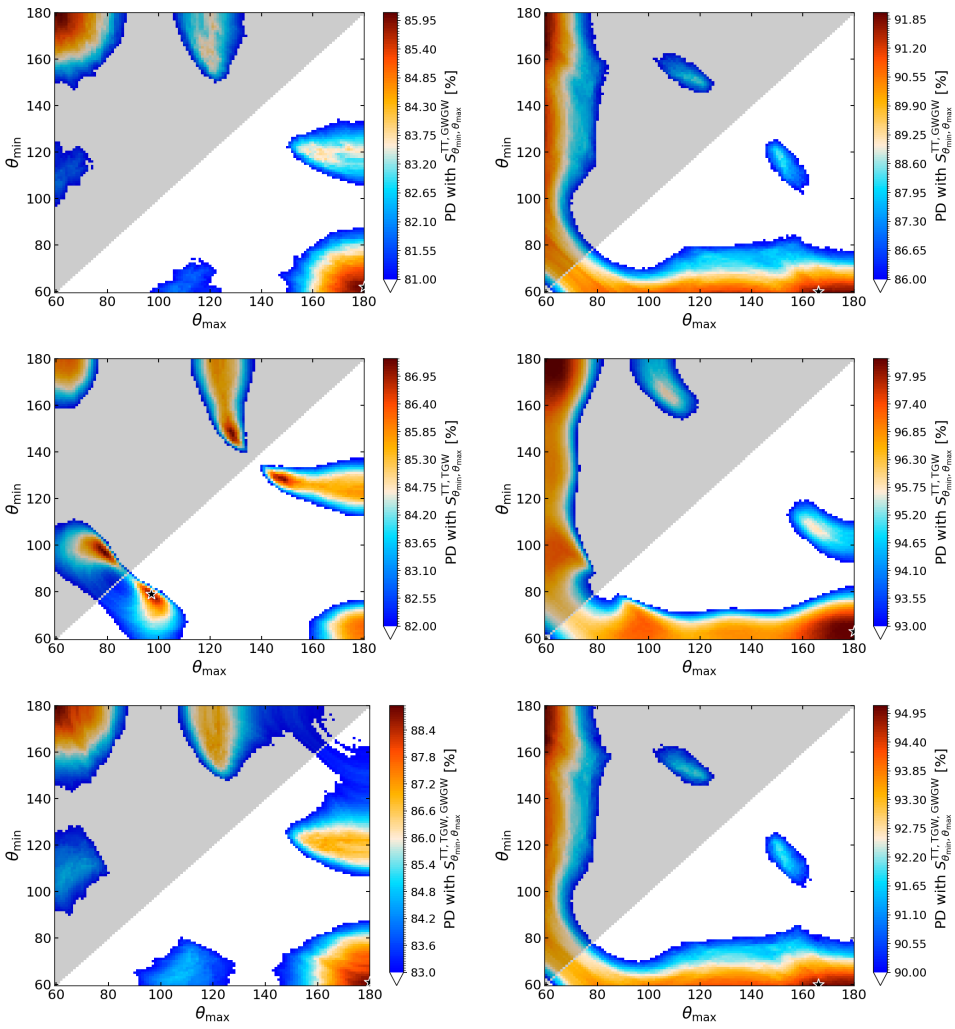

Figure 26: *Top:* optimal angles for the combination of TT and GWGW. *Center:* optimal angles for the combination of TT and TGW. *Bottom:* optimal angles for the combination of TT, TGW and GWGW. The left and right panels show respectively the results when we assume either full-sky or masked SMICA as our CMB observation. The star shows the best angular range. Here, we assume $\ell_{\rm max} = 4$.

Full-sky	$S^{\rm GWGW}_{\theta_{\rm min},\theta_{\rm max}}$		$S^{\rm TGW}_{\theta_{\rm min},\theta_{\rm max}}$		$S^{\rm TT,GWGW}_{\theta_{\rm min},\theta_{\rm max}}$		$S^{\rm TT,TGW}_{\theta_{\rm min},\theta_{\rm max}}$		$S^{\rm TT,TGW,GWGW}_{\theta_{\rm min},\theta_{\rm max}}$	
	$\theta_{\rm min}$	$\theta_{\rm max}$	$\theta_{\rm min}$	$\theta_{\rm max}$	$\theta_{\rm min}$	$\theta_{\rm max}$	$\theta_{\rm min}$	$\theta_{\rm max}$	$\theta_{\rm min}$	$\theta_{\rm max}$
$\ell_{\rm max} = 4$	63°	180°	77°	99°	62°	180°	79°	97°	61°	180°
$\ell_{\rm max} = 6$	56°	121°	65°	115°	55°	120°	68°	116°	54°	118°
$\ell_{\rm max} = 10$	58°	124°	71°	108°	58°	124°	72°	109°	57°	120°

Mask-sky	$S^{\rm GWGW}_{\theta_{\rm min},\theta_{\rm max}}$		$S^{\rm TGW}_{\theta_{\rm min},\theta_{\rm max}}$		$S^{\rm TT,GWGW}_{\theta_{\rm min},\theta_{\rm max}}$		$S^{\rm TT,TGW}_{\theta_{\rm min},\theta_{\rm max}}$		$S^{\rm TT,TGW,GWGW}_{\theta_{\rm min},\theta_{\rm max}}$	
	$\theta_{\rm min}$	$\theta_{\rm max}$	$\theta_{\rm min}$	$\theta_{\rm max}$	$\theta_{\rm min}$	$\theta_{\rm max}$	$\theta_{\rm min}$	$\theta_{\rm max}$	$\theta_{\rm min}$	$\theta_{\rm max}$
$\ell_{\rm max} = 4$	60°	167°	60°	180°	60°	166°	63°	180°	60°	166°
$\ell_{\rm max} = 6$	50°	95°	54°	129°	42°	122°	55°	180°	40°	122°
$\ell_{\rm max} = 10$	74°	77°	61°	132°	60°	88°	62°	134°	59°	88°

Table 2: Optimal angles for every observable and combination of them.

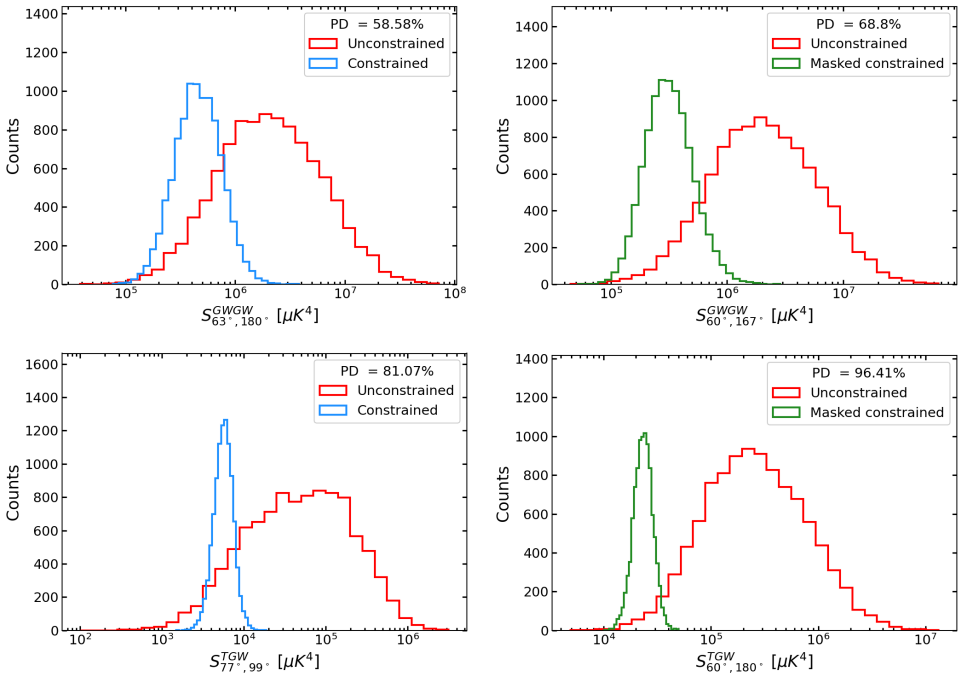

Figure 27: *Top:* $S^{\mathrm{GWGW}}_{\theta_{\mathrm{min}},\theta_{\mathrm{max}}}$ distributions for the full-sky and masked cases. *Bottom:* $S^{\mathrm{TGW}}_{\theta_{\mathrm{min}},\theta_{\mathrm{max}}}$ distributions for the full-sky and masked cases. Angles $\theta_{\mathrm{min}}, \theta_{\mathrm{max}}$ are chosen to be optimal in both cases. Here we assume $\ell_{\mathrm{max}} = 4$.

We repeat the same for the joint analyses of the CMB temperature, CGWB, and their cross-correlation. We obtain Fig. 28 using $S^{\mathrm{TT,GWGW}}_{\theta_{\mathrm{min}},\theta_{\mathrm{max}}}$, $S^{\mathrm{TT,TGW}}_{\theta_{\mathrm{min}},\theta_{\mathrm{max}}}$ and $S^{\mathrm{TT,TGW,GWGW}}_{\theta_{\mathrm{min}},\theta_{\mathrm{max}}}$. All the results on PDs are summarized in Tab. 3. This shows some interesting features: looking at the masked case, we notice not only an overall consistency on the PDs obtained changing ℓ_{max} on each probe, but also there seems to be a certain pattern on how different probes perform at each ℓ_{max}. Indeed, ranking probes with ascending PD-ordering, the pattern remains the same for all the masked case. This does not hold for the full-sky case.

How can these results be used in the presence of a CGWB measurement? Consider our highest PD assuming $\ell_{\mathrm{max}} = 4$, thus the one given by the masked $S^{\mathrm{TT,TGW}}_{63^\circ,180^\circ}$ analysis. Exploiting the right central panel of Fig. 28 we show different shaded areas corresponding to the different conclusions that can be drawn. First, these regions are obtained by computing the range of each histogram that encapsulates the 99% percent of the simulations. This identifies five different parts of this plot:

- two gray regions corresponding to the values of $S^{\mathrm{TT,TGW}}_{63^\circ,180^\circ}$ that are not consistent with neither the constrained nor unconstrained realizations;
- the green and red regions, where the observation falls within the constrained or unconstrained histograms;
- the intersection of the green and red regions (resulting in a darker region), in which we are not sure if the eventual observation follows the constrained or unconstrained distribution.

Depending on the region where a future measurement of the CGWB will fall, we can conclude the following:

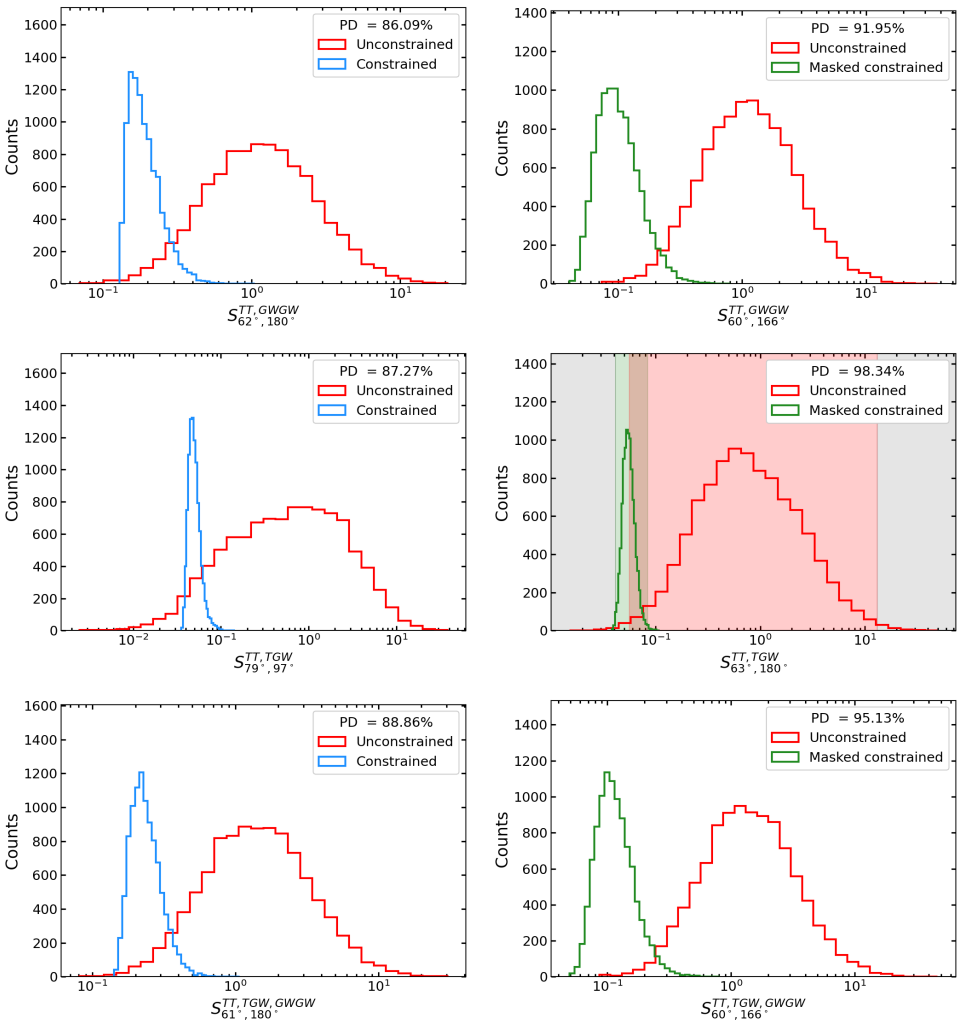

Figure 28: *Top:* $S^{\mathrm{TT,GWGW}}_{\theta_{\min},\theta_{\max}}$ distributions for the full-sky and masked cases. *Center:* $S^{\mathrm{TT,TGW}}_{\theta_{\min},\theta_{\max}}$ distributions for full-sky and masked cases. The right plot also shows shaded areas corresponding to different conclusions that one may draw if a future observation happens to be in those (see the end of Sec. 10.3.1). *Bottom:* $S^{\mathrm{TT,TGW,GWGW}}_{\theta_{\min},\theta_{\max}}$ distributions for full-sky and masked cases. Angles $\theta_{\min},\theta_{\max}$ are chosen to be optimal in all cases and we assume $\ell_{\max}=4$.

Full-sky	$S^{\mathrm{GWGW}}_{\theta_{\min},\theta_{\max}}$	$S^{\mathrm{TGW}}_{\theta_{\min},\theta_{\max}}$	$S^{\mathrm{TT,GWGW}}_{\theta_{\min},\theta_{\max}}$	$S^{\mathrm{TT,TGW}}_{\theta_{\min},\theta_{\max}}$	$S^{\mathrm{TT,TGW,GWGW}}_{\theta_{\min},\theta_{\max}}$
	PD	PD	PD	PD	PD
$\ell_{\max}=4$	58.58%	81.07%	86.09%	87.27%	88.86%
$\ell_{\max}=6$	60.75%	90.44%	87.61%	94.29%	90.35%
$\ell_{\max}=10$	62.27%	88.99%	88.51%	93.4%	91.22%

Mask-sky	$S^{\mathrm{GWGW}}_{\theta_{\min},\theta_{\max}}$	$S^{\mathrm{TGW}}_{\theta_{\min},\theta_{\max}}$	$S^{\mathrm{TT,GWGW}}_{\theta_{\min},\theta_{\max}}$	$S^{\mathrm{TT,TGW}}_{\theta_{\min},\theta_{\max}}$	$S^{\mathrm{TT,TGW,GWGW}}_{\theta_{\min},\theta_{\max}}$
	PD	PD	PD	PD	PD
$\ell_{\max}=4$	68.8%	96.41%	91.95%	98.34%	95.13%
$\ell_{\max}=6$	73.12%	96.98%	94.23%	98.9%	96.36%
$\ell_{\max}=10$	65.24%	96.9%	88.57%	98.89%	91.94%

Table 3: PDs for every observable and combination of them.

- If it falls into the gray region, we may conclude that ΛCDM cannot explain the observed value of $S^{\mathrm{TT,TGW}}_{63^\circ,180^\circ}$. Therefore, we need to find a more comprehensive model that can explain this.
- If it falls inside the green one, we can say that our observation is well explained by our model; however, we cannot say anything more that this (being consistent, the fluke hypothesis remains valid).
- If the measurement is in the red region, we can draw two different conclusions: either the ΛCDM model is unable to describe the observations and the fluke hypothesis can be rejected, or the CGWB signal is not correlated (constrained) to the current measurements of the CMB temperature anisotropies (this indeed is an assumption).
- If the observation falls at the intersection, it could be following the ΛCDM prediction (green curve), preventing us from rejecting the fluke hypothesis.

This reasoning can also be applied to the other fields, or combinations of them, knowing that the distributions at the optimal angle maximize our ability to get useful information from the CGWB.

In conclusion, in Sec. B.4 we show the optimal angles and the distributions in the optimal range assuming the more optimistic cases of $\ell_{\mathrm{max}} = 6$ and $\ell_{\mathrm{max}} = 10$.

10.3.2 *Significance of the anomaly*

Until now, we have explored the fluke hypothesis, finding that GWs can be crucial in rejecting at least some of the assumptions of the ΛCDM model. Despite this, as mentioned above, we cannot conclude anything regarding the actual significance of the anomaly with such an analysis.

At the end of the previous section, we mentioned that in the green region and at the intersection of the green and red of the right central panel of Fig. 28 we cannot draw any meaningful conclusions since the fluke hypothesis still holds.

Here we look at the same problem, but from the perspective of the significance of the anomaly, thus making use of the newly defined estimator in Eq. 356.

Applying this to the SMICA maps, we obtain Fig. 29. We can see that the SMICA is characterized by a low angular covariance irrespective of the angular range considered, since each score consistently lowers than most ΛCDM realizations. In terms of significance, full-sky and masked SMICA correspond, respectively, to 0.82σ and 2.41σ. This confirms what has already been found in the literature; i. e. masking increases the significance of the anomaly, meaning that high-latitude points drive it.

We now apply this reasoning to the CGWB. In this case, the role of data is played by our constrained realizations. The top panels of Fig. 30 show the

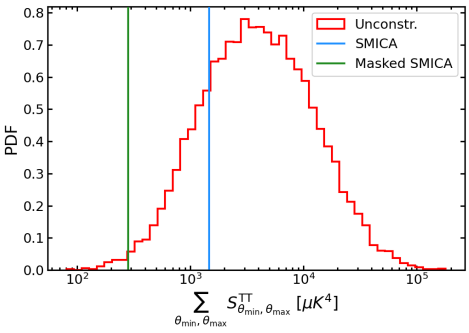

Figure 29: Value of S^{TT} for full-sky and masked SMICA and 10000 ΛCDM realizations of CMB temperature ($\ell_{max} = 4$).

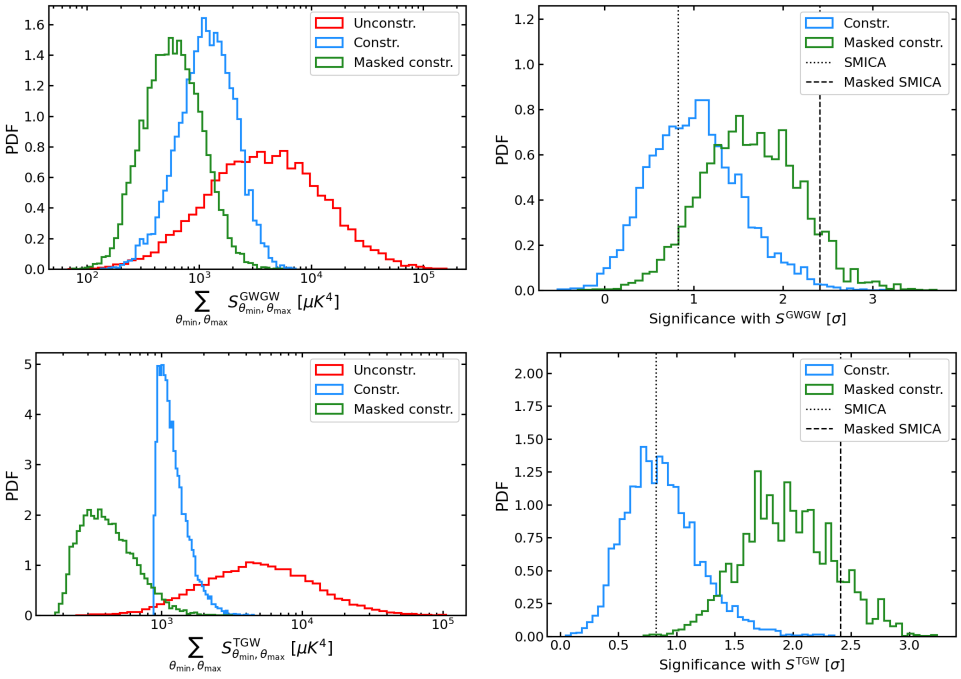

Figure 30: *Top:* values of S^{GWGW} for full-sky and masked constrained realizations of the CGWB and the corresponding significance in terms of σ w. r. t. the unconstrained realizations. *Bottom:* same quantities for S^{TGW}. The dotted and dashed vertical lines indicate the full-sky and masked significance of SMICA alone, respectively.

results; the left panel shows the values of S^{GWGW} and the right panel their significance corresponding to the ΛCDM realizations.

Repeating the procedure for TGW, we obtain the bottom panels of Fig. 30. In addition, in this case, TGW seems to perform similarly w. r. t. GWGW, providing consistent values for the significance. However, both of them essentially fail to increase the significance that one can get from TT.

Going to the joint analyzes, we obtain Fig. 31 for $S^{TT,GWGW}$, $S^{TT,TGW}$ and $S^{TT,TGW,GWGW}$.

Once again, we ask ourselves: how can these results be used in the presence of an eventual measurement of the CGWB? The answer is essentially the same as the one at the end of Sec. 10.3.1, with an important exception. In fact, we already know how to interpret a future observation falling in the red or gray region. However, this time we can associate each constrained realization with a significance in the form of sigma distance. Therefore, the green region corresponds to high-significance realizations (where one can claim that the anomaly is the result of a physical phenomenon), while the intersection corresponds to low-significance ones (where further investiga-

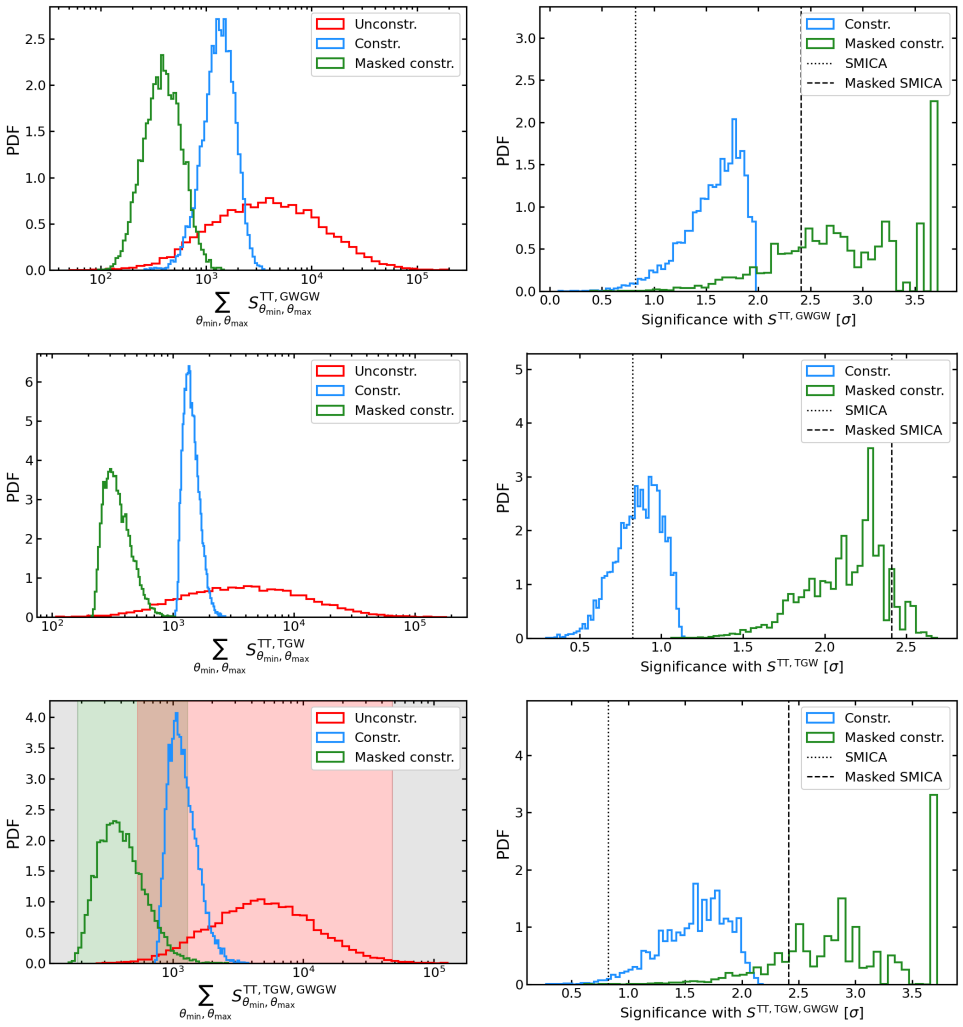

Figure 31: *Top:* values of $S^{TT,GWGW}$ for full-sky and masked constrained realizations of the CGWB and the corresponding significance in terms of σ w. r. t. the unconstrained realizations. *Center:* same quantities for $S^{TT,TGW}$. *Bottom:* same quantities for $S^{TT,TGW,GWGW}$. The vertical lines dotted and dashed indicate the full-sky and masked significance of SMICA alone, respectively.

	Full-sky					
	Signi. S^{SMICA}	S^{GWGW}	S^{TGW}	$S^{\mathrm{TT,GWGW}}$	$S^{\mathrm{TT,TGW}}$	$S^{\mathrm{TT,TGW,GWGW}}$
$\ell_{\mathrm{max}} = 4$	0.82σ	63.13%	52.95%	98.34%	62.93%	98.81%
$\ell_{\mathrm{max}} = 6$	1.3σ	38.49%	39.33%	97.59%	54.59%	98.59%
$\ell_{\mathrm{max}} = 10$	1.18σ	47.15%	45.02%	98.3%	57.67%	99.01%
	Mask-sky					
	Signi. S^{SMICA}	S^{GWGW}	S^{TGW}	$S^{\mathrm{TT,GWGW}}$	$S^{\mathrm{TT,TGW}}$	$S^{\mathrm{TT,TGW,GWGW}}$
$\ell_{\mathrm{max}} = 4$	2.41σ	7.57%	12.34%	72.53%	7.78%	81.67%
$\ell_{\mathrm{max}} = 6$	2.37σ	1.96%	1.23%	81.34%	0.31%	90.11%
$\ell_{\mathrm{max}} = 10$	2.17σ	0.13%	0.46%	58.33%	0.15%	70.08%

Table 4: Percentage of constrained realizations that improve the significance of SMICA, which is shown in the first column.

tion is needed to assess the origin of the anomaly). In other words, having accounted for the look-elsewhere effect allows us to get useful information on all the possible values of the estimator but the intersection.

Talking about the actual results, we summarize them in Tab. 4. Here, we compare the performances of the various combinations of observables by counting how many constrained realizations reach a better significance w. r. t. SMICA alone.

For $\ell_{\mathrm{max}} = 4$, despite what we find in Sec. 10.3.1, the best combination seems to be TT + TGW + GWGW, which achieves the 98.81% and the 81.67% of the constrained realizations, improving the significance of SMICA (full-sky and masked, respectively). Therefore, to determine the actual significance of the anomaly with GWs and to assess the physical origin of the anomaly, it is crucial to observe the autospectrum. In fact, this brings the majority of information when combined with TT, as shown by the last and second to last columns of the Tab. 4.

10.4 SUMMARY AND CONCLUSIONS

Since COBE [32, 202, 207], we have measured a low two-point angular correlation function of the CMB temperature on large scales. This feature has been reassessed both by WMAP [152, 208, 209] and Planck [174, 210, 211] suggesting that it is not the product of some systematic, given that the three experiments are independent in this regard. Still, it is not clear whether the so-called lack-of-correlation anomaly is the product of some non-standard physics or whether it is the manifestation of the fact that we live in a rare realization of the ΛCDM model. Since we already have a cosmic-variance-limited measurement of CMB temperature on low and intermediate scales, this latter possibility has to be explored with some observable other than temperature. An example is the E-mode polarization of CMB photons, which

is correlated with the temperature and can provide new information on the anomaly [193, 212–214]. In this work, we study the ability of the CGWB to shed light on this matter [49, 50, 104, 138, 140, 233]. This is done by exploiting both the autospectrum of the CGWB and its cross-spectrum with CMB temperature (hereby named TGW). In fact, we know that this primordial signal has a great degree of correlation with the temperature of the CMB [187]. Thus, we can produce both constrained and unconstrained realizations of the CGWB using the SMICA temperature map as our CMB observation. Since we know that the lack-of-correlation anomaly is enhanced when the galactic plane is removed [209, 217, 218], this is done while considering both full-sky and masked Planck's SMICA. These maps are smoothed with a Gaussian beam with FWHM $= 2^\circ$ and degraded to $N_{\rm side} = 64$. We have not shown this in the main body of this work, but we also repeated the analysis assuming a smoothing of FWHM $= 0.92^\circ$ (thus the grid scale corresponding to $N_{\rm side} = 64$) and FWHM $= 4^\circ$. As expected, the former case brings some differences caused by pixelization effects, which is why it is usually advisable to smooth maps with a beam two or three times bigger than the grid scale. Instead, the latter produces identical results w. r. t. our choice of 2°, proving that it is sufficiently large. When performing the analysis, we must also take into account that GWs are notably difficult to observe. Thus, we consider three different choices of what the maximum multipole is that we can observe in a signal-dominated way, i. e. $\ell_{\rm max} = 4, 6$ and 10. Depending on the assumption one makes for the monopole radiation of GWs, this can be obtained with one of the future GW interferometers or using a combination of them (for example, LISA [220–224], DECIGO [225], ET [226, 227] and CE [228]).

Summarizing the methodology followed in this chapter, in Sec. 10.2.1 we define the dataset we exploit to perform our analysis, while in Sec. 10.2.2 we generalize the full-sky expression of the constrained realizations to account for the multipole couplings brought by the presence of a mask (see also Sec. B.1). Then, after having defined the key quantity on which the lack-of-correlation manifests, i. e. , the two-point angular correlation function (see Sec. 10.2.3), in Sec. 10.2.4 we follow Copi et al. [212] to define an estimator to quantify the anomaly. In particular, by integrating the two-point angular correlation function (squared) over a certain angular range $[\theta_{\rm min}, \theta_{\rm max}]$, one can define the quantity named $S_{\theta_{\rm min},\theta_{\rm max}}$ for each field considered (in our case TT, TGW, and GWGW). Furthermore, [193] defines an estimator capable of combining those of two different observables. Therefore, in our case, we define three combined estimators $S^{\rm TT,GWGW}_{\theta_{\rm min},\theta_{\rm max}}$, $S^{\rm TT,TGW}_{\theta_{\rm min},\theta_{\rm max}}$, and $S^{\rm TT,TGW,GWGW}_{\theta_{\rm min},\theta_{\rm max}}$, which encode the information of all the observables considered. In Sec. 10.2.5, we follow again Copi et al. [212], to define a way to maximize the amount of information that we can obtain by adding CGWB to the estimate. In particular, computing the constrained and unconstrained realizations of the CGWB (considering both the full-sky and the masked version of SMICA), we count how many unconstrained realizations can recover higher values of $S^{\rm GWGW}_{\theta_{\rm min},\theta_{\rm max}}$ w. r. t. the 99th percentile of the constrained ones.

This defines what we call the PD of the two distributions. When this PD is maximal, we can say that the CGWB is as sensitive as possible to what is observed in the CMB (in terms of lack of correlation). The specific angular range found is named the "optimal angular range". The same procedure is also performed for $S^{\mathrm{TGW}}_{\theta_{\mathrm{min}},\theta_{\mathrm{max}}}$, $S^{\mathrm{TT,GWGW}}_{\theta_{\mathrm{min}},\theta_{\mathrm{max}}}$, $S^{\mathrm{TT,TGW}}_{\theta_{\mathrm{min}},\theta_{\mathrm{max}}}$ and $S^{\mathrm{TT,TGW,GWGW}}_{\theta_{\mathrm{min}},\theta_{\mathrm{max}}}$. Finally, in Sec. 10.2.6 we define a new estimator for the lack-of-correlation which takes into account the so-called look-elsewhere effect. Indeed, to study the significance of the anomaly, we must find a way to marginalize the angular-range information so that we recover the anomaly irrespective of the particular range. In this way, we are able to provide a forecast of the improvement brought about by the CGWB in terms of the significance of the lack-of-correlation anomaly.

Summarizing now the results, in Sec. 10.3.1 we report the results for the optimal angular ranges. We find that, in general, passing from the full-sky treatment to the masked treatment increases the PDs obtained. This confirms that the anomaly seems to increase in significance together with the angle from the galactic plane. In addition, when considering one field at a time, TGW seems to be a consistently better probe to test the fluke hypothesis w. r. t. GWGW. Furthermore, using different combinations of fields, we show that TT + TGW is the best combination to test the fluke hypothesis. In fact, even in the most pessimistic case of $\ell_{\mathrm{max}} = 4$ we obtain a PD of 96.41% in the optimal angular range $[63^\circ, 180^\circ]$ (see Tab. 2 and Tab. 3). This PD can be compared with the ones in [212] regarding E-mode polarization, showing that GWs are actually much more restrictive in testing the fluke hypothesis. As discussed in Sec. 10.3.1, this means that this combination of observables is extremely good for testing this hypothesis, maximizing the probability of rejecting the ΛCDM model in the event that a future observation happens to be outside the distribution shown in Fig. 28, with the corresponding level of significance. Regarding the comparison with different assumptions on ℓ_{max}, we note that the best results in terms of PDs are obtained with $\ell_{\mathrm{max}} = 6$, suggesting that the lack of correlation signal lives in the first six multipoles (see Sec. B.4 for the plots). Overall, we also show that there always seems to be a high-PD region near the range where the original $S_{1/2}$ estimator is defined [203]. As mentioned in Sec. 10.3.1, another interesting feature of this analysis is depicted in Tab. 3: the masked case seems to give more consistent results in terms of PDs against a change of ℓ_{max} or used probes. Indeed, there seems to be a fixed order of probes at each ℓ_{max} when we rank them for ascending PD. This does not hold for the full-sky case. Then, one might argue that the masked sky provides a more faithful representation of reality due to its stronger consistency. Another feature emerges when changing the ℓ_{rmmax} of the analysis (see Sec. B.4) Indeed, increasing the number of multipoles acts in different ways on the optimal regions: the GWGW realizations start concentrating towards the $\approx 75^\circ$ scale and the TGW abandon $\theta_{\mathrm{max}} \simeq 180^\circ$ in favor of $\approx 130^\circ$. Hence, the various combined estimators report a combination of the preferred regions of the two, or three, probes involved.

In Sec. 10.3.2, we show the results for the actual significance of the anomaly. Firstly, when applying our newly defined estimator to the CMB temperature alone, we obtain a significance of 0.82σ and 2.41σ for full-sky and masked SMICA respectively. This confirms that masking the sky greatly enhances the significance of this anomaly (in our case of a factor three). Also, Tab. 4 shows the significance of TT alone when increasing the number of multipoles. It peaks at $\ell_{\max} = 6$, suggesting in accordance with the optimal angular range analysis that the anomaly lives in that multipole range. Focusing then on the CGWB contributions, despite what we find analyzing the optimal angular ranges, we point out that the autospectrum GWGW is crucial to obtain a good level of significance when including a CGWB observation. The best results in this sense are given by the full combination TT + TGW + GWGW, which provides 98.81% (81.67%) of the realizations improving the current significance w. r. t. full-sky (masked) SMICA (see Tab. 4). Unlike what we could conclude with the analysis of optimal angles alone, using the new estimator for the significance, not only can we reject the ΛCDM model if a measurement of the CGWB falls outside the predicted distribution, but also we can associate an actual significance to a measurement following those curves. Comparing again different assumptions on $\ell_{\max}$ and focusing on the full combination of observables, the significance remains fairly stable in all cases in the full-sky case. Also, we observe that the constrained realizations of GWGW and TGW are always centered on the significance of SMICA alone (see Sec. B.4). For the masked case, the results are behaving more complexly. Starting from $\ell_{\max} = 6$, having included two extra multipoles seems to act as we expect, assuming that the anomaly lives in the first six multipoles as our analysis suggests. Indeed, comparing the S-estimator distributions with the results shown in the main body for $\ell_{\max} = 4$, they appear to be in the same relative position w. r. t. the unconstrained realizations, but with a shrunken dispersion (resulting in more peaked histograms). Thus, the same "anomalous signal" is present and gets better constrained by the higher number of multipoles. This is also testified by the increase in the significance obtained (see Tab. 4). When considering the case of $\ell_{\max} = 10$, the situation gets flipped over. The S-estimator distributions approach tends to move toward the mean of the unconstrained distribution (even getting superimposed to the full-sky case for GWGW alone), resulting in an overall loss of significance. Together with the optimal range analysis and the significance of TT alone, this suggests the following interpretation: if the anomaly actually lives in the first six multipoles, we may expect that including more and more non-anomalous multipoles should decrease the significance since these would distribute as the ΛCDM ones. In other words, since we are summing over the considered multipole range (see eq. (351)), these new multipoles are pushing the overall distribution toward the standard behavior.

Here, we use `NaMaster` to compute the angular power spectrum of masked skies (see Sec. 10.2.1). In particular, this approach is applied whenever we need the spectrum of masked SMICA to compute the estimators or when we need to compute the spectrum of TGW while masking the CMB sky. Al-

though this provides an unbiased estimate of the spectra, it does not minimize their variance. For this reason, it would be interesting to explore this anomaly with an analogous analysis employing some maximum likelihood estimator, which instead allows one to get a minimal variance estimate of the spectra [215, 234, 235].

Another interesting aspect to explore in the time ahead has been emphasized by Hansen et al. [236]. They show the evidence of the presence of an extra-galactic foreground on top of the CMB temperature data. Indeed, if their claim is found to be correct, it would mean that the variance measured on large scales is actually enhanced by this signal. Therefore, mitigating this foreground from our maps would bring the variance of the first CMB multipoles even lower than its current value, suggesting that the significance of the lack-of-correlation anomaly might increase (even assuming TT alone). By extension, if this hypothesis is correct, the CGWB might become crucial to boost the significance to the level of an actual tension. In fact, in Sec. 10.3.2 we show that in some cases the CGWB is expected to provide a significance near the 4σ level, even with current data.

Concluding, here we just consider the CMB temperature and the CGWB. Instead, we know that CGWB also shares a correlation with E-mode polarization [187, 198]. Thus, this framework can be extended to all three of them. In this context, future experiments such as Lite (Light) satellite for the studies of B-mode polarization and Inflation from cosmic background Radiation Detection (LiteBIRD) [237] could be crucial to finally assess the physical origin of this anomaly, given that LiteBIRD is expected to be fully cosmic-variance-limited on the large-scale polarization [238].

Part IV

STATISTICS AND DATA ANALYSIS

In this part of the Thesis, our focus shifts towards delving into the methodologies employed for data analysis in Cosmology. We introduce two key techniques that play pivotal roles in Bayesian and frequentist approaches: the Markov-Chain Monte-Carlo (MCMC) analysis and the Profile Likelihood (PL) analysis. These complementary methods are united by a critical element known as the "Likelihood". The MCMC analysis provides a powerful Bayesian perspective on exploring parameter space, allowing us to derive meaningful insights from our data. Simultaneously, the PL analysis, a cornerstone of the frequentist approach, offers an independent means of scrutinizing the same data, ensuring robust and unbiased conclusions, particularly for parameters with less stringent constraints. Our investigation focuses on the tensor sector of the parameter space, where we apply both MCMC and PL techniques. By presenting the results of these analyses, we aim to offer a comprehensive understanding of the tensor sector and underscore the importance of employing various statistical tools to gain insights into the complexities of the Cosmos.

11

BAYESIAN STATISTICS

BAYESIAN statistics, alongside the frequentist approach, constitutes a fundamental component of data analysis, particularly in Cosmology. In this section, we provide an overview of the basics of Bayesian statistics and introduce the Markov Chain Monte Carlo (MCMC) technique. The MCMC method is widely used in Cosmology to extract parameter information from datasets.
For further insights, consult [239].

11.1 BASICS

In the pursuit of scientific understanding, we endeavor to assign a numerical measure to our confidence in a hypothesis encapsulated within the spectrum of real numbers from 0 to 1. This numerical representation signifies the probability that the hypothesis is true, a fundamental concept in the realm of scientific reasoning [240].
Consider two statements X and Y and some set of available information I. The Bayes theorem states

$$\text{prob}(\text{X}|\text{Y},\text{I}) = \frac{\text{prob}(\text{Y}|\text{X},\text{I})\text{prob}(\text{X}|\text{I})}{\text{prob}(\text{Y}|\text{I})} \ . \tag{357}$$

It is trivial to generalize this statement to a set of propositions whose degree of belief is summarized by $\text{prob}(A, B, C, \ldots|I)$. We might be interested in one of these propositions regardless of the others; this leads to a procedure named *marginalization*: if now we call X the hypothesis we are interested in and Y_k with $k = 1, \ldots, N$ the rest[79], the marginalization procedure reads as follows:

$$\text{prob}(\text{X}|\text{I}) = \sum_{\text{k}=1}^{\text{N}} \text{prob}(\text{X}, \text{Y}_\text{k}|\text{I}) \ . \tag{358}$$

If instead the alternatives are a continuum of values (such as the values of a parameter), marginalization is recast to

$$\text{prob}(\text{X}|I) = \int_{y_1}^{y_2} \text{PDF}(\text{X}, \text{Y}|\text{I}) dy \ , \tag{359}$$

79 Which we assume to be exclusive and mutually exclusive.

where the Probability Density Function (PDF) is

$$\mathrm{PDF}(\mathrm{X}, \mathrm{Y} = y|I) \equiv \lim_{\delta y \to 0} \frac{\mathrm{PDF}(\mathrm{X}, y - \delta y \leq \mathrm{Y} \leq y + \delta y|\mathrm{I})}{\delta y} \tag{360}$$

and we assume $\mathrm{y}_1 \leq \mathrm{Y} \leq \mathrm{y}_2$.

If now we substitute

$$\mathrm{Y} \rightarrow \text{Data from an experiment} \tag{361}$$
$$\mathrm{X} \rightarrow \text{Hypothesis that we want to probe} \tag{362}$$
$$\mathrm{I} \rightarrow \text{Theory providing some preliminary information ,} \tag{363}$$

we can rewrite Eq. 357 as

$$\mathrm{prob}(\text{Hypo.}|\text{Data}) = \frac{\mathrm{prob}(\text{Data}|\text{Hypo.})\mathrm{prob}(\text{Hypo.})}{\mathrm{prob}(\text{Data})} , \tag{364}$$

where: $\mathrm{prob}(\text{Hypo.}|\text{Data}) \equiv P(h|d)$ is the posterior distribution;
$\mathrm{prob}(\text{Data}|\text{Hypo.}) \equiv \mathcal{L}(d|h)$ is the Likelihood distribution;
$\mathrm{prob}(\text{Hypo.}) \equiv \Pi(h)$ is the prior distribution;
$\mathrm{prob}(\text{Data}) \equiv \mathcal{E}(d)$ is the evidence distribution.

This encapsulates the essence of Bayesian analysis, where we explore the probability associated with a parameter adopting a specific value, taking into consideration the information provided by the available data.

11.2 AN APPLICATION: PARAMETER ESTIMATION

Let us consider an example of a parameter estimation problem, the classic coin toss.

We toss a coin N times and get M heads. Is the coin fair or not? The likelihood is a binomial distribution:

$$\mathcal{L}(\text{Data}|H, \mathrm{I}) \propto H^{\mathrm{M}}(1 - H)^{\mathrm{N}-\mathrm{M}} , \tag{365}$$

where H is the probability to get a head and $H = 0.5$ defines a fair coin.

What about the prior? If we are in a dodgy casino, we may be suspicious of the coin and choose a uniform prior between $H = 0$ (two-tailed coin) and $H = 1$ (two-headed coin), and we assign a null probability otherwise ($H < 0$ or $H > 1$). If instead we are playing with a trusted friend, we may choose a prior peaked around $H = 0.5$, e. g. a Gaussian with some σ.

This last paragraph may sound strange to the most frequentist-minded readers. Indeed, we want to apply this reasoning to science, so any subjectivity seems at least problematic. This is a characteristic feature of Bayesian statistics, where we may expect different answers from different prior beliefs, and we must live with it (this concept is crucial to understand Chap. 13). Despite this, if our problem is well defined, we expect that two observers start-

ing from the same prior will end up with the same posterior (in the limit of many tosses). Furthermore, if the data provide enough information, we expect them to "dominate" the posterior anyway, even starting from different priors.

Going back to our tossing problem and choosing the uniform prior, we can now write our posterior as

$$\begin{cases} P(H|\text{Data,I}) \propto H^{\text{M}}(1-H)^{\text{N}-\text{M}} & 0 \leq H \leq 1 \\ P(H|\text{Data,I}) = 0 & \text{otherwise} \end{cases} . \tag{366}$$

Note that we ignored $\mathcal{E}(\text{Data})$ since it is just a normalization constant.

In a pure Bayesian framework, Eq. 366 represents the solution of the problem; however, we would not be satisfied with that. In fact, we would like to provide an estimate of H and an error bar. The most common estimator for H is the maximum of the posterior, i. e. the value H_0 for which the following holds

$$\left.\frac{\mathrm{d}P}{\mathrm{d}H}\right|_{H_0} = 0 \quad \text{and} \quad \left.\frac{\mathrm{d}^2P}{\mathrm{d}H^2}\right|_{H_0} < 0 \, . \tag{367}$$

Note that if the prior is flat, it can be treated as a normalization constant and $P \propto \mathcal{L}$; thus, this procedure would also lead to the maximum of likelihood.

To obtain the error bar, the most common procedure is to look at the posterior curvature at maximum. Working with the logarithm of P, we can write

$$\begin{aligned} \log P(H) &= \log P(H_0) \\ &\quad + \left.\frac{\mathrm{d}\log P(H)}{\mathrm{d}H}\right|_{H_0} (H-H_0) + \frac{1}{2}\left.\frac{\mathrm{d}^2\log P(H)}{\mathrm{d}H^2}\right|_{H_0} (H-H_0)^2 + \dots \\ &= \log P(H_0) + \frac{1}{2}\left.\frac{\mathrm{d}^2\log P(H)}{\mathrm{d}H^2}\right|_{H_0} (H-H_0)^2 \, , \end{aligned} \tag{368}$$

where we exploit the fact that the first derivative is null at the maximum and we truncate the Taylor expansion at the second-order. This means that we can write

$$P(H) \propto \exp\left\{ \frac{1}{2}\left.\frac{\mathrm{d}^2\log P(H)}{\mathrm{d}H^2}\right|_{H_0} (H-H_0)^2 \right\} , \tag{369}$$

which is a Gaussian distribution. Hence, truncating to the leading term in the expansion amounts to approximating the posterior distribution as a Gaussian, whose error bar is

$$\sigma = \left(- \left. \frac{\mathrm{d}^2 \log P(H)}{\mathrm{d}H^2} \right|_{H_0} \right)^{-1/2} . \tag{370}$$

Note that of course one has to be careful and check whether this is a suitable approximation for the specific problem under study. For example, this approach fails in the case of an asymmetric or multimodal posterior distribution. Note also that often in the literature one reports the mean of the posterior instead of its maximum. Of course, in the Gaussian case those coincide, however for very skewed distributions they give different information. Indeed, the maximum of the distribution represents the most probable value of the parameter of interest, while the mean is the expectation value of the parameter given its PDF (the 1D posterior). Thus, for very non-Gaussian distributions, it may be wiser to report solely a credible interval (see Sec. 11.3.2).

Furthermore, the same procedure to obtain an estimate of H applied to the likelihood distribution brings the equivalent formulas for the maximum likelihood estimate, where the error bar is the Fisher error. In other words, in such a case maximizing the likelihood is the same as minimizing a chi-squared.

Concluding this application, it can be shown that in our tossing example, the best estimate of H_0 and its error bar are

$$\widehat{H}_0 = \frac{\mathrm{M}}{\mathrm{N}} \quad \text{and} \quad \sigma = \sqrt{\frac{H_0(1-H_0)}{N}} , \tag{371}$$

as we may have expected from the beginning.

Before proceeding, we could have considered an arbitrarily difficult problem here to showcase this procedure. This simple approach to get the best estimate and the error bar still holds if:

1. the variable considered is Gaussian,
2. data are independent,
3. the model for the parameter is linear.

For example, if these conditions are not attained, it is not guaranteed that truncating the posterior to second-order is a good approximation. Furthermore, even if we find a problem in which conditions are respected, it can be analytically challenging (or even impossible) to solve the problem, especially if marginalization is involved[80]. For these reasons, we would like to have a method to sample numerically the posterior. The way forward is the MCMC technique [241–245].

80 Even a seemingly simple function can become a nightmare to integrate multiple times over different parameters.

11.3 THE MARKOV-CHAIN MONTE-CARLO TECHNIQUE

Let us recall the problem we want to solve. We know that

$$P(\vec{\theta}|\vec{D}, I) = \frac{\mathcal{L}(\vec{D}|\vec{\theta})\Pi(\vec{\theta}|I)}{\int \mathcal{L}(\vec{D}|\vec{\theta})\Pi(\vec{\theta}|I)d\vec{\theta}}\,, \tag{372}$$

where: $\vec{\theta}$ = vector of parameters of our model;
$\vec{D}$ = vector of data from some experiment;
$\mathcal{E}(\vec{D}) = \int \mathcal{L}(\vec{D}|\vec{\theta})\Pi(\vec{\theta}|I)d\vec{\theta}$.

Both $P(\vec{\theta})$ and the marginalization procedure are often impossible to describe analytically. In real life, we could have up to 10^6 parameters on which to marginalize.

The idea of a MCMC is that you produce a random walk in the parameter space; starting from some value $\vec{\theta}_0$, you move to $\vec{\theta}_1$ with some prescription to perform the step $\vec{\theta}_0 \to \vec{\theta}_1$. Repeating the process N times, you end up with

$$\left\{\vec{\theta}_0, \vec{\theta}_1, \dots, \vec{\theta}_t, \vec{\theta}_{t+1}, \dots, \vec{\theta}_N\right\}. \tag{373}$$

If a certain set of "rules" is respected, after a transient the points are sampled from the posterior distribution.

Going through these rules and theorems is outside the scope of this Thesis, however, we mention the main steps to achieve our final goal.

NO MEMORY A sequence of random variables on a discrete state space Ω is a Markov chain if the probability that the random variable at step t (x_t) assumes the state s_t depends only on the previous step of the chain:

$$P(x_t = s_t|x_{t-1} = s_{t-1}, x_{t-2} = s_{t-2}, \dots) = P(x_t = s_t|x_{t-1} = s_{t-1})\,. \tag{374}$$

This means that a Markov chain is memoryless, since knowledge of the full past is irrelevant in determining the next step.

HOMOGENEITY We define *transition probability*

$$P(x_t = s_t|x_{t-1} = s_{t-1}) \qquad \forall(s_{t+1}, s_t) \in \Omega \times \Omega\,. \tag{375}$$

A Markov chain is *homogeneous* if the transition probability between two states depends only on the initial and final state, and not on "time" t.

ERGODICITY A Markov chain is *ergodic* if any state can be reached from any other state (not necessarily in one step).

STATIONARY DISTRIBUTION A *stationary distribution* of a Markov chain is a distribution $p(\vec{x})$ in the space of states for which

$$P(\vec{y}) = \sum_{x \in \Omega} P(\vec{y}|\vec{x}) P(\vec{x}) \tag{376}$$

A state is also *recurrent* if there is a probability 1 that after leaving it, we will return to that state. On the contrary, the state is said to be *transient*. Furthermore, a recurrent state can be said *positive* or *null* if the expected return time is finite or infinite, respectively.

LIMITING DISTRIBUTION The probability distribution to which the chain converges after an infinite number of steps is called *limiting distribution*:

$$\lim_{n \to \infty} P(x_n = s_n | x_0 = s_0) \ . \tag{377}$$

CONVERGENCE A Markov chain does not necessarily admit a limiting distribution, but a finite, ergodic, positive recurrent and aperiodic Markov chain always converges to a limiting distribution as $n \to \infty$. This distribution is also the stationary distribution.

DETAILED BALANCE Calling P the transition distribution, a Markov chain is reversible if there exists a probability distribution π in the space of states Ω such that

$$P(x|y)\pi(y) = P(y|x)\pi(x) \ . \tag{378}$$

This relation is called *detailed balance* and a reversible Markov chain has a stationary distribution given by π.

Finally, we have all the ingredients we need to build a MCMC. Indeed, now we can find a suitable reversible chain, using the detailed balance equation, which converges to the posterior.

In Cosmology, the main algorithms are the Metropolis-Hastings algorithm [241, 246, 247], the Gibbs sampling [248–251], and the Hamilton sampling [252, 253]. Here, we just show briefly the idea behind the first one.

11.3.1 *Metropolis-Hastings algorithm*

Looking at Eq. 372, we call $\widetilde{P}(\vec{\theta})$ the numerator of the RHS, which is the only interesting part in a parameter estimation problem. Starting from an initial state $\vec{x}_0$, we recursively update the state as follows: call $\vec{x}_t$ the parameter vector at time t. Consider a proposal transition probability Q and generate a new vector $\vec{y}$ such that

$$\vec{y} \sim Q(\cdot|\vec{x}_t) \ . \tag{379}$$

Now you accept or reject the new value $\vec{y}$ with the following probability:

$$\alpha(\vec{x}_{t+1} = \vec{y}|\vec{x}_t) \equiv \min\left\{1, \frac{\widetilde{P}(\vec{y})Q(\vec{x}|\vec{y})}{\widetilde{P}(\vec{x})Q(\vec{y}|\vec{x})}\right\} . \tag{380}$$

If $\vec{y}$ is rejected, repeat the process from $\vec{x}_t$, otherwise move to $\vec{x}_{t+1}$ and repeat.

It can be shown that, assuming ergodicity, the Markov chain generated with the Metropolis-Hastings algorithm is reversible and has the posterior as a stationary distribution [239].

11.3.2 *Bayesian Intervals*

Whatever algorithm we choose to use, in the end we will have a series of points in parameter space that we can marginalize just by building histograms on the parameter of interest. Name θ the parameter, and we would have a function $P(\theta|D)$ describing the marginal probability distribution. Thus, we can build Bayesian interval (or credible interval) with a certain level of significance α finding the values $\left[\theta_{lo}, \theta_{up}\right]$ that satisfy

$$\alpha = \int_{\theta_{lo}}^{\theta_{up}} P(\theta|D)d\theta . \tag{381}$$

This computation does not provide a unique solution, thus one needs to choose a prescription to obtain an interval. One of the available methods is to start from the maximum and find the requested integral value by drawing horizontal lines on the posterior and taking the 2 intersecting points as the extremes of integration. This method will automatically shift from one-tail and two-tail credible intervals and is used for example by the well-known `getdist` package [254].

If a physical boundary is present, e. g. θ cannot be negative, this information is naturally embedded in the prior definition which could be

$$\Pi(\theta) = \begin{cases} 0 & \theta < 0 \\ 1 & \theta \geq 0 \end{cases} . \tag{382}$$

This procedure is now very simple thanks to the MCMC and also the interpretation of the limits obtained is also quite simple. In Bayesian statistics, the parameters are treated as random variables, therefore the boundaries are really a statistical statement on the true value of θ: if we repeat the experiment N times, in α% of the experiments we would find θ inside the interval.

Despite this, in the following section we will show that there are some subtleties to take into account in the Bayesian case.

11.4 PITFALLS OF MCMC

We want to spend some words on the issues that one could encounter when employing such a technique.

For example, even if we say that a MCMC solves the problem of analytically describing the posterior, it is not trivial at all to make the chain converge. Computationally speaking, this is a demanding process that can potentially last forever if it is not properly set. For example, a crucial aspect is the choice of the proposal transition probability: the more we choose it similar to the final posterior, the faster the chain is to converge. Another key ingredient in this context is the degeneracy between parameters, which can make convergence hard to achieve (different algorithms behave differently in this regard). Even in the ideal case, where we properly choose every aspect of the proposal probability, the chain can take several days (or weeks) to fully converge.

Furthermore, we mention that a certain degree of subjectivity in Bayesian statistics is brought by the choice of the prior. However, we could try to make it as objective as possible with a set of rules. For example, we could consider the *Jeffreys' prior* defined as

$$\Pi(\theta) \propto \sqrt{\det(I(\theta))}\,, \tag{383}$$

where

$$I_{ij} = -\left\langle \frac{\partial^2 \ln P(D|\theta}{\partial\theta_i \partial\theta_j} \right\rangle \tag{384}$$

is the Fisher information. One can show that the Jeffreys prior is invariant under reparametrization of parameters.

Another notable example is the *reference prior*. We define the Kullback-Leibler divergence as

$$D_n[\Pi, P] = \int P(\theta|D) \ln \frac{P(\theta|D)}{\Pi(\theta)} d\theta\,, \tag{385}$$

which represents the gain in information provided by data. In other words, this measure the increase of information passing from describing some phenomenon with prior knowledge $\Pi(\theta)$ to the posterior $P(\theta|D)$, which, of course, takes advantage of having some informative data. The reference prior is chosen to maximize $\langle D_n[\Pi, P]\rangle$.

Despite this, some prior dependence might still be present even in the most sophisticated prior selection (as stated previously, this is just a characteristic of Bayesian analysis that we must deal with). Furthermore, often one chooses a simple constant prior not because it actually represents the actual prior belief on the parameter, but because it allows one to produce intervals whose frequentist properties can be studied. In fact, remember that if the prior is chosen to be flat, $P(\theta|D) \propto \mathcal{L}(D|\theta)$.

We conclude with an important remark: of course, Bayesian statistics is fully consistent and robust, and these effects do not pose any intrinsic problem to this framework or to the interpretation of the results. For every prior we choose, the final posterior will still represent the most probable region of parameter space given the data we have and the assumptions we make. However, we must be aware that different prior choices may affect our final results, so we must be clear about this dependence. For example, repeating the analysis with multiple choices provides a transparent view of the problem being studied.

12 FREQUENTIST STATISTICS

Together with Bayesian statistics, frequentist statistics completes the toolbox for data analysis and model inference. As demonstrated in Chap. 11, MCMC analysis may be influenced by prior choices and volume effects. In contrast, the frequentist approach provides an analysis that is independent of both. However, caution is warranted when comparing the outcomes of these two complementary methodologies, as they yield different insights from the same dataset.
This chapter, primarily drawing from [255] and the Particle Data Group (PDG)[81], introduces fundamental concepts of hypothesis testing in a frequentist context. Our objective is to present the PL technique as an alternative to MCMC. PL has gained significant traction in Cosmology, especially when exploring extensions beyond the standard ΛCDM model to more exotic and unconstrained scenarios.

12.1 VOLUME EFFECTS ON BAYESIAN STATISTICS

There is a subtle problem as to how we can interpret the results of a MCMC. In a multidimensional problem, if a large part of the probability volume is in a certain area, the final posterior will be drawn towards that region just as a result of the marginalization procedure that is performed when the result is given on a single parameter [256]. An example is a "Pinocchio-shaped" posterior as shown in Fig. 32 [257]. In fact, there is a large region of relatively low probability around $\theta_1 = 2$ and a small region with high probability around $\theta_1 = 7$. When marginalizing over θ_2, Nygaard et al. [257] obtain the blue line of the top panel. However, if instead they plot the maximum of the likelihood for each value of θ_1 they obtain the red one. It is clear that the two lines are pushing us to very different conclusions about the parameter. These effects on the PDF resulting from marginalization are commonly called *volume effects*. As the dependence on the prior (see Chap. 11), these are not internal issues of the Bayesian statistics, which is still a robust framework, but rather a feature that must be understood and properly characterized.

The second procedure shown in Fig. 32 is called PL, which is the main topic of this chapter. However, before jumping to its definition we must introduce some important concept of frequentist statistics.

12.2 HYPOTHESIS TESTING

Consider a generic hypothesis H_0; a frequentist test of H_0 is a rule that tells us for which data x we can reject H_0. We can also define a region ω of the

81 https://pdg.lbl.gov/.

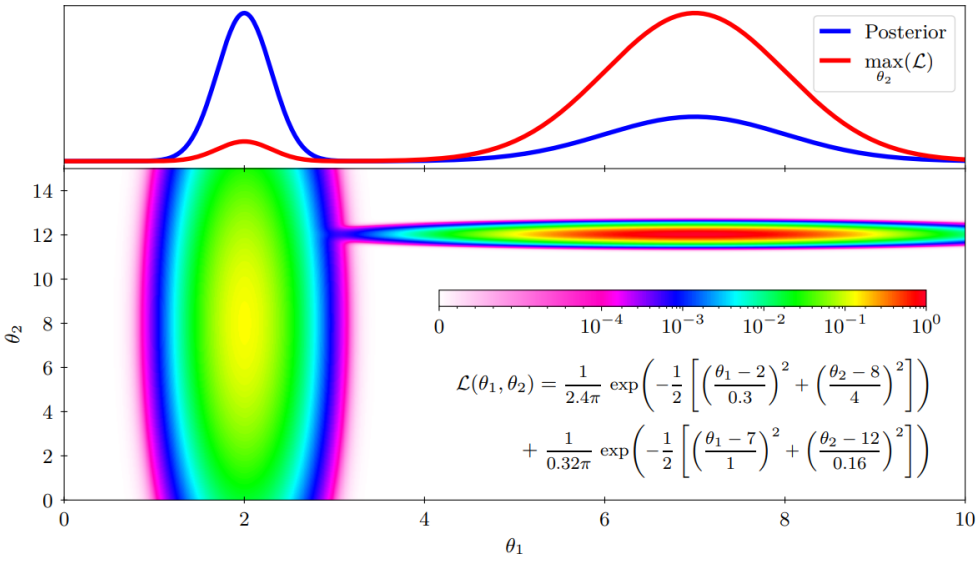

Figure 32: Example of a posterior which brings to volume effects when marginalization is applied. Figure extracted from [257].

data space where the probability is under a certain *significance level* α such that

$$P(x \in \omega | H_0) \leq \alpha \, . \tag{386}$$

Say now that H_0 is some null hypothesis for a certain signal to be observed and H_1 represent instead a detection. How can we claim a detection, i. e. reject H_0?

We can use the *Neyman-Pearson lemma* to maximize the "rejection power" of a test; in fact, the lemma states that the region ω should be chosen in such a way that

$$\lambda(x) = \frac{f(x|H_1)}{f(x|H_0)} > c_\alpha \qquad \forall x \in \omega \, , \tag{387}$$

where: c_α = is a value determined from the significance level α;
$f(x|\cdot)$ = PDF of the data given a hypothesis.

At this point, it is also convenient to define a *test statistic* of data $t(x)$ as a scalar function of the data in such a way that the boundary of the region ω is a constant surface $t(x)$. In fact, another way to define the Neyman-Pearson lemma is to say that Eq. 387, which is essentially a likelihood ratio, represents the optimal test statistic [255]. Despite the apparent simplicity of these definitions, as mentioned in Chap. 11, it could be difficult to work analytically with such objects, so often one moves to some Monte-Carlo approach.

To quantify the agreement of some data with a hypothesis, say H_0, we can use the *p-value*, defined as the probability of finding some statistic t in the region of less compatibility with H_0 w. r. t. to the value in the observed data

t_{obs}. E. g. if we consider a situation in which the bigger is t the poorer the compatibility with H_0 becomes, we can write the p-value as

$$p = \int_{t_{obs}}^{\infty} f(t|H_0)dt \ . \tag{388}$$

Often, one converts this number into a significance Z by computing the amount of standard deviations of a Gaussian random variable that brings you to the observed value:

$$Z = \Phi^{-1}(1-p) \ , \tag{389}$$

where Φ is the cumulative distribution of a standard Gaussian.

12.3 DEALING WITH NUISANCE PARAMETERS

Up to now, we have worked with an underlying assumption: H_0 and H_1 must be simple hypothesis, which for example do not depend on other undetermined parameters. Suppose now that we want to test some hypothetical value of a parameter θ, but the model contains a nuisance parameter ν. Assuming the same definition of the p-value as before and a test statistic q_θ, we can write

$$p_\theta(\nu) = \int_{q_\theta^{obs}}^{\infty} f(q_\theta|\theta, nu)dq_\theta \ , \tag{390}$$

which of course depend on the value of ν. In a frequentist environment, θ is rejected if the p-value is less than α *for all* values of ν. This is solved if we manage to find a q_θ independent of ν, however, this is not easy to achieve. An approximate solution is given by the PL ratio. Firstly, we define the PL: assuming to have a likelihood $\mathcal{L}(\theta, \nu)$, i. e. a function of both θ and ν, the PL on θ is given by

$$\mathcal{L}_p(\theta) = \max_\nu \mathcal{L}(\theta, \nu) \ . \tag{391}$$

In other words, for each value of θ, the value of ν is chosen to maximize the function $\mathcal{L}$, leaving in the end a function $\mathcal{L}_p$ which depends only on the profiled parameter.

The PL ratio in given by

$$\lambda_p(\theta) = \frac{\max_\nu \mathcal{L}(\theta, \nu)}{\max_{\theta,\nu} \mathcal{L}(\theta, \nu)} \ , \tag{392}$$

so the ratio of the PL and the absolute maximum of the likelihood. Provided that certain conditions are satisfied, Wilks' theorem states that $-2\ln\lambda_p(\theta)$ follows a χ^2 distribution in the limit of a large data sample and independent of the values of ν. In a real application, e. g. with a finite sample, θ will retain

some dependence on ν, which will cause some deviation from the behavior of χ^2 (see Chap. 14).

12.4 INTERVALS

As mentioned in Chap. 11, to obtain some results from an experiment, we would like to report an estimate of θ as $\widehat{\theta} \pm \sigma_\theta$. With distributions that are not Gaussian or if there are physical boundaries on the values of θ, this may not be possible; therefore, we need a way to extract *confidence intervals*. In Sec. 11.3.2 we showed the procedure to obtain the Bayesian intervals, or credible intervals; instead, here we show the frequentist equivalent.

The procedure here is slightly more involved due to the nature of frequentist intervals: in fact, now the true value parameters is not a random variable, but rather fixed values that nature choose. Thus, the boundaries obtained from a set of data are specific for the experiment considered and represent the random variable in this case. Repeating the experiment would cause these bounds to fluctuate. In this context, the *coverage probability* refers to the fraction of intervals that contain the true value of the parameters among the N different repetitions of the experiment. The confidence intervals are then determined to have a coverage probability greater than or equal to a certain CL.

12.4.1 *Neyman Construction*

As before, consider some data x and their PDF $f(x|\theta)$, where θ is some parameter. Once we fix a significance level α, we can find, for each value of θ, an interval $[x_1(\theta, \alpha), x_2(\theta, \alpha)]$ such that

$$\text{prob}(x_1 < x < x_2|\theta) = \int_{x_1}^{x_2} f(x|\theta)dx \geq \alpha \, . \tag{393}$$

Repeating this process for a set of values of θ and drawing each segment $[x_1, x_2]$ in a plot, we can find the so-called *confidence belt* (see Fig. 33).

Performing an experiment means having a measured value of $x = x_0$, thus the confidence interval of θ is found by drawing a vertical line at x_0 in that plot. In fact, the interval consists of all values of θ for which the corresponding segment $[x_1(\theta, \alpha), x_2(\theta, \alpha)]$ is intercepted by the vertical line. Suppose that the true value of θ is θ_0; Fig. 33 shows that

$$\theta_0 \in [\theta_1(x), \theta_2(x)] \iff x \in [x_1(\theta_0), x_2(\theta_0)] \, . \tag{394}$$

Once again, if we repeat the experiment, $[\theta_1, \theta_2]$ would change but would cover the true value with the requested level of significance.

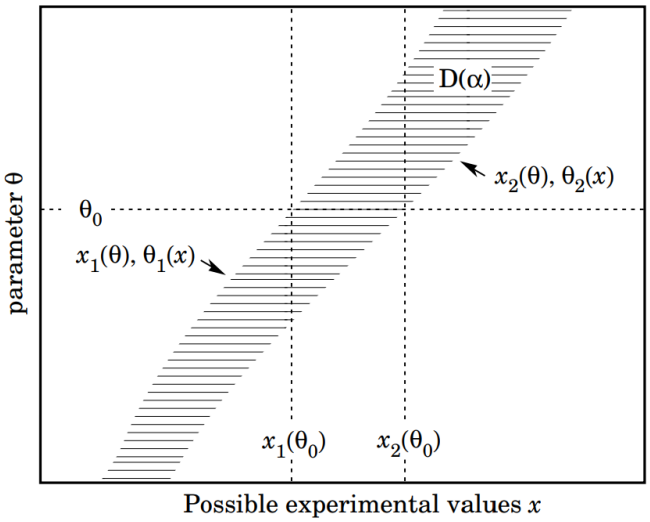

Figure 33: Example of confidence belt constructed à la Neyman. Figure extracted from [255].

12.4.2 *Feldman-Cousins*

Note that, actually, Eq. 393 does not define uniquely x_1 and x_2, therefore, we need another equation to close the system. For example, we could impose the condition of *central intervals*, i. e. asking that the probability below x_1 and the one above x_2 are identical and equal to $\alpha/2$. In other cases, we may want to report an upper or lower limit on some parameter, but this decision cannot be taken a posteriori by looking at the data (so-called "flip-flopping"). The way to solve both of these problems is given by Feldman and Cousins [258].

To construct the confidence intervals, we could consider a hypothesis test that the true value is θ; then, recalling the definitions of the p-value above, the interval is found by imposing $p_\theta = \alpha$. If we choose a test statistic as

$$\lambda(x,\theta) = \frac{f(x|\theta)}{f(x|\widehat{\theta})}\,, \tag{395}$$

i. e. a likelihood ratio where $\widehat{\theta}$ maximizes $f(x|\theta)$, we obtain the Feldman-Cousins (FC) prescription; in particular, to construct the bounds à la FC one has to enforce Eq. 393 while asking $\lambda(x_1,\theta) = \lambda(x_2,\theta)$.

This prescription not only recovers the correct coverage probability, it is also able to naturally account for any eventual physical boundaries of the parameters, shifting "automatically" from a two-sided interval to a one-sided one. Suppose that

$$f(x|\theta) = \frac{1}{\sqrt{2\pi}}\exp\left(-\frac{(x-\theta)^2}{2}\right) \tag{396}$$

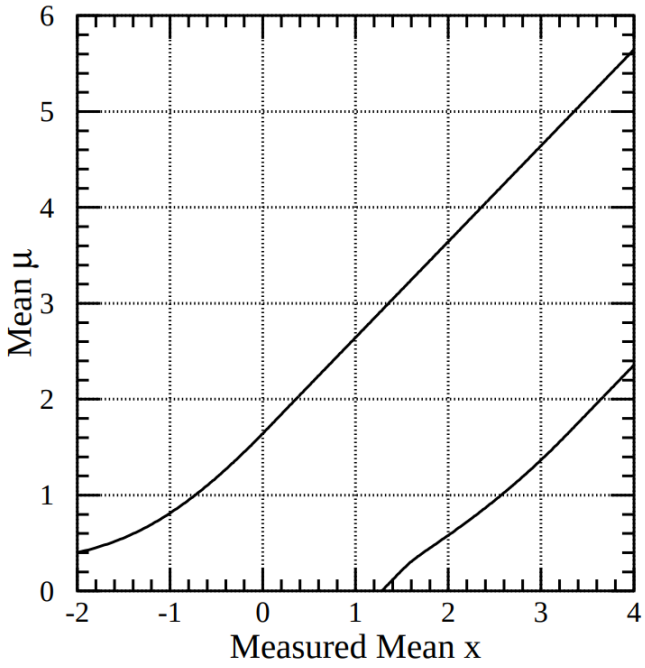

Figure 34: FC confidence belt with a physical bound $\mu \geq 0$. Figure extracted from [258].

and that θ must be non-negative. Our physically allowed best estimate of θ is $\widehat{\theta} = \max(0, x)$; then, we can write

$$\lambda(x,\theta) = \frac{f(x|\theta)}{f(x|\widehat{\theta})} = \begin{cases} \exp\left(-\frac{(x-\theta)^2}{2}\right) & \text{if} \quad x \geq 0 \\ \exp\left(x\theta - \frac{\theta^2}{2}\right) & \text{if} \quad x < 0 \end{cases} . \tag{397}$$

Searching now for $[x_1(\theta,\alpha), x_2(\theta,\alpha)]$ results in Fig. 34 (note that $\theta = \mu$ in the figure). Note that if the measured value of x is too close to the physical limit or is negative, the correspondent vertical line would intercept only $x_1(\theta,\alpha)$, automatically defining an upper limit on θ. At some point, increasing the measured value, we would instead intercept also $x_2(\theta,\alpha)$, shifting to a two-sided confidence interval. For this reason, the FC intervals are also said to be *unified* [258].

13

CONSTRAINING THE TENSOR SECTOR WITH MCMC

HERE, *we push the boundaries of our understanding in the tensor sector of the parameter space primarily from a Bayesian perspective, as discussed in Chap. 11. The significance of measuring the tensor-to-scalar ratio and the introduction of the tensor spectral tilt are highlighted in Chap. 5. We have seen that the standard single-field inflation model sets the tensor spectral tilt to* $n_t = -r/8$. *Despite this, in this chapter, based on Galloni et al. [259], we take a more exploratory approach by allowing* n_t *to vary. This investigation aims to embrace a broader framework, avoiding the imposition of single-field inflation.*

13.1 MCMC ANALYSIS

Let us report some details on the technique used to extract these constraints from the data, i. e. the MCMC analysis [241–245] (see also Chap. 11). We use `Cobaya` [260] to run our MCMC chains[82], whose results are analyzed through `GetDist`[83] [254], and `CAMB` [84][245, 261, 262] to generate the CMB spectra.

13.1.1 *ΛCDM parameters*

For what regards the 6 ΛCDM parameters $\{A_s, n_s, \Omega_b h^2, \Omega_{cdm} h^2, \theta_s, \tau_{reio}\}$, which are not the focus of this work, we only mention that we choose uniform and very wide priors, as is usually done to include as little information as possible. Also, these parameters are very well constrained, so the choice of the prior is not as important (see Chap. 11). It is important to let them vary to fully capture the variance of the tensor parameters [263]. In particular, Tab. 5 reports the ranges of the uniform priors we choose, together with the usual meaning of the parameters. Note that, if not otherwise stated, these parameters are always kept free to vary. For further details on how the newly available data affect this sector of parameters, see Sec. C.1 and [190, 263–265].

13.1.2 *Tensor parameters*

For what concerns the tensor sector of the parameters, we must give some more details.

82 https://github.com/CobayaSampler/cobaya.
83 https://github.com/cmbant/getdist.
84 https://github.com/cmbant/CAMB.

Parameter	Prior Range
$log(10^{10}A_s)$	$[1.61, 3.91]$
n_s	$[0.8, 1.2]$
$\Omega_b h^2$	$[0.005, 0.1]$
$\Omega_{cdm} h^2$	$[0.001, 0.99]$
θ_s	$[0.5, 10]$
τ_{reio}	$[0.01, 0.8]$
$r_{0.01}$	$[10^{-5}, 3]$
n_t	$[-5, 5]$
r_1	$[0, 3]$
r_2	$[0, 3]$

Table 5: Prior ranges for the ΛCDM parameters + the tensor sector. Here A_s, n_s are the amplitude and the tilt of the scalar primordial perturbations, Ω_b, Ω_{cdm} are the energy densities of baryons and cold dark matter, h is the Hubble constant H_0 divided by 100, θ_s is the angular scale of the sound horizon at recombination, and τ_{reio} is the optical depth of reionization. Instead, $r_{0.01}$ is the tensor-to-scalar ratio at 0.01 Mpc^{-1}, n_t is the tensor spectral tilt and r_1, r_2 are two tensor-to-scalar ratios at two arbitrary scales $(k_1, k_2) = (0.002, 0.02)$ Mpc $^{-1}$.

As we showed in Chap. 5, the tensor power spectrum is customarily parametrized as a power law around an arbitrary pivot scale k_*

$$P_t(k) = A_s r \left(\frac{k}{k_*}\right)^{n_t} . \tag{398}$$

Naively, one would choose a uniform prior for both r and n_t, such as $0 < r < 3$ and $-5 < n_t < 5$, however, we have to keep in mind that we actually have not detected r yet. Thus, for extremely low values of the amplitude, n_t will be completely free to vary in its prior ranges, producing a pathological behavior of the final posteriors.

In a Bayesian context, there are two ways to solve the issue (for an alternative prior-independent method, see [266]):

- the first consists of imposing a cut to the lowest values of the amplitude, typically setting the threshold value at some undetectable level for the considered experiments. For example, Cabass et al. [267] show the efficacy of this method while choosing $r > 0.001$. Today, this threshold value is exactly the target sensitivity of experiments such as LiteBIRD; therefore, one may want to choose a less aggressive cut. Throughout the remainder of this paper, we will refer to this approach as the Single-Scale Approach (SSA).

- On the other hand, what Ade et al. [268] did to solve the issue (subsequently repeated in [54]) is to actually re-parameterize the tensor power spectrum using two different tensor-to-scalar ratios (r_1, r_2) at

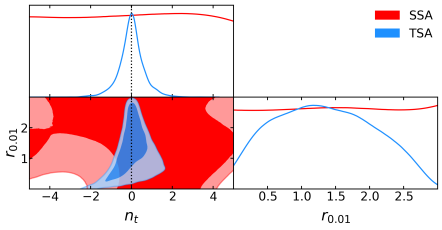

Figure 35: 1D and 2D sampled priors on the $(r_{0.01}, n_t)$ plane, obtained using the SSA or the TSA. The vertical dotted line represents scale-invariance, i. e. $n_t = 0$.

two different pivot scales (k_1, k_2), which are arbitrarily chosen. This, in fact, allows us to solve the problem: when r_1 approaches 0, r_2 will do so accordingly without producing any pathological behavior. Then, from (r_1, r_2) one can recover $(r_{\tilde{k}}, n_t)$ through

$$\begin{aligned} n_t &= [\log(r_2/r_1)/\log(k_2/k_1)] + n_s - 1 \,, \\ r_{\tilde{k}} &= r_1(\tilde{k}/k_1)^{n_t - n_s + 1} \,, \end{aligned} \tag{399}$$

where $\tilde{k}$ is some arbitrary scale (typically $\tilde{k} = 0.01\,\mathrm{Mpc}^{-1}$). Specifically, Akrami et al. [54] choose $(k_1, k_2) = (0.002, 0.02)\,\mathrm{Mpc}^{-1}$, imposing uniform priors on (r_1, r_2). For obvious reasons, we will refer to this approach as the Two-Scales Approach (TSA).

13.1.3 *Robustness test: priors*

Both approaches have their strengths and weaknesses; however, it is important to emphasize them to make a conscious choice on which to use.

The first test we perform is to run an MCMC analysis on the priors alone, without introducing any other source of information (see Tab. 5 for the specific values of the prior ranges), such as the likelihoods of the considered probes. In other words, this is a behavior check on the priors of the SSA and TSA, focused on the plane $(r_{0.01}, n_t)$ (also the ΛCDM parameters are kept free to vary). This allows us to obtain "sampled" priors to compare with the input ones and to gauge prior information on derived parameters.

Fig. 35 shows the marginalized 1D distributions and the marginalized 2D 68% and 95% CL[85]. Here, we can see that the sampled prior on $(r_{0.01}, n_t)$ using the SSA are flat, as expected since the sampling is performed directly on those two parameters. For what regards the TSA, Fig. 35 instead shows a neat preference for values of $r_{0.01}$ different from zero, thus mimicking a detection (for the derived parameter $r_{0.01}$ here we impose $r_{0.01} \in [0, 3]$). The marginalized distribution gives $0.08 < r_{0.01} < 2.61$ at 95% CL. In addition, there is a pretty strong pull on n_t towards scale invariance ($n_t = 0$), giving $-1.33 < n_t < 1.31$ at 95% CL. This suggests that while this method will solve the pathological behavior of n_t, it might also introduce a bias, especially if the dataset does not well constrain these parameters (in this case, the likelihood will dominate the final posterior). To explore this behavior

85 From now on, every 2D plot will show the 68% and 95% CL.

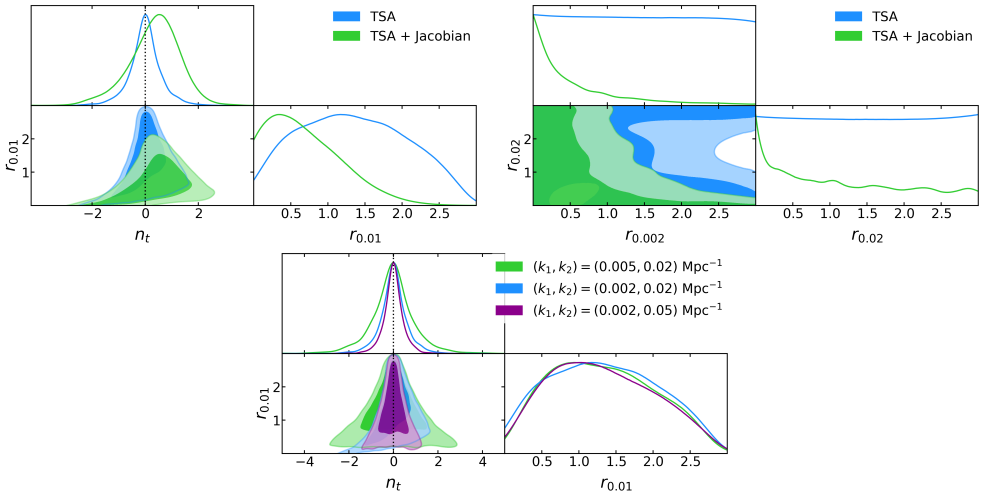

Figure 36: *Top:* 1D and 2D sampled priors on the $(r_{0.01}, n_t)$ plane (left) and on the (r_1, r_2) plane (right), obtained using the TSA with and without the Jacobian reweighting (see Eq. 400). The vertical dotted line represents scale-invariance, i. e. $n_t = 0$. *Bottom:* 1D and 2D sampled priors in the $(r_{0.01}, n_t)$ plane, obtained using the TSA with $(k_1, k_2) = (0.005, 0.02)$, $(0.002, 0.02)$ or $(0.002, 0.05)$ Mpc^{-1}. The vertical dotted line represents scale-invariance, i. e. $n_t = 0$.

more thoroughly, we also repeat this latter test on the TSA while reweighting the sample on the Jacobian of the transformation $(r_1, r_2) \leftrightarrow (r_{\tilde{k}}, n_t)$:

$$J = \frac{r_{0.01}}{r_1 r_2} \times \frac{1}{\log(k_1/k_2)} \,. \tag{400}$$

Indeed, this procedure has been used in the literature to alleviate this bias introduced by the prior (e. g. *Planck 2018*). As the top left panel of Fig. 36 shows, this seems to mitigate the amount of information introduced by the priors of the TSA but does not completely solve the problem. In particular, we obtain $r_{0.01} < 1.67$ and $-1.90 < n_t < 2.11$ at 95% CL. Thus, on one side the sampled priors are not mimicking a detection of the tensor-to-scalar ratio anymore, however, we still obtain a range of variation of n_t roughly equal to 4 units. This same range is very similar to what we obtain using the SSA on the state-of-the-art dataset (see Sec. 13.4), thus the results obtained through the TSA might be affected by bias, even when including the Jacobian. The top right panel on Fig. 36 shows that the sampled priors on r_1 and r_2 are correctly flat and are remapped to non-flat distributions by the Jacobian. In accordance with what we show here, for example, Planck 2018 shows that re-weighting the sampling allows obtaining a final posterior shifted towards $r_{0.01} = 0$ [54].

In the TSA, we can further test the choice of arbitrary scales (k_1, k_2), which in [54] are chosen to be $(0.002, 0.02)$ Mpc^{-1}. Thus, we repeat the prior analysis for $(k_1, k_2) = (0.002, 0.05)$ Mpc^{-1} and $(k_1, k_2) = (0.005, 0.02)$ Mpc^{-1}. Note that in the first case, we increase the separation between k_1 and k_2, while in the latter case we decrease it. In other words, we are testing the dependence of the prior on the leverage arm given by $k_2 - k_1$, which will affect the capability to recover n_t. The bottom panel of Fig. 36 shows that the sampled prior in the tensor-to-scalar ratio is only partially affected by the choice of scales, while the one in the tilt changes significantly as expected. Indeed, a larger leverage arm exacerbates the preference for scale invariance and vice versa. Thus, while using the TSA, one must be careful of what scales to use.

For example, the largest and smallest scales that an experiment has access to should provide an upper bound on the leverage arm length. However, going for this choice will produce the most peaked prior distribution possible on n_t.

Despite this, both cases analyzed here seem to break more prominently the degeneracy between $r_{0.01}$ and n_t w. r. t. the choice $(k_1, k_2) = (0.002, 0.02)$ Mpc^{-1}. Notice that this test depends to some degree on the fact that the MCMC sample is finite. Indeed, after convergence, the MCMC stops exploring the parameter space, potentially under-representing low-probability regions. In Sec. C.2 we perform it in an alternative way, i. e. directly from the coordinate transformation equations shown above, and so taking care of this effect. The conclusions do not change following this method, however, we can explain better the behavior of the region at low $r_{0.01}$ and high n_t of Fig. 36 (left panel). Indeed, in that low-probability region, there are no samples to be re-weighted, thus the probability drops to zero because the sample is finite (see Fig. 83 in Sec. C.2). In this specific case, this leads to an underestimation of the upper bound of the tilt. In general, this may or may not be the case depending on the specific choice between k_1 and k_2. Thus, together with the leverage arm, one should also keep this in mind when choosing those scales.

13.1.4 *Robustness test: mock dataset*

We perform another robustness check on the two approaches: we fix the 6 ΛCDM parameters to the best-fit values of Planck(2018) [190] and we allow only the tensor sector to vary. Then, instead of running the MCMC analysis on actual data (i. e. with the likelihood of some experiment), we define an exact likelihood for the B-mode spectrum [269]:

$$-2\log\mathcal{L} = \sum_\ell (2\ell+1)\left[\frac{\widehat{C}_\ell^{BB}}{\bar{C}_\ell^{BB}} - \log\left|\frac{\widehat{C}_\ell^{BB}}{\bar{C}_\ell^{BB}}\right| - 1\right]. \tag{401}$$

Here, $\widehat{C}_\ell^{BB}$ is a fiducial BB spectrum, and $\bar{C}_\ell^{BB}$ is the theoretical prediction based on the MCMC step. Notice that we do not introduce any source of instrumental noise. Instead, we use lensing as our noise level: indeed, we can write both the fiducial and theoretical spectra as $C_\ell^{BB} = C_\ell^{prim.} + C_\ell^{lens.}$, where $C_\ell^{prim.}$ is the primordial spectrum coming from the presence of an inflationary background of GWs, obtained fixing $r_{0.01}, n_t$, whereas $C_\ell^{lens.}$ is the contribution given by the lensing of polarized photons by mass distributions (see Fig. 10). In other words, this likelihood represents a mock data set from which we try to extract the fiducial values of the tensor parameters and their 95% CL intervals.

As for the fiducial choice of the BB spectrum, we want to reproduce the case in which the primordial spectrum is below the noise, in order to see how the two approaches deal with a non-detection of the tensor spectrum. For this reason, we choose $(r_{0.01}, n_t) = (10^{-4}, 0.3)$. The results are summarized

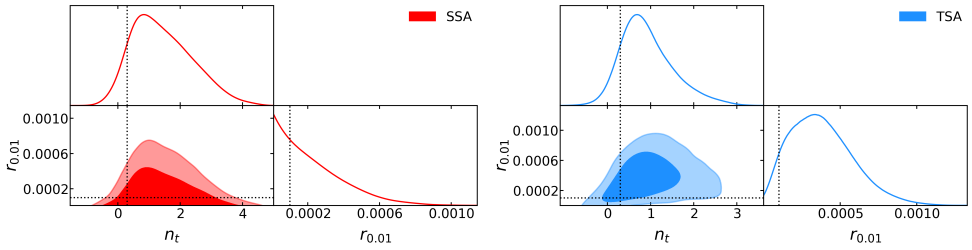

Figure 37: 1D and 2D posteriors on the $(r_{0.01}, n_t)$ plane, obtained using the SSA with an exact likelihood on the B-mode spectrum. The dotted markers indicate the fiducial values for $(r_{0.01}, n_t) = (10^{-4}, 0.3)$.

$r_{0.01}$	Best-fit	95% CL
SSA	1.00×10^{-4}	$[0.1, 6.0] \times 10^{-4}$
TSA	0.95×10^{-4}	$[0.2, 7.6] \times 10^{-4}$
n_t	Best-fit	95% CL
SSA	0.30	$[-0.24, 3.43]$
TSA	0.30	$[-0.15, 2.30]$

Table 6: 95% CL and best-fit values obtained with SSA and TSA when using an exact likelihood on the B-mode spectrum. The fiducial values are $(r_{0.01}, n_t) = (10^{-4}, 0.3)$.

in the left and right panels of Fig. 37. The 95% CL ranges that we obtain are instead shown in Tab. 6.

From this table, together with the figure, one can see that both approaches are able to recover approximately the correct value of the amplitude and tilt as the best fit of the MCMC run. Regarding the estimation of the 95% CL, the SSA provides a slightly stricter bound on the amplitude and a broader one on the tilt, as one can expect from Sec. 13.1.3. Fig. 38 highlights this by comparing the posterior distributions in n_t obtained with the exact likelihood with the priors shown in Fig. 35. Notice that the distributions of Fig. 38 are normalized to their maximum. We can also test an arbitrary choice affecting the SSA, i. e. the cut-off at low r. In fact, SSA results could be driven by marginalization effects: in a multidimensional problem, if a large part of the volume of probability is in a certain area, the final posterior will be drawn toward that region just as a result of the marginalization procedure that one performs when giving the result on a single parameter [256].

To investigate this potential problem, as a first step, we repeat this analysis assuming $r_{0.01}^{cut} = 10^{-4}, 10^{-5}, 10^{-6}$. Notice that the first value is equal to the fiducial tensor-to-scalar ratio, so that case will show what happens if we cut some relevant part of the parameter space, marginalizing the rest. The other

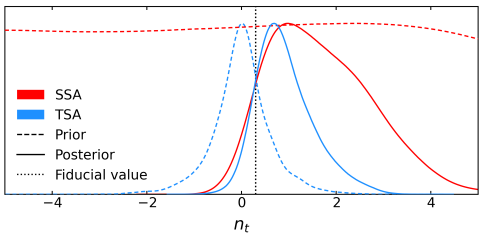

Figure 38: 1D posterior on the n_t, obtained using the SSA and the TSA with an exact likelihood on the B-mode spectrum. The dashed lines represent the sampled prior distributions obtained in Fig. 35. The dotted line indicates the fiducial value of $n_t = 0.3$.

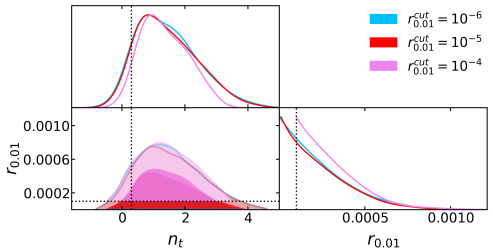

Figure 39: 1D and 2D posteriors on the $(r_{0.01}, n_t)$ plane, obtained using the SSA and changing the cut-off at low amplitudes: $r^{cut}_{0.01} = 10^{-4}, 10^{-5}, 10^{-6}$. The dotted markers indicate the fiducial values for $(r_{0.01}, n_t) = (10^{-4}, 0.3)$.

$r_{0.01}$	Best-fit	95% CL
$r^{cut}_{0.01} = 10^{-6}$	1.03×10^{-4}	$[0.01, 6.09] \times 10^{-4}$
$r^{cut}_{0.01} = 10^{-5}$	1.00×10^{-4}	$[0.10, 5.95] \times 10^{-4}$
$r^{cut}_{0.01} = 10^{-4}$	1.11×10^{-4}	$[1.00, 6.25] \times 10^{-4}$
n_t	Best-fit	95% CL
$r^{cut}_{0.01} = 10^{-6}$	0.30	$[-0.28, 3.54]$
$r^{cut}_{0.01} = 10^{-5}$	0.30	$[-0.24, 3.43]$
$r^{cut}_{0.01} = 10^{-4}$	0.31	$[0.002, 2.92]$

Table 7: 95% CL and best-fit values obtained with SSA when using an exact likelihood in the B-mode spectrum. The fiducial values are $(r_{0.01}, n_t) = (10^{-4}, 0.3)$. Here, we also assumed a different value of the cutoff at low amplitudes, $r^{cut}_{0.01} = 10^{-4}, 10^{-5}, 10^{-6}$.

two cutoffs are below the fiducial value; thus, they will test the stability of the estimate when we exclude a region with little-to-no posterior volume. Focusing on the first cutoff value, Fig. 39 shows that cutting an interesting part of the parameter space does have consequences on the final posterior, as expected. Indeed, looking at the 1D posterior of $r_{0.01}$ the posterior area below $r^{cut}_{0.01} = 10^{-4}$ is redistributed on the allowed region, providing a worse bound on the parameter. On the other hand, the estimate of n_t improves. In fact, the most extreme values of the tilt are obtained by the MCMC analysis for very low values of $r_{0.01}$, which in this case are completely neglected.

Then, focusing on the other two cases, Fig. 39 shows that the analysis is stable in both $r_{0.01}, n_t$ as soon as the cut is performed underneath the fiducial value since the corresponding posterior volume is small. Indeed, the posteriors obtained in these cases are nearly identical. Tab. 7 summarizes the results of this test.

Secondly, we inquire about an eventual over-weighting of the region near the cut-off in $r_{0.01}$ when using the SSA. Indeed, we already said that without the cutoff n_t would be completely unconstrained near $r = 0$. This means that near 0 there would be a lot of posterior volume, producing an over-weighting of the region of low tensor-to-scalar ratio, affecting the final results through the marginalization procedure. If this is the case, the contours should be dependent on the width of the n_t-prior, since the larger it is, the more available volume there would be. The prior is changed from

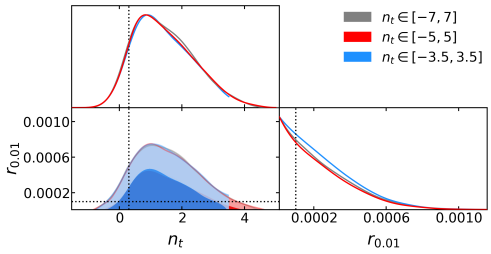

Figure 40: 1D and 2D posteriors on the $(r_{0.01}, n_t)$ plane, obtained using the SSA while changing prior range on n_t: $n_t \in [-5, 5]$, $n_t \in [-7, 7]$ and $n_t \in [-3.5, 3.5]$.

$n_t \in [-5, 5]$ to $n_t \in [-7, 7]$ and to $n_t \in [-3.5, 3.5]$ (cutting a relevant part of the posterior volume). The results are shown in Fig. 40, and, as expected, the difference comes from how much posterior volume has been excluded in the various cases.

Therefore, once the cutoff $r_{0.01}^{cut}$ (prior on n_t) is taken sufficiently low (large enough) to avoid excluding a relevant portion of the posterior volume, the SSA results will not change significantly.

In light of these tests and given that we want to provide reliable bounds in the tensor sector, avoiding a prior-induced detection, we choose to produce our baseline results with the SSA, assuming $r_{0.01}^{cut} = 10^{-5}$. In fact, one of the most promising models for describing tensor modes is the Starobinsky model [84], which predicts $r \approx 0.004$, so 10^{-5} is more than two orders of magnitude lower, as was 10^{-6} in the robustness test. For n_t we stick to the prior range reported in Tab. 5. These choices ensure that we do not exclude a large portion of the posterior volume, thus we do not introduce any additional marginalization effect. This would artificially increase the upper bound of $r_{0.01}$ as a result of having used an aggressive $r_{0.01}^{cut}$, or having excluded a priori some inflationary model characterized by a high $|n_t|$. However, we must keep in mind that SSA might be affected by volume effects toward $r = 0$.

Despite this, in Sec. C.3 we report the results obtained with the TSA, while assuming $(k_1, k_2) = (0.002, 0.02)$ Mpc^{-1} (as done in [54]) and no Jacobian transformation reweighting. This allows one to have a complete Bayesian picture on the tensor sector of parameter space.

13.2 DATASETS

Before going to the new bounds on $(r_{0.01}, n_t)$, we must understand what data are available in the market. In Chap. 5 we have seen what imprints a CGWB would leave on our Universe. Here, we focus on CMB, PTAs and GW interferometers.

We will divide this section according to the different experiments. Here, we just collect the ones that have been used to obtain the current bounds on the tensor parameters and those that we want to use to update the constraints. As partially shown in Fig. 10, there are many others that we will not mention.

13.2.1 *Planck satellite*

In most parameter estimation problems concerning CMB, Planck satellite data play a key role. Indeed, the current bounds on $(r_{0.01}, n_t)$ are obtained using data from *Planck* Release 3 (PR3) in the form of publicly available likelihoods (see [270] and [119, 271] for further details). In particular, sticking to the common nomenclature, we will call the ones used here:

- "*plikTTTEEE*", encoding the high-ℓ parts of CMB temperature, E-mode polarization, and their cross-correlation, i. e. the TT, EE, and TE spectra [270];
- "*lowlTT*", encoding the low-ℓ parts of the TT spectrum [270];
- "*lowlEE*", encoding the low-ℓ parts of the EE spectrum [270];
- "*lensing*": encoding the presence of gravitational potentials along the line of sight, which will convert EE $\rightarrow$ BB [270, 272].

For the sake of notation, we will refer to the combination of these 4 likelihoods as "PL18". Furthermore, recently the Planck Collaboration has released *Planck* Release 4 (PR4), exploiting the NPIPE end-to-end pipeline [264, 265, 273]. This instead consists of

- High ℓ Likelihood for Polarized Planck (HiLLiPoP)[86], encoding the high-ℓ region of TT,TE and EE;
- Low ℓ Likelihood for Polarized Planck (LoLLiPoP)[87], encoding the low-ℓ one of EE, EB and BB.

Note that LoLLiPoP contains information on B-modes, whereas PL18 does not. With these additional likelihoods, we define another abbreviation, i. e. "PL21". This corresponds explicitly to *plikTTTEEE*+*lowlTT*+LoLLiPoP+*lensing*, in such a way that the high multipole part is still carried out by the likelihood of PR3, together with the low-ℓ part of temperature and lensing. Instead, the low-ℓ part of E-mode, B-modes, and their cross-correlation is described through the PR4. In principle, PR4 is not independent of PR3, thus one has to be careful on combining them. In our case, we isolate the PR4 contribution to the low-ℓ part of the polarization fields (LoLLiPoP), so that we can still combine it with products of PR3 encoding different multipole ranges, or fields, assuming them to be independent.

13.2.2 *BICEP/Keck Array*

Together with Planck, the BICEP/Keck array data have been crucial in obtaining our current knowledge on tensor perturbations. As for Planck, the data are available through public likelihoods, named:

86 https://github.com/planck-npipe/hillipop
87 https://github.com/planck-npipe/lollipop

- "BK15", representing the measurement of BICEP2/Keck Array of the B-mode polarization [119];
- "BK18", representing the newly released dataset from BICEP3/Keck Array [263].

13.2.3 *LIGO-Virgo-KAGRA interferometers*

As mentioned above, CMB alone can only probe the largest scales of the tensor primordial spectrum (approximately $k \simeq 10^{-2}$ Mpc^{-1}). In fact, even in the ideal case of no instrumental noise, the cosmological B-mode contribution would be several orders of magnitude lower than the lensing contribution on small scales (see Fig. 10). On the other hand, GW interferometers are probing scales almost 18 orders of magnitude away from the CMB ones (approximately $k \simeq 10^{16}$ Mpc^{-1}), thus they provide a way to strongly constrain small scales. This line of reasoning hides a caveat though: in order to obtain helpful information on the tilt from GW interferometers, we must assume that n_t remains constant on the huge range of frequencies dividing CMB from interferometers, which could not be the case in nature [274–276]. However, given that we have not yet detected the amplitude of the tensor modes, i. e. r, it is already challenging to constrain the tensor tilt n_t; thus, we choose to neglect any running of the tensor tilt, as commonly done in the literature.

Currently, interferometers provide only upper bounds on the energy density of GWs at their frequency range. Indeed, knowing the minimal energy density detectable by a GW interferometer and assuming our parametrization of the tensor power spectrum (see Eq. 398), one can extract a bound on how blue tilted the primordial spectrum can be. In particular, one can translate $(r_{0.01}, n_t)$ into an energy density at some reference frequency f with [54, 267]

$$\Omega_{GW}(f) = \frac{r_{0.01} A_s}{24 z_{eq}} \left(\frac{f}{f_{CMB}} \right)^{n_t} , \tag{402}$$

where $f_{CMB} \sim 10^{-17}$ Hz is the frequency corresponding to the chosen pivot scale (i. e. $k = 0.01$ Mpc^{-1}) and $z_{eq} \simeq 3400$ is the redshift of the matter-radiation equality [54].

The datasets from GWs interferometers will be named:

- "LV15", referring to the results after the first observing run of LIGO-Virgo-KAGRA (LVK). The upper bound on the energy density at a reference frequency of $f_{LVK} = 20$ Hz is $\Omega_{GW}(f_{LVK}) < 1.7 \times 10^{-7}$ at 95% CL. Note that this was obtained by assuming a scale-invariant spectrum [134].
- "LV18", referring to the results after the second observing run of LVK. This time, the bound on the energy density we consider is marginal-

ized on the value of the spectral tilt and at a frequency of 25 Hz. In particular, $\Omega_{GW}(25\ \mathrm{Hz}) < 3.4 \times 10^{-8}$ at 95% CL [135].

- "LV21", referring to the results after the third observing run of LVK. The upper bound reported is $\Omega_{GW}(25\ \mathrm{Hz}) < 6.6 \times 10^{-9}$ at 95% CL, obtained once again marginalizing over the spectral tilt [277].

Note that these datasets are not independent. Instead, they are the result of a longer observation time and of a progressive improvement of the systematics that affect LVK. For this reason, we cannot combine them since the information provided by LV15 is already contained in LV18, etc.

As regards the actual inclusion of these bounds, one may encode them in an MCMC analysis as a half-Gaussian prior to the energy density of GWs predicted with Eq. 402, having the 95% limit at the value reported by LVK (this approach is used in [54]); an alternative, but equivalent way would be to define a Gaussian likelihood for LVK, centered in $\mu_{LVK} = 0$ and having a dispersion σ_{LVK} that is half of the 95% bound provided by LVK:

$$-2\log\left(\mathcal{L}_{LVK}\right) = \frac{\left(\Omega_{GW} - \mu_{LVK}\right)^2}{\sigma_{LVK}^2}\ , \tag{403}$$

where Ω_{GW} is the value extracted from the MCMC analysis for a specific set of parameters (this is how we include it in our analysis).

13.2.4 *NANOGrav*

Together with these data, we also want to study the consequences of the claim from North American Nanohertz Observatory for Gravitational Waves (NANOGrav) collaboration [133]. In fact, they report a significant detection of a common signal among several pulsars, but they do not obtain a clear detection of the spatial correlation of those, which would be the definitive proof of the stochastic origin of the signal. Despite this, it is interesting to include this dataset in our analysis, implying the assumption of a cosmological origin[88].

As regards the actual bound, there is an intermediate step we must take w. r. t. the LVK case. NANOGrav Collaboration reports its data in terms of amplitude A_{CP} and spectral tilt α_{CP} (see [133] for details); therefore, we must first obtain the corresponding Ω_{GW}. In particular [30, 278]:

$$\Omega_{\mathrm{GW}}(f) = \frac{2\pi^2}{3H_0^2} f^2 h_c^2(f)\ , \tag{404}$$

where h_c is the power spectrum of the characteristic GW strain reading

$$h_c(f) = A_{CP}\left(\frac{f}{f_{yr}}\right)^{\alpha_{CP}}\ . \tag{405}$$

88 At the time [259] was written, the latest results of NANOGrav were not present [132].

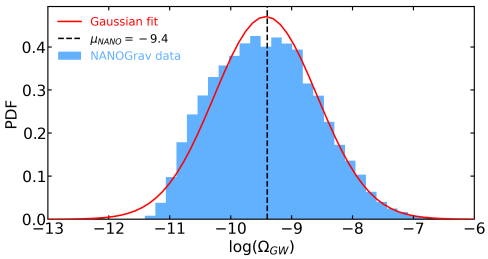

Figure 41: NANOGrav data marginalized over the spectral index. The solid curve represents the Gaussian likelihood we used for our analysis.

Now, each $\{A_{CP}, \alpha_{CP}\}$ couple will correspond to a function $\Omega_{\rm GW}(f)$. However, mimicking what is done for the LVK results, we are interested in the reference frequency of the experiment, thus we fix the frequency to $f = f_{NANO} = 1\ \mathrm{yr}^{-1}$ (which corresponds to $k_{NANO} \simeq 2.0 \times 10^7\ \mathrm{Mpc}^{-1}$), such that

$$\Omega_{\rm GW}(f_{yr}) = \frac{2\pi^2}{3H_0^2} f_{yr}^2 A_{CP}^2 \,. \tag{406}$$

This does not depend on α_{CP}; at this point, one can verify that the logarithm of Ω_{GW} follows approximately a Gaussian distribution, thus we fit it to find the bound: $\log(\Omega_{\rm GW}) = -9.4 \pm 0.8$. This procedure allows us to get Fig. 41, which is obtained from the NANOGrav chains[89]. To include this bound in the MCMC, one may follow the same procedure proposed for the LVK, thus defining a likelihood as

$$-2\log(\mathcal{L}_{NANO}) = \frac{[\log(\Omega_{\rm GW}) - \mu_{NANO}]^2}{\sigma_{NANO}^2} \,. \tag{407}$$

Differently from the LVK case, now $\mu_{NANO} \neq 0$. Finally, to refer to this dataset we will use "NANO".

We collect all the names and abbreviations in Tab. 8.

Name	Likelihoods	Description
PL18	plikTTTEEE+lowlTT+lowlEE+lens.	Combination from PR3 [270, 272]
PL21	plikTTTEEE+lowlTT+LoLLiPoP+lens.	Combination of PR3 and PR4 [264, 270, 272]
BK15	BICEP2/Keck array	BICEP2/Keck Array likelihood [119]
BK18	BICEP3/Keck array	BICEP3/Keck Array likelihood [113]
LV15	LIGO-Virgo-KAGRA	LVK likelihood with 2015 data [134]
LV18	LIGO-Virgo-KAGRA	LVK likelihood with 2018 data [135]
LV21	LIGO-Virgo-KAGRA	LVK likelihood with 2021 data [277]
NANO	NANOGrav	NANOGrav likelihood with 2021 data [133]

Table 8: Names of the main likelihoods, or collection of them, used here.

89 The dataset and further information can be found at https://github.com/nanograv/12p5yr_stochastic_analysis.

13.3 STATE-OF-THE-ART

In this section, we will briefly go through the combination of datasets that have been implemented to obtain the current bounds on $r_{0.01}$ (or $r_{0.05}$) and n_t (the literature on this is quite vast, thus we consider only a few of the most recent works).

Akrami et al. [54] (Planck 2018) consider two combinations while studying the ΛCDM+r_1+r_2 model (TSA):

- PL18 + BK15, obtaining $r_{0.01} < 0.076$ and $-0.55 < n_t < 2.54$ at 95% CL, obtained by exploiting TSA with $(k_1, k_2) = (0.002, 0.02)$ Mpc^{-1}.
- PL18 + BK15 + LV15, resulting in $r_{0.01} < 0.066$ and $-0.76 < n_t < 0.52$ at 95% CL, using TSA with $(k_1, k_2) = (0.002, 0.02)$ Mpc^{-1}.

From this, it is clear that CMB experiments are not able to constrain very well the bluest tilts of the spectrum. Instead, the addition of LV15 (as a half-Gaussian prior) severely cuts the allowed range of n_t. Notice that LV15 is obtained by fixing the spectral tilt to scale invariance, while the MCMC is performed by letting it vary.

Tristram et al. [114] explored the PR4 on the ΛCDM+$r_{0.05}$ model, thus keeping n_t fixed to its single-field slow-roll prediction: $n_t = -r_{0.05}/8$, where 0.05 Mpc^{-1} is the pivot scale of scalar perturbations. Given that they report their results for this scale, we will compute a very rough estimate of the corresponding bound on $r_{0.01}$. In particular, if they report $r_{0.05} < X$ at 95% CL, we will use Eq. 399, $n_t = -X/8$, and the best-fit value of n_s of *Planck 2018* to get the corresponding $r_{0.01} < X'$ bound (we will report this in parenthesis). The most relevant (for this work) cases analyzed in [114] are:

- LoLLiPoP, which yields $r_{0.05} < 0.069$ at 95% CL ($r_{0.01} < 0.066$).
- HiLLiPoP(only TT)+*lowlTT*+LoLLiPoP, yielding $r_{0.05} < 0.060$ at 95% CL ($r_{0.01} < 0.057$).
- HiLLiPoP(only TT)+*lowlTT*+LoLLiPoP+BK15, yielding $r_{0.05} < 0.044$ at 95% CL ($r_{0.01} < 0.042$).

Ade et al. [113] presented the new release of data from the BICEP/Keck Array (here BK18). While keeping the ΛCDM parameters fixed and using $n_t = -r_{0.05}/8$, they obtain $r_{0.05} < 0.036$ at 95% CL ($r_{0.01} < 0.034$).

Finally, Tristram et al. [263] used PR4 and BK18 to obtain the state-of-the-art upper bound on $r_{0.05}$ on the ΛCDM+$r_{0.05}$ model ($n_t = -r_{0.05}/8$). In particular, they consider HiLLiPoP + *lowlTT* + LoLLiPoP + BK18 + BAO + *lensing*, finding $r_{0.05} < 0.032$ at 95% CL ($r_{0.01} < 0.030$). Notice that, they consider a dataset we are not including here, which is BAO from [279].

This set of bounds, especially Tristram et al. [263] for what regards $r_{0.05}$, and Akrami et al. [54] for what regards n_t, represent the current state-of-the-art. As mentioned before, for the ones with n_t fixed, we compute in parenthesis a corresponding $r_{0.01}$ value, however, comparing them with the

results we are about to show is not so trivial. In fact, we let n_t vary, thus our results on $r_{0.01}$ will be marginalized on the tilt. However, that rough correspondence can help put this work in perspective w.r.t the rest of the literature.

13.4 RESULTS

Finally, let us report the results of our analysis. This has been performed using the SSA on the complete ΛCDM+$r_{0.01}$+n_t parameter space, assuming $r_{0.01}^{cut} = 10^{-5}$. The priors for these parameters are flat and their ranges are shown in Tab. 5 (in Sec. C.3 we also show the results for the TSA case). In terms of convergence, we used the Gelman-Rubin test to determine when to stop the MCMC runs [280]. Given the number of dataset combinations, the number of varied parameters making the convergence difficult to achieve, and the finite CPU hours available, we assumed a minimal level of convergence of $R - 1 < 0.04$. For a few selected cases (the most constraining ones), we instead assumed $R - 1 < 0.01$ in order to explore more thoroughly the tails of the distribution and to avoid over/underestimating our bounds. Regarding the size of the MCMC chains, we quantify it using the "total weights" given by `GetDist`. Indeed, when a proposed step of the chain is rejected, the weight of the current point in parameter space will increase, as if it is counted once again. In other words, this quantity represents the total number of steps, regardless of their being accepted, or not. As an example, the shortest length obtained (PL18 + BK18) is $\sim 27,000$, while the longest is $\sim 141,000$ (PL21 + BK18 + LV21).

We performed the MCMC runs for most of the relevant permutations of Planck, BICEP/Keck, and LVK data, searching for the most constraining one. Instead, given the nature of the NANOGrav claim, and knowing the results of our analysis, we keep the discussion on that dataset separated from the others.

Tab. 9 reports the one-dimensional 95% CL for each combination analyzed. Assuming PL18 + BK15 to be our "starting point"[90], the first 4 rows show the individual improvements brought by various datasets. Among them, it is clear that BK18 prominently improves the bound on the tensor-to-scalar ratio (as shown by [113, 263]), while shifting the allowed range of n_t towards lower values w. r. t. PL18 + BK15.

The next 4 cases feature combinations of different upgrades w. r. t. PL18 + BK15. Given that we want to privilege the stricter bound on the tensor-to-scalar ratio, PL21 + BK18 + LV21 is what we consider our best dataset to constrain the tensor sector, resulting in

$$r_{0.01} < 0.028 \quad \text{and} \quad -1.37 < n_t < 0.42\,, \tag{408}$$

90 As mentioned before this is essentially the state-of-the-art combination for what regards the case in which n_t is allowed to vary. Notice that here we are not including LV15, since it is actually obtained assuming scale-invariance at the typical frequency range of interferometers.

	$r_{0.01}$ 95% CL	n_t 95% CL	**R − 1 test**
PL18+BK15	< 0.056	[-0.22, 4.16]	0.032
PL18+BK18	< 0.032	[-0.98, 3.46]	0.033
PL18+BK15+LV18	< 0.059	[-1.00, 0.45]	0.039
PL18+BK15+LV21	< 0.057	[-0.91, 0.42]	0.025
PL18+BK18+LV21	< 0.032	[-1.14, 0.42]	0.034
PL21+BK15	< 0.049	[-0.60, 4.34]	0.010
PL21+BK18	< 0.029	[-1.21, 3.54]	0.016
PL21 + BK18 + LV21	< 0.028	[-1.37, 0.42]	0.006
PL18+BK15+NANO	< 0.071	[0.44, 0.83]	0.028
PL21+BK18+NANO	< 0.033	[0.47, 0.85]	0.005

Table 9: 95% CL intervals of the 10 considered combinations of datasets. Our main result is PL21 + BK18 + LV21. Here we also show the results of the Gelman-Rubin test for each combination.

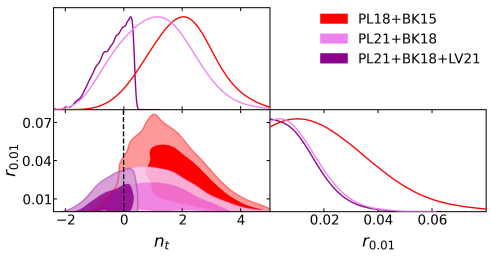

Figure 42: 2D 68 and 95% CL contours in the $(r_{0.01}, n_t)$-plane for PL18+BK15, PL21+BK18 and PL21+BK18+LV21. The dashed black line is the well-known slow-roll single-field prediction $n_t = -r/8 = -2\epsilon$.

at 95% CL, which is the main result of this work and represents the most constraining bound on the tensor-to-scalar perturbation ratio to our knowledge.

We show the 2D posterior contours of this case in Fig. 42, compared to some other relevant cases: PL18 + BK15 (representing the state of the art) and PL21 + BK18 (to underline the improvement carried out by LV21). Furthermore, in Fig. 43 we show the posterior distribution on the plane $r_{0.002} - n_s$ for the same datasets as in Fig. 42. To do so, we mimic figure 8 of [54], showing a few relevant inflationary scenarios and fixing n_t to its standard single-field prediction. As already highlighted by [113, 263], we confirm with improved sensitivity that all potentials for the single-field inflationary models we show are ruled out by the data. The same can be said of natural inflation, which is well outside the 95% CL region.

13.4.1 *Marginalization effects*

In Chap. 11 we argue that marginalization effects should be taken into account to check the sanity of our results. Instead of performing a full PL analysis (which will be the topic of Chap. 14), here we show the "profile distribution" for our most constraining dataset, i. e. PL21 + BK18 + LV21. In fact, Gómez-Valent [256] presented this technique as an approximation

3 http://pla.esac.esa.int/pla/#home

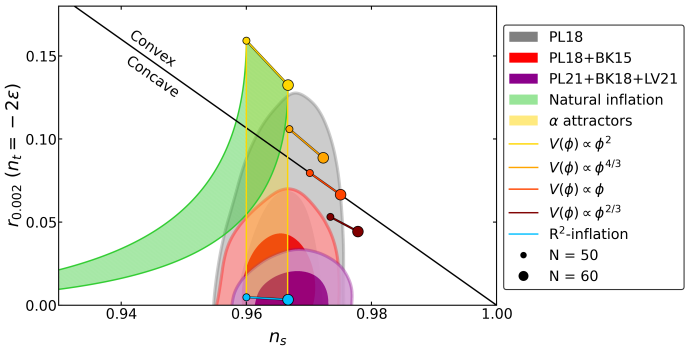

Figure 43: 2D 68 and 95% CL intervals in the $(r_{0.002}, n_s)$-plane for PL18 (publicly available MCMC chains[3]), PL18 + BK15 and PL21 + BK18 + LV21. $r_{0.002}$ is obtained from our chains assuming the standard prediction $n_t = -r/8 = -2\epsilon$.

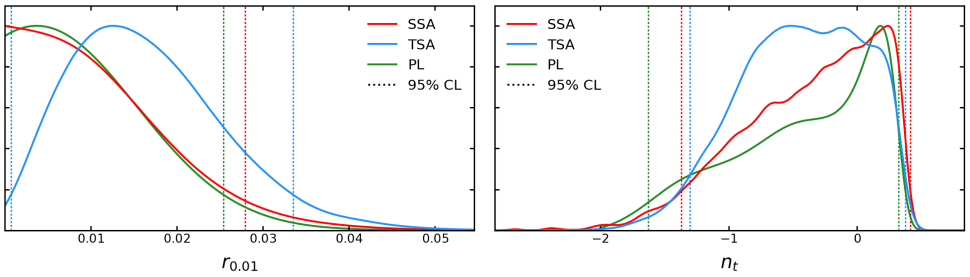

Figure 44: 1D results on $r_{0.01}$ and n_t, obtained using SSA, TSA, and PL on our most constraining dataset, that is, PL21 + BK18 + LV21. This plot refers to the case with 30 bins. The vertical dotted lines represent the boundaries of the SSA and TSA 95% CL intervals. Note that SSA gives a single-tail bound on $r_{0.01}$ while the TSA provides a two-tail one. Also, the green dotted lines indicate the 95% confidence intervals of the profile distribution. These are also summarized in Tab. 10.

of the PL useful if one already has an MCMC to exploit and proved its robustness on highly dimensional likelihoods, such as Planck's. To obtain the profile distributions on $r_{0.01}$ and n_t, we follow the following procedure:

1. starting from our MCMC chains, we bin the values of $r_{0.01}$ or n_t;
2. in each bin, we search for the minimum value of χ^2.
3. Then, we fit a polynomial[4], using the mean value of the profiled parameter in the bin as the x-coordinate;
4. the resulting curve represents χ^2 as a function of this parameter.

This procedure indeed approximates an actual PL, which instead is performed point-by-point via some minimization algorithm over all the non-fixed parameters (see Chap. 12). In this case, instead, the very low computation time of this technique (of the order of a fraction of a second) comes at the cost of having to choose a binning strategy. In fact, the value of χ^2 in each bin is "noisy", since it is not guaranteed that it has reached its absolute minimum. Clearly, the larger the bin, the more probable it is to find the real minimum of χ^2, and the larger the uncertainty on the x-axis. In other words, one has to find the right trade-off between having small bins and populating them sufficiently. In our case, we focus mainly on $r_{0.01}$, for which we explore 4 different binning strategies in the range $[0, 0.05]$ with 10, 30, 50, and 100 bins. Instead, we bin n_t in $[-2.0, 0.48]$ with 100 bins.

Fig. 44 shows the results for $r_{0.01}$ (30 bins) and n_t, respectively (see also Tab. 10). In terms of 95% confidence intervals, we obtain $-1.63 < n_t < 0.32$.

4 In the case of a Gaussian likelihood this would simply be a parabola, which is the case for $r_{0.01}$. For the n_t distribution, which is highly non-Gaussian, we use a polynomial with a degree equal to 8.

	$r_{0.01}$ 95% CL	n_t 95% CL
SSA	< 0.028	$[-1.37,\ 0.42]$
TSA	$[0.01,\ 0.033]$	$[-1.30,\ 0.37]$
	$r_{0.01}$ 95% CI	n_t 95% CI
PL	< 0.025	$[-1.63,\ 0.32]$

Table 10: 95% CL obtained with SSA and the TSA compared to the 95% confidence intervals of the profile distribution.

For $r_{0.01}$ we obtain $r_{0.01} < 0.028$, 0.025, 0.025 and 0.024 using 10, 30, 50, and 100 bins, respectively. In addition, we compare PL with both the SSA and the TSA results. The left panel shows that the SSA and the PL are very similar, even if the SSA seems to obtain slightly more conservative results. This shows that marginalization effects have only a partial role in obtaining our result for PL21 + BK18 + LV21. Note that the case with 10 bins, thus the one in which it is more probable that χ^2 reaches its absolute minimum, gives the same result as our MCMC. However, there is no guarantee that this has the correct coverage probability (see Chap. 14).

On the other hand, it is clear that the bias observed in the TSA case is due to the informative prior discussed in Sec. 13.1.3.

Looking at the right panel, both the SSA and TSA are fairly similar to the PL distribution, with the former being slightly more conservative, as expected.

13.4.2 *Including NANOGrav*

In order to study the posterior distribution of $r_{0.01}$ and n_t when including the NANOGrav dataset, we do not use LV18 or LV21. Also, let us recall that performing this analysis for NANOGrav implies the assumption of a cosmological origin of the measured signal.

The last two rows of Tab. 9 (see also Fig. 46) show the results of PL18 + BK15 + NANO and PL21 + BK18 + NANO, together with all other 8 combinations. Notice that there is a discrepancy between the estimated 1D 95% CL bound of n_t obtained exploiting NANOGrav or LVK. The reference frequency of NANOGrav is $f_{NANO} = 1\ \mathrm{yr}^{-1} \simeq 32\times$ nHz $\rightarrow k_{NANO} \simeq 2.0 \times 10^7\ \mathrm{Mpc}^{-1}$, instead of the LVK one is $f_{LVK} = 25$ Hz $\rightarrow k_{LVK} \simeq 1.6 \times 10^{16}\ \mathrm{Mpc}^{-1}$, thus they are separated by 9 orders of magnitude. This discrepancy suggests that the signal detected by the NANOGrav collaboration cannot be a cosmological background signal characterized by a simple power-law [281–283]. In fact, fitting the NANOGrav bound on Ω_{GW} at k_{NANO} with our best-fit power-law of PL21 + BK18 + NANO would make it inconsistent with the LVK bound we have at k_{LVK}. This is represented visually in Fig. 45 where it is clear that a single power-law cannot fit both NANO and LVK. Here, we also show some examples of models fitting them, as a SU(2) model [281, 282,

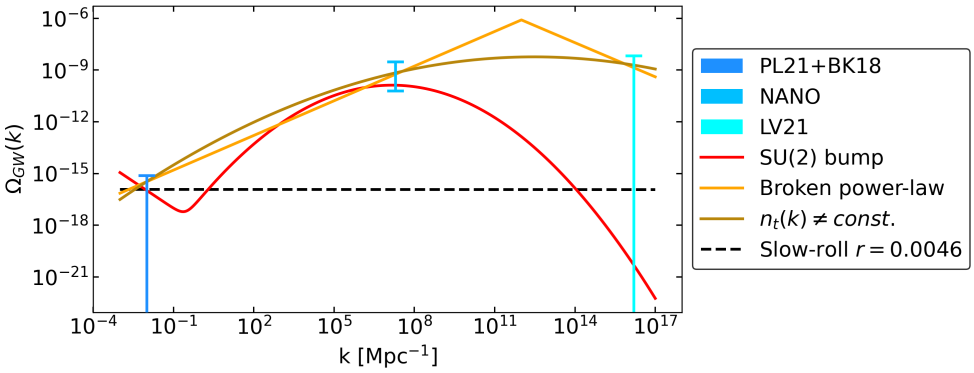

Figure 45: Illustrative representation of the current bounds on the GW energy density. Here, we show that a simple power law is not enough if one wants to include every dataset.

284], a broken power-law [283], and a power-law with a non-null running of n_t [274–276].

This is consistent with what has already been found in the literature [281–283]. In fact, there is a zoology of different models trying to explain the NANOGrav claim in a cosmological fashion; however, this is beyond the scope of this work.

13.5 SUMMARY AND CONCLUSIONS

In this chapter, we have obtained new Bayesian bounds on the tensor-to-scalar ratio r and the tensor spectral index n_t. We have exploited newly released datasets from both an EM point of view, i. e. BICEP/Keck 2018 [113] and Planck PR4 [114], and a GW perspective, that is, LVK collaboration data [277]. In particular, the complementarity of Planck and BK measurements allows us to better constrain the amplitude of the tensor perturbation spectrum, while the information at small scales coming from LVK can cut the values of permitted spectral tilts.

To obtain reliable bounds on the tensor sector, we have studied the behavior and performances of two approaches encoding r and n_t into our MCMC analysis, i. e. the SSA and the TSA. The former consists of sampling directly these two parameters while cutting the lowest values of r at some undetectable threshold $r^{cut}_{0.01}$ [267]; in the latter, one defines two tensor-to-scalar ratios r_1 and r_2 (at scales k_1 and k_2) with which the parameter space is explored [54]. Then $r_{0.01}$ and n_t are recovered as functions of r_1 and r_2 (see Eq. 399). In Sec. 13.1 we perform different tests to assess how a priori and arbitrary choices affect both methods. In particular, we inspect the prior information injected in the TSA by the coordinate transformation (see also Sec. C.2) and the performance of both approaches on a mock dataset.

Starting from the TSA, in Sec. 13.1 we find that the informative prior on $r_{0.01}$ biases the results toward higher values w. r. t. what data suggest to the point that $r_{0.01} = 0$ is excluded at more than 95% CL. In addition, the informative prior on n_t introduces a strong pull toward scale-invariance ($n_t = 0$) disfavoring inflationary models characterized by a large $|n_t|$.

With respect to SSA, we find that the main weakness is marginalization effects. Thus, even if one considers a very low $r^{cut}_{0.01}$ and a large prior in n_t

(thus without excluding a priori a large part of the posterior volume), there might be a push towards small values of $r_{0.01}$, caused by the presence of a large posterior volume near $r_{0.01}$.

Despite this, the SSA seems to be more robust against a priori arbitrary choices w. r. t. to the TSA (see Sec. 13.1.4). Thus, we provide our baseline results in Sec. 13.4 using the SSA (Sec. C.3 reports the TSA results).

We have analyzed 10 combinations of the available datasets and we have found that the most constraining consists of a combination of Planck PR3 (high-ℓ part of TT, EE, and TE, low-ℓ part of TT and lensing) and PR4 (low-ℓ part of EE, BB, and EB), BK18, and the last release from LVK. Together they provide $r < 0.028$ and $-1.37 < n_t < 0.42$ at 95% CL with a sensitivity on r of $\sigma_r = 0.0086$. To our knowledge, these are the most constraining bounds available in the literature for what concerns an inflationary scenario characterized by a power-law. Standard single-field slow-roll prediction for the spectral tilt ($n_t = -r/8 = -2\epsilon$) is still completely compatible with our results. The TSA gives $0.001 < r < 0.033$ and $-1.32 < n_t < 0.37$ at 95% CL on the same combination of datasets, which seems to be consistent with the biases mentioned before.

Furthermore, to assess the possible influence of marginalization effects on our main result with the SSA, in Sec. 13.4 we compute the profile distribution of our MCMC chain using the technique proposed in [256], which approximates the results of a PL (see Chap. 14). The agreement between this and our SSA marginalized distributions suggests that our results are driven by data and not by marginalization effects, which surely play a role, but not a significant one. In fact, for each binning strategy, we assumed, the upper bound of $r_{0.01}$ provided by the profile distribution is always less than or equal to $r_{0.01} < 0.028$, demonstrating the robustness of our result. Instead, the biases on the TSA find confirmation when comparing it with the profile distribution.

In addition, we have considered two additional combinations of data sets that account for the NANOGrav collaboration results [133]. In these cases, we found an apparent inconsistency in the allowed range of n_t w. r. t. what we have obtained using LVK data as our small-scale dataset, according to what has already been underlined in the literature. Specifically, we have obtained $r < 0.033$ and $0.47 < n_t < 0.85$ at 95% CL. If we assume that NANOGrav common-signal has a cosmological origin, one must abandon the single power-law description of the tensor power spectrum, given that NANOGrav and LVK cannot be reconciled in such a context. Instead, one may consider Axion-SU(2) spectator field [281, 282, 284], broken power-law description of the primordial tensor spectrum [283], GW contribution to the relativistic degrees of freedom [285, 286], k-dependence of the tensor tilt [274–276], cosmic strings [287], phase transitions [288], domain walls or large-amplitude curvature perturbations [289] to obtain a framework accounting for all constraints at all scales (see also Chap. 4 and Chap. 5).

In conclusion, in Fig. 46 we translate the results presented in Tab. 9 into a visual representation to help comparing the different datasets.

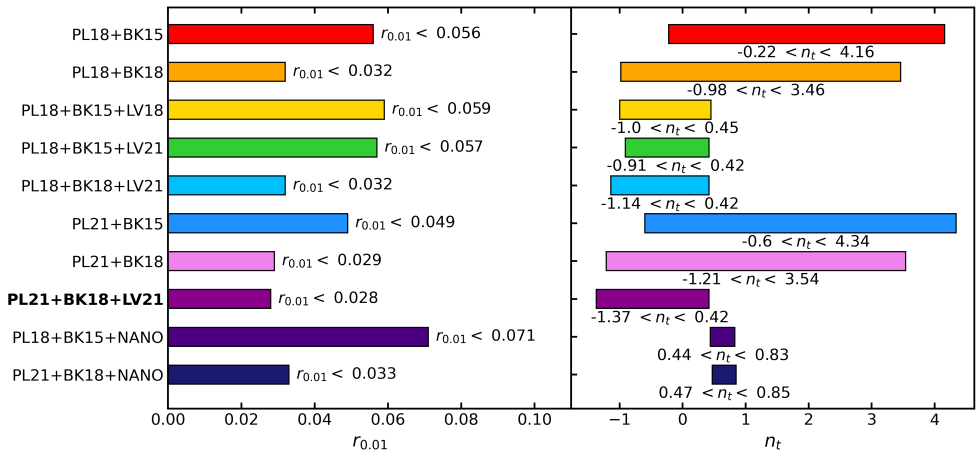

Figure 46: 95% CL intervals for $r_{0.01}$ and n_t, considering different datasets, given in Tab. 8. Our main result is PL21+BK18+LV21.

In the future, CMB space missions such as LiteBIRD [237] will provide an unprecedented capability of measuring the large-scale part of the B-mode spectrum. Indeed, the target sensitivity of LiteBIRD alone is $\sigma_r = 0.001$ (a factor ~ 9 better than the sensitivity obtained here); thus it will allow us to obtain crucial information of the inflationary model which took place in nature (for some insights, see [290]).

14

CONSTRAINING THE TENSOR SECTOR WITH PROFILE LIKELIHOOD

Previously in Chap. 13, we demonstrated the procedure to derive updated CL intervals from a Bayesian perspective. A critical consideration involves the potential impact of volume effects, which, while not intrinsic to the Bayesian framework, can contribute to an incomplete or potentially misleading portrayal of the tensor sector of the parameter space.
In Chap. 13, our approach to data involved an approximate technique resembling a PL. This chapter extends our analysis to incorporate the latest datasets, employing both MCMC and PL, with particular emphasis on the latter technique.
This chapter draws on collaborative work conducted with the IJCLab in Orsay (France), which will be referred to as "Galloni et al. (in prep.)". As the project is still in progress at the time of writing, the results presented should be treated as preliminary.

14.1 DATASET

In Chap. 13 we go through the datasets used in [259]. Here, we update the previous combinations to the latest available data.

14.1.1 *Planck PR3 and PR4*

This study uses Planck sky measurements from the PR4 maps[5]. These maps are generated through the NPIPE processing pipeline, producing calibrated frequency maps in both temperature and polarization using data from both the Planck Low-Frequency Instrument (LFI) and the High-Frequency Instrument (HFI). The NPIPE process, detailed in [291], incorporates data from previously overlooked repointing periods, along with several enhancements that reduce noise and systematic errors across frequencies and component-separated maps, enhancing consistency between different frequencies.

We use Planck likelihoods that cover the multipole range from $\ell = 2$ to $\ell = 2500$. For large angular scales in temperature, we consider Commander TT likelihood (lowlT) based on a Bayesian posterior Gibbs sampling (see Chap. 11) that combines astrophysical component separation and likelihood estimation [43, 270]. For large angular scales in polarization, we use the LoLLiPoP likelihood (lolEB) based on the Hamimeche-Lewis approximation for the EE, BB and EB power spectra [263]. At small angular scales, we use alternatively HiLLiPoP or CamSpec which both are capable of combining

5 Available on the Planck Legacy Archive: http://pla.esac.esa.int.

TT, TE and EE CMB spectra over a large fraction of the sky (75% and 80% respectively). HiLLiPoP is a multi-frequency likelihood based on cross-spectra of the 100, 143 and 217 GHz frequency maps, with astrophysical models for the residuals of foreground emissions [29]. CamSpec is based on cross-spectra at 143 and 217 GHz which are pre-processed by a cleaning procedure using the 545 GHz maps as a template of Galactic dust emission [292].

All Planck likelihoods are based on PR4 (with the exception of lowlT, based on PR3).

14.1.2 *BICEP/Keck Array*

We use the BICEP/Keck likelihood (BK18), representing data gathered by the BICEP2, Keck Array, and BICEP3 CMB polarization experiments up to the 2018 observing season [113]. This likelihood is based on the Hamimeche-Lewis approximation [293] for the joint likelihood of the BB auto- and cross-spectra obtained across multiple frequency maps: BICEP/Keck (two at 95 GHz, one each at 150 and 220 GHz), WMAP (23 and 33 GHz), and Planck (PR4 at 30, 44, 143, 217, and 353 GHz). Covering an effective area of roughly 400 square degrees (equivalent to 1% of the sky), this dataset is centered on a region characterized by minimal foreground emission. The data model encompasses Galactic dust and synchrotron emission, incorporating correlations between dust and synchrotron components.

14.1.3 *LIGO-Virgo-KAGRA Interferometers*

GW interferometers probe scales ($k \sim 10^{16}\,\mathrm{Mpc}^{-1}$) nearly 18 orders of magnitude above those probed by the CMB ($k \sim 10^{-2}\,\mathrm{Mpc}^{-1}$), offering a potent means to constrain small scales.

We adopt the same approach as described in Chap. 13.

14.1.4 *Combinations of Data*

We consider a *baseline* combination of datasets:

- *Planck* PR3 lowl TT [43, 270],
- *Planck* PR4 LoLLiPoP [263],
- *Planck* PR4 lensing [294],
- BICEP/Keck array 2018 (BK18) [113],
- LVK 2021 (LVK21) [277],

Note that these datasets do not cover the high ℓ part of CMB, thus we define on top of *baseline* the 2 combinations of datasets we explore in this work as

1. *baseline* + CamSpec [292]

2. *baseline* + HiLLiPoP [29]

For notation sake, we will avoid writing "baseline" every time referring to these two combinations of datasets. Any eventual modification will be emphasized.

Note that we slightly modified the high-ℓ likelihoods (both HiLLiPoP and CamSpec) to avoid any correlation with the low-ℓ LoLLiPoP. Indeed, to maximize the information coming from BB, we use LoLLiPoP up to $\ell = 150$ and consequently adjust the ℓ_{min} of high-ℓ likelihoods for EE at $\ell = 151$.

As previously done in [263], we neglect correlations between *Planck* and BICEP/Keck datasets and simply multiply the likelihood distributions. This is justified because the BK18 spectra are estimated on 1% of the sky, while the *Planck* analysis is derived from 50% of the sky.

14.2 METHODOLOGY

We will not enter the details of either MCMC or PL, given that they have been discussed in Chap. 11 and Chap. 12. Still, let us spend some words on the latter.

To derive a confidence region that has the correct frequentist coverage properties, one can make use of the likelihood ratio statistics. For multi-parametric spaces, this amounts to constructing the likelihood profile: for fixed values of the parameter of interest (p_i), we look for the maximum of the likelihood function in all the other dimensions (for both the physical parameters and the nuisance parameters). We then have access to the function $\chi^2_{min}(p_i) = -2 \ln \mathcal{L}_{max}(p_i)$.

The best fit (or $\min(\chi^2_{min}(p_i))$) gives the mean value of the parameter under consideration. This procedure ensures that its determination is independent of any change of variable, making it parameterization invariant; furthermore, no integration is performed, since we do not have to marginalize as in a Bayesian framework (see Chap. 11), thus this procedure is also robust to any volume effect.

The error on the parameter p can be deduced from the shape of the $\chi^2_{min}(p_i)$ function. For a parabolic shape (i. e. Gaussian estimator distribution), the 1σ error bounds are simply obtained by a cut at $\chi^2_{min}(p_i) - \min(\chi^2_{min}(p_i)) = 1$. For more asymmetric shape of the χ^2 function near the minimum, or when dealing with physical boundaries, one needs to make use of the FC prescription and the Neyman construction (see Sec. 12.4).

Finally, in Chap. 11 we do not mention a byproduct of PL: *co-profiles*. Not only do we obtain a function $\chi^2_{min}(p_i)$, but also $N - 1$ functions $p_j(p_i)$ where $j \neq i$. These co-profiles allow us to gauge the direction of degeneracy of other parameters on the profiled one and are very useful as a diagnostic tool of the PL procedure.

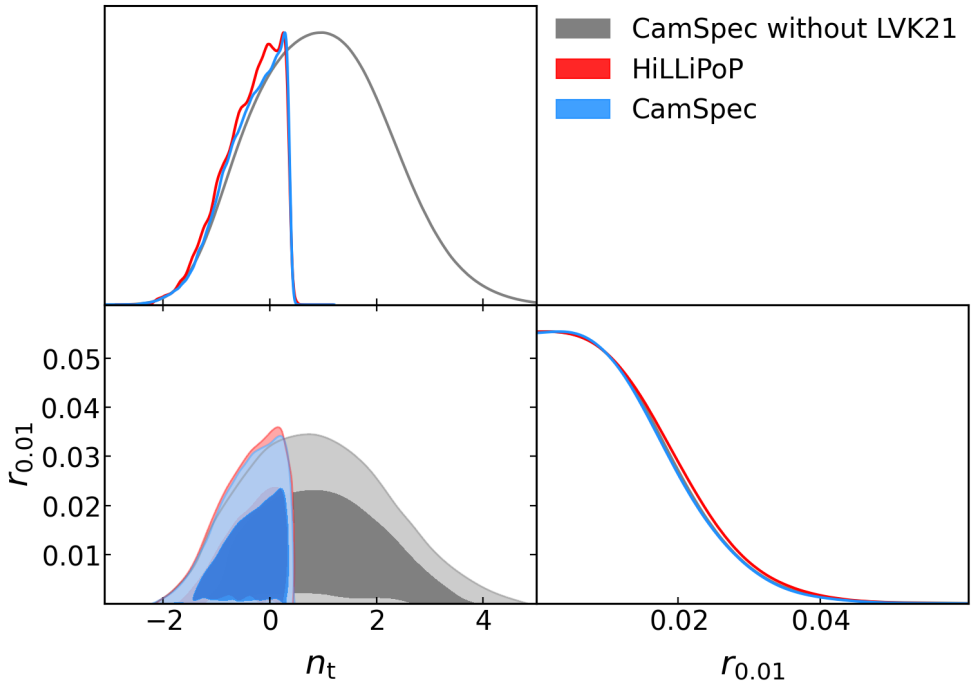

Figure 47: 2D posterior of $r_{0.01} - n_t$ for *baseline* + CamSpec and *baseline* + HiLLiPoP.

From a more pragmatic point of view, here, we consider `CAMB` as a Boltzmann solver [245, 261, 262] and the `MINUIT` algorithm[6] to minimize our likelihoods [295] [7].

As done for the MCMC, we use `Cobaya` to compute the PL. Together with the MCMC infrastructure, this code is capable of providing the maximum likelihood; thus, by modifying it, we can build our PLs. `Cobaya` also offers two alternative minimizers: `py-BOBYQA` [296] and `scipy` [297], however, in our case, `MINUIT` outperformed both. For this reason, we contributed to the addition of `MINUIT` as an alternative minimization method in the official release of `Cobaya`. Furthermore, at the time of writing, the new module of `Cobaya` that we use to perform PLs is being reviewed for approval in the official release.

One of the difficulties in constructing the PL is the precision with which we need to determine the values of $\chi^2_{min}(p_i)$. We must rely both on a very accurate minimizer and on a possible boost to the accuracy parameters of the Boltzmann code [298]. Various configurations have been tested here that are further detailed in Sec. D.1.

14.3 MCMC RESULTS

Here we report the results of the MCMC preformed on the *baseline* combination plus CamSpec or HiLLiPoP. Fig. 47 shows the resulting 2D posteriors.

6 We may refer to this algorithm with `iMinuit`, which is the python wrapper of `MINUIT`.

7 We will use the expression "minimize a likelihood", we refer to the fact that we can obtain the maximum of $\mathcal{L}$ by minimizing its logarithm. Of course, the two are totally equivalent.

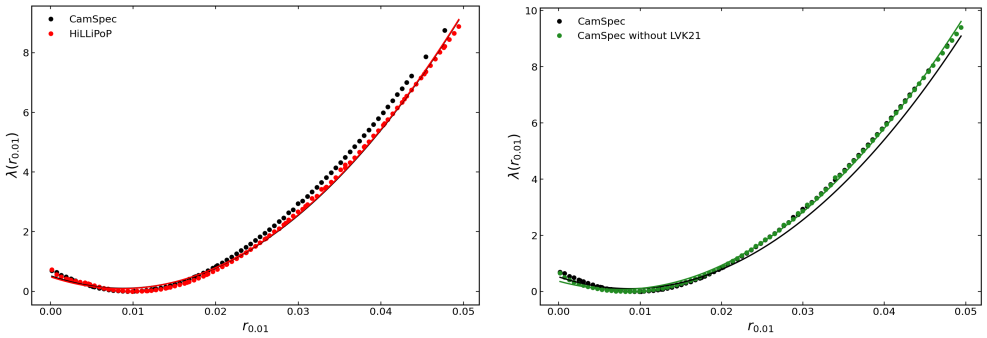

Figure 48: *Left:* Comparison of PL between HiLLiPoP and CamSpec. *Right:* Different considering LVK21 or not.

The 95% CL marginalized intervals for HiLLiPoP are

$$r_{0.01} < 0.029 \quad \text{and} \quad -1.39 < n_t < 0.41 \,, \tag{409}$$

while for CamSpec

$$r_{0.01} < 0.028 \quad \text{and} \quad -1.36 < n_t < 0.42 \,. \tag{410}$$

Furthermore, we repeat the analysis of CamSpec removing LVK21 to gauge the contribution of GW interferometers. As expected, LVK21 severely constrains the blue tilts; removing it yields

$$r_{0.01} < 0.029 \quad \text{and} \quad -1.35 < n_t < 3.36 \,. \tag{411}$$

These are very similar to the results of [259] presented in Chap. 13 [8]. When using GW interferometers they obtained $r_{0.01} < 0.028$ and $-1.37 < n_t < 0.42$ at 95% CL. This suggests that the tensor sector has remained stable after updating the dataset to PR4, since it is dominated by the low-ℓ part. The most relevant difference is the slightly more conservative bound provided by HiLLiPoP. As regards the case without LVK21 likelihood, they obtained $r_{0.01} < 0.029$ and $-1.21 < n_t < 3.54$ at 95% CL. In this case, the bound on the tensor-to-scalar ratio has remained identical, while the one on the tilt has shifted a little to the left.

14.4 PROFILE LIKELIHOOD RESULTS

14.4.1 *Tensor-to-scalar Ratio*

First, we apply the PL described in Chap. 12 to the tensor-to-scalar ratio. Our underlying model is ΛCDM + $r_{0.01}$ + n_t, so the likelihoods are minimized both w. r. t. the standard ΛCDM parameters and n_t (together with all the nuisance parameters in each likelihood). Fig. 48 shows the results for the combinations of datasets defined above.

All of them are very similar, however, one can note that HiLLiPoP tends to provide slightly shallower bounds w. r. t. CamSpec, as in the MCMC case.

8 In that work, PR3 was used both for the high-ℓ part of *Planck* (*plik*) and for the lensing. Thus, one should compare these sets of intervals with care.

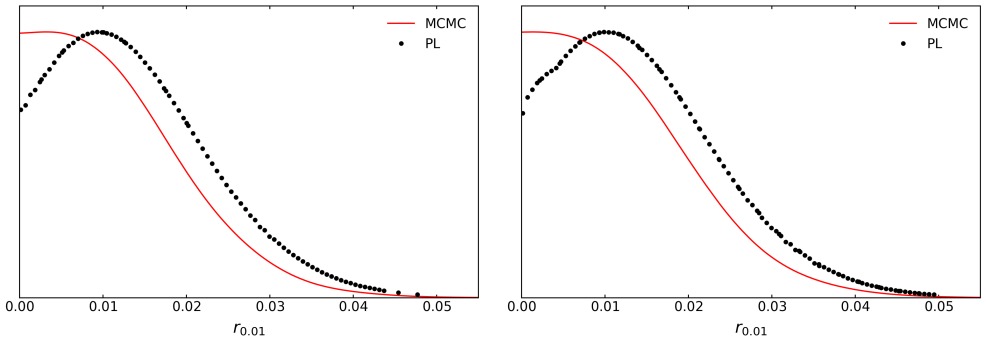

Figure 49: Comparison between the 1D marginalized posteriors and the profiles on $r_{0.01}$.

Despite this, the most striking feature of this plot is found when focusing on the parabolic fit we show with solid lines. Indeed, using the complete set of points to fit a parabola results in a poor description of χ^2 around the minimum. From Chap. 12 we know that the PL is expected to follow a χ^2 distribution if Wilks' theorem is satisfied. This seems to hold near the absolute minimum and not far away from it. In fact, if we exclude the points with $r_{0.01} \gtrsim 0.02$, we recover Gaussianity.

Before quantitatively reporting the confidence intervals using the FC prescription, we show in Fig. 49 the comparison between the PL points and the posterior distribution obtained in the previous section for CamSpec. This suggests that some volume effect is present in the Bayesian framework, pushing the posterior towards $r = 0$. Note that this feature is not present in Chap. 13 using the profile distribution. This also suggests that this approximate technique fails to detect this volume effect, so one must be careful when using such a shortcut.

If we now forget about the FC prescription, we could try to integrate the curve underlying the PL points. This amounts of applying a Bayesian reasoning to a PL, which is not a likelihood and, more importantly, is not the PDF of $r_{0.01}$. Thus, it is difficult to give an interpretation of the result, and we are not guaranteed at all that it has the correct coverage probability [299]. Despite this, we find that the 95% integral of the distribution gives $r_{0.01} < 0.028$.

14.4.2 *Feldman-Cousins for $r_{0.01}$*

We now apply the FC prescription to recover the confidence interval with the correct coverage probability and accounting for the physical limit $r_{0.01} \geq 0$.

We have seen in Chap. 12 that for a Gaussian distribution with parameter θ we can include a physical bound in a frequentist framework by using the following test statistic

$$\lambda(\theta) = \frac{f(x|\theta)}{f(x|\widehat{\theta})} = \begin{cases} \exp\left(-\frac{(x-\theta)^2}{2}\right) & \text{if} \quad x \geq 0 \\ \exp\left(x\theta - \frac{\theta^2}{2}\right) & \text{if} \quad x < 0 \end{cases} . \tag{412}$$

However, we mentioned above that the PL points we get from both CamSpec and HiLLiPoP are not following a χ^2 distribution far away from the

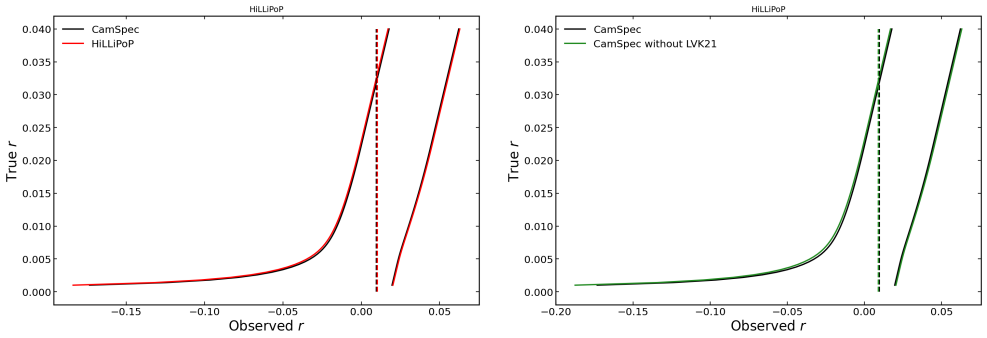

Figure 50: FC belts for CamSpec and CamSpec without LVK21 (left), and CamSpec and HiLLiPoP (right).

best-fit value of $r_{0.01}$. Furthermore, Fig. 49 shows an additional characteristic of HiLLiPoP; in fact, at the lowest values of $r_{0.01}$, the PL presents a "bump". In Sec. D.3 we explore the possibility of generalizing the FC prescription to more complex curves that fit our data. Still, for the purpose of this section, the solution has already been suggested: near the best-fit the PL is Gaussian. However, what does *near* mean? Since we are interested in precisely describing the best-fit value, we can look at the chi^2-distance between χ^2_{min} and the value of our fit at the same value of $r_{0.01}$. If we use the complete set of points, we typically get quite large distances, so we cut the considered points until we minimize this quantity. The results are shown in Fig. 50 for CamSpec. We call this approach "partial Gaussian" to emphasize that we are discarding a part of the PL. In the case of HiLLiPoP, we also exclude the points belonging to the extra bump mentioned above.

In terms of upper bounds, we obtain

$$\begin{aligned} r_{0.01} &< 0.032 \quad \text{with CamSpec,} \\ r_{0.01} &< 0.032 \quad \text{with CamSpec without LVK21,} \\ r_{0.01} &< 0.033 \quad \text{with HiLLiPoP.} \end{aligned} \tag{413}$$

All these bounds are more conservative w. r. t. Sec. 14.3, showing that the MCMC seems to be affected by some volume effect toward $r = 0$.

14.4.3 *Tensor Spectral Tilt*

Looking at the PL for n_t in Fig. 51, it is clear that we are far from a χ^2 distribution. In such an extreme case, it is hard to extract solid statistical results in terms of coverage probability.

In principle, to build the FC intervals we need the analytical expression of the likelihood as a function of the profiled parameter (see Chap. 12 and Sec. D.3); however in this case it is clear that we do not have that. Alternatively, we could empirically build the likelihood. This requires the capability of simulate reliably the data for any value of n_t. Even though this route is feasible, it is outside the scope of this work.

The only thing we can do is qualitatively describe the PL we get. Let us start as in Sec. 14.4.1 by comparing CamSpec and HiLLiPoP: the most striking feature of Fig. 53 is the presence of two "plateaus" in the PLs at blue and red

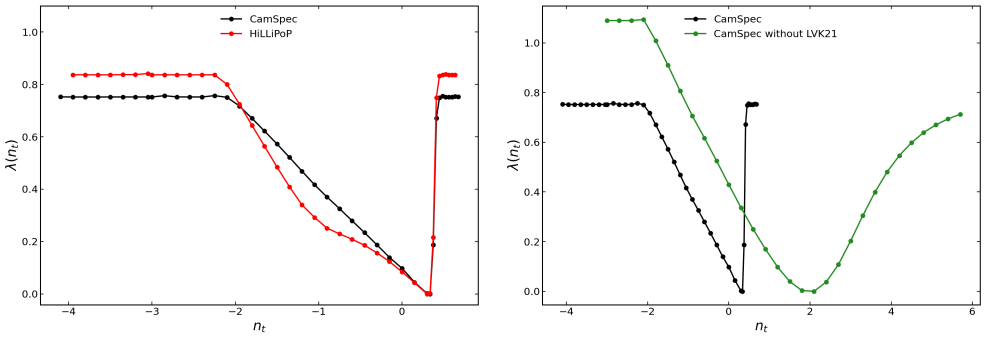

Figure 51: PL on the tensor spectral tilt. *Left:* comparison between Campsec and HiLLiPoP. *Right:* comparison between CamSpec with and without LVK21.

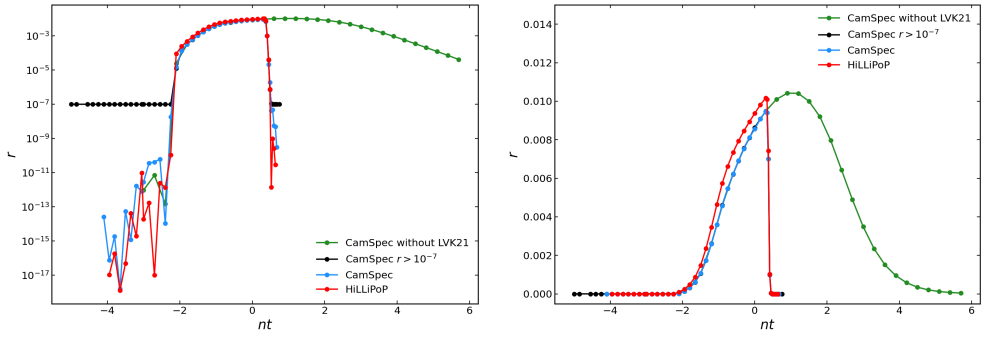

Figure 52: Co-profiles of $r_{0.01}$ as a function of the profiled value of n_t. On the left we use a logarithmic axis for $r_{0.01}$ to underline the behavior at small values. On the right, the axis is linear, showing that the behavior resembles the posteriors obtained in Sec. 14.3.

tilts. Furthermore, we can see that both datasets do not have clear upper or lower bounds. Finally, note that both plateaus have a quite low value of λ. Furthermore, we note that the plateaus of HiLLiPoP are slightly higher than the ones of CamSpec. The former also shows a "bump" at $n_t \sim -1$. These characteristics raise some questions: why do we not see the same plateaus in the MCMC analysis of Sec. 14.3? What does it mean to have no bounds on n_t?

To answer both questions, we can look at the co-profiles mentioned in Sec. 14.2. For example, we can look at $r_{0.01}(n_t)$, since the likelihoods are minimized w. r. t. the tensor-to-scalar ratio too.

Focusing on the left panel of Fig. 52, which shows the results, we can see that to accommodate more and more extreme values of n_t, the tensor-to-scalar ratio is suppressed to very small values. This is exactly the reason behind the analysis we show in Chap. 13 with SSA and TSA. Indeed, if we do not impose a lower cutoff in $r_{0.01}$, the datasets we consider are not sufficient to constrain n_t given that one can always find a value of $r_{0.01}$ low enough to accommodate any tilt. This is the reason why we do not have a clear upper or lower bound on n_t in Fig. 51. In obtaining that figure, we encounter numerical problems as we try to probe more extreme tilts, and the $r_{0.01}$ tends to zero.

Thus, the reason why we do not see these plateaus in Sec. 14.3 is also clear: by assuming $r_{0.01} > 10^{-5}$ we do not allow the chain to explore these regions of parameter space. Despite this, the values of $r_{0.01}$ found by the PL minimization are so low ($r_{0.01} \sim 10^{-10} - 10^{-17}$) that even without the

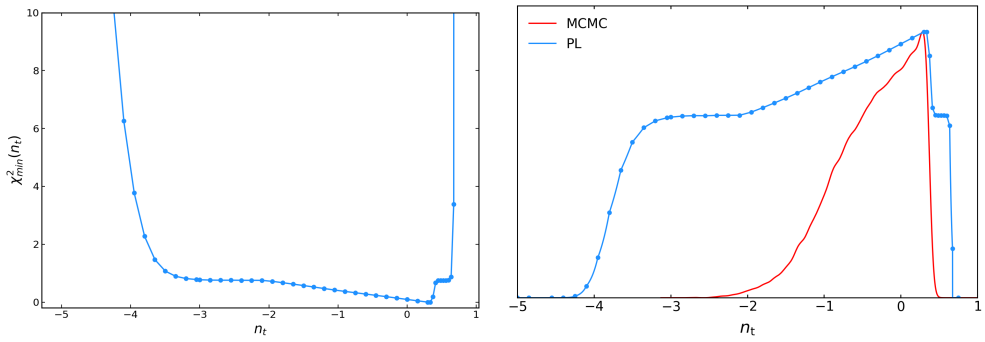

Figure 53: *Left:* Comparison between PL on n_t and the Gaussian prescription to obtain the confidence intervals. *Right:* Comparison between the PL and the MCMC results on n_t.

SSA cutoff it would be impossible to explore that region with our MCMC[9]. Finally, not that the region explored by the MCMC corresponds to the region of the co-profile with the highest values of $r_{0.01}$. This also corresponds to the region of the PL between the plateaus.

Looking instead at the right panel of Fig. 51, we can see that removing LVK21 brings us to an even less constraining scenario for blue tilts.

To obtain constraints on n_t, we can try to mimic the MCMC procedure. For example, we try to profile the tilt while asking $r_{0.01} > 10^{-7}$. The results are shown in the left panel of Fig. 53. First, note that as soon as the tensor-to-scalar ratio is restricted, we recover both an upper and a lower bound. In fact, even with $r_{0.01} = 10^{-7}$, at some point the tilt will be so red that the corresponding B-modes should be observed by LoLLiPoP. Thus, this will make χ^2 diverge to infinity.

Furthermore, we show in the right panel of Fig. 53 the comparison between the PL and the 1D marginalized posterior from the MCMC analysis. This clearly shows the difference between the two approaches caused by the features we just discussed.

14.5 2D PROFILE

An alternative way to obtain constraints on n_t is to fix the value of $r_{0.01}$. Say, for example, that we fix the tensor-to-scalar ratio to the value predicted by Starobinski inflation $r_{0.01} \sim 0.0046$ (see Chap. 5). The profile on n_t would be the one shown in Fig. 54.

Note that the plateaus are not present in this PL and we get both an upper and a lower bound, in agreement with what we would expect from the previous discussion. Also, note that the lower bound is found well before the one of Fig. 53, due to the fact that this value of $r_{0.01}$ does not allow for very red tilts.

Furthermore, we can reiterate this procedure for an array of values of $r_{0.01}$, effectively getting a 2D PL on the tensor sector of parameters. With such a tool, we can extract the PL of n_t for any hypothetical value of the tensor-to-scalar ratio, and vice versa.

9 This is not strictly impossible, but rather extremely unlikely. Indeed, it is a well-known feature of uniform priors to poorly explore the region where the parameter of interest is extremely close to the boundaries

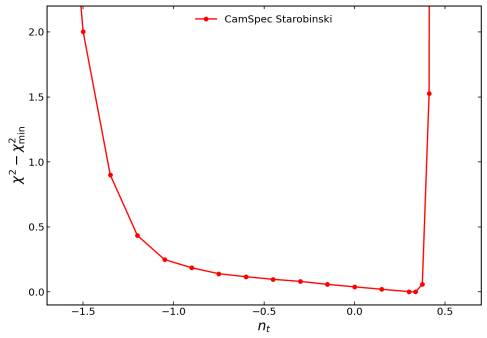

Figure 54: PL on n_t assuming Starobinski inflation.

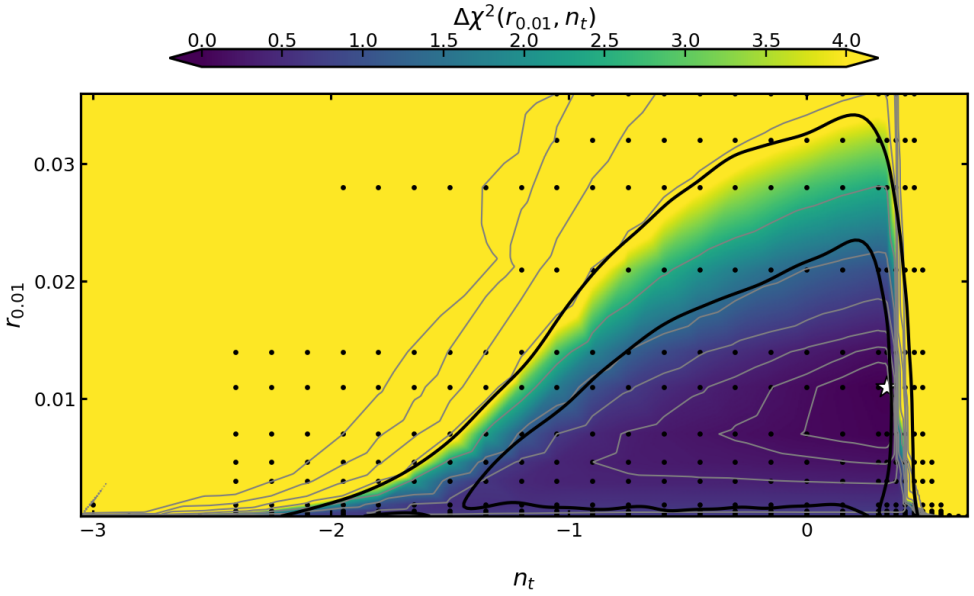

Figure 55: 2D PL on $r_{0.01}$ and n_t. The star indicates the absolute minimum we find with this procedure, whereas the gray lines show some iso-χ^2 curves to emphasize the 2D shape of the profile. The black dots are the points in which a minimization is performed. Furthermore, we show in black solid the 2D marginalized posterior.

Of course, such an analysis is very demanding in terms of Central Processing Unit (CPU) time, given that we have to iterate an already computationally heavy procedure. For this reason, we perform it only on CamSpec, which is our fastest combination of datasets. We showed before that this dataset does not differ much from HiLLiPoP, therefore the results we are about to present can be taken as representative of both. Still, we again emphasize the difference in plateau levels and the presence of a bump for HiLLiPoP shown in Fig. 51. These may change the results; we plan to explore this in the future.

We assume a range of the tensor-to-scalar ratio from a maximum of $r_{0.01} = 0.028$, saturating the bound in Sec. 14.3, to a minimum of $r_{0.01} = 10^{-6}$, for a total of $N = 15$ steps. The range in n_t varies case by case, as Fig. 55 shows. Then, we interpolate these points to get a smooth surface that represents the result for $N \to \infty$.

Here, if we imagine intersecting this surface with any horizontal (vertical) plane for a value of $r_{0.01}$ (n_t), we would obtain the PL of n_t ($r_{0.01}$) conditioned on that value.

Furthermore, we can overplot the marginalized 2D posterior from Sec. 14.3 to obtain the solid black contour in Fig. 55.

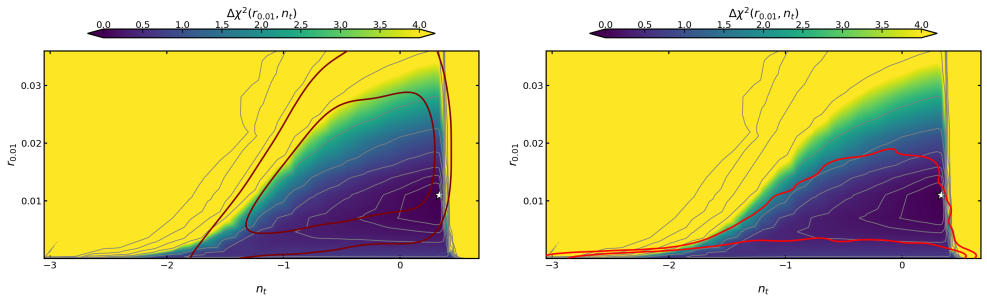

Figure 56: *Left:* Comparison between the 2D PL on $r_{0.01}$ and n_t and the 2D marginalized posterior when following the TSA. *Right:* Same comparison but exploiting the SSA with a log-uniform prior on $r_{0.01}$.

Note that the posterior seems to follow the same behavior as the iso-χ^2 curves. This suggests that in the context where we do not allow $r_{0.01} \to 0$, the MCMC and the PL agree to each other; this means that there are no volume effects on the $r_{0.01} - n_t$ plane. On the other hand, these effects manifest when we integrate over n_t as in Sec. 14.3.

In other words, this 2D PL shows that the marginalized 2D posterior obtained with the MCMC procedure described in Chap. 13 (i. e. the SSA) is not affected by volume effects. However, when reporting the results for $r_{0.01}$ alone is necessary, an extra marginalization in n_t must be made. Instead, in Fig. 87 of Sec. C.3 we show that typically TSA brings to posteriors that significantly detach from $r = 0$ and tend to increase this gap towards the red tilts. Both of these features are not present in our 2D PL suggesting that those are artifacts induced by the prior.

In response to this result, we tested the TSA on the same dataset explored here, thus repeating the MCMC analysis presented above while sampling r_1 and r_2 (see Chap. 13). Furthermore, we employ a SSA with a log-uniform prior on $r_{0.01}$. This set of "initial conditions" of the MCMC encompass the most "popular" choices explored in the literature. The results are shown in Fig. 56, which proves that both the TSA and the log-uniform prior on $r_{0.01}$ bring to a clear mismatch with the 2D PL, even though in opposite directions.

This confirms the discussion above and suggests that the SSA is the approach that reproduces more faithfully the 2D frequentist results.

14.6 SUMMARY AND CONCLUSIONS

In this chapter, we explore the tensor sector of parameter space utilizing the latest available data. Specifically, while allowing all the ΛCDM parameters to freely vary (see Sec. D.2), we focus on the tensor-to-scalar ratio $r_{0.01}$ and the tensor spectral tilt n_t. Our dataset encompasses information from *Planck* satellite, covering both CMB temperature and polarization, alongside polarization data sourced from the BICEP/Keck array. Given that these experiments lack access to the small scales of the tensor spectrum, we incorporate the LVK upper bound on the energy density of GWs to constrain this region (see Sec. 14.1). Within this data ensemble, we define two combinations of datasets explored in this work. The key distinction between the two lies in the choice of the high ℓ likelihood, either CamSpec or HiLLiPoP.

In Sec. 14.2, we outline our methodological approach. Firstly, we assume for the MCMC analysis the same setup explored in Chap. 13, and in particular the SSA. Secondly, we introduce the PL, discussed in more detail in Chap. 12. We already mentioned that the Bayesian approach may encounter volume effects arising from the marginalization procedure in a multi-dimensional parameter space, potentially influencing conclusions, especially for relatively unconstrained parameters. In this context, the PL offers a volume-effect-independent means to explore these aspects and present an alternative perspective on the tensor sector. Both the MCMC and the PL are executed using a modified version of `Cobaya`, leveraging `CAMB` for power spectra computation and `MINUIT` for chi^2 minimization (see also Sec. D.1). This version of `Cobaya` that we have developed, featuring the capability to perform a PL, will soon be made publicly available.

From a Bayesian standpoint (Sec. 14.3), the tensor sector of the parameter space appears to have remained robust following the dataset update compared to [259]. Specifically, utilizing HiLLiPoP yields $r_{0.01} < 0.029$ and $-1.39 < n_t < 0.41$ at a 95% CL, while with CamSpec, we obtain $r_{0.01} < 0.028$ and $-1.36 < n_t < 0.42$ at 95% CL. Both results align well with the prior state-of-the-art bounds from Chap. 13. Additionally, we replicate the analysis with CamSpec, excluding the likelihood from LVK, resulting in a significantly broader upper bound on n_t as anticipated: $r_{0.01} < 0.029$ and $-1.35 < n_t < 3.36$ at 95% CL. This underscores the critical role played by GW interferometers in constraining the tensor spectral tilt.

In Sec. 14.4.1, we scrutinize the PL of $r_{0.01}$. Upon inspecting the profiles derived from our dataset combinations, we observe a departure from a Gaussian distribution, especially for points in far away from the absolute minimum (refer to Fig. 49). While this non-Gaussian behavior is anticipated when Wilks' theorem is not applicable, it is noteworthy that the departure impacts points close to the minimum too, particularly in the HiLLiPoP case. To restore the validity of Wilks' theorem, we discard these points and apply the FC prescription in Sec. 14.4.2 (see also Sec. D.3). The results indicate that CamSpec (with and without LVK) yields $r_{0.01} < 0.032$ at 95% CL, whereas HiLLiPoP leads to $r_{0.01} < 0.033$. Both results show a more conservative stance compared to the MCMC analysis, suggesting that the latter could be influenced by volume effects.

Having said this, we must emphasize the difference between a Bayesian and a frequentist statement on $r_{0.01}$. In a Bayesian context, the upper bound on the tensor-to-scalar ratio is a statistical statement grounded in the posterior, representing the PDF of $r_{0.01}$ given the data. This means that $r_{0.01} < 0.028$ (or 0.029 for HiLLiPoP) signifies the most probable region to locate the true value of the parameter within our assumptions, with probability determined by the CL. As demonstrated in Chap. 13, different assumptions yield distinct results, showcasing an inherent characteristic of Bayesian analysis, especially for insufficiently constrained parameters. For example, the TSA analyzed in Chap. 13 brings to a "2σ detection" of $r_{0.01}$ as a result of the prior choice. Conversely, the PL result $r_{0.01} < 0.032$ (or 0.033 for HiLLiPoP)

is a statistical statement about the likelihood, i.e. the PDF of data given the theoretical model. In other words, $r_{0.01} = 0.032$ represents the largest value of the tensor-to-scalar ratio that can consistently explain our data in 95% of N hypothetical repetitions of the Universe. Of course, this consideration assumes the correctness of the ΛCDM model used to describe the Universe.

The results for the tensor spectral tilt are presented in Sec. 14.4.3. As evident from Fig. 51, employing the FC prescription utilized in Sec. 14.4.2 is not feasible here, as the profile does not exhibit a Gaussian shape. Moreover, the absence of a distinct bound, either lower or upper, suggests the potential accommodation of highly extreme spectral tilts at the expense of driving $r_{0.01}$ toward zero (refer to Fig. 52). This is fundamentally linked to the problematic behavior of the MCMC method mentioned earlier. As in that scenario, imposing a lower cutoff to $r_{0.01}$ resolves this issue, as depicted in Fig. 53. However, due to the intricate shape of the profile, extracting a reliable confidence interval remains challenging, as there is no assurance of achieving the correct frequentist coverage probability.

Moreover, after illustrating the PL while fixing $r_{0.01}$ to the value predicted by Starobinski inflation, we conduct a 2D PL analysis involving both $r_{0.01}$ and n_t (Sec. 14.5). In Fig. 55, a noteworthy agreement between this 2D PL and the 2D marginalized posterior obtained with the SSA is evident. This suggests two key observations: firstly, it indicates that no volume effects are induced by other parameters (physical or nuisance) on this 2D plane; secondly, as a consequence, the volume effects emphasized in Sec. 14.4.1 are generated by the integration in n_t. This result prompted us to explore the consequences of other commonly used priors on $r_{0.01} - n_t$. For this reason, we re-run the MCMC for CamSpec, adopting both the aforementioned TSA and an SSA with a log-uniform prior on $r_{0.01}$ [10]. Subsequently, in Fig. 56, we present the same comparison between 2D posterior and 2D PL. The figure clearly indicates that these two alternative approaches result in a mismatch (i.e., a volume effect) that is not present in the SSA case. In particular, the TSA seems to be pushed toward relatively high values of $r_{0.01}$, as already demonstrated by [259]. On the contrary, the log-uniform case induces a significant push on $r_{0.01}$ toward zero.

Embracing the philosophy that achieving correspondence between frequentist and Bayesian approaches is at least desirable [255, 299], the SSA appears to be the most suitable choice to mitigate additional volume effects on the 2D plane. Nevertheless, it is important to reiterate that no formal contradiction exists in any of the Bayesian methods mentioned above. However, it is crucial to be aware and transparent of the effects introduced by the assumptions employed.

In this work, we do not provide any frequentist bound on n_t, given the issues mentioned above. However, a potential avenue for obtaining it exists. Specifically, we could simulate N realizations of the CMB with M different values of n_t to empirically derive the likelihood. This would allow us to

10 We will refer to this as the "log-uniform case".

build the FC belt and extract bounds with the correct coverage probability. We leave this for future exploration.

In summary, this chapter delivers a comprehensive and statistically robust analysis of the tensor sector of parameter space. Beyond offering an updated perspective utilizing the latest datasets, the analysis underscores the significance of probing relatively unconstrained parameters with frequentist approaches, complementing the widely used Bayesian methods. This insight proves valuable for forthcoming investigations into CMB polarization, such as with LiteBIRD, and for any endeavors exploring extensions to the standard ΛCDM model.

15

CONCLUSIONS

Here, we summarize the journey outlined in this thesis. The manuscript is organized into four parts, divided into two groups. The first group includes Part I and Part II, where we lay down the theoretical foundations necessary for subsequent discussions. Initially, we introduce the key elements of our current understanding of the Universe, overlooking the presence of GWs. We then incorporate tensor perturbations to examine the implications of their existence and the imprints they generate as they propagate to us.
The second group stems from the first, addressing two fundamental questions: What happens if we deviate from the standard cosmological model? What insights do we have into the tensor sector of parameters with current data? Part III delves into the first question, while Part IV tackles the latter.
This exploration provides a glimpse into the origins of our Universe, with a particular focus on the inflationary model at its core. Here, we will present the main conclusions drawn from this extensive exploration.

15.1 ADDING TENSOR PERTURBATIONS TO A "SCALAR" UNIVERSE

In Part I, we begin by introducing the basics of Cosmology (Chap. 1). A crucial concept is the thermal coupling between particle species and the thermal bath. The moment of decoupling determines the physics to which a particle is sensitive, making information before decoupling inaccessible (see Chap. 2).

This concept enables us to trace the thermal history of the Universe, revealing its "Big-Bang evolution". However, this description conceals flaws, manifesting as a fine-tuning of initial conditions to match current observations (Chap. 3). Here, inflation justifies its existence, resolving inconsistencies in the hot Big-Bang model.

In Chap. 4, we dive into the basics of the inflationary paradigm, focusing on the single-field slow-roll model. Toward the end of the chapter, we introduce a key actor: the CMB. This radiation, a consequence of the thermal decoupling of photons, exhibits characteristic anisotropies stemming from quantum fluctuations of the inflaton during inflation.

Studying the consequences of adding GWs to our Universe's recipe is the focus of Part II. In Chap. 5, we explore predictions of single-field slow-roll inflation and more complex scenarios. The key takeaway is that GWs leave specific imprints, such as the B-mode polarization of CMB photons.

Additionally, GWs constitute a primordial background (CGWB) characterized similarly to CMB photons using the Boltzmann equations (Chap. 6). We show the complete computation to pass from the Boltzmann equations to the

final angular power spectra of the CGWB. One of the key messages here is that GWs are not coupled with the "rest-of-the-world" below energies of the Planck mass. This is a crucial difference w. r. t. photons, which allows us to have a direct window on the physics of inflation. Having introduced tensor perturbations, this section provides a complete picture of the Universe.

15.2 DEPARTURES FROM THE STANDARD MODEL OF COSMOLOGY

In Part III, we test departures from the standard model. The cosmological principle assumes the Universe is homogeneous and isotropic. However, Chap. 7 presents observational hints of potential violations, specifically the CMB anomalies. In particular, we delve into the hemispherical power asymmetry in Chap. 8, which can be described as a modulating field acting on the scalar perturbations. We perform the complete computation that accounts for this anomaly when we consider the Boltzmann equations of the CGWB. This brings us to the first theoretical results of this work: in previous studies (see [181]) the ISW effect was neglected for the CMB case. Here, we not only include this effect, but also provide equivalent equations for the CGWB.

In Chap. 9, our focus shifts to the practical implementation of these expressions, which involves a modification of the CLASS Boltzmann solver. Additionally, we introduce a generalized form of the well-known constrained realization formulas, enabling the simulation of a CGWB sky based on Planck CMB maps. Notably, this generalization accounts for the couplings between multipoles introduced by the modulating field. These tools play a pivotal role in forecasting the potential of GWs in aiding the measurement of such a modulating field, crucial for explaining the observed anomaly. Our approach involves assuming a cosmic-variance-limited observation and considering the capabilities of future space-based GW interferometers, namely LISA and BBO. Despite the inherent complexity associated with measuring primordial GWs, our analysis demonstrates that BBO holds significant promise in helping us unravel the physical origin of the hemispherical power asymmetry.

In Chap. 10, our attention shifts to a distinct CMB anomaly known as the lack-of-correlation. Specifically, the two-point angular correlation of temperature perturbations in photons exhibits an unexpected consistency with no correlation on scales larger than 60°, a departure from the predictions of the ΛCDM model. The motivation behind this chapter mirrors that of Chap. 8: can an observation of the CGWB assist in elucidating the physical nature of this feature?

Once again, we introduce a generalization of the constrained realization expressions, this time incorporating the effects of a mask on the CMB sky. Additionally, we define a novel estimator tailored for this anomaly, capable of addressing the so-called "look-elsewhere" effect. Moreover, for each considered observable (or combination thereof), we identify the optimal angular range for future investigations into this anomaly. Finally, we establish that a GW observation would significantly enhance the statistical significance of

detecting the lack-of-correlation, even under the most pessimistic scenario considered in this study.

15.3 STATISTICS AND DATA ANALYSIS

In Part IV, our attention turns to the statistical methods and data analysis underpinning the current understanding of our Universe. Specifically, Chap. 11 delves into Bayesian statistics and introduces the widely recognized MCMC analysis. In the realm of Cosmology, adopting a Bayesian perspective is a natural choice, given our reliance on a single realization of the Universe for analysis. However, it is crucial to acknowledge that the MCMC analysis can be influenced by volume effects, potentially leading to misleading conclusions on certain parameters, especially when these parameters lack robust constraints from the data. To address this, we explore an alternative approach in Chap. 12, focusing on frequentist statistics, i. e. a methodology independent of prior choices and volume effects. Here, we introduce the PL analysis, serving as a complementary tool to the MCMC approach. This dual perspective allows for a more robust and comprehensive examination of the data, enhancing our ability to draw meaningful conclusions about the fundamental parameters of the Universe.

In Chap. 13, we examine the Bayesian perspective on the tensor sector of the parameter space. The chapter provides a comprehensive analysis of the consequences arising from two different prior choices commonly employed in the literature.

Following a series of tests to determine the most reliable approach for constraint derivation, we analyze 10 distinct combinations of datasets, incorporating information from sources such as CMB, GW interferometers, and PTA data. This collective effort culminates in establishing the most stringent upper bound on the tensor-to-scalar ratio currently available in the literature.

However, the obtained result might be influenced by the volume effects mentioned earlier. Therefore, in Chap. 14, we explore the frequentist counterpart of this analysis. Initially, we update the datasets considered to include the most recent ones available in the market. Subsequently, we conduct both a MCMC and a PL analysis to provide a comprehensive understanding of the tensor sector of the parameter space. As of the current writing, this project is still a work in progress; nonetheless, it has already yielded intriguing insights.

From a Bayesian standpoint, we reaffirm results consistent with those in Chap. 13; however, we highlight their susceptibility to volume effects.

On the other hand, we present the inaugural PL performed on the tensor spectral tilt and the first 2D PL on the tensor sector. The latter implies a concurrence between the MCMC and PL outcomes when employing a single-scale approach to sample the tensor sector, aligning with the discourse in Chap. 13.

In essence, Chap. 13 and Chap. 14 collectively constitute a thorough and statistically sound data analysis of the tensor sector of the parameter space.

These chapters underscore a crucial aspect of the present and future exploration of primordial GWs and, consequently, the inflationary model. In the absence of a tensor-to-scalar detection, it becomes imperative to remain cognizant of potential prior dependencies, volume effects, and biases. Therefore, a Bayesian approach should involve studying the effects of different priors that may encapsulate diverse prior beliefs. Furthermore, the integration of a PL is vital for a comprehensive evaluation of MCMC results, recognizing the fundamental distinction between credible and confidence intervals.

15.4 FUTURE PROSPECTS

This Thesis encapsulates a portion of the work accomplished over the course of three years in pursuit of this Philosophiae Doctor (PhD) degree. It serves as a foundational platform for my ongoing and future explorations in the realms of inflation and primordial GWs.

In Chap. 9 and Chap. 10, we demonstrated that GWs emerge as invaluable tools to scrutinize the physical nature of CMB anomalies. Specifically, the cross-correlation between the CMB and the CGWB opens avenues for intriguing analyses. Utilizing the tools developed in these chapters, we can extend our investigations to different features connecting GWs and CMB photons.

In the field of data analysis, we showcased in Chap. 13 and Chap. 14 a robust approach to confining the tensor-to-scalar ratio and the tensor spectral tilt, employing both Bayesian and frequentist perspectives. Nevertheless, numerous potential refinements to these analyses beckon for exploration in the future. For example, can we employ more sophisticated statistical tools to scrutinize these parameters? Or, is there room for improvement in our depiction of the likelihood, capturing the probability of observed data given our theoretical framework? Although these questions serve as examples, I think that the response to both is affirmative.

In conclusion, this Thesis did not investigate my participation in the LiteBIRD collaboration. I actively contribute to various working groups dedicated to the science of inflation, cross-correlation with galaxy surveys, simulation of the experiment's future performance, and the likelihood analysis of its results. Throughout this manuscript, I underscored the importance of measuring B-modes, directly linked to primordial GWs, thereby emphasizing the heightened relevance of future measurements in this domain.

Part V

APPENDICES

A

APPENDIX TO THE STATISTICAL ISOTROPY ANALYSIS

A.1 SCALAR VS TENSOR CONTRIBUTIONS TO THE ANISOTROPIES

As mentioned in Chap. 8, part of both the CMB and the CGWB anisotropies are induced by the presence of tensor perturbations of the metric. Here we explore the role of both scalar and tensor contributions to the anisotropies of the CGWB, the CMB and their cross-correlation, emphasizing their dependency on the tensor spectral tilt n_t. In the case of CMB, the solution of the Boltzmann equation for the tensor modes will be proportional to the integral of a source function defined as [189, 300]

$$S^{(T)}_{Temp.} = -\chi' e^{-\kappa} + pol. \,, \tag{414}$$

where (T) stands for tensor, κ is the optical depth and $pol.$ stands for the contribution of polarization on which we are not interested (see Sec.3.6 of [300] for further detail). On the other hand, the analogous solution in the case of the CGWB is proportional to [49]

$$S^{(T)}_{GW} = -\chi' \,. \tag{415}$$

These source functions will then play a role in the solutions for either $\Theta_{\ell m}$ or $\Gamma_{\ell m}$. However, let us recall that in order to characterize the statistical behavior of Θ, Γ we turn to their angular power spectrum, given that they are fields of null mean. The expression for their spectra will then contain the square of the appropriate source function, since $\left\langle X_{\ell m} X^*_{\ell' m'} \right\rangle \propto C^{XX}_\ell$ with $X = \Theta, \Gamma$. Then, Eq. 414 and Eq. 415 generate a positive contribution of the angular power spectrum $\propto (h')^2$.

Furthermore, the C^{XX}_ℓ will also depend on the primordial tensor power spectrum, which we parametrize as a power-law (see Sec. 9.1). Indeed, Fig. 57 shows that a negative spectral index n_t (red tilt) enhance the tensor anisotropies on large scales, which actually reach the same order of the scalar induced

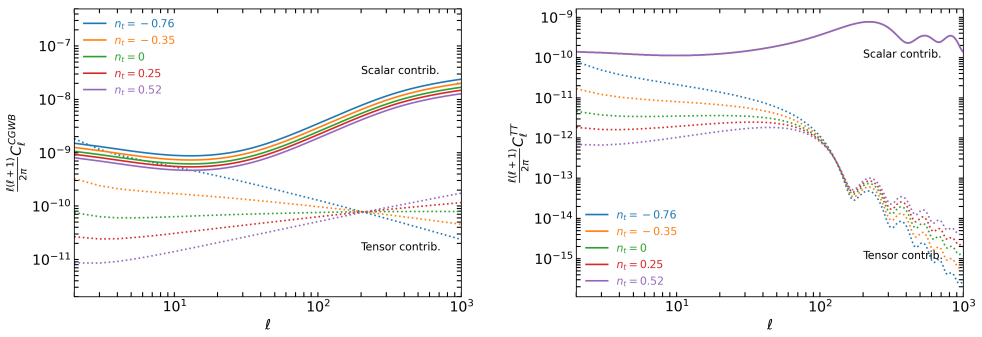

Figure 57: CGWB (left) and CMB temperature (right) angular power spectrum when we assume different values for the tensor spectral tilt n_t and we do not consider any effect due to the modulation ($\omega_1 = 0$). Scalar induced anisotropies are reported in solid lines, whereas the tensor induced ones with dotted lines.

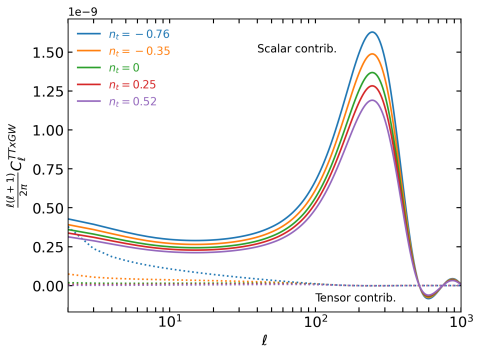

Figure 58: Cross-correlation CMBxCGWB angular power spectrum when we assume different values for the tensor spectral tilt n_t and we do not consider any effect due to the modulation ($\omega_1 = 0$). Scalar induced anisotropies are reported in solid lines, whereas the tensor induced ones with dotted lines.

anisotropies. From the right panel of Fig. 57, it is clear that in the case of the CMB only the tensor contribution will depend on n_t through the primordial spectrum, as expected. Instead, for the CGWB, the left panel of Fig. 57 allows us to distinguish the dependence of the scalar (see Sec. 9.1 for more details) and the tensor contributions.

The same reasoning holds also for the cross-correlation between CMB and CGWB. Indeed, its angular power spectrum contains the product of the source functions coming from CMB and CGWB. Once again the result is a positive contribution ($\propto (\chi')^2$) and the overall spectrum depends on the primordial power spectrum of the tensor perturbations, thus the spectral index n_t. Fig. 58 shows this dependence for both the scalar and tensor contributions.

Finally, all of these spectra and their dependencies on n_t generate what we see in Fig. 15, where the tensor induced anisotropies are contributing to increase the correlation coefficient.

B

APPENDIX TO THE LACK-OF-CORRELATION ANALYSIS

B.1 WINDOW FUNCTION IN A PARTIAL SKY

In Sec. 10.2 we generalize the formula for constrained realizations to the cut-sky case. In doing so, we use the window function of a mask, so here we give more details on this quantity.

Assume to have an observable field X, which gets decomposed using spherical harmonics. This provides an efficient description of an observation in terms of the $a_{\ell m}$ coefficients. However, these will have different values and different statistics depending on the fraction of the sky one is able to observe. In particular, the relation between FS and CS coefficients is [231, 232]

$$\begin{aligned} a_{\ell m}^{\mathrm{CS}} &= \int_{cut-sky} X(\theta,\phi) Y^*_{\ell m}(\theta,\phi)\, \mathrm{d}(\cos\theta)\, \mathrm{d}\phi \\ &= \int_{cut-sky} \sum_{\ell' m'} a^{\mathrm{FS}}_{\ell' m'} Y_{\ell' m'}(\theta,\phi) Y^*_{\ell m}(\theta,\phi)\, \mathrm{d}(\cos\theta)\, \mathrm{d}\phi \\ &= \sum_{\ell' m'} a^{\mathrm{FS}}_{\ell' m'} \int_{cut-sky} Y_{\ell' m'}(\theta,\phi) Y^*_{\ell m}(\theta,\phi)\, \mathrm{d}(\cos\theta)\, \mathrm{d}\phi \end{aligned} \tag{416}$$

.

In the full-sky case, the integral gives $\delta_{\ell\ell'}\delta_{mm'}$ thank to the orthogonality of the spherical harmonics on the complete sky. However, on a portion of the sphere, they are not orthogonal, so $\ell - \ell'$ couplings will emerge.

We can write Eq. 416 as a function of a window function W defined by the particular mask we are using as

$$a^{\mathrm{CS}}_{\ell m} = a^{\mathrm{FS}}_{\ell' m'} W^{\ell' m'}_{\ell m} \,, \tag{417}$$

where repeated indexes are summed over. Thus, in order to estimate the full-sky coefficients from a partial sky observation we must compute $W^{\ell' m'}_{\ell m}$. Since one typically works with maps divided in pixels, we can write the discretized window function as a sum over the unmasked pixels p [232]

$$W^{\ell' m'}_{\ell m} = \sum_{p \,\in\, CS} Y_{\ell' m'}(p) Y^*_{\ell m}(p) \Omega_p \,, \tag{418}$$

where Ω_p is the angular area of the pixel and the spherical harmonics are evaluated in the center of each pixel. This sum will depend on the considered pixelization (N_{side} parameter of `Healpy`), but it will tend to the continuous integration as the pixel size goes to zero. Note that in the case of very aggressive masks, the window function may become singular.

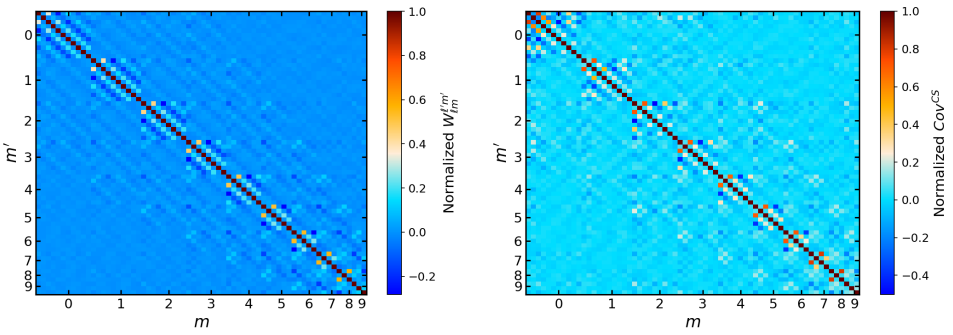

Figure 59: The left panel shows the window function obtained from the common intensity mask at $N_{\rm side} = 64$ and computed from Eq. 418. The right panel shows the covariance of the cut-sky spherical harmonic coefficients, as defined in Eq. 419. For both panels, we mark the m-blocks, following the usual indexing of the $a_{\ell m}$s (note that the last block for $m = 10$ is not labeled for visualization purposes). Here we assume $\ell_{\rm max} = 10$.

An alternative route to obtain the window function is to use partial sky realizations of the considered field. Indeed, looking at the covariance of the $a^{\rm CS}_{\ell m}$ we can write (here we drop the indexes for the sake of notation)

$$\begin{aligned} \left\langle \left(a^{\rm CS}\right)^* a^{\rm CS} \right\rangle &= W^* \left\langle \left(a^{\rm FS}\right)^* a^{\rm FS} \right\rangle W \\ &= W^* D W \\ &= \left(D^{1/2} W\right)^* \left(D^{1/2} W\right) , \end{aligned} \tag{419}$$

where D is a matrix with the angular power spectrum in the diagonal elements (see Eq. 344). In the last line, we obtain the classic definition of the Cholesky decomposition. This shows that having an empirical covariance obtained from N cut-sky realizations of X is equivalent to having computed the window function of the mask while knowing the angular power spectrum of the observable. In particular, we can write

$$\begin{aligned} D^{1/2} W &= Chol.\left(Cov^{\rm CS}\right) \\ W &= D^{-1/2} \times Chol.\left(Cov^{\rm CS}\right) , \end{aligned} \tag{420}$$

obtaining the window function from the cut-sky realizations. Obviously, this alternative way will depend on the realizations used and their number.

At this point, we can specify the window function to our case, hence to the common intensity mask of Planck (see Sec. 10.2.1). We compute the window function from Eq. 418 and using $N_{\rm side} = 64$. Fig. 59 shows the real part of the obtained matrix assuming $\ell_{\rm max} = 10$ and of the full covariance matrix $W^* D W$ (the imaginary part of both is negligible w. r. t. the real one) normalized to the diagonal elements to emphasize the correlation structures. The figure shows that the window function is not block diagonal. Instead, coefficients with different m will get slightly correlated. Indeed, Mortlock, Challinor, and Hobson [232] show that in the case of symmetric, constant latitude cuts, the window function goes exactly to a block diagonal matrix. Still, the elements correlating different orientations are negligible with respect to elements belonging to the same m. To highlight this feature, we labeled in the figure the different m-blocks, which contain the $\ell - \ell'$ correlations.

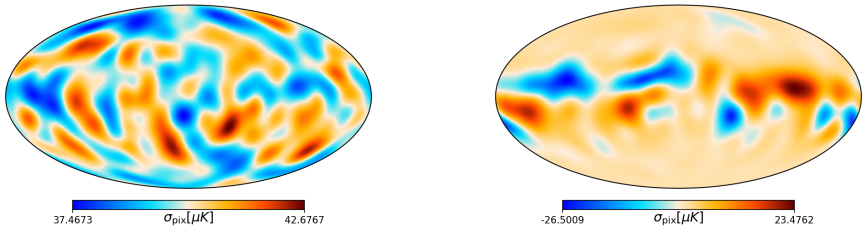

Figure 60: Pixel standard deviation across the sky for the true full-sky coefficients and the reconstructed ones.

B.1.1 *Sky variance of the reconstructed coefficients*

As shown in Eq. 347, we use this window function to reconstruct the full-sky spherical harmonics coefficients, however this must come at a cost. Indeed, assuming to have a very aggressive mask, it is intuitive to expect that not all the harmonic modes can be recovered, especially if the typical angular scale of those is comparable with the width of the mask. In more mathematical terms, the window function would be singular, thus one cannot invert it to compute the reconstructed full-sky coefficients from the cut-sky ones [232]. In our case, the W is invertible, however we expect the reconstructed coefficients to be more noisy than the true ones. To verify this, we generate 1000 full-sky realizations, we mask each and we reconstruct the $\widehat{a}^{\rm FS}_{\ell m}$. Then, we compute the standard deviation of each pixel to investigate whether an extra scatter is present w. r. t. the full-sky dispersion. Focusing on the $\ell_{\rm max} = 10$ case, Fig. 60 shows the results: on the left we plot the standard deviation pixel by pixel of the true $a^{\rm FS}_{\ell m}$, while on the right we plot the extra standard deviation induced by the reconstruction procedure.

Note that this contribution concentrates around masked areas of the sky (see Fig. 22), suggesting that we pay the price of a full-sky description by increasing the noisiness of those regions, as expected.

B.2 ANGULAR CORRELATION FUNCTIONS FOR THE CGWB

In Sec. 10.2.3 we show the angular correlation functions for GWGW and TGW, however, we limit the angular range to the one accessible imposing $\ell_{\rm max} = 4$. This is done to account for the performance of future GW interferometers. Despite this, it is interesting to have a look at the 2-point angular correlation function on all scales, as predicted by ΛCDM. Indeed, the angular power spectrum of the CGWB is very similar to the one of CMB temperature due to their high correlation, but they diverge on small scales ($\ell \gtrapprox 100$). Hence, Fig. 61 shows $C(\theta)$ for GWGW and TGW when assuming $\ell_{\rm max} = 2000$. Indeed, note that both the GWGW and the TGW present the typical "sinusoidal" behavior on large scales. Instead, on small ones GWGW tend to very high values since the CGWB spectrum is not dumped as the CMB temperature one.

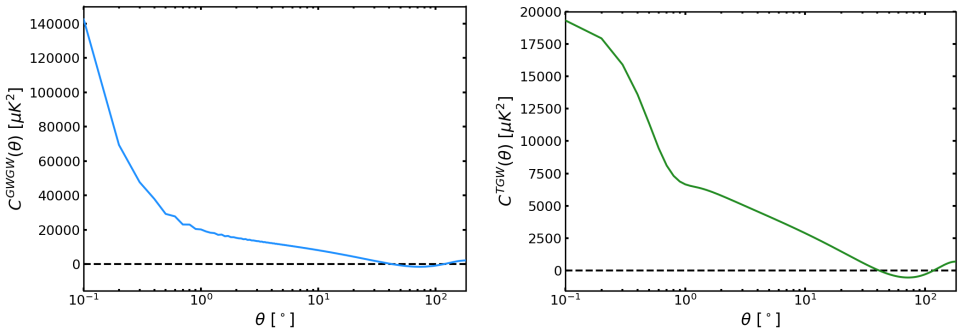

Figure 61: Angular correlation function $C(\theta)$ of GWGW (left) and TGW (right) assuming $\ell_{\rm max} = 2000$.

	Mask-sky									
	$S^{\rm GWGW}_{\theta_{\rm min},\theta_{\rm max}}$		$S^{\rm TGW}_{\theta_{\rm min},\theta_{\rm max}}$		$S^{\rm TT,GWGW}_{\theta_{\rm min},\theta_{\rm max}}$		$S^{\rm TT,TGW}_{\theta_{\rm min},\theta_{\rm max}}$		$S^{\rm TT,TGW,GWGW}_{\theta_{\rm min},\theta_{\rm max}}$	
	$\theta_{\rm min}$	$\theta_{\rm max}$	$\theta_{\rm min}$	$\theta_{\rm max}$	$\theta_{\rm min}$	$\theta_{\rm max}$	$\theta_{\rm min}$	$\theta_{\rm max}$	$\theta_{\rm min}$	$\theta_{\rm max}$
$\ell_{\rm max} = 4$	60°	179°	60°	180°	60°	178°	61°	180°	60°	180°
$\ell_{\rm max} = 6$	37°	98°	54°	127°	40°	99°	52°	180°	44°	99°
$\ell_{\rm max} = 10$	66°	77°	60°	132°	38°	94°	58°	173°	36°	128°

Table 11: Optimal angles for every observable and combination of them while assuming a different FWHM for smoothing SMICA products.

B.3 CHANGING THE SMOOTHING SCALE

In Sec. 10.2.1, we said that we smooth SMICA products with a Gaussian beam with FWHM $= 2°$. Thus, one could ask what difference would a different smoothing strategy bring to the analysis? To explore this aspect, we repeat all the analysis while choosing FWHM $\simeq 0.92°$, which is the angular scale corresponding to $N_{\rm side} = 64$. We find that the full-sky analysis is totally unaffected by the smoothing choice giving identical results. On the other hand, the masked analysis shows some differences, shown in Tab. 11, Tab. 12, and Tab. 13. The most significant one in found in the percentage of realizations improving SMICA significance. Indeed, assuming a less aggressive smoothing and to use all the observables (TT, TGW and GWGW), allows us to obtain almost the 90% of them above SMICA in all the considered cases (see last column of Tab. 13). Despite this, in the main body of this work we decided to keep the 2°-smoothing since we think that it is safer to stick with a bigger FWHM to avoid mask-induced effects. To test this, we also repeat the analysis while smoothing with a FWHM $= 4°$. We do not show the results for this case, since they are completely identical to the ones in Sec. 10.3 suggesting that our 2° choice is sufficient to get rid of any pixelization dependence.

	Mask-sky				
	$S^{\mathrm{GWGW}}_{\theta_{\mathrm{min}},\theta_{\mathrm{max}}}$	$S^{\mathrm{TGW}}_{\theta_{\mathrm{min}},\theta_{\mathrm{max}}}$	$S^{\mathrm{TT,GWGW}}_{\theta_{\mathrm{min}},\theta_{\mathrm{max}}}$	$S^{\mathrm{TT,TGW}}_{\theta_{\mathrm{min}},\theta_{\mathrm{max}}}$	$S^{\mathrm{TT,TGW,GWGW}}_{\theta_{\mathrm{min}},\theta_{\mathrm{max}}}$
	PD	PD	PD	PD	PD
$\ell_{\mathrm{max}} = 4$	72.0%	96.33%	93.51%	98.32%	96.15%
$\ell_{\mathrm{max}} = 6$	77.11%	96.84%	95.88%	98.78%	97.4%
$\ell_{\mathrm{max}} = 10$	71.64%	96.75%	93.51%	98.72%	95.71%

Table 12: PDs for every observable and combination of them while assuming a different FWHM for smoothing SMICA products.

		Mask-sky				
	Signi. S^{SMICA}	S^{GWGW}	S^{TGW}	$S^{\mathrm{TT,GWGW}}$	$S^{\mathrm{TT,TGW}}$	$S^{\mathrm{TT,TGW,GWGW}}$
$\ell_{\mathrm{max}} = 4$	2.41σ	12.73%	14.86%	79.32%	9.35%	86.37%
$\ell_{\mathrm{max}} = 6$	2.37σ	8.13%	1.19%	90.31%	0.34%	94.52%
$\ell_{\mathrm{max}} = 10$	2.17σ	3.81%	1.35%	87.33%	0.42%	91.35%

Table 13: Percentage of constrained realizations that improve the significance of SMICA, which is shown in the first column. Here we assume a different FWHM for smoothing SMICA products

B.4 OPTIMISTIC GWS DETECTION

Here, we show some of the results of the same analysis performed in the main body if we change the assumption on ℓ_{max}. Indeed, we just showed the most pessimistic case of $\ell_{\mathrm{max}} = 4$. For the sake of brevity, we cannot show everything as we did in the main body. Instead, we will show exclusively the results when we assume masked SMICA to be our CMB observation.

B.4.1 *Optimal angles with* $\ell_{\mathrm{max}} = 6$

We show here the results of the optimal angles analysis for $S^{\mathrm{GWGW}}_{\theta_{\mathrm{min}},\theta_{\mathrm{max}}}$ on Fig. 62 and on Fig. 63 for $S^{\mathrm{TGW}}_{\theta_{\mathrm{min}},\theta_{\mathrm{max}}}$.

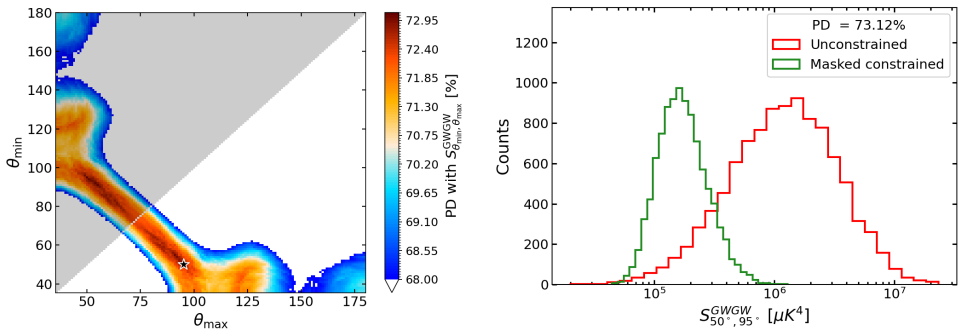

Figure 62: Optimal angles for GWGW. The left and right panels show respectively optimal angles analysis and the results at the optimal range. Here we assume $\ell_{\mathrm{max}} = 6$.

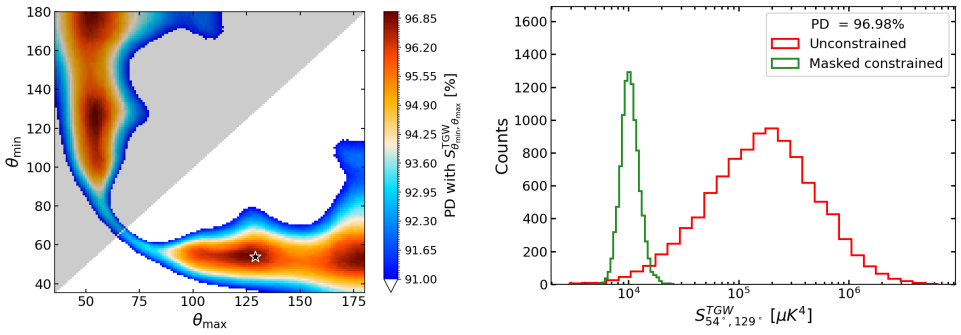

Figure 63: Optimal angles for TGW. The left and right panels show respectively optimal angles analysis and the results at the optimal range. Here we assume $\ell_{max} = 6$.

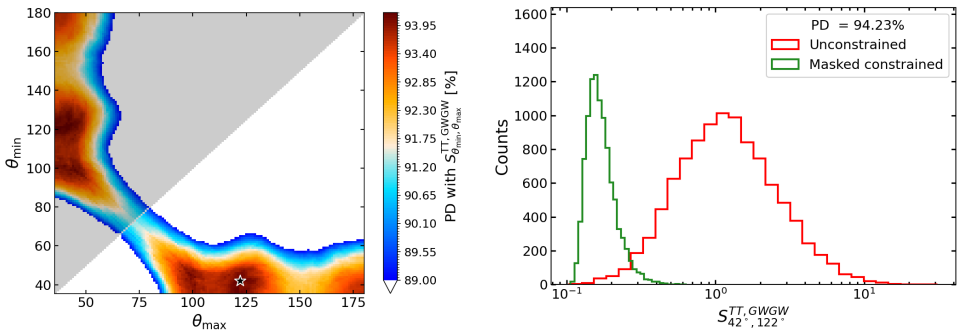

Figure 64: Optimal angles for the combination of TT and GWGW. The left and right panels show respectively optimal angles analysis and the results at the optimal range. Here we assume $\ell_{max} = 6$.

Instead, Fig. 64, Fig. 65 and Fig. 66 show the same respectively for $S^{TT,GWGW}_{\theta_{min},\theta_{max}}$, $S^{TT,TGW}_{\theta_{min},\theta_{max}}$ and $S^{TT,TGW,GWGW}_{\theta_{min},\theta_{max}}$. As mentioned in Sec. 10.3.1, there always seems to be relatively high-PD region where the original $S_{1/2}$ estimator is defined, i. e. between 60° and 180°.

B.4.2 *Significance with* $\ell_{max} = 6$

As done in Sec. 10.2.6, we report here the significance analysis performed using the newly defined estimator of Eq. 356. Here, we can also show the full-sky results given that we can plot both in the same figure. Starting from S^{GWGW}, we obtain Fig. 67, while for S^{TGW} we get Fig. 68.

Switching to the multi-field analysis, we obtain Fig. 69, Fig. 70 and Fig. 71 for $S^{TT,GWGW}$, $S^{TT,TGW}$, and $S^{TT,TGW,GWGW}$.

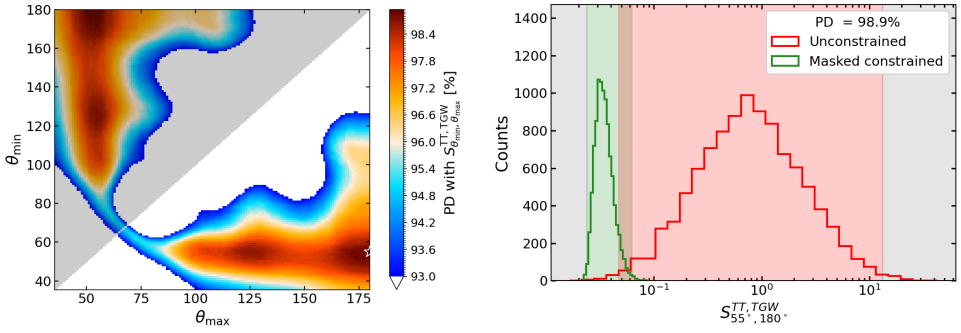

Figure 65: Optimal angles for the combination of TT and TGW. The left and right panels show respectively optimal angles analysis and the results at the optimal range. Here we assume $\ell_{max} = 6$.

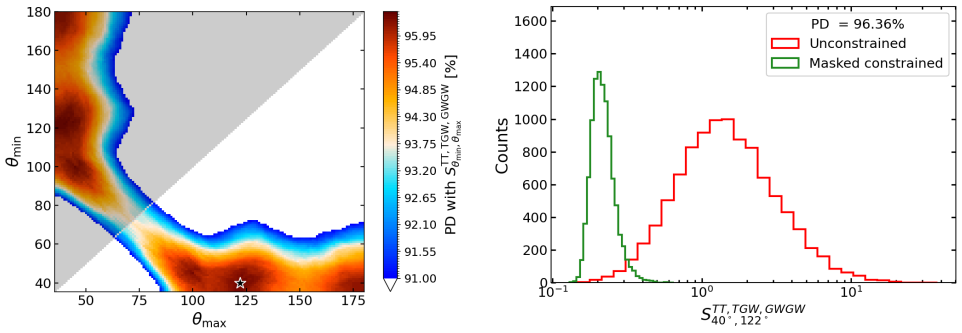

Figure 66: Optimal angles for the combination of TT, TGW, and GWGW. The left and right panels show respectively optimal angles analysis and the results at the optimal range. Here we assume $\ell_{max} = 6$.

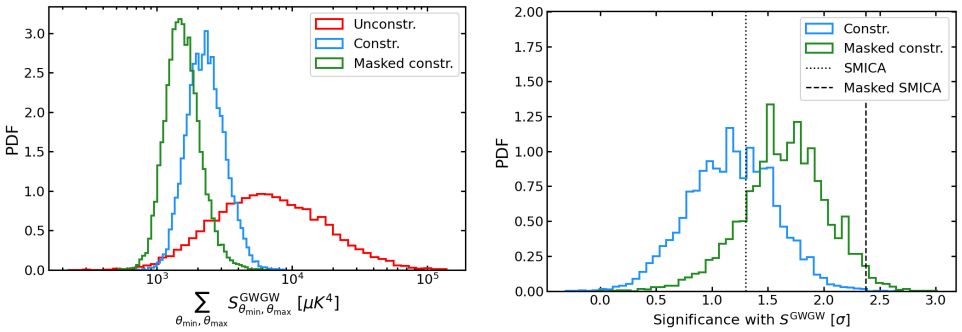

Figure 67: Values of S^{GWGW} and their corresponding significance in terms of σ w. r. t. the unconstrained realizations ($\ell_{max} = 6$). The vertical lines indicate the significance of SMICA alone.

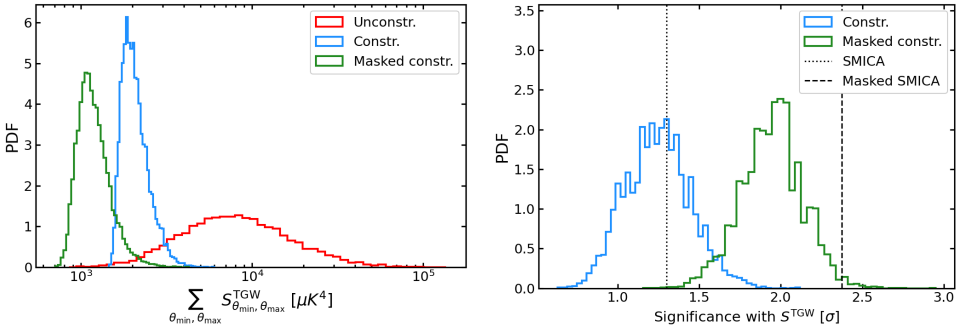

Figure 68: Values of S^{TGW} and their corresponding significance in terms of σ w. r. t. the unconstrained realizations ($\ell_{max} = 6$). The vertical lines indicate the significance of SMICA alone.

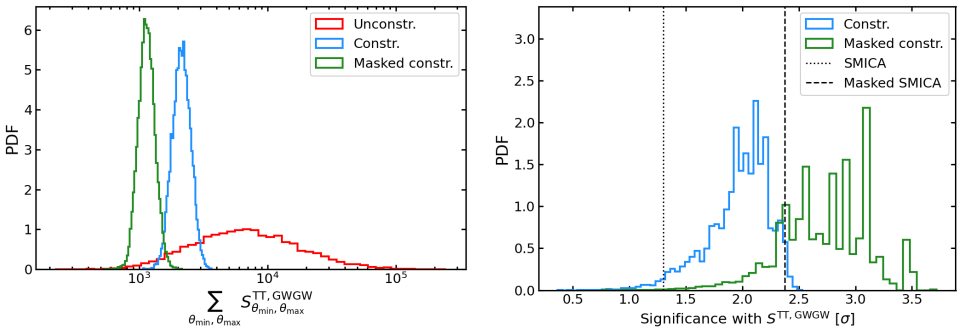

Figure 69: Values of $S^{TT,GWGW}$ and their corresponding significance in terms of σ w. r. t. the unconstrained realizations ($\ell_{max} = 6$). The vertical lines indicate the significance of SMICA alone.

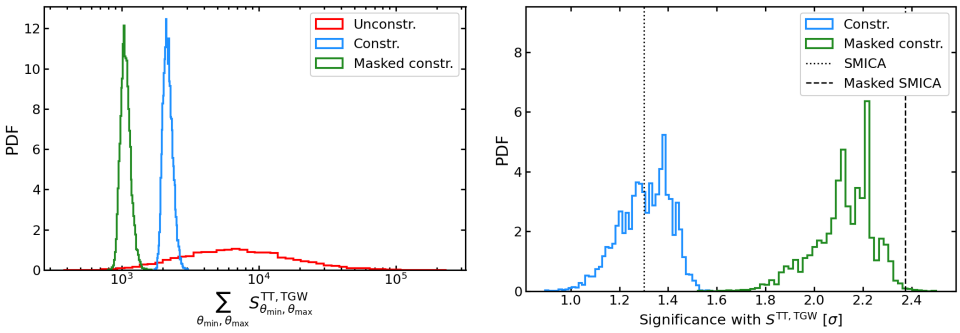

Figure 70: Values of $S^{TT,TGW}$ and their corresponding significance in terms of σ w. r. t. the unconstrained realizations ($\ell_{max} = 6$). The vertical lines indicate the significance of SMICA alone.

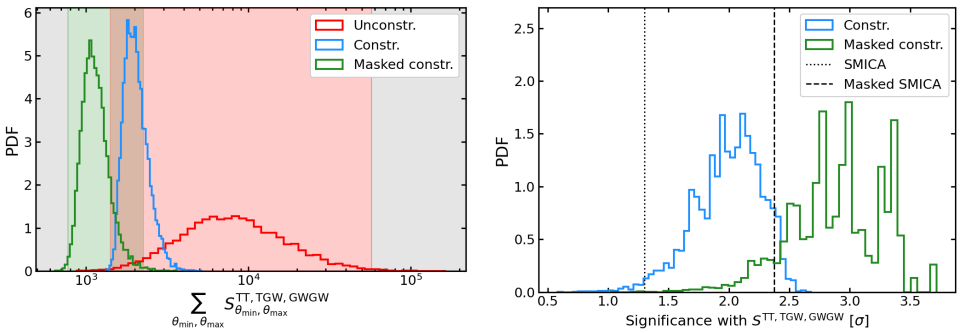

Figure 71: Values of $S^{TT,TGW,GWGW}$ and their corresponding significance in terms of σ w. r. t. the unconstrained realizations ($\ell_{max} = 6$). The vertical lines indicate the significance of SMICA alone.

B.4.3 *Optimal angles with* $\ell_{max} = 10$

We repeated the same thing for $\ell_{max} = 10$. Firstly, for $S^{GWGW}_{\theta_{min},\theta_{max}}$ we obtain Fig. 72 and Fig. 73 for $S^{TGW}_{\theta_{min},\theta_{max}}$.

Instead, Fig. 74, Fig. 75 and Fig. 76 show the same respectively for $S^{TT,GWGW}_{\theta_{min},\theta_{max}}$, $S^{TT,TGW}_{\theta_{min},\theta_{max}}$ and $S^{TT,TGW,GWGW}_{\theta_{min},\theta_{max}}$. Once again, there seems to be relatively high-PD region where the original $S_{1/2}$ estimator is defined.

B.4.4 *Significance with* $\ell_{max} = 10$

As regards the significance, starting from S^{GWGW}, we obtain Fig. 77, while for S^{TGW} we get Fig. 78.

Switching to the multi-field analysis, we obtain Fig. 79, Fig. 80 and Fig. 81 for $S^{TT,GWGW}$, $S^{TT,TGW}$, and $S^{TT,TGW,GWGW}$.

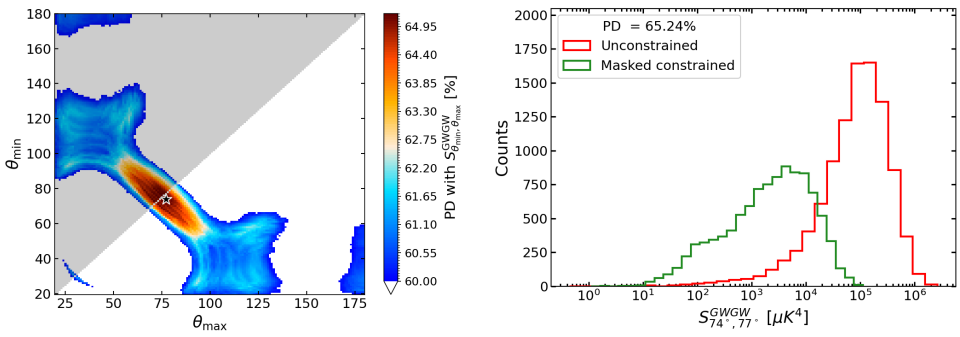

Figure 72: Optimal angles for GWGW. The left and right panels show respectively optimal angles analysis and the results at the optimal range. Here we assume $\ell_{max} = 10$.

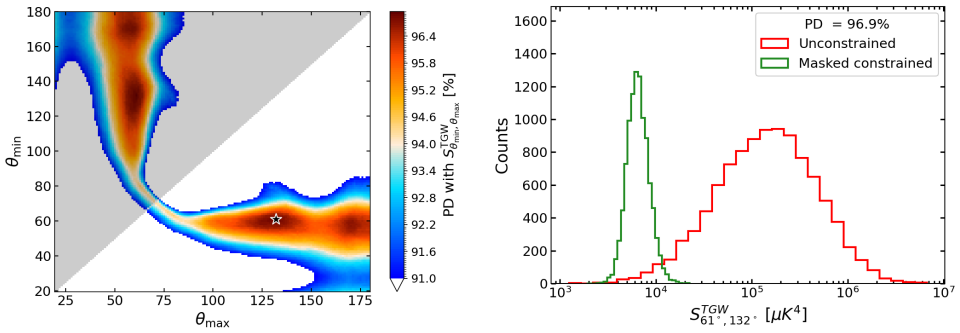

Figure 73: Optimal angles for TGW. The left and right panels show respectively optimal angles analysis and the results at the optimal range. Here we assume $\ell_{\rm max} = 10$.

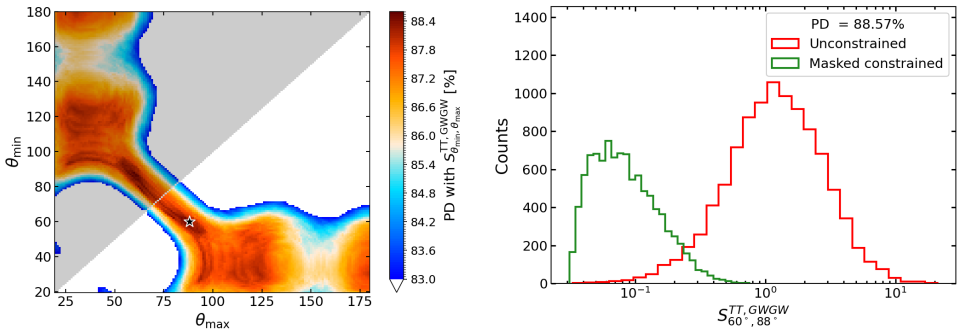

Figure 74: Optimal angles for the combination of TT and GWGW. The left and right panels show respectively optimal angles analysis and the results at the optimal range. Here we assume $\ell_{\rm max} = 10$.

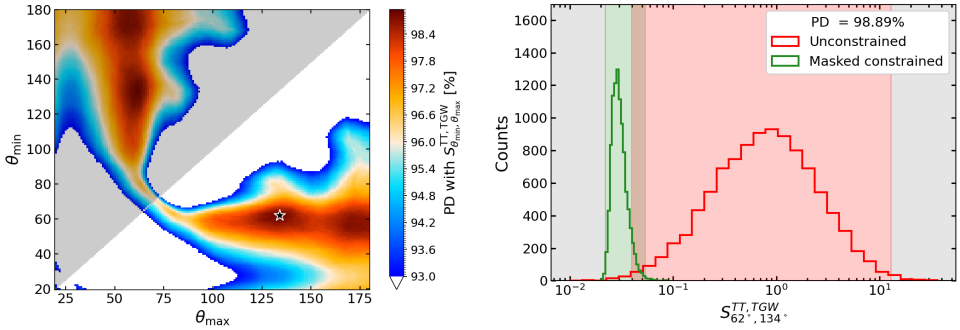

Figure 75: Optimal angles for the combination of TT and TGW. The left and right panels show respectively optimal angles analysis and the results at the optimal range. Here we assume $\ell_{\rm max} = 10$.

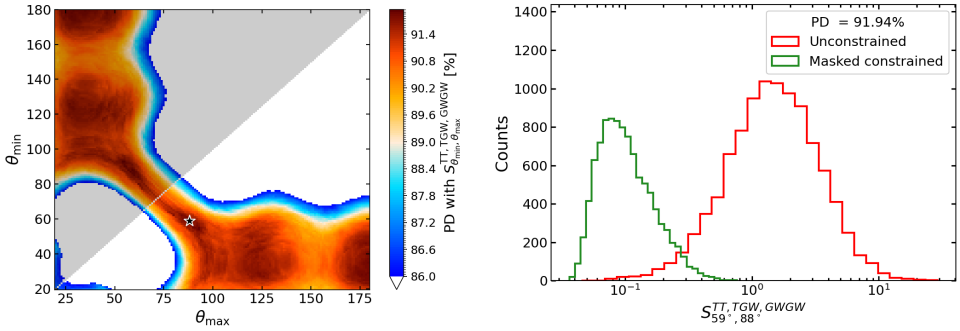

Figure 76: Optimal angles for the combination of TT, TGW, and GWGW. The left and right panels show respectively optimal angles analysis and the results at the optimal range. Here we assume $\ell_{\rm max} = 10$.

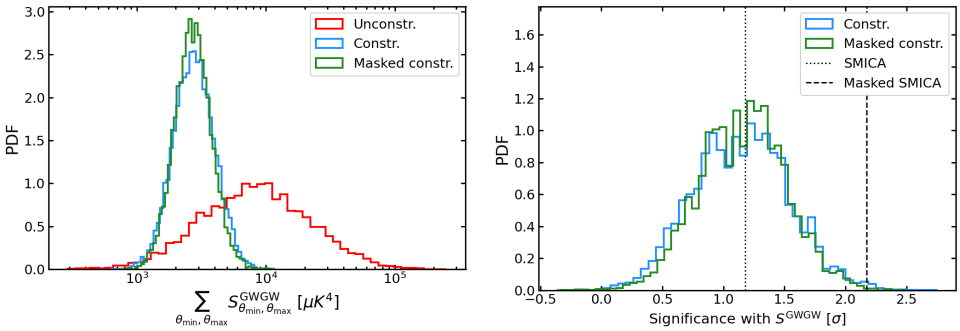

Figure 77: Values of S^{GWGW} and their corresponding significance in terms of σ w. r. t. the unconstrained realizations ($\ell_{max} = 10$). The vertical lines indicate the significance of SMICA alone.

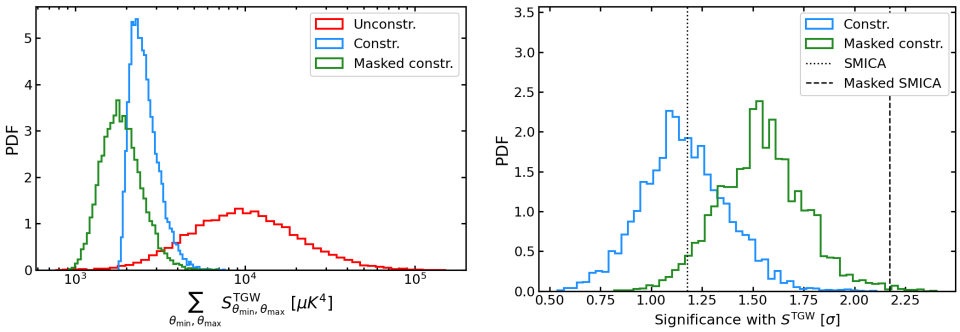

Figure 78: Values of S^{TGW} and their corresponding significance in terms of σ w. r. t. the unconstrained realizations ($\ell_{max} = 10$). The vertical lines indicate the significance of SMICA alone.

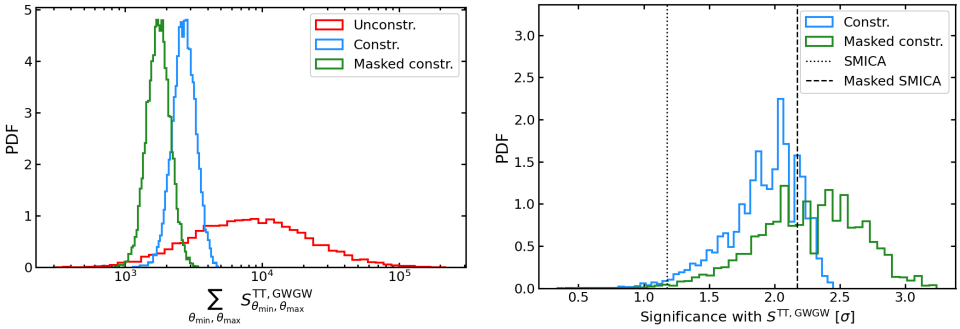

Figure 79: Values of $S^{TT,GWGW}$ and their corresponding significance in terms of σ w. r. t. the unconstrained realizations ($\ell_{max} = 10$). The vertical lines indicate the significance of SMICA alone.

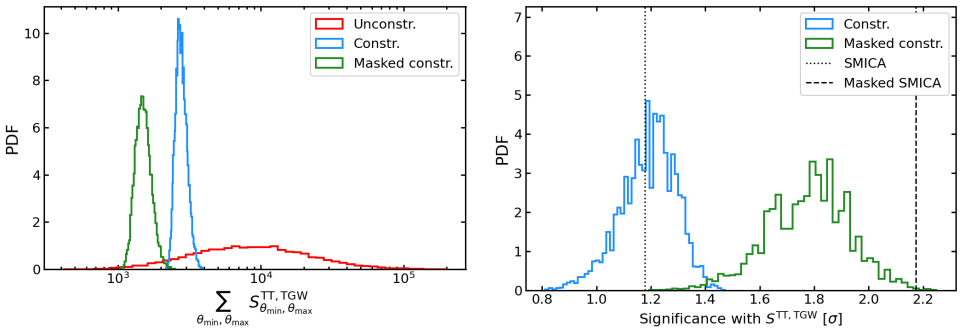

Figure 80: Values of $S^{TT,TGW}$ and their corresponding significance in terms of σ w. r. t. the unconstrained realizations ($\ell_{max} = 10$). The vertical lines indicate the significance of SMICA alone.

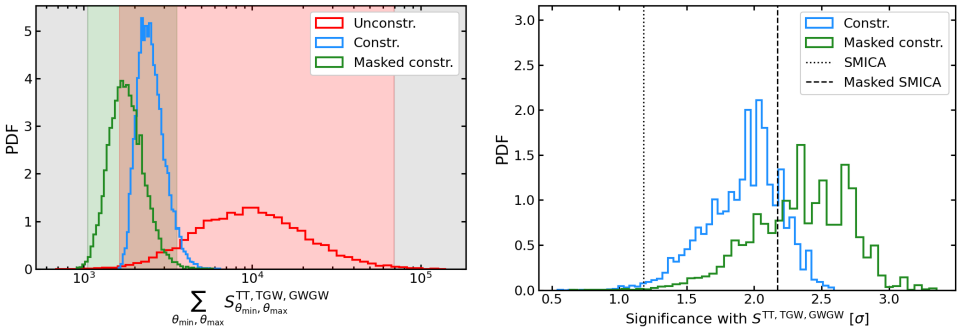

Figure 81: Values of $S^{\mathrm{TT,TGW,GWGW}}$ and their corresponding significance in terms of σ w. r. t. the unconstrained realizations ($\ell_{\mathrm{max}} = 10$). The vertical lines indicate the significance of SMICA alone.

C

APPENDIX TO THE MCMC ANALYSIS

C.1 CONSTRAINTS ON THE ΛCDM PARAMETERS

Fig. 82 (see also Tab. 14 for mean values and standard deviations) shows the posterior distribution for the 6 ΛCDM parameters for the most constraining combination for the tensor sector, i. e. PL21+BK18+LV21, compared to PL18+BK15, PL18+BK18, and PL21+BK18. The results shown here refer to our baseline approach to the tensor sector, i. e. SSA (see the beginning of Sec. 13.4 for a summary of the assumptions used). Looking at the first two

Parameter	**PL18+BK15**	**PL18+BK18**	**PL21+BK18**	**PL21+BK18+LV21**
$\log\left(10^{10}A_s\right)$	3.046 ± 0.014	3.044 ± 0.014	3.053 ± 0.012	3.053 ± 0.012
n_s	0.9654 ± 0.0040	0.9652 ± 0.0042	0.9676 ± 0.0039	0.9676 ± 0.0039
$\Omega_b h^2$	0.02239 ± 0.00015	0.02238 ± 0.00014	0.02241 ± 0.00014	0.02241 ± 0.00014
$\Omega_{cdm} h^2$	0.1200 ± 0.0012	0.1200 ± 0.0012	0.1194 ± 0.0011	0.1194 ± 0.0011
τ_{reio}	0.0549 ± 0.0073	0.0542 ± 0.0074	0.0603 ± 0.0061	0.0602 ± 0.0061
H_0	67.38 ± 0.53	67.37 ± 0.53	67.62 ± 0.51	67.61 ± 0.52

Table 14: Mean and standard deviation of the 6 ΛCDM parameters using a selection of the analyzed dataset.

columns, we know that the constraints on the 6 ΛCDM parameter are essentially driven by PL18. Thus, we can compare our results with *Planck* 2018 ones [190], which are extremely compatible with ours (almost identical).

Instead, it is less trivial to compare the other two columns with the literature, given that, to our knowledge, our combination of datasets PL21 has not been explored. Despite this, we know that the main differences are caused

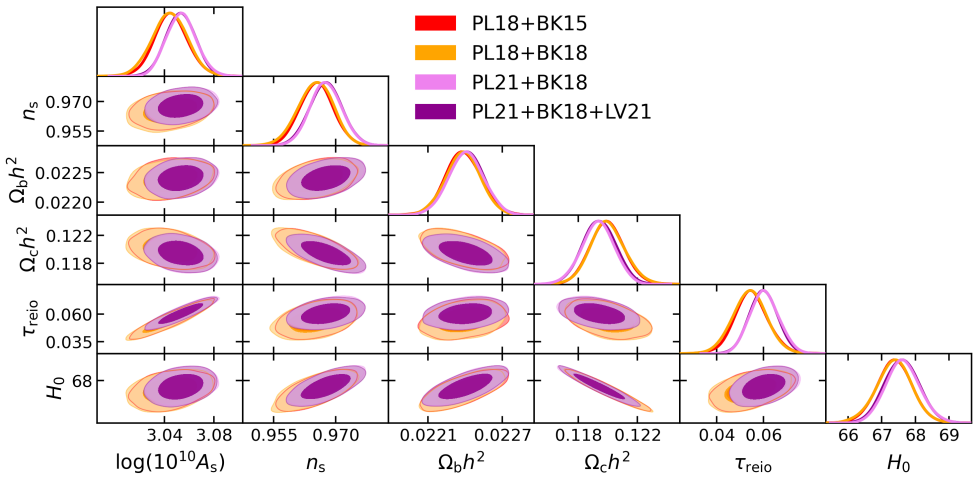

Figure 82: Posterior distribution for $\log\left(10^{10}A_s\right)$, n_s, $\Omega_b h^2$, $\Omega_{cdm} h^2$, τ_{reio} and H_0.

by the fact that LoLLiPoP provides a better characterization of the low-ℓ part of the polarization, while HiLLiPoP gives almost identical results w. r. t. PR3 [114]. Then, we can, for example, compare Tab. 14 with [266]. They report the best-fit values on the ΛCDM parameters (together with all the others) obtained using HiLLiPoP + *lowlTT* + LoLLiPoP + BK18 + BAO ([279]) + *lensing*. These values are almost identical to the mean values we obtain from the MCMC; thus, the two are extremely compatible given our error bars. Since the difference w. r. t. *Planck* 2018 reported in [266] is due to LoLLiPoP, we can confirm the same shifts; however, note that the results of [266] are obtained through a PL.

The general behavior of our results can also be found in [114]. In particular, it seems that the major effect of PR4 is to push for slightly higher values of $\left\{\log\left(10^{10}A_s\right), n_s, \tau_{reio}\right\}$ w. r. t. *Planck* 2018. However, notice that they do not exploit the high-ℓ part of polarization and lensing; therefore, one has to be careful in comparing [114] with this work.

In conclusion, Adam et al. [301] constrains the reionization history using *plikTT* + *lowlTT* + LoLLiPoP + *lensing*, finding $\tau_{reio} = 0.058^{+0.011}_{-0.012}$. This combination is very similar to the one used here (PL21+BK18), the difference is the high-ℓ part of polarization and BK18, and the result is compatible with ours. This confirms the shift we find in this parameter, which probably is also driving the increase in $\log\left(10^{10}A_s\right)$ through their degeneracy. Also, n_s and H_0 are positively correlated with τ_{reio} (although not as strongly as $\log\left(10^{10}A_s\right)$), thus also their slight shift may be explained by the pull on the optical depth (at least partially). The opposite seems to happen to $\Omega_c h^2$, which is anti-correlated with τ_{reio}.

C.2 COORDINATE TRANSFORMATION

In Sec. 13.1, we perform a test to assess the prior information injected by the coordinate transformation $(r_1 - r_2) \to (r_{0.01} - n_t)$ characterizing the TSA. To do so, we performed an MCMC analysis on priors alone, finding that the TSA has a strong pull toward scale invariance ($n_t = 0$) and tends to exclude $r_{0.01} = 0$.

Now, given the nature of the MCMC analysis, one may ask himself if the results shown are flawed by the fact that the sampling is finite. Indeed, at some point, the MCMC converges and stops exploring the parameter space. To answer the question, we take here a more direct approach to the problem, which does not imply any sampling effect. Indeed, we can find the probability according to the TSA of a point in the $r_{0.01} - n_t$ plane given the prior probability distribution of the TSA on the $r_1 - r_2$ plane (Tab. 5) and recalling Eq. 399. It reads

$$\mathcal{P}^{\rm TSA}(r_{0.01}, n_t) = \mathcal{P}(r_1, r_2)\Big|_{r_{1/2}=r_{1/2}(r_{0.01},n_t)} \left|\frac{d(r_1, r_2)}{d(r_{0.01}, n_t)}\right| . \tag{421}$$

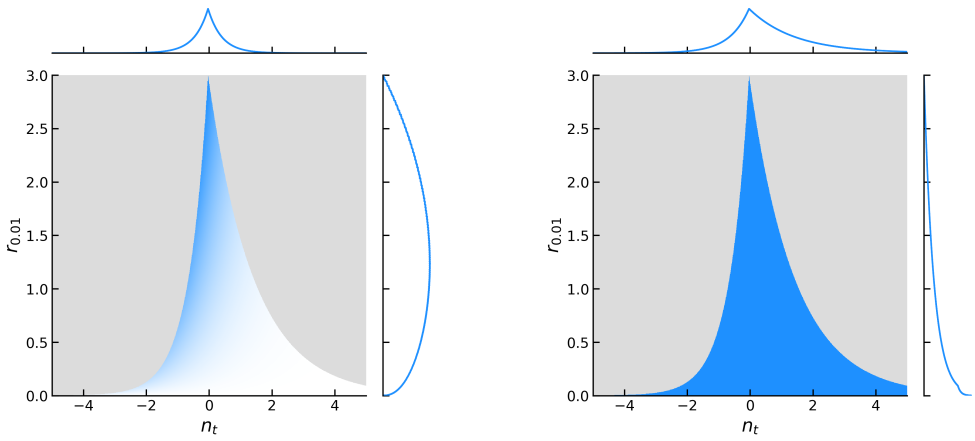

Figure 83: 1D and 2D histograms on the $(r_{0.01}, n_t)$ plane, obtained from a uniform grid of points in the $(r_1 - r_2)$ plane. The left panel shows the simple result of the coordinate transformation, while the right one is the Jacobian reweighting.

Here, $\mathcal{P}(r_1, r_2)$ acts as a "selection function": for each $r_{0.01}$ and n_t, it gives a constant factor if the corresponding r_1 and r_2 are within their prior ranges, zero otherwise. The second term is the inverse Jacobian of the coordinate transformation. As mentioned in Sec. 13.1.3, because of its nature an MCMC cannot explore regions of very low probability, since it is a finite sampling. So, plotting $\mathcal{P}^{\text{TSA}}$ we can have a look at the distribution to which the MCMC tends while the steps go to infinity. The left panel of Fig. 83 shows this, while we color in gray the points where the probability is identically null. As you can see, the region at low $r_{0.01}$ and high n_t has a negligible probability, which however is not zero. Instead, the gray region corresponds to the $r_{0.01} - n_t$ points bringing to $r_1 - r_2$ points outside their prior.

We can now reweigh the obtained distribution. The weights are given by the ratio

$$\frac{\mathcal{P}^{\text{SSA}}(r_{0.01}, n_t)}{\mathcal{P}^{\text{TSA}}(r_{0.01}, n_t)} = \frac{\mathcal{U}(r_{0.01})\mathcal{U}(n_t)}{\mathcal{P}^{\text{TSA}}(r_{0.01}, n_t)}\,, \tag{422}$$

where $\mathcal{U}(r_{0.01}), \mathcal{U}(n_t)$ are the uniform distributions reported in Tab. 5. Thus, it is clear that the re-weighted probability goes back to a constant. Despite this, note that reweighting cannot recover completely the SSA prior, since a large portion of the SSA prior is excluded because it brings you outside of the $r_1 - r_2$ priors (the gray region). For this reason, the bias carried by using the TSA can only be alleviated, but not solved, even when considering the theoretical probability distribution.

Compared with Sec. 13.1.3, even if the 2D histograms seem quite different from the distributions shown in Fig. 35 and Fig. 36, we remind the reader that the contour plots are obtained by using a Gaussian kernel. If we apply a kernel to the histograms shown in Fig. 83 we obtain very similar contours.

On the other hand, note that the marginalized 1D histograms are very similar to those shown in Fig. 35 and Fig. 36. The 95% CL intervals for the left panel are $0.15 < r_{0.01} < 2.68$ and $-1.33 < n_t < 1.27$ which are consistent with those of Sec. 13.1. For what regards the right panel, we get $r_{0.01} < 2.11$ and $-1.61 < n_t < 3.90$ at 95% CL. Thus, as in Sec. 13.1, the 2σ detection of $r_{0.01}$ is no longer there, while the pull toward scale invariance is

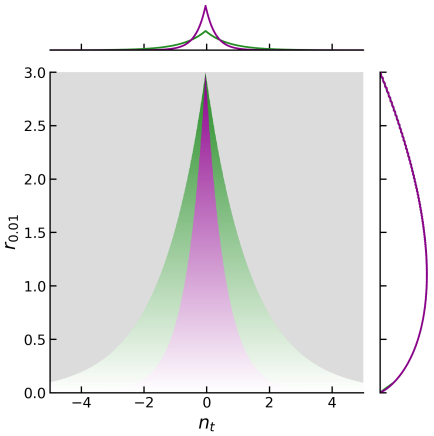

Figure 84: 1D and 2D histograms on the $(r_{0.01}, n_t)$ plane, obtained from a uniform grid of point in the $(r_1 - r_2)$ plane when changing the leverage arm. The green one is obtained with $(k_1, k_2) = (0.005, 0.02)$ Mpc^{-1} and the purple on with $(k_1, k_2) = (0.002, 0.05)$ Mpc^{-1}, mimicking Sec. 13.1.

just alleviated. Note that the upper bound on n_t is the most affected by the finite sampling, as expected. Thus, if one wants to use the TSA to study some datasets and use reweighting to alleviate the bias, some extra attention must be given to the length of the sampling. The larger the better to represent the low-probability regions. Still randomly exploring these regions may be unfeasible. In general, the same could be said for any MCMC analysis, however, we find the TSA to be particularly sensitive to this.

With the same method, we can also show what happens when we change the lever arm $k_2 - k_1$. As expected, the results shown in Fig. 84 are similar to those in Sec. 13.1.

In conclusion, this alternative way of exploring the prior information brought by the TSA leaves our conclusions of Sec. 13.1.3 unchanged.

C.3 RESULTS USING THE TSA

As mentioned at the end of Sec. 13.1.4, despite the choice we made to report our main results, we also performed the analysis using TSA. This allows us to appreciate the differences in the final posteriors due to the aspects underlined in Sec. 13.1. Sticking to [54] we choose $(k_1, k_2) = (0.002, 0.02)$ Mpc^{-1} and the priors shown in Tab. 5.

Tab. 15 reports the one-dimensional 95% CL for each combination analyzed, together with the best fit, mean values, and the convergence parameters (see Tab. 9 for the SSA results). In particular, we can notice that the most constraining is again PL21+BK18+LV21 (see Sec. 13.2 for more details on the likelihoods we include in the analysis), which results in $0.001 < r_{0.01} < 0.033$ and $-1.30 < n_t < 0.37$ at 95% CL. For this case, we show the 2D contours in Fig. 85, compared to some other relevant cases: PL18+BK15 (representing the state of the art) and PL21+BK18 (to underline the improvement carried out by small-scale measurement).

Both Tab. 15 and Fig. 85 show that the TSA mimics a 2σ-detection on every dataset we considered, while generally shrinking the bounds obtained on the tilt (see Sec. 13.1).

	$r_{0.01}$ 95% CL	n_t 95% CL	R − 1 test
PL18+BK15	[0.004, 0.079]	[-0.62, 2.63]	0.008
PL18+BK18	[0.003, 0.039]	[-1.07, 2.10]	0.016
PL18+BK15+LV18	[0.001, 0.070]	[-0.77, 0.42]	0.010
PL18+BK15+LV21	[0.001, 0.070]	[-0.79, 0.39]	0.013
PL18+BK18+LV21	[0.001, 0.035]	[-1.09, 0.39]	0.019
PL21+BK15	[0.002, 0.064]	[-1.06, 2.68]	0.027
PL21+BK18	[0.001, 0.035]	[-1.43, 1.74]	0.035
PL21+BK18+LV21	[0.001, 0.033]	[-1.30, 0.37]	0.005

Table 15: 95% CL intervals of the 8 considered combinations of datasets. These have been obtained through the TSA. Here we also show the results of the Gelman-Rubin test for each combination.

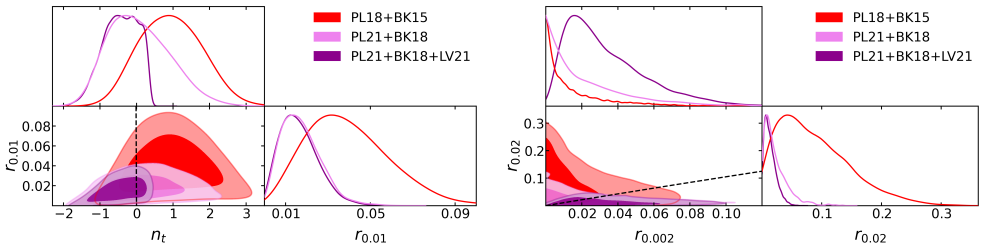

Figure 85: 2D 68 and 95% CL intervals in the $(r_{0.01}, n_t)$ plane (left) and the (r_1, r_2) plane (right) for PL18+BK15, PL21+BK18 and PL21+BK18+LV21 using the TSA. The dashed black line is the well-known slow-roll single-field prediction $n_t = -r/8 = -2\epsilon$.

With Fig. 86, one can compare the results on the 95% CL intervals for $r_{0.01}$ and n_t from SSA and TSA visually, mimicking Fig. 46.

On a more technical note, the 95% CL intervals shown in Tab. 15 are obtained using `GetDist`, which will try to find the values of $r_{0.01}$ or n_t between which the integral of the posterior gives 95% of the total. It will attempt to do so in a two-tail fashion; if it fails, meaning that the upper or lower bound does not exist, it will shift to a single-tail. Thus, in the case of TSA, `GetDist` is capable of recovering a two-tailed bound consistently with every dataset. To avoid this, we would have to worsen the 1D and 2D smoothing scale parameters of `GetDist`, together with the approximation used by the package to account for the prior bounds (the keywords are "boundary_correction_order"

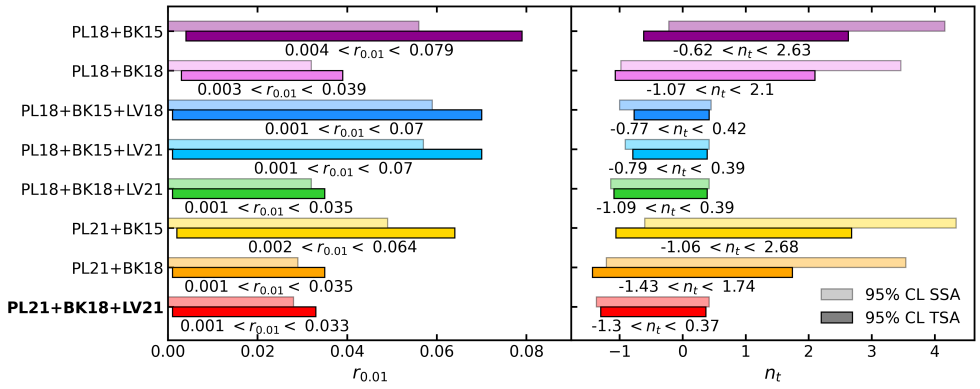

Figure 86: 95% CL intervals for $r_{0.01}$ and n_t, considering different datasets, given in Tab. 8. Here we compare SSA and TSA. Our main result is PL21+BK18+LV21.

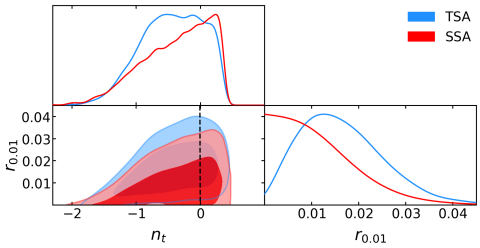

Figure 87: 1D and 2D posteriors on the $r_{0.01}$ and n_t, obtained using the SSA and the TSA on the PL21+BK18+LV21 dataset. The dashed lines represent the single-field slow-roll prediction for $n_t = -2\epsilon$.

and "mult_bias_correction_order", which are left by default to first-order correction [11]).

Furthermore, we can compare the first row of Tab. 9 with the results of *Planck* 2018 [54], mentioned in Sec. 13.3. *Planck* reports $r_{0.01} < 0.076$ and $-0.55 < n_t < 2.54$ at 95% CL, whereas we obtain a 2σ detection on $r_{0.01}$ and slightly wider bounds on n_t. As mentioned above, if we set the 1D and 2D smoothing scale parameters to 0.35 and 0.40 (these are units of the width of the `GetDist` bins), respectively, and the approximations to account for the prior bounds to their minimum, we recover the exactly the bound on the amplitude $r_{0.01} < 0.076$, while we obtain a larger bound on the tilt, that is $-0.79 < n_t < 2.68$. This residual difference in the tilt may be due to a different level of convergence between the two analyses. Note that we run our MCMC very deep into convergence to ensure a careful exploration of the tails of the distributions.

In Fig. 87 we also show the comparison between the posterior distributions obtained using the SSA and the TSA on the PL21+BK18+LV21 dataset.

11 For more details on these parameters, see https://getdist.readthedocs.io/en/latest/index.html .

D

APPENDIX TO THE PL ANALYSIS

D.1 TESTS ON THE ACCURACY

In Chap. 14 we mention that to perform a precise PL, it is crucial to efficiently minimize the likelihood, reaching in each point of the profiled parameter the absolute minimum of the conditional likelihood (and not a local one). Thus, to verify the precision of our minimizing procedure, we performed different tests. For instance, we fix the tensor-to-scalar ratio to $r = 0.02$ and minimize the likelihood eight times, storing the result of each. We repeat this while changing the accuracy parameters of `CAMB` and of `MINUIT`. The dispersion of the results is an indication of the precision of the minimization performed by `MINUIT`, since it gauges the reliability of recovering the absolute minimum. In addition, the value at which these points tend depends to some degree on the accuracy of the Boltzmann solver [298].

In particular, the parameters we considered for these tests are

- `stra` of `MINUIT`, which allows to change the "strategy" of the minimization from *fast* (`stra` $= 0$), *balanced* (`stra` $= 1$) and *accurate* (`stra` $= 2$). The default value is `stra` $= 1$.
- `AccuracyBoost` of `CAMB`, which controls several other accuracy parameters of the Boltzmann solver. The default value is 1.
- `lAccuracyBoost` of `CAMB`, which is related to the resolution in ℓ space of the Boltzmann solver. The default value is 1.

Fig. 88 shows the different sets of minima we obtain, where we define

STANDARD ACCURACY $\rightarrow$ Default settings;

HIGH ACCURACY IMINUIT $\rightarrow$ `stra` $= 2$;

HIGH ACCURACY CAMB $\rightarrow$ `AccuracyBoost` $= 2$ and `lAccuracyBoost` $= 2$;

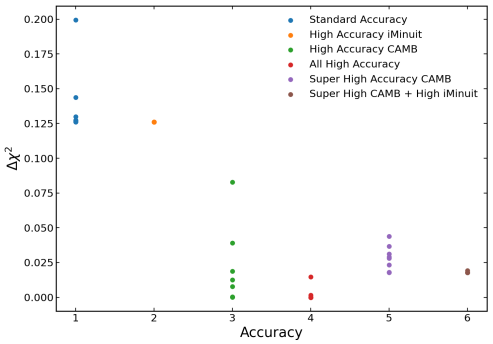

Figure 88: Different set of minima obtained with different settings for the accuracy of `CAMB` and `MINUIT`.

Parameter	Prior	Parameter	Prior
$log(10^{10}A_s)$	$[1.61, 3.91]$	τ_{reio}	$[0.01, 0.8]$
n_s	$[0.8, 1.2]$	θ_{MC}	$[0.5, 10]$
$\Omega_b h^2$	$[0.005, 0.1]$	$r_{0.01}$	$[10^{-5}, 3]$
$\Omega_{cdm} h^2$	$[0.001, 0.99]$	n_t	$[-5, 5]$

Table 16: Priors on the parameters of ΛCDM + $r_{0.01}$ + n_t. Here, A_s is the scalar perturbations amplitude, n_s the scalar spectral tilt, Ω_b and Ω_{cdm} are the abundances of baryons and CDM, $h \equiv H_0/100$ is the Hubble constant divided by 100, τ_{reio} the optical depth and θ_{MC} is an approximate quantity representing the sound horizon.

ALL HIGH ACCURACY → `stra` = 2, `AccuracyBoost` = 2 and `lAccuracyBoost` = 2;

SUPER HIGH ACCURACY CAMB → `AccuracyBoost` = 3 and `lAccuracyBoost` = 3;

SUPER HIGH CAMB + HIGH IMINUIT → `stra` = 2, `AccuracyBoost` = 3 and `lAccuracyBoost` = 3.

It is clear that these settings have an effect on the values that we obtain for the minimum. Fig. 88 shows that when we increase the accuracy of `MINUIT` the dispersion of the points gets severally reduced. Instead, the absolute minimum we obtain here is given by increasing the accuracy of `CAMB` to *high*, since going to *super high* actually increases the values of χ^2. Despite this, all of these non-default settings increase significantly the computation time necessary to minimize the likelihood, so is it worth?

First, note that even with *high* `CAMB` accuracy, the typical χ^2 decreases of $\sim$ 0.125. Still, if this difference is just a constant offset between the two configurations, it will essentially disappear when we normalize the likelihood values on the absolute minimum (see Chap. 12 for the definition of PL). Furthermore, note that although increasing the accuracy of *MINUIT* leads all points to converge to the absolute minimum, it is not worth it in terms of computation time. In fact, usually more than half of the points with the default `MINUIT` converge to the same point, so statistically we always get at least one point there.

Despite these considerations, we also build a parabolic fit for each accuracy configuration (with $\mathcal{O}(10)$ points) to verify that we can stick to the default settings. We find no significant differences in the final PL.

D.2 CONSTRAINTS ON THE ΛCDM PARAMETERS

As mentioned in Sec. 10.2, the focus of this work is the tensor sector of parameter space, which consists of $r_{0.01}$ and n_t. Despite this, to correctly capture the variability in these parameters, it is also important to sample all the other ΛCDM and nuisance parameters. First, we define a set of priors in

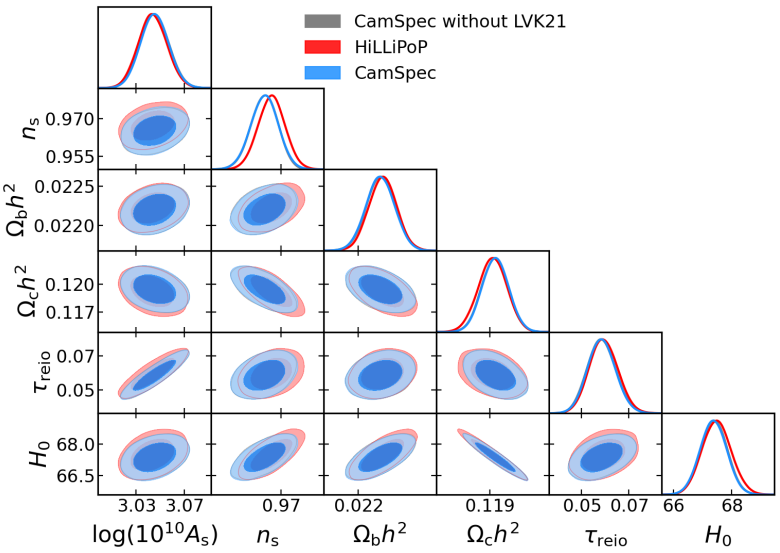

Figure 89: ΛCDM contours for the explored combinations of parameters (see Sec. 14.1).

Tab. 16, encoding our knowledge about the physical parameters. For what regards the nuisance parameters of the various likelihoods, we stick to the default settings.

In addition, we fix the number of relativistic degrees of freedom to $N_{\rm eff} = 3.046$, asking for a massive neutrino with $M_\nu = 0.06$ eV.

In Sec. 14.3, the results on the tensor sectors are discussed, while here we show those on the ΛCDM parameters. In fact, Fig. 89 shows the triangle plot of what we may call the "scalar" sector of parameters. Note that here we substitute $\theta_{\rm MC}$ with H_0 as it is a more physical parameter controlling the sound horizon. Here, we consider CamSpec with and without LVK21, and HiLLiPoP, showing that they are all compatible with each other.

To be more quantitative, we also report in Tab. 17 the mean values and standard deviations of these parameters.

As expected, removing LVK21 brings no difference on the ΛCDM parameters. The only noticeable difference is found by looking at n_s for CamSpec and HiLLiPoP, which is estimated to be slightly higher (approximately $0.5\sigma_{n_s}$ higher) by the latter. This feature is also remarked in [29]. For completeness, we also mention that HiLLiPoP also estimates H_0 to be higher of $\sim 0.2\sigma_{H_0}$.

D.3 GENERALIZED FELDMAN-COUSINS

In Chap. 12 we discussed the FC prescription to obtain confidence intervals with the correct frequentist coverage probability in the presence of a physical boundary. The resulting procedure is known for Gaussian or Poisson distributions. In Chap. 14 we mentioned that our PL seems to depart from a Gaussian far from the minimum. Although this is expected, we ask ourselves whether it is possible to generalize the FC prescription for a more complex curve fitting our PL.

We consider two simple alternatives that have two characteristics: we require that one of the parameters of the function corresponds to the position

Parameter	CamSpec	HiLLiPoP	CamSpec without LVK21
$log(10^{10}A_s)$	3.046 ± 0.012	3.044 ± 0.012	3.045 ± 0.012
n_s	0.9653 ± 0.0039	0.9673 ± 0.0039	0.9653 ± 0.0038
$\Omega_b h^2$	0.02220 ± 0.00013	0.02222 ± 0.00013	0.02220 ± 0.00013
$\Omega_{cdm} h^2$	0.1194 ± 0.0010	0.1192 ± 0.0011	0.1194 ± 0.0010
τ_{reio}	0.0586 ± 0.0059	0.0594 ± 0.0060	0.0586 ± 0.0059
H_0	67.37 ± 0.46	67.49 ± 0.50	67.40 ± 0.45
$r_{0.01}$	< 0.028	< 0.029	< 0.029
n_t	$-1.36 < n_t < 0.42$	$-1.39 < n_t < 0.41$	$-1.35 < n_t < 3.36$

Table 17: Summary of the constraints on the ΛCDM + $r_{0.01}$ + n_t model. For the 6 ΛCDM parameters we report the mean and the standard deviation; instead, we report the 95% CL intervals for the tensor sector, as done in Sec. 14.3.

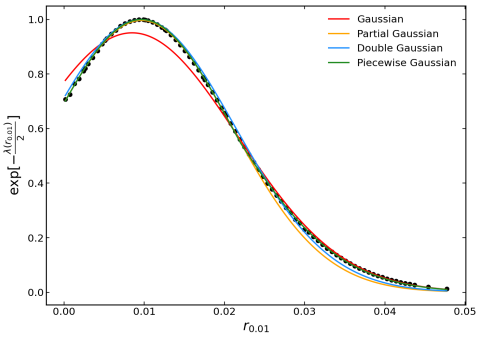

Figure 90: Fits of different curves on the CamSpec PL.

of the maximum; in addition, we will consider only this parameter as free to vary in the FC procedure. In other words, the curve we choose will shift to the right or to the left with the maximum position while keeping its "shape" unchanged.

In particular, we consider what we call *double Gaussian*, defined as

$$P(x|\mu, \Delta\mu, \sigma_1, \sigma_2, A) \propto \exp\left[-\frac{(x-\mu)^2}{2\sigma_1}\right] + A\exp\left[-\frac{(x-\mu-\Delta\mu)^2}{2\sigma_2}\right], \tag{423}$$

and *piecewise Gaussian*, which reads

$$P(x|\mu, \Delta\mu, \sigma_1, \sigma_2, x_{sep}) \propto \begin{cases} \exp\left[-\frac{(x-\mu)^2}{2\sigma_1}\right] & \text{for} \quad x \leq x_{sep} \\ \exp\left[-\frac{(x-\mu-\Delta\mu)^2}{2\sigma_2}\right] & \text{for} \quad x > x_{sep} \end{cases}. \tag{424}$$

Of course, these curves do not find any physical justification, but are born from the pragmatic attempt to fit our PL with analytical formulas. Parameter values are estimated by fitting Eq. 423 and Eq. 424 to our PL; the left panel of Fig. 90 shows that these formulas allow us to recover quite well the shape of the tail.

In the case of HiLLiPoP, we also explore the scenario where we exclude points for $r_{0.01} > 0.022$ and we fit the double Gaussian to recover the bump shown in Fig. 49.

We perform the FC computation, as shown in Chap. 12, again asking $\mu_{best} = \max(0, x)$ and keeping fixed the values of the parameters different from μ. We find that the upper bounds given by the FC belts do not change significantly, thus in the main body we just stick to the partial Gaussian to characterize the various upper bounds.

BIBLIOGRAPHY

[1] A. Riotto. "Inflation and the Theory of Cosmological Perturbations." In: (2002). arXiv: hep-ph/0210162.

[2] N. Bartolo et al. "Non-Gaussianity from Inflation: Theory and Observations." In: *Physics Reports* 402.3-4 (Nov. 2004), pp. 103–266. ISSN: 0370-1573. DOI: 10.1016/j.physrep.2004.08.022. eprint: astro-ph/0406398.

[3] Scott Dodelson. *Modern Cosmology*. Academic Press, Elsevier Science, 2003. DOI: 10.1016/B978-0-12-219141-1.X5019-0.

[4] E. W. Kolb and M. S. Turner. *The Early Universe*. Vol. 69. Westview Press, 1990, pp. 1–547. DOI: 10.1201/9780429492860.

[5] M.P. Hobson, G.P. Efstathiou, and A.N. Lasenby. *General Relativity: An Introduction for Physicists*. Cambridge University Press, Oct. 2006. DOI: 10.1017/CBO9780511790904.

[6] Sean Carroll. *Spacetime and Geometry: An Introduction to General Relativity; International Ed.* Essex: Pearson Education, Aug. 2013. DOI: 1292026634.

[7] Hirokazu Fujii and Yuzuru Yoshii. "An Improved Cosmic Crystallography Method to Detect Holonomies in Flat Spaces." In: *Astronomy & Astrophysics* 529 (2011), A121. ISSN: 0004-6361, 1432-0746. DOI: 10.1051/0004-6361/201116521. arXiv: 1103.1466 [astro-ph.CO].

[8] P.A.R. Ade, N. Aghanim, C. Armitage-Caplan, et al. "Planck 2013 Results. XXVI. Background Geometry and Topology of the Universe." In: *Astronomy & Astrophysics* 571 (Oct. 2014), A26. ISSN: 0004-6361, 1432-0746. DOI: 10.1051/0004-6361/201321546. arXiv: 1303.5086 [astro-ph.CO].

[9] Ralf Aurich and Sven Lustig. "The Hantzsche-Wendt Manifold in Cosmic Topology." In: *Classical and Quantum Gravity* 31.16 (2014), p. 165009. ISSN: 0264-9381, 1361-6382. DOI: 10.1088/0264-9381/31/16/165009. arXiv: 1403.2190 [astro-ph.CO].

[10] Yashar Akrami et al. "The Search for the Topology of the Universe Has Just Begun." In: IFT-UAM/CSIC-22-128 (Oct. 2022). arXiv: 2210.11426 [astro-ph.CO].

[11] Pip Petersen et al. "Cosmic Topology I: Limits on Orientable Euclidean Manifolds from Circle Searches." In: *Journal of Cosmology and Astroparticle Physics* 01.01 (Jan. 2023), p. 030. ISSN: 1475-7516. DOI: 10.1088/1475-7516/2023/01/030. arXiv: 2211.02603 [astro-ph.CO].

[12] Johannes R. Eskilt et al. "Cosmic Topology. Part II. Eigenmodes, Correlation Matrices, and Detectability of Orientable Euclidean Manifolds." In: (June 2023). DOI: 10.48550/arXiv.2306.17112. arXiv: 2306.17112 [astro-ph.CO].

[13] O. Lahav et al. "Dynamical Effects of the Cosmological Constant." In: *Monthly Notices of the Royal Astronomical Society* 251.1 (July 1991), pp. 128–136. ISSN: 0035-8711. DOI: 10.1093/mnras/251.1.128. eprint: https://academic.oup.com/mnras/article-pdf/251/1/128/18523334/mnras251-0128.pdf.

[14] Christian G. Böhmer and Nyein Chan. "Dynamical Systems in Cosmology." In: *Dynamical and Complex Systems* (Dec. 2016), pp. 121–156. DOI: 10.1142/9781786341044_0004.

[15] G. Lemaitre. "The Expanding Universe." In: *Annales Soc. Sci. Bruxelles A* 29 (1997), pp. 641–680. DOI: 10.1023/A:1018855621348.

[16] Cormac O'Raifeartaigh and Simon Mitton. "Interrogating the Legend of Einstein's "Biggest Blunder"." In: *Physics in Perspective* 20.4 (Nov. 2018), pp. 318–341. ISSN: 1422-6944, 1422-6960. DOI: 10.1007/s00016-018-0228-9. arXiv: 1804.06768 [physics.hist-ph].

[17] George F.R. Ellis and Henk van Elst. "Cosmological Models: Cargese Lectures 1998." In: *NATO Sci. Ser. C* 541 (1999), pp. 1–116. DOI: 10.1007/978-94-011-4455-1_1. arXiv: gr-qc/9812046.

[18] A Emir Gümrükçüo, Carlo R Contaldi, and Marco Peloso. "Inflationary Perturbations in Anisotropic Backgrounds and Their Imprint on the Cosmic Microwave Background." In: *Journal of Cosmology and Astroparticle Physics* 2007.11 (Nov. 2007), pp. 005–005. ISSN: 1475-7516. DOI: 10.1088/1475-7516/2007/11/005.

[19] D. Baumann. "Inflation." In: *Theoretical Advanced Study Institute in Elementary Particle Physics: Physics of the Large and the Small*. 2011, pp. 523–686. DOI: 10.1142/9789814327183_0010. arXiv: 0907.5424 [hep-th].

[20] Maxim Pospelov and Josef Pradler. "Big Bang Nucleosynthesis as a Probe of New Physics." In: *Annual Review of Nuclear and Particle Science* 60.1 (Nov. 2010), pp. 539–568. ISSN: 1545-4134. DOI: 10.1146/annurev.nucl.012809.104521.

[21] A. A. Penzias and R. W. Wilson. "A Measurement of Excess Antenna Temperature at 4080 Mc/s." In: *The Astrophysical Journal* 142 (1965), pp. 419–421. ISSN: 0004-637X. DOI: 10.1086/148307.

[22] D. J. Fixsen et al. "The Cosmic Microwave Background Spectrum from the FullCOBEFIRAS Data Set." In: *The Astrophysical Journal* 473.2 (Dec. 1996), pp. 576–587. ISSN: 1538-4357. DOI: 10.1086/178173.

[23] D. J. Fixsen. "The Temperature of the Cosmic Microwave Background." In: *The Astrophysical Journal* 707.2 (Dec. 2009), pp. 916–920. ISSN: 0004-637X, 1538-4357. DOI: 10.1088/0004-637X/707/2/916. arXiv: 0911.1955 [astro-ph].

[24] Jonathan R Pritchard and Abraham Loeb. "21 Cm Cosmology in the 21st Century." In: *Reports on Progress in Physics* 75.8 (July 2012), p. 086901. ISSN: 1361-6633. DOI: 10.1088/0034-4885/75/8/086901.

[25] Arianna Favale, Adrià Gómez-Valent, and Marina Migliaccio. "Cosmic Chronometers to Calibrate the Ladders and Measure the Curvature of the Universe. A Model-Independent Study." In: *Monthly Notices of the Royal Astronomical Society* 523.3 (June 2023), p. 3406. ISSN: 0035-8711, 1365-2966. DOI: 10.1093/mnras/stad1621. arXiv: 2301.09591 [astro-ph.CO].

[26] Viviana Cuozzo et al. "DEMNUni: Cross-Correlating the Nonlinear ISWRS Effect with CMB-lensing and Galaxies in the Presence of Massive Neutrinos." In: (Sept. 2023). DOI: 10.48550/arXiv.2307.15711. arXiv: 2307.15711 [astro-ph.CO].

[27] Federico De Luca et al. "The Three Hundred Project: Dynamical State of Galaxy Clusters and Morphology from Multi-Wavelength Synthetic Maps." In: (Nov. 2020). DOI: 10.1093/mnras/stab1073. arXiv: 2011.09002 [astro-ph.CO].

[28] Javier Carrón Duque et al. "A Novel Cosmic Filament Catalogue from SDSS Data." In: *Astronomy & Astrophysics* 659 (Mar. 2022), A166. ISSN: 0004-6361, 1432-0746. DOI: 10.1051/0004-6361/202141538. arXiv: 2106.05253 [astro-ph].

[29] M. Tristram et al. "Cosmological Parameters Derived from the Final (PR4) Planck Data Release." In: *Astronomy & Astrophysics* (2024). ISSN: 0004-6361, 1432-0746. DOI: 10.1051/0004-6361/202348015. arXiv: 2309.10034 [astro-ph.CO].

[30] M. C. Guzzetti et al. "Gravitational Waves from Inflation." In: *Riv. Nuovo Cim.* 39.9 (2016), pp. 399–495. DOI: 10.1393/ncr/i2016-10127-1. arXiv: 1605.01615 [astro-ph.CO].

[31] Milton Abramowitz, I. Stegun, and A. G. Greenhill. *Handbook of Mathematical Functions with Formulas, Graphs and Mathematical Tables*. 1971.

[32] N.W. Boggess et al. "The COBE Mission - Its Design and Performance Two Years after Launch." In: *Astrophysical Journal* 397 (1992), pp. 420–429. DOI: 10.1086/171797.

[33] George F. Smoot. "COBE Observations and Results." In: *Conference on 3K cosmology* (1999). DOI: 10.1063/1.59326.

[34] Wayne Hu. "Wandering in the Background: A CMB Explorer." In: *arXiv e-prints* (Aug. 1995), astro–ph/9508126. arXiv: astro-ph/9508126.

[35] D. J. Eisenstein. "Dark Energy and Cosmic Sound." In: *New Astronomy Reviews* 49.7 (2005), pp. 360–365. ISSN: 1387-6473. DOI: 10.1016/j.newar.2005.08.005.

[36] Daniel J. Eisenstein et al. "Detection of the Baryon Acoustic Peak in the Large-Scale Correlation Function of SDSS Luminous Red Galaxies." In: *The Astrophysical Journal* 633.2 (Nov. 2005), pp. 560–574. ISSN: 1538-4357. DOI: 10.1086/466512.

[37] R.K. Sachs and A.M. Wolfe. "Perturbations of a Cosmological Model and Angular Variations of the Microwave Background." In: *Astrophysical Journal* 147 (1967), pp. 73–90. DOI: 10.1007/s10714-007-0448-9.

[38] M.J. Rees and D.W. Sciama. "Large Scale Density Inhomogeneities in the Universe." In: *Nature* 217 (1968), pp. 511–516. DOI: 10.1038/217511a0.

[39] Ethan T. Vishniac. "Reionization and Small-Scale Fluctuations in the Microwave Background." In: *The Astrophysics Journal* 322 (Nov. 1987), p. 597. DOI: 10.1086/165755.

[40] A. Blanchard and J. Schneider. "Gravitational Lensing Effect on the Fluctuations of the Cosmic Background Radiation." In: *Astronomy & Astrophysics* 184.1-2 (Oct. 1987), pp. 1–6.

[41] Radek Stompor et al. "Maximum Likelihood Algorithm for Parametric Component Separation in Cosmic Microwave Background Experiments." In: *Monthly Notices of the Royal Astronomical Society* 392 (2009), p. 216. ISSN: 0035-8711. DOI: 10.1111/j.1365-2966.2008.14023.x. arXiv: 0804.2645 [astro-ph].

[42] V. Stolyarov et al. "All-Sky Component Separation for the Planck Mission." In: *Monthly Notices of the Royal Astronomical Society* 336.1 (2002), pp. 97–111. ISSN: 0035-8711. DOI: 10.1046/j.1365-8711.2002.05683.x. arXiv: astro-ph/0105432.

[43] H. K. Eriksen et al. "Joint Bayesian Component Separation and CMB Power Spectrum Estimation." In: *The Astrophysical Journal* 676 (2008), pp. 10–32. ISSN: 0004-637X. DOI: 10.1086/525277. arXiv: 0709.1058 [astro-ph].

[44] J. Delabrouille, J.-F. Cardoso, and G. Patanchon. "Multidetector Multicomponent Spectral Matching and Applications for Cosmic Microwave Background Data Analysis." In: *Monthly Notices of the Royal Astronomical Society* 346.4 (2003), p. 1089. ISSN: 0035-8711. DOI: 10.1111/j.1365-2966.2003.07069.x. arXiv: astro-ph/0211504.

[45] J. Delabrouille et al. "A Full Sky, Low Foreground, High Resolution CMB Map from WMAP." In: *Astronomy and Astrophysics* 493 (2009), p. 835. ISSN: 0004-6361. DOI: 10.1051/0004-6361:200810514. arXiv: 0807.0773 [astro-ph].

[46] C. L. Bennett et al. "First-Year Wilkinson Microwave Anisotropy Probe (WMAP) Observations: Foreground Emission." In: *The Astrophysical Journal Supplement Series* 148 (2003), p. 97. ISSN: 0067-0049. DOI: 10.1086/377252. arXiv: astro-ph/0302208.

[47] Alessandro Carones et al. *Analysis of NILC Performance on B-modes Data of Sub-Orbital Experiments*. Aug. 2022. arXiv: 2208.12059.

[48] Alessandro Carones et al. "Multi-Clustering Needlet-ILC for CMB B-modes Component Separation." In: 525.2 (Aug. 2023), pp. 3117–3135. DOI: 10.1093/mnras/stad2423. arXiv: 2212.04456 [astro-ph.CO].

[49] N. Bartolo et al. "Anisotropies and Non-Gaussianity of the Cosmological Gravitational Wave Background." In: *Physical Review D* 100.12 (Dec. 2019). ISSN: 2470-0029. DOI: 10.1103/physrevd.100.121501. eprint: 1908.00527.

[50] N. Bartolo et al. "Characterizing the Cosmological Gravitational Wave Background: Anisotropies and Non-Gaussianity." In: *Physical Review D* 102.2 (July 2020). ISSN: 2470-0029. DOI: 10.1103/physrevd.102.023527. eprint: 1912.09433.

[51] B.P. Abbott, Rich Abbott, Thomas D. Abbott, et al. "GW170817: Observation of Gravitational Waves from a Binary Neutron Star Inspiral." In: *Physical Review Letters* 119.16 (Oct. 2017), p. 161101. ISSN: 0031-9007, 1079-7114. DOI: 10.1103/PhysRevLett.119.161101. arXiv: 1710.05832 [gr-qc].

[52] B. P. Abbott et al. "GW170817: Implications for the Stochastic Gravitational-Wave Background from Compact Binary Coalescences." In: *Physical Review Letters* 120.9 (Mar. 2018), p. 091101. ISSN: 1079-7114. DOI: 10.1103/PhysRevLett.120.091101. arXiv: 1710.05837 [gr-qc].

[53] Nicola Bartolo et al. "Probing Non-Gaussian Stochastic Gravitational Wave Backgrounds with LISA." In: *Journal of Cosmology and Astroparticle Physics* 2018.11 (Nov. 2018), pp. 034–034. ISSN: 1475-7516. DOI: 10.1088/1475-7516/2018/11/034. eprint: 1806.02819.

[54] Y. Akrami et al. "Planck 2018 Results. X. Constraints on Inflation." In: *Astronomy & Astrophysics* 641 (Sept. 2020), A10. ISSN: 0004-6361, 1432-0746. DOI: 10.1051/0004-6361/201833887. arXiv: 1807.06211 [astro-ph].

[55] V. Acquaviva et al. "Second-Order Cosmological Perturbations from Inflation." In: *Nuclear Physics B* 667.1-2 (2003), pp. 119–148. ISSN: 05503213. DOI: 10.1016/S0550-3213(03)00550-9. arXiv: astro-ph/0209156.

[56] S. Matarrese, S. Mollerach, and M. Bruni. "Relativistic Second-Order Perturbations of the Einstein-de Sitter Universe." In: *Physical Review D* 58.4 (1998), p. 043504. ISSN: 0556-2821, 1089-4918. DOI: 10.1103/PhysRevD.58.043504. arXiv: astro-ph/9707278.

[57] Daniel Baumann et al. "Gravitational Wave Spectrum Induced by Primordial Scalar Perturbations." In: *Physical Review D* 76.8 (2007), p. 084019. ISSN: 1550-7998, 1550-2368. DOI: 10.1103/PhysRevD.76.084019. arXiv: hep-th/0703290.

[58] Kishore N. Ananda, Chris Clarkson, and David Wands. "The Cosmological Gravitational Wave Background from Primordial Density Perturbations." In: *Physical Review D* 75.12 (2007), p. 123518. ISSN: 1550-7998, 1550-2368. DOI: 10.1103/PhysRevD.75.123518. arXiv: gr-qc/0612013.

[59] Silvia Mollerach, Diego Harari, and Sabino Matarrese. "CMB Polarization from Secondary Vector and Tensor Modes." In: *Physical Review D* 69.6 (2004), p. 063002. ISSN: 1550-7998, 1550-2368. DOI: 10.1103/PhysRevD.69.063002. arXiv: astro-ph/0310711.

[60] Christian Fidler et al. "The Intrinsic B-mode Polarisation of the Cosmic Microwave Background." In: *Journal of Cosmology and Astroparticle Physics* 07.07 (2014), p. 011. ISSN: 1475-7516. DOI: 10.1088/1475-7516/2014/07/011. arXiv: 1401.3296 [astro-ph.CO].

[61] N. Bartolo et al. "The Maximal Amount of Gravitational Waves in the Curvaton Scenario." In: *Physical Review D* 76.6 (2007), p. 061302. ISSN: 1550-7998, 1550-2368. DOI: 10.1103/PhysRevD.76.061302. arXiv: 0705.4240 [astro-ph].

[62] Masahiro Kawasaki, Naoya Kitajima, and Shuichiro Yokoyama. "Gravitational Waves from a Curvaton Model with Blue Spectrum." In: *Journal of Cosmology and Astroparticle Physics* 08.08 (Aug. 2013), p. 042. ISSN: 1475-7516. DOI: 10.1088/1475-7516/2013/08/042. arXiv: 1305.4464 [astro-ph.CO].

[63] Matteo Biagetti, Matteo Fasiello, and Antonio Riotto. "Enhancing Inflationary Tensor Modes through Spectator Fields." In: *Physical Review D* 88.10 (Nov. 2013), p. 103518. ISSN: 1550-7998, 1550-2368. DOI: 10.1103/PhysRevD.88.103518. arXiv: 1305.7241 [astro-ph.CO].

[64] Matteo Biagetti et al. "Gravitational Waves and Scalar Perturbations from Spectator Fields." In: *Journal of Cosmology and Astroparticle Physics* 04.04 (Apr. 2015), p. 011. ISSN: 1475-7516. DOI: 10.1088/1475-7516/2015/04/011. arXiv: 1411.3029 [astro-ph.CO].

[65] Tomohiro Fujita, Jun'ichi Yokoyama, and Shuichiro Yokoyama. "Can a Spectator Scalar Field Enhance Inflationary Tensor Mode?" In: *Progress of Theoretical and Experimental Physics* 2015.4 (Apr. 2015), 043E01. ISSN: 2050-3911. DOI: 10.1093/ptep/ptv037. arXiv: 1411.3658 [astro-ph.CO].

[66] Jessica L. Cook and Lorenzo Sorbo. "Particle Production during Inflation and Gravitational Waves Detectable by Ground-Based Interferometers." In: *Physical Review D* 85.2 (Jan. 2012). ISSN: 1550-2368. DOI: 10.1103/physrevd.85.023534. arXiv: 1109.0022 [astro-ph, physics:gr-qc, physics:hep-ph, physics:hep-th].

[67] Lorenzo Sorbo. "Parity Violation in the Cosmic Microwave Background from a Pseudoscalar Inflaton." In: *Journal of Cosmology and Astroparticle Physics* 06.06 (2011), p. 003. ISSN: 1475-7516. DOI: 10.1088/1475-7516/2011/06/003. arXiv: 1101.1525 [astro-ph.CO].

[68] Neil Barnaby, Ryo Namba, and Marco Peloso. "Phenomenology of a Pseudo-Scalar Inflaton: Naturally Large Nongaussianity." In: 04 (2011), p. 009. DOI: 10.1088/1475-7516/2011/04/009. arXiv: 1102.4333 [astro-ph.CO].

[69] Neil Barnaby and Marco Peloso. "Large Non-Gaussianity in Axion Inflation." In: *Physical Review Letters* 106.18 (May 2011). ISSN: 1079-7114. DOI: 10.1103/physrevlett.106.181301. arXiv: 1011.1500 [hep-ph].

[70] Ryo Namba et al. "Scale-Dependent Gravitational Waves from a Rolling Axion." In: *Journal of Cosmology and Astroparticle Physics* 01.01 (Jan. 2016), p. 041. ISSN: 1475-7516. DOI: 10.1088/1475-7516/2016/01/041. arXiv: 1509.07521 [astro-ph.CO].

[71] P. Campeti et al. "LiteBIRD Science Goals and Forecasts. A Case Study of the Origin of Primordial Gravitational Waves Using Large-Scale CMB Polarization." In: (Dec. 2023). DOI: 10.48550/arXiv.2312.00717. arXiv: 2312.00717 [astro-ph.CO].

[72] Neil Barnaby, Enrico Pajer, and Marco Peloso. "Gauge Field Production in Axion Inflation: Consequences for Monodromy, Non-Gaussianity in the CMB, and Gravitational Waves at Interferometers." In: *Physical Review D* 85.2 (2012), p. 023525. ISSN: 1550-7998, 1550-2368. DOI: 10.1103/PhysRevD.85.023525. arXiv: 1110.3327 [astro-ph.CO].

[73] Shinji Mukohyama et al. "Blue Tensor Spectrum from Particle Production during Inflation." In: *Journal of Cosmology and Astroparticle Physics* 08.08 (2014), p. 036. ISSN: 1475-7516. DOI: 10.1088/1475-7516/2014/08/036. arXiv: 1405.0346 [astro-ph.CO].

[74] Lev Kofman, Andrei Linde, and Alexei Starobinsky. "Reheating after Inflation." In: *Physical Review Letters* 73.24 (1994), pp. 3195–3198. ISSN: 0031-9007. DOI: 10.1103/PhysRevLett.73.3195. arXiv: hep-th/9405187.

[75] Lev Kofman, Andrei Linde, and Alexei Starobinsky. "Towards the Theory of Reheating After Inflation." In: *Physical Review D* 56.6 (1997), pp. 3258–3295. ISSN: 0556-2821, 1089-4918. DOI: 10.1103/PhysRevD.56.3258. arXiv: hep-ph/9704452.

[76] A. D. Linde. "Chaotic Inflation." In: *Physics Letters B* 129 (1983), pp. 177–181. ISSN: 0370-2693. DOI: 10.1016/0370-2693(83)90837-7.

[77] Andrei Linde. "Hybrid Inflation." In: *Physical Review D* 49.2 (1994), pp. 748–754. ISSN: 0556-2821. DOI: 10.1103/PhysRevD.49.748. arXiv: astro-ph/9307002.

[78] Andreas Albrecht and Paul J. Steinhardt. "Cosmology for Grand Unified Theories with Radiatively Induced Symmetry Breaking." In: *Physical Review Letters* 48.17 (1982), pp. 1220–1223. DOI: 10.1103/PhysRevLett.48.1220.

[79] Thomas P. Sotiriou and Valerio Faraoni. "F(R) Theories Of Gravity." In: *Reviews of Modern Physics* 82.1 (2010), pp. 451–497. ISSN: 0034-6861, 1539-0756. DOI: 10.1103/RevModPhys.82.451. arXiv: 0805.1726 [gr-qc].

[80] Antonio De Felice and Shinji Tsujikawa. "Inflationary Gravitational Waves in the Effective Field Theory of Modified Gravity." In: *Physical Review D* 91.10 (May 2015), p. 103506. ISSN: 1550-7998, 1550-2368. DOI: 10.1103/PhysRevD.91.103506. arXiv: 1411.0736 [hep-th].

[81] Yong Cai, Yu-Tong Wang, and Yun-Song Piao. "Oscillation in Power Spectrum of Primordial Gravitational Wave as a Signature of Higher-Order Stringy Corrections." In: *Journal of High Energy Physics* 02.2 (Feb. 2016), p. 059. ISSN: 1029-8479. DOI: 10.1007/JHEP02(2016)059. arXiv: 1508.07114 [hep-th].

[82] Gregory Walter Horndeski. "Second-Order Scalar-Tensor Field Equations in a Four-Dimensional Space." In: *International Journal of Theoretical Physics* 10.6 (1974), pp. 363–384. ISSN: 1572-9575. DOI: 10.1007/BF01807638.

[83] C. Brans and R. H. Dicke. "Mach's Principle and a Relativistic Theory of Gravitation." In: *Phys. Rev.* 124 (1961). Ed. by Jong-Ping Hsu and D. Fine, pp. 925–935. DOI: 10.1103/PhysRev.124.925.

[84] Alexei Starobinsky. "A New Type of Isotropic Cosmological Models Without Singularity." In: *Physics Letters B* 91 (Mar. 1980), pp. 99–102. DOI: 10.1016/0370-2693(80)90670-X.

[85] C. Armendariz-Picon, T. Damour, and V. Mukhanov. "K-Inflation." In: *Physics Letters B* 458.2-3 (1999), pp. 209–218. ISSN: 03702693. DOI: 10.1016/S0370-2693(99)00603-6. arXiv: hep-th/9904075.

[86] Xingang Chen et al. "Observational Signatures and Non-Gaussianities of General Single Field Inflation." In: *Journal of Cosmology and Astroparticle Physics* 01.01 (2007), p. 002. ISSN: 1475-7516. DOI: 10.1088/1475-7516/2007/01/002. arXiv: hep-th/0605045.

[87] David Wands et al. "An Observational Test of Two-field Inflation." In: *Physical Review D* 66.4 (2002), p. 043520. ISSN: 0556-2821, 1089-4918. DOI: 10.1103/PhysRevD.66.043520. arXiv: astro-ph/0205253.

[88] Layne C. Price et al. "Gravitational Wave Consistency Relations for Multifield Inflation." In: *Physical Review Letters* 114.3 (Jan. 2015), p. 031301. ISSN: 0031-9007, 1079-7114. DOI: 10.1103/PhysRevLett.114.031301. arXiv: 1409.2498 [astro-ph.CO].

[89] Sabino Matarrese and Antonio Riotto. "Large-Scale Curvature Perturbations with Spatial and Time Variations of the Inflaton Decay Rate." In: *Journal of Cosmology and Astroparticle Physics* 08.08 (2003), p. 007. ISSN: 1475-7516. DOI: 10.1088/1475-7516/2003/08/007. arXiv: astro-ph/0306416.

[90] Dario Cannone, Gianmassimo Tasinato, and David Wands. "Generalised Tensor Fluctuations and Inflation." In: *Journal of Cosmology and Astroparticle Physics* 01.01 (Jan. 2015), p. 029. ISSN: 1475-7516. DOI: 10.1088/1475-7516/2015/01/029. arXiv: 1409.6568 [astro-ph.CO].

[91] Leila Graef and Robert Brandenberger. "Breaking of Spatial Diffeomorphism Invariance, Inflation and the Spectrum of Cosmological Perturbations." In: *Journal of Cosmology and Astroparticle Physics* 10.10 (Oct. 2015), p. 009. ISSN: 1475-7516. DOI: 10.1088/1475-7516/2015/10/009. arXiv: 1506.00896 [astro-ph.CO].

[92] Yong Cai, Yu-Tong Wang, and Yun-Song Piao. "Propagating Speed of Primordial Gravitational Waves and Inflation." In: *Physical Review D* 94.4 (Aug. 2016), p. 043002. ISSN: 2470-0010, 2470-0029. DOI: 10.1103/PhysRevD.94.043002. arXiv: 1602.05431 [astro-ph.CO].

[93] Giulia Capurri et al. "Let Effective Field Theory of Inflation Flow: Stochastic Generation of Models with Red/Blue Tensor Tilt." In: *Journal of Cosmology and Astroparticle Physics* 2020.11 (Nov. 2020), pp. 037–037. ISSN: 1475-7516. DOI: 10.1088/1475-7516/2020/11/037. arXiv: 2006.10781 [astro-ph].

[94] Florian Schulze et al. "GW_CLASS: Cosmological Gravitational Wave Background in the Cosmic Linear Anisotropy Solving System." In: *JCAP* 10.ET-0151A-23, TTK-23-30 (2023), p. 025. DOI: 10.1088/1475-7516/2023/10/025. arXiv: 2305.01602 [gr-qc].

[95] Lorenzo Valbusa Dall'Armi et al. "Adiabatic or Non-Adiabatic? Unraveling the Nature of Initial Conditions in the Cosmological Gravitational Wave Background." In: (July 2023). DOI: 10.48550/arXiv.2307.11043. arXiv: 2307.11043 [astro-ph.CO].

[96] Yuki Watanabe and Eiichiro Komatsu. "Improved Calculation of the Primordial Gravitational Wave Spectrum in the Standard Model." In: *Physical Review D* 73.12 (2006), p. 123515. ISSN: 1550-7998, 1550-2368. DOI: 10.1103/PhysRevD.73.123515. arXiv: astro-ph/0604176.

[97] Sachiko Kuroyanagi, Kazunori Nakayama, and Jun'ichi Yokoyama. "Prospects of Determination of Reheating Temperature after Inflation by DECIGO." In: *Progress of Theoretical and Experimental Physics* 2015.1 (Jan. 2015), 013E02. ISSN: 2050-3911. DOI: 10.1093/ptep/ptu176. arXiv: 1410.6618 [astro-ph.CO].

[98] Latham A. Boyle and Paul J. Steinhardt. "Probing the Early Universe with Inflationary Gravitational Waves." In: *Physical Review D* 77.6 (2008), p. 063504. ISSN: 1550-7998, 1550-2368. DOI: 10.1103/PhysRevD.77.063504. arXiv: astro-ph/0512014.

[99] Sachiko Kuroyanagi et al. "Implications of the B-mode Polarization Measurement for Direct Detection of Inflationary Gravitational Waves." In: *Physical Review D* 90.6 (Sept. 2014), p. 063513. ISSN: 1550-7998, 1550-2368. DOI: 10.1103/PhysRevD.90.063513. arXiv: 1406.1369 [astro-ph.CO].

[100] Kazunori Nakayama et al. "Probing Reheating Temperature of the Universe with Gravitational Wave Background." In: *Journal of Cosmology and Astroparticle Physics* 06.06 (2008), p. 020. ISSN: 1475-7516. DOI: 10.1088/1475-7516/2008/06/020. arXiv: 0804.1827 [astro-ph].

[101] Tristan L. Smith, Elena Pierpaoli, and Marc Kamionkowski. "A New Cosmic Microwave Background Constraint to Primordial Gravitational Waves." In: *Physical Review Letters* 97.2 (2006), p. 021301. ISSN: 0031-9007, 1079-7114. DOI: 10.1103/PhysRevLett.97.021301. arXiv: astro-ph/0603144.

[102] G. Mangano et al. "A Precision Calculation of the Effective Number of Cosmological Neutrinos." In: *Physics Letters B* 534.1-4 (2002), pp. 8–16. ISSN: 03702693. DOI: 10.1016/S0370-2693(02)01622-2. arXiv: astro-ph/0111408.

[103] Luca Pagano, Laura Salvati, and Alessandro Melchiorri. "New Constraints on Primordial Gravitational Waves from Planck 2015." In: *Physics Letters B* 760 (Sept. 2016), pp. 823–825. ISSN: 03702693. DOI: 10.1016/j.physletb.2016.07.078. arXiv: 1508.02393 [astro-ph.CO].

[104] L. Valbusa Dall'Armi et al. "Imprint of Relativistic Particles on the Anisotropies of the Stochastic Gravitational-Wave Background." In: *Physical Review D* 103.2 (Jan. 2021). ISSN: 2470-0029. DOI: 10.1103/physrevd.103.023522. eprint: 2007.01215.

[105] Steven Weinberg. "Damping of Tensor Modes in Cosmology." In: *Physical Review D* 69.2 (2004), p. 023503. ISSN: 1550-7998, 1550-2368. DOI: 10.1103/PhysRevD.69.023503. arXiv: astro-ph/0306304.

[106] James B. Dent et al. "Damping of Primordial Gravitational Waves from Generalized Sources." In: *Physical Review D* 88.8 (Oct. 2013), p. 084008. ISSN: 1550-7998, 1550-2368. DOI: 10.1103/PhysRevD.88.084008. arXiv: 1307.7571 [astro-ph.CO].

[107] A. Mangilli et al. "The Impact of Cosmic Neutrinos on the Gravitational-Wave Background." In: *Physical Review D* 78.8 (2008), p. 083517. ISSN: 1550-7998, 1550-2368. DOI: 10.1103/PhysRevD.78.083517. arXiv: 0805.3234 [astro-ph].

[108] Shohei Saga, Kiyotomo Ichiki, and Naoshi Sugiyama. "Impact of Anisotropic Stress of Free-Streaming Particles on Gravitational Waves Induced by Cosmological Density Perturbations." In: *Physical Review D* 91.2 (Jan. 2015), p. 024030. ISSN: 1550-7998, 1550-2368. DOI: 10.1103/PhysRevD.91.024030. arXiv: 1412.1081 [astro-ph.CO].

[109] Arthur Lue, Limin Wang, and Marc Kamionkowski. "Cosmological Signature of New Parity-Violating Interactions." In: *Physical Review Letters* 83.8 (1999), pp. 1506–1509. ISSN: 0031-9007, 1079-7114. DOI: 10.1103/PhysRevLett.83.1506. arXiv: astro-ph/9812088.

[110] Mingzhe Li and Xinmin Zhang. "Cosmological CPT Violating Effect on CMB Polarization." In: *Physical Review D* 78.10 (2008), p. 103516. ISSN: 1550-7998, 1550-2368. DOI: 10.1103/PhysRevD.78.103516. arXiv: 0810.0403 [astro-ph].

[111] Maresuke Shiraishi, Angelo Ricciardone, and Shohei Saga. "Parity Violation in the CMB Bispectrum by a Rolling Pseudoscalar." In: *Journal of Cosmology and Astroparticle Physics* 11.11 (Nov. 2013), p. 051. ISSN: 1475-7516. DOI: 10.1088/1475-7516/2013/11/051. arXiv: 1308.6769 [astro-ph.CO].

[112] Nicola Bartolo et al. "Parity-Violating and Anisotropic Correlations in Pseudoscalar Inflation." In: *Journal of Cosmology and Astroparticle Physics* 01.01 (Jan. 2015), p. 027. ISSN: 1475-7516. DOI: 10.1088/1475-7516/2015/01/027. arXiv: 1411.2521 [astro-ph.CO].

[113] P. A. R. Ade et al. "BICEP / Keck XIII: Improved Constraints on Primordial Gravitational Waves Using Planck, WMAP, and BICEP/Keck Observations through the 2018 Observing Season." In: *Physical Review Letters* 127.15 (Oct. 2021), p. 151301. ISSN: 0031-9007, 1079-7114. DOI: 10.1103/PhysRevLett.127.151301. arXiv: 2110.00483 [astro-ph].

[114] M. Tristram et al. "Planck Constraints on the Tensor-to-Scalar Ratio." In: *Astronomy & Astrophysics* 647 (Mar. 2021), A128. ISSN: 0004-6361, 1432-0746. DOI: 10.1051/0004-6361/202039585. arXiv: 2010.01139 [astro-ph.CO].

[115] Steve K. Choi et al. "The Atacama Cosmology Telescope: A Measurement of the Cosmic Microwave Background Power Spectra at 98 and 150 GHz." In: *Journal of Cosmology and Astroparticle Physics* 2020.12 (Dec. 2020), pp. 045–045. DOI: 10.1088/1475-7516/2020/12/045. eprint: 2007.07289.

[116] J. T. Sayre et al. "Measurements of B-mode Polarization of the Cosmic Microwave Background from 500 Square Degrees of SPTpol Data." In: *Physical Review D* 101.12 (June 2020). DOI: 10.1103/physrevd.101.122003. eprint: 1910.05748.

[117] P. A. R. Ade et al. "A Measurement of the Cosmic Microwave Background B-mode Polarization Power Spectrum at Subdegree Scales from Two Years of POLARBEAR Data." In: *The Astrophysical Journal* 848.2 (Oct. 2017), p. 121. DOI: 10.3847/1538-4357/aa8e9f. eprint: 1705.02907.

[118] S. Adachi et al. "A Measurement of the Degree-scale CMB B-mode Angular Power Spectrum with POLARBEAR." In: *The Astrophysical Journal* 897.1 (July 2020), p. 55. DOI: 10.3847/1538-4357/ab8f24. eprint: 1910.02608.

[119] P. A. R. Ade et al. "BICEP2 / Keck Array x: Constraints on Primordial Gravitational Waves Using Planck, WMAP, and New BICEP2/Keck Observations through the 2015 Season." In: *Physical Review Letters* 121 (2018), p. 221301. DOI: 10.1103/PhysRevLett.121.221301. arXiv: 1810.05216 [astro-ph.CO].

[120] Akito Kusaka et al. "Results from the Atacama B-mode Search (ABS) Experiment." In: *Journal of Cosmology and Astroparticle Physics* 09.09 (Sept. 2018), p. 005. DOI: 10.1088/1475-7516/2018/09/005. arXiv: 1801.01218 [astro-ph.CO].

[121] D. Barkats et al. "Degree-Scale Cosmic Microwave Background Polarization Measurements from Three Years of BICEP1 Data." In: *The Astrophysical Journal* 783.2 (Mar. 2014), p. 67. DOI: 10.1088/0004-637X/783/2/67. arXiv: 1310.1422 [astro-ph.CO].

[122] C. L. Bennett et al. "Nine-Year Wilkinson Microwave Anisotropy Probe (WMAP) Observations: Final Maps and Results." In: *The Astrophysical Journal* 208.2 (Oct. 2013), p. 20. DOI: 10.1088/0067-0049/208/2/20. arXiv: 1212.5225 [astro-ph.CO].

[123] D. Araujo et al. "Second Season QUIET Observations: Measurements of the CMB Polarization Power Spectrum at 95 GHz." In: *The Astrophysical Journal* 760.2 (Nov. 2012), p. 145. DOI: 10.1088/0004-637x/760/2/145. eprint: 1207.5034.

[124] M. L. Brown et al. "Improved Measurements of the Temperature and Polarization of the CMB from QUaD." In: *The Astrophysical Journal* 705.1 (Oct. 2009), pp. 978–999. DOI: 10.1088/0004-637x/705/1/978. eprint: 0906.1003.

[125] Fabian Schmidt, Enrico Pajer, and Matias Zaldarriaga. "Large-Scale Structure and Gravitational Waves III: Tidal Effects." In: *Physical Review D* 89.8 (Apr. 2014), p. 083507. ISSN: 1550-7998, 1550-2368. DOI: 10.1103/PhysRevD.89.083507. arXiv: 1312.5616 [astro-ph.CO].

[126] Liang Dai, Donghui Jeong, and Marc Kamionkowski. "Anisotropic Imprint of Long-Wavelength Tensor Perturbations on Cosmic Structure." In: *Physical Review D* 88.4 (Aug. 2013), p. 043507. ISSN: 1550-7998, 1550-2368. DOI: 10.1103/PhysRevD.88.043507. arXiv: 1306.3985 [astro-ph.CO].

[127] Fabian Schmidt and Donghui Jeong. "Large-Scale Structure with Gravitational Waves II: Shear." In: *Physical Review D* 86.8 (2012), p. 083513. ISSN: 1550-7998, 1550-2368. DOI: 10.1103/PhysRevD.86.083513. arXiv: 1205.1514 [astro-ph.CO].

[128] Fabian Schmidt and Donghui Jeong. "Cosmic Rulers." In: *Physical Review D* 86.8 (2012), p. 083527. ISSN: 1550-7998, 1550-2368. DOI: 10.1103/PhysRevD.86.083527. arXiv: 1204.3625 [astro-ph.CO].

[129] Liang Dai, Marc Kamionkowski, and Donghui Jeong. "Total Angular Momentum Waves for Scalar, Vector, and Tensor Fields." In: *Physical Review D* 86.12 (2012), p. 125013. ISSN: 1550-7998, 1550-2368. DOI: 10.1103/PhysRevD.86.125013. arXiv: 1209.0761 [astro-ph.CO].

[130] Christopher J. Moore, Robert H. Cole, and Christopher P. L. Berry. "Gravitational-Wave Sensitivity Curves." In: *Classical and Quantum Gravity* 32.1 (Dec. 2014), p. 015014. ISSN: 0264-9381, 1361-6382. DOI: 10.1088/0264-9381/32/1/015014. arXiv: 1408.0740 [gr-qc].

[131] Bhal Chandra Joshi. "Pulsar Timing Arrays." In: *International Journal of Modern Physics D* 22.01 (2013), p. 1341008. ISSN: 0218-2718, 1793-6594. DOI: 10.1142/S0218271813410083. arXiv: 1301.5730 [astro-ph.IM].

[132] Gabriella Agazie et al. "The NANOGrav 15-Year Data Set: Evidence for a Gravitational-Wave Background." In: 951.1 (June 2023), p. L8. DOI: 10.3847/2041-8213/acdac6. arXiv: 2306.16213 [astro-ph.HE].

[133] Zaven Arzoumanian et al. "The NANOGrav 12.5 Yr Data Set: Search for an Isotropic Stochastic Gravitational-wave Background." In: *The Astrophysical Journal Letters* 905.2 (Dec. 2020), p. L34. ISSN: 2041-8213. DOI: 10.3847/2041-8213/abd401. eprint: 2009.04496.

[134] B. P. Abbott et al. "Upper Limits on the Stochastic Gravitational-Wave Background from Advanced LIGO's First Observing Run." In: *Physics Review Letters* 118.12 (Mar. 2017), p. 121101. DOI: 10.1103/PhysRevLett.118.121101. arXiv: 1612.02029 [gr-qc].

[135] B. P. Abbott et al. "Search for the Isotropic Stochastic Background Using Data from Advanced LIGO's Second Observing Run." In: *Physical Review D* 100.6 (Sept. 2019), p. 061101. ISSN: 2470-0029. DOI: 10.1103/PhysRevD.100.061101. arXiv: 1903.02886 [gr-qc].

[136] Nicola Bartolo, Sabino Matarrese, and Antonio Riotto. "Cosmic Microwave Background Anisotropies at Second Order: I." In: *Journal of Cosmology and Astroparticle Physics* 2006.06 (June 2006), pp. 024–024. ISSN: 1475-7516. DOI: 10.1088/1475-7516/2006/06/024. eprint: astro-ph/0604416.

[137] Nicola Bartolo, Sabino Matarrese, and Antonio Riotto. "CMB Anisotropies at Second-Order II: Analytical Approach." In: *Journal of Cosmology and Astroparticle Physics* 2007.01 (Jan. 2007), pp. 019–019. ISSN: 1475-7516. DOI: 10.1088/1475-7516/2007/01/019. eprint: astro-ph/0610110.

[138] Carlo R. Contaldi. "Anisotropies of Gravitational Wave Backgrounds: A Line of Sight Approach." In: *Physics Letters B* 771 (Aug. 2017), pp. 9–12. ISSN: 0370-2693. DOI: 10.1016/j.physletb.2017.05.020. eprint: 1609.08168.

[139] Sascha Husa. "Michele Maggiore: Gravitational Waves. Volume 1: Theory and Experiments." In: 41 (2009), pp. 1667–1669. DOI: 10.1007/s10714-009-0762-5.

[140] Michael Geller et al. "Primordial Anisotropies in the Gravitational Wave Background from Cosmological Phase Transitions." In: *Physical Review Letters* 121.20 (Nov. 2018). ISSN: 1079-7114. DOI: 10.1103/physrevlett.121.201303. arXiv: 1803.10780 [hep-ph].

[141] N. Bartolo et al. "Gravitational Wave Anisotropies from Primordial Black Holes." In: *Journal of Cosmology and Astroparticle Physics* 2020.02 (Feb. 2020), pp. 028–028. ISSN: 1475-7516. DOI: 10.1088/1475-7516/2020/02/028. eprint: 1909.12619.

[142] N. Bartolo et al. "Primordial Black Hole Dark Matter: LISA Serendipity." In: *Physical Review Letters* 122.21 (May 2019). ISSN: 1079-7114. DOI: 10.1103/physrevlett.122.211301. eprint: 1810.12218.

[143] N. Bartolo et al. "Testing Primordial Black Holes as Dark Matter with LISA." In: *Physical Review D* 99.10 (May 2019). ISSN: 2470-0029. DOI: 10.1103/physrevd.99.103521. eprint: 1810.12224.

[144] Nicola Bartolo et al. "Photon-Graviton Scattering: A New Way to Detect Anisotropic Gravitational Waves?" In: *Physical Review D* 98.2 (July 2018). ISSN: 2470-0029. DOI: 10.1103/physrevd.98.023518. eprint: 1804.06298.

[145] Charles W. Misner, K. S. Thorne, and J. A. Wheeler. *Gravitation*. San Francisco: W. H. Freeman, 1973. ISBN: 978-0-691-17779-3.

[146] Eiichiro Komatsu. "The Pursuit of Non-Gaussian Fluctuations in the Cosmic Microwave Background." PhD thesis. Tohoku U., 2001. arXiv: astro-ph/0206039.

[147] Y. Akrami et al. *Planck 2018 Results. IX. Constraints on Primordial Non-Gaussianity*. May 2019. DOI: 10.48550/arXiv.1905.05697. arXiv: 1905.05697.

[148] Max Tegmark, Angelica de Oliveira-Costa, and Andrew Hamilton. "A High Resolution Foreground Cleaned CMB Map from WMAP." In: *Physical Review D* 68.12 (Dec. 2003), p. 123523. ISSN: 0556-2821, 1089-4918. DOI: 10.1103/PhysRevD.68.123523. arXiv: astro-ph/0302496.

[149] Angelica de Oliveira-Costa et al. "The Significance of the Largest Scale CMB Fluctuations in WMAP." In: *Physical Review D* 69.6 (Mar. 2004), p. 063516. ISSN: 1550-7998, 1550-2368. DOI: 10.1103/PhysRevD.69.063516. arXiv: astro-ph/0307282.

[150] C. J. Copi, D. Huterer, and G. D. Starkman. "Multipole Vectors–a New Representation of the CMB Sky and Evidence for Statistical Anisotropy or Non-Gaussianity at 2<=l<=8." In: *Physical Review D* 70.4 (Aug. 2004), p. 043515. ISSN: 1550-7998, 1550-2368. DOI: 10.1103/PhysRevD.70.043515. arXiv: astro-ph/0310511.

[151] H. K. Eriksen et al. "Asymmetries in the Cosmic Microwave Background Anisotropy Field." In: *The Astrophysical Journal* 605.1 (Apr. 2004), pp. 14–20. ISSN: 1538-4357. DOI: 10.1086/382267. eprint: astro-ph/0307507.

[152] C. Monteserin et al. "A Low CMB Variance in the WMAP Data." In: *Monthly Notices of the Royal Astronomical Society* 387.1 (June 2008), pp. 209–219. ISSN: 0035-8711, 1365-2966. DOI: 10.1111/j.1365-2966.2008.13149.x. arXiv: 0706.4289 [astro-ph].

[153] Kate Land and Joao Magueijo. "Is the Universe Odd?" In: *Physical Review D* 72.10 (Nov. 2005), p. 101302. ISSN: 1550-7998, 1550-2368. DOI: 10.1103/PhysRevD.72.101302. arXiv: astro-ph/0507289.

[154] Jaiseung Kim and Pavel Naselsky. "Anomalous Parity Asymmetry of the Wilkinson Microwave Anisotropy Probe Power Spectrum Data at Low Multipoles." In: *The Astrophysical Journal* 714.2 (May 2010), pp. L265–L267. ISSN: 2041-8205, 2041-8213. DOI: 10.1088/2041-8205/714/2/L265. arXiv: 1001.4613 [astro-ph].

[155] A. Gruppuso et al. "New Constraints on Parity Symmetry from a Re-Analysis of the WMAP-7 Low Resolution Power Spectra." In: *Monthly Notices of the Royal Astronomical Society* 411.3 (Mar. 2011), pp. 1445–1452. ISSN: 00358711. DOI: 10.1111/j.1365-2966.2010.17773.x. arXiv: 1006.1979 [astro-ph].

[156] M. Cruz et al. *Detection of a Non-Gaussian Spot in WMAP*. Sept. 2004. DOI: 10.1111/j.1365-2966.2004.08419.x/abs/. arXiv: astro-ph/0405341.

[157] P. Vielva et al. "Detection of Non-Gaussianity in the WMAP 1-Year Data Using Spherical Wavelets." In: *The Astrophysical Journal* 609.1 (July 2004), pp. 22–34. ISSN: 0004-637X, 1538-4357. DOI: 10.1086/421007. arXiv: astro-ph/0310273.

[158] Craig J. Copi et al. "Large-Angle Anomalies in the CMB." In: *Advances in Astronomy* 2010 (2010), pp. 1–17. ISSN: 1687-7969, 1687-7977. DOI: 10.1155/2010/847541. arXiv: 1004.5602 [astro-ph, physics:gr-qc, physics:hep-th].

[159] Dominik J. Schwarz et al. "CMB Anomalies after Planck." In: *Classical and Quantum Gravity* 33.18 (Sept. 2016), p. 184001. ISSN: 0264-9381, 1361-6382. DOI: 10.1088/0264-9381/33/18/184001. arXiv: 1510.07929 [astro-ph].

[160] Jessica Muir, Saroj Adhikari, and Dragan Huterer. "Covariance of CMB Anomalies." In: *Physical Review D* 98.2 (July 2018), p. 023521. ISSN: 2470-0010, 2470-0029. DOI: 10.1103/PhysRevD.98.023521. arXiv: 1806.02354 [astro-ph].

[161] J. Richard Gott III, Adrian L. Melott, and Mark Dickinson. "The Sponge-like Topology of Large-Scale Structure in the Universe." In: *The Astrophysical Journal* 306 (July 1986), p. 341. ISSN: 0004-637X. DOI: 10.1086/164347.

[162] J. Richard Gott Iii et al. "Topology of Microwave Background Fluctuations - Theory." In: *The Astrophysical Journal* 352 (Mar. 1990), p. 1. ISSN: 0004-637X, 1538-4357. DOI: 10.1086/168511.

[163] Wesley N. Colley, I. I. I. Gott, and Changbom Park. "Topology of COBE Microwave Background Fluctuations." In: *Monthly Notices of the Royal Astronomical Society* 281.4 (Aug. 1996), pp. L82–L84. ISSN: 0035-8711, 1365-2966. DOI: 10.1093/mnras/281.4.L82. arXiv: astro-ph/9601084.

[164] K. R. Mecke, T. Buchert, and H. Wagner. "Robust Morphological Measures for Large-Scale Structure in the Universe." In: *Astronomy and Astrophysics* 288 (Aug. 1994), pp. 697–704. ISSN: 0004-6361. DOI: 10.48550/arXiv.astro-ph/9312028.

[165] Jens Schmalzing and Krzysztof M. Górski. "Minkowski Functionals Used in the Morphological Analysis of Cosmic Microwave Background Anisotropy Maps." In: *Monthly Notices of the Royal Astronomical Society* 297.2 (June 1998), pp. 355–365. ISSN: 0035-8711. DOI: 10.1046/j.1365-8711.1998.01467.x.

[166] Serge Winitzki and Arthur Kosowsky. "Minkowski Functional Description of Microwave Background Gaussianity." In: *New Astronomy* 3.2 (Mar. 1998), pp. 75–99. ISSN: 1384-1076. DOI: 10.1016/S1384-1076(97)00046-8.

[167] Dimitri Novikov, Stephane Colombi, and Olivier Doré. "Skeleton as a Probe of the Cosmic Web: The 2D Case." In: *Monthly Notices of the Royal Astronomical Society* 366.4 (Mar. 2006), pp. 1201–1216. ISSN: 0035-8711, 1365-2966. DOI: 10.1111/j.1365-2966.2005.09925.x. arXiv: astro-ph/0307003.

[168] H. K. Eriksen et al. "Testing for Non-Gaussianity in the Wilkinson Microwave Anisotropy Probe Data: Minkowski Functionals and the Length of the Skeleton." In: *The Astrophysical Journal* 612.1 (Sept. 2004), pp. 64–80. ISSN: 0004-637X, 1538-4357. DOI: 10.1086/422570. arXiv: astro-ph/0401276.

[169] Frode K. Hansen et al. "Asymmetries in the Local Curvature of the Wilkinson Microwave Anisotropy Probe Data." In: *The Astrophysical Journal* 607.2 (Apr. 2004), p. L67. ISSN: 0004-637X. DOI: 10.1086/421904.

[170] Chan-Gyung Park. "Non-Gaussian Signatures in the Temperature Fluctuation Observed by the Wilkinson Microwave Anisotropy Probe." In: *Monthly Notices of the Royal Astronomical Society* 349.1 (Mar. 2004), pp. 313–320. ISSN: 1365-2966, 0035-8711. DOI: 10.1111/j.1365-2966.2004.07500.x. arXiv: astro-ph/0307469.

[171] Pratyush Pranav et al. "Unexpected Topology of the Temperature Fluctuations in the Cosmic Microwave Background." In: *Astronomy & Astrophysics* 627 (July 2019), A163. ISSN: 0004-6361, 1432-0746. DOI: 10.1051/0004-6361/201834916. arXiv: 1812.07678 [astro-ph].

[172] Pratyush Pranav. "Anomalies in the Topology of the Temperature Fluctuations in the Cosmic Microwave Background: An Analysis of the NPIPE and FFP10 Data Releases." In: *Astronomy & Astrophysics* 659 (Mar. 2022), A115. ISSN: 0004-6361, 1432-0746. DOI: 10.1051/0004-6361/202140291. arXiv: 2111.15427 [astro-ph].

[173] F. K. Hansen et al. "Power Asymmetry in Cosmic Microwave Background Fluctuations from Full Sky to Sub-degree Scales: Is the Universe Isotropic?" In: *The Astrophysical Journal* 704.2 (Oct. 2009), pp. 1448–1458. ISSN: 0004-637X, 1538-4357. DOI: 10.1088/0004-637X/704/2/1448. arXiv: 0812.3795 [astro-ph].

[174] Y. Akrami et al. "Planck 2018 Results. VII. Isotropy and Statistics of the CMB." In: *Astronomy & Astrophysics* 641 (Sept. 2020), A7. ISSN: 0004-6361, 1432-0746. DOI: 10.1051/0004-6361/201935201. arXiv: 1906.02552 [astro-ph].

[175] Fabian Schmidt and Lam Hui. "Cosmic Microwave Background Power Asymmetry from Non-Gaussian Modulation." In: *Physical Review Letters* 110.1 (Jan. 2013), p. 011301. DOI: 10.1103/PhysRevLett.110.011301. eprint: 1210.2965.

[176] Christian T. Byrnes and Ewan R.M. Tarrant. "Scale-Dependent Non-Gaussianity and the CMB Power Asymmetry." In: *Journal of Cosmology and Astroparticle Physics* 2015.07 (July 2015), pp. 007–007. ISSN: 1475-7516. DOI: 10.1088/1475-7516/2015/07/007. eprint: 1502.07339.

[177] Christian T. Byrnes et al. "The Hemispherical Asymmetry from a Scale-Dependent Inflationary Bispectrum." In: *Journal of Cosmology and Astroparticle Physics* 2016.06 (June 2016), pp. 025–025. ISSN: 1475-7516. DOI: 10.1088/1475-7516/2016/06/025. eprint: 1511.03129.

[178] Amjad Ashoorioon and Tomi Koivisto. "Hemispherical Anomaly from Asymmetric Initial States." In: *Physical Review D: Particles and Fields* 94.4 (Aug. 2016), p. 043009. DOI: 10.1103/PhysRevD.94.043009. eprint: 1507.03514.

[179] Saroj Adhikari, Sarah Shandera, and Adrienne L. Erickcek. "Large-Scale Anomalies in the Cosmic Microwave Background as Signatures of Non-Gaussianity." In: *Physical Review D: Particles and Fields* 93.2 (Jan. 2016), p. 023524. DOI: 10.1103/PhysRevD.93.023524. eprint: 1508.06489.

[180] F. K. Hansen et al. "Isotropic Non-Gaussian $_{\mathrm{NL}}$-like Toy Models That Reproduce Cosmic Microwave Background Anomalies." In: *Astronomy & Astrophysics* 626 (June 2019), A13. ISSN: 1432-0746. DOI: 10.1051/0004-6361/201833698. eprint: 1806.08531.

[181] C. Dvorkin, H. V. Peiris, and W. Hu. "Testable Polarization Predictions for Models of CMB Isotropy Anomalies." In: *Physical Review D* 77.6 (Mar. 2008). ISSN: 1550-2368. DOI: 10.1103/physrevd.77.063008. eprint: 0711.2321.

[182] Giacomo Galloni et al. "Test of the Statistical Isotropy of the Universe Using Gravitational Waves." In: *Journal of Cosmology and Astroparticle Physics* 2022.09 (Sept. 2022), p. 046. ISSN: 1475-7516. DOI: 10.1088/1475-7516/2022/09/046. arXiv: 2202.12858 [astro-ph, physics:gr-qc]. (Visited on 11/24/2022).

[183] Julien Lesgourgues. "The Cosmic Linear Anisotropy Solving System (CLASS) I: Overview." In: (Apr. 2011). arXiv: 1104.2932 [astro-ph.IM].

[184] Diego Blas, Julien Lesgourgues, and Thomas Tram. "The Cosmic Linear Anisotropy Solving System (CLASS). Part II: Approximation Schemes." In: *Journal of Cosmology and Astroparticle Physics* 2011.7 (July 2011), p. 034. DOI: 10.1088/1475-7516/2011/07/034. arXiv: 1104.2933 [astro-ph.CO].

[185] Peter Adshead et al. "Multimessenger Cosmology: Correlating Cosmic Microwave Background and Stochastic Gravitational Wave Background Measurements." In: *Physical Review D: Particles and Fields* 103.2 (2021), p. 023532. DOI: 10.1103/PhysRevD.103.023532. arXiv: 2004.06619 [astro-ph.CO].

[186] Ameek Malhotra et al. "Cross-Correlations as a Diagnostic Tool for Primordial Gravitational Waves." In: *Journal of Cosmology and Astroparticle Physics* 2021.03 (Mar. 2021), p. 088. ISSN: 1475-7516. DOI: 10.1088/1475-7516/2021/03/088. arXiv: 2012.03498 [astro-ph, physics:gr-qc, physics:hep-ph, physics:hep-th].

[187] Angelo Ricciardone et al. "Cross-Correlating Astrophysical and Cosmological Gravitational Wave Backgrounds with the Cosmic Microwave Background." In: *Physical Review Letters* 127.27 (Dec. 2021), p. 271301. ISSN: 0031-9007, 1079-7114. DOI: 10.1103/PhysRevLett.127.271301. arXiv: 2106.02591 [astro-ph, physics:gr-qc].

[188] Ema Dimastrogiovanni et al. "Testing the Early Universe with Anisotropies of the Gravitational Wave Background." In: *JCAP* 02.02 (2022), p. 040. DOI: 10.1088/1475-7516/2022/02/040. arXiv: 2109.03077 [astro-ph.CO].

[189] Uros Seljak and Matias Zaldarriaga. "A Line-of-Sight Integration Approach to Cosmic Microwave Background Anisotropies." In: *The Astrophysical Journal* 469 (Oct. 1996), p. 437. ISSN: 1538-4357. DOI: 10.1086/177793. eprint: astro-ph/9603033.

[190] N. Aghanim et al. "Planck 2018 Results. VI. Cosmological Parameters." In: *Astronomy & Astrophysics* 641 (Sept. 2020), A6. ISSN: 0004-6361, 1432-0746. DOI: 10.1051/0004-6361/201833910. arXiv: 1807.06209 [astro-ph].

[191] K. M. Górski et al. "HEALPix: A Framework for High-Resolution Discretization and Fast Analysis of Data Distributed on the Sphere." In: *Astrophysical Journal* 622.2 (Apr. 2005), pp. 759–771. DOI: 10.1086/427976. arXiv: astro-ph/0409513.

[192] Yehuda Hoffman and Erez Ribak. "Constrained Realizations of Gaussian Fields: A Simple Algorithm." In: *APJL* 380 (Oct. 1991), p. L5. DOI: 10.1086/186160.

[193] Caterina Chiocchetta et al. "Lack-of-Correlation Anomaly in CMB Large Scale Polarisation Maps." In: *Journal of Cosmology and Astroparticle Physics* 2021.08 (Aug. 2021), p. 015. ISSN: 1475-7516. DOI: 10.1088/1475-7516/2021/08/015. arXiv: 2012.00024 [astro-ph].

[194] F. H. C. Marriott. "Multivariate Statistics: A Vector Space Approach." In: *Journal of the Royal Statistical Society: Series C (Applied Statistics)* 33.3 (1984), pp. 319–319. DOI: 10.2307/2347710.

[195] Martin Bucher and Thibaut Louis. "Filling in CMB Map Missing Data Using Constrained Gaussian Realizations." In: 424 (2012), p. 1694. DOI: 10.1111/j.1365-2966.2012.21138.x. arXiv: 1109.0286 [astro-ph.CO].

[196] David Alonso et al. "The N_ℓ of Gravitational Wave Background Experiments." In: *Physical Review D* 101.12 (June 2020), p. 124048. ISSN: 2470-0010, 2470-0029. DOI: 10.1103/PhysRevD.101.124048. arXiv: 2005.03001 [astro-ph, physics:gr-qc].

[197] Nicola Bartolo et al. "Probing Anisotropies of the Stochastic Gravitational Wave Background with LISA." In: *Journal of Cosmology and Astroparticle Physics* 2022.11 (Nov. 2022), p. 009. DOI: 10.1088/1475-7516/2022/11/009. arXiv: 2201.08782 [astro-ph.CO].

[198] Matteo Braglia and Sachiko Kuroyanagi. "Probing Pre-Recombination Physics by the Cross-Correlation of Stochastic Gravitational Waves and CMB Anisotropies." In: *Physical Review D* 104.12 (Dec. 2021), p. 123547. ISSN: 2470-0010, 2470-0029. DOI: 10.1103/PhysRevD.104.123547. arXiv: 2106.03786 [astro-ph].

[199] Nathan J. Secrest et al. "A Test of the Cosmological Principle with Quasars." In: *The Astrophysical Journal Letters* 908.2 (Feb. 2021), p. L51. ISSN: 2041-8213. DOI: 10.3847/2041-8213/abdd40. eprint: 2009.14826.

[200] Eoin Ó. Colgáin. "Probing the Anisotropic Universe with Gravitational Waves." In: (Mar. 2022). arXiv: 2203.03956 [astro-ph.CO].

[201] Giacomo Galloni et al. "Unraveling the CMB Lack-of-Correlation Anomaly with the Cosmological Gravitational Wave Background." In: *Journal of Cosmology and Astroparticle Physics* 2023.10 (Oct. 2023), p. 013. ISSN: 1475-7516. DOI: 10.1088/1475-7516/2023/10/013.

[202] G. Hinshaw et al. "2-Point Correlations in the COBE DMR 4-Year Anisotropy Maps." In: *The Astrophysical Journal* 464.1 (June 1996), pp. L25–L28. ISSN: 0004637X. DOI: 10.1086/310076. arXiv: astro-ph/9601061.

[203] D. N. Spergel et al. "First Year Wilkinson Microwave Anisotropy Probe (WMAP) Observations: Determination of Cosmological Parameters." In: *The Astrophysical Journal Supplement Series* 148.1 (Sept. 2003), pp. 175–194. ISSN: 0067-0049, 1538-4365. DOI: 10.1086/377226. arXiv: astro-ph/0302209.

[204] Craig J. Copi et al. "The Uncorrelated Universe: Statistical Anisotropy and the Vanishing Angular Correlation Function in WMAP Years 1-3." In: *Physical Review D* 75.2 (Jan. 2007), p. 023507. ISSN: 1550-7998, 1550-2368. DOI: 10.1103/PhysRevD.75.023507. arXiv: astro-ph/0605135.

[205] Craig J. Copi et al. "No Large-Angle Correlations on the Non-Galactic Microwave Sky." In: *Monthly Notices of the Royal Astronomical Society* 399.1 (Oct. 2009), pp. 295–303. ISSN: 00358711, 13652966. DOI: 10.1111/j.1365-2966.2009.15270.x. arXiv: 0808.3767 [astro-ph].

[206] Craig J. Copi et al. "Lack of Large-Angle TT Correlations Persists in WMAP and Planck." In: *Monthly Notices of the Royal Astronomical Society* 451.3 (Aug. 2015), pp. 2978–2985. ISSN: 0035-8711. DOI: 10.1093/mnras/stv1143. eprint: 1310.3831.

[207] C. L. Bennett et al. "4-Year COBE DMR Cosmic Microwave Background Observations: Maps and Basic Results." In: *The Astrophysical Journal* 464.1 (June 1996), pp. L1–L4. ISSN: 0004637X. DOI: 10.1086/310075. arXiv: astro-ph/9601067.

[208] M. Cruz et al. "Anomalous Variance in the WMAP Data and Galactic Foreground Residuals." In: *Monthly Notices of the Royal Astronomical Society* 412.4 (Apr. 2011), pp. 2383–2390. ISSN: 00358711. DOI: 10.1111/j.1365-2966.2010.18067.x. arXiv: 1005.1264 [astro-ph].

[209] A. Gruppuso. "Two-Point Correlation Function of WMAP 9 Year Data." In: *Monthly Notices of the Royal Astronomical Society* 437.3 (Jan. 2014), pp. 2076–2082. ISSN: 0035-8711, 1365-2966. DOI: 10.1093/mnras/stt1937. arXiv: 1310.2822 [astro-ph].

[210] P. A. R. Ade et al. "Planck 2013 Results. XXIII. Isotropy and Statistics of the CMB." In: *Astronomy & Astrophysics* 571 (Nov. 2014), A23. ISSN: 0004-6361, 1432-0746. DOI: 10.1051/0004-6361/201321534. arXiv: 1303.5083 [astro-ph].

[211] P. A. R. Ade et al. "Planck 2015 Results. XVI. Isotropy and Statistics of the CMB." In: *Astronomy & Astrophysics* 594 (Oct. 2016), A16. ISSN: 0004-6361, 1432-0746. DOI: 10.1051/0004-6361/201526681. arXiv: 1506.07135 [astro-ph].

[212] C. J. Copi et al. "Large-Angle CMB Suppression and Polarization Predictions." In: *Monthly Notices of the Royal Astronomical Society* 434.4 (Oct. 2013), pp. 3590–3596. ISSN: 0035-8711, 1365-2966. DOI: 10.1093/mnras/stt1287. arXiv: 1303.4786 [astro-ph].

[213] M. Billi et al. *Polarisation as a Tracer of CMB Anomalies: Planck Results and Future Forecasts*. June 2019. DOI: 10.48550/arXiv.1901.04762. arXiv: 1901.04762.

[214] Amanda Yoho et al. "Microwave Background Polarization as a Probe of Large-Angle Correlations." In: *Physical Review D* 91.12 (June 2015), p. 123504. ISSN: 1550-7998, 1550-2368. DOI: 10.1103/PhysRevD.91.123504. arXiv: 1503.05928 [astro-ph].

[215] Rui Shi et al. "Testing CMB Anomalies in E-mode Polarization with Current and Future Data." In: *The Astrophysical Journal* 945.1 (Mar. 2023), p. 79. ISSN: 0004-637X, 1538-4357. DOI: 10.3847/1538-4357/acb339. arXiv: 2206.05920 [astro-ph].

[216] Y. Akrami et al. "Planck 2018 Results. IV. Diffuse Component Separation." In: *Astronomy & Astrophysics* 641 (Sept. 2020), A4. ISSN: 0004-6361, 1432-0746. DOI: 10.1051/0004-6361/201833881. arXiv: 1807.06208 [astro-ph].

[217] A. Gruppuso et al. "Low Variance at Large Scales of WMAP 9 Year Data." In: *Journal of Cosmology and Astroparticle Physics* 2013.07 (July 2013), pp. 047–047. ISSN: 1475-7516. DOI: 10.1088/1475-7516/2013/07/047. arXiv: 1304.5493 [astro-ph].

[218] U. Natale et al. "Is the Lack of Power Anomaly in the CMB Correlated with the Orientation of the Galactic Plane?" In: *Journal of Cosmology and Astroparticle Physics* 2019.12 (Dec. 2019), pp. 052–052. ISSN: 1475-7516. DOI: 10.1088/1475-7516/2019/12/052. arXiv: 1908.10637 [astro-ph].

[219] David Alonso, Javier Sanchez, and Anže Slosar. "A Unified Pseudo-C_ℓ Framework." In: *Monthly Notices of the Royal Astronomical Society* 484.3 (Apr. 2019), pp. 4127–4151. ISSN: 0035-8711, 1365-2966. DOI: 10.1093/mnras/stz093. arXiv: 1809.09603 [astro-ph].

[220] Pau Amaro-Seoane et al. "Laser Interferometer Space Antenna." In: *arXiv e-prints* (2017). arXiv: 1702.00786 [astro-ph.IM].

[221] Enrico Barausse et al. "Prospects for Fundamental Physics with LISA." In: *General Relativity and Gravitation* 52.8 (Aug. 2020). ISSN: 1572-9532. DOI: 10.1007/s10714-020-02691-1. eprint: 2001.09793.

[222] Nicola Bartolo et al. "Science with the Space-Based Interferometer LISA. IV: Probing Inflation with Gravitational Waves." In: *Journal of Cosmology and Astroparticle Physics* 2016.12 (Dec. 2016), pp. 026–026. ISSN: 1475-7516. DOI: 10.1088/1475-7516/2016/12/026. eprint: 1610.06481.

[223] Chiara Caprini et al. "Reconstructing the Spectral Shape of a Stochastic Gravitational Wave Background with LISA." In: *Journal of Cosmology and Astroparticle Physics* 2019.11 (Nov. 2019), pp. 017–017. ISSN: 1475-7516. DOI: 10.1088/1475-7516/2019/11/017. eprint: 1906.09244.

[224] Mauro Pieroni and Enrico Barausse. "Foreground Cleaning and Template-Free Stochastic Background Extraction for LISA." In: *Journal of Cosmology and Astroparticle Physics* 2020.07 (July 2020), pp. 021–021. ISSN: 1475-7516. DOI: 10.1088/1475-7516/2020/07/021. eprint: 2004.01135.

[225] Seiji Kawamura et al. "The Japanese Space Gravitational Wave Antenna - DECIGO." In: *Classical and Quantum Gravity* 23.8 (Mar. 2006), S125–S131. DOI: 10.1088/0264-9381/23/8/s17.

[226] B. Sathyaprakash et al. *Scientific Potential of Einstein Telescope*. 2012. arXiv: 1108.1423 [gr-qc].

[227] Michele Maggiore et al. "Science Case for the Einstein Telescope." In: *Journal of Cosmology and Astroparticle Physics* 2020.03 (Mar. 2020), pp. 050–050. ISSN: 1475-7516. DOI: 10.1088/1475-7516/2020/03/050. eprint: 1912.02622.

[228] B. P. Abbott et al. "Exploring the Sensitivity of next Generation Gravitational Wave Detectors." In: *Classical and Quantum Gravity* 34.4 (Jan. 2017), p. 044001. ISSN: 1361-6382. DOI: 10.1088/1361-6382/aa51f4. arXiv: 1607.08697 [astro-ph.IM].

[229] Giulia Piccirilli et al. *A Cross-Correlation Analysis of CMB Lensing and Radio Galaxy Maps*. Aug. 2022. DOI: 10.48550/arXiv.2208.07774. arXiv: 2208.07774.

[230] David Alonso et al. "Detecting the Anisotropic Astrophysical Gravitational Wave Background in the Presence of Shot Noise through Cross-Correlations." In: *Physical Review D* 102.2 (July 2020), p. 023002. ISSN: 2470-0010, 2470-0029. DOI: 10.1103/PhysRevD.102.023002. arXiv: 2002.02888 [astro-ph, physics:gr-qc, physics:hep-th].

[231] Krzysztof M. Gorski. "On Determining the Spectrum of Primordial Inhomogeneity from the COBE DMR Sky Maps: I. Method." In: *The Astrophysical Journal* 430 (Aug. 1994), p. L85. ISSN: 0004-637X, 1538-4357. DOI: 10.1086/187444. arXiv: astro-ph/9403066.

[232] Daniel J. Mortlock, Anthony D. Challinor, and Michael P. Hobson. "Analysis of Cosmic Microwave Background Data on an Incomplete Sky." In: *Monthly Notices of the Royal Astronomical Society* 330.2 (Feb. 2002), pp. 405–420. ISSN: 00358711, 13652966. DOI: 10.1046/j.1365-8711.2002.05085.x. arXiv: astro-ph/0008083.

[233] Vasyl Alba and Juan Maldacena. "Primordial Gravity Wave Background Anisotropies." In: *Journal of High Energy Physics* 2016.3 (Mar. 2016). ISSN: 1029-8479. DOI: 10.1007/jhep03(2016)115. eprint: 1512.01531.

[234] Max Tegmark. "How to Measure CMB Power Spectra without Losing Information." In: *Physical Review D* 55.10 (May 1997), pp. 5895–5907. ISSN: 0556-2821, 1089-4918. DOI: 10.1103/PhysRevD.55.5895. arXiv: astro-ph/9611174.

[235] S. Vanneste et al. "Quadratic Estimator for CMB Cross-Correlation." In: *Physical Review D* 98.10 (Nov. 2018), p. 103526. ISSN: 2470-0010, 2470-0029. DOI: 10.1103/PhysRevD.98.103526. arXiv: 1807.02484 [astro-ph].

[236] Frode K. Hansen et al. *Cosmic Microwave Background Anomalies Explained: A Strong Impact of Nearby Galaxies on Observed CMB Large Scale Fluctuations*. Apr. 2023. DOI: 10.48550/arXiv.2305.00268. arXiv: 2305.00268 [astro-ph].

[237] M. Hazumi et al. "LiteBIRD: A Satellite for the Studies of B-Mode Polarization and Inflation from Cosmic Background Radiation Detection." In: *Journal of Low Temperature Physics* 194.5-6 (2019), pp. 443–452. DOI: 10.1007/s10909-019-02150-5.

[238] E. Allys et al. "Probing Cosmic Inflation with the LiteBIRD Cosmic Microwave Background Polarization Survey." In: *Progress of Theoretical and Experimental Physics* (Nov. 2022), ptac150. ISSN: 2050-3911. DOI: 10.1093/ptep/ptac150. arXiv: 2202.02773 [astro-ph].

[239] D. S. Sivia and J. Skilling. *Data Analysis - A Bayesian Tutorial*. 2nd ed. Oxford Science Publications. Oxford University Press, 2006.

[240] R. T. Cox. "Probability, Frequency and Reasonable Expectation." In: *American Journal of Physics* 14.1 (Jan. 1946), pp. 1–13. DOI: 10.1119/1.1990764.

[241] Nicholas Metropolis and S. Ulam. "The Monte Carlo Method." In: *Journal of the American Statistical Association* 44.247 (1949), pp. 335–341. ISSN: 01621459.

[242] Roger Eckhardt. "Stan Ulam, John von Neumann, and the Monte Carlo Method." In: *Los Alamos Science* 15 (1987), pp. 131–136.

[243] Dirk P. Kroese et al. "Why the Monte Carlo Method Is so Important Today." In: *WIREs Computational Statistics* 6.6 (2014), pp. 386–392. DOI: 10.1002/wics.1314. eprint: https://wires.onlinelibrary.wiley.com/doi/pdf/10.1002/wics.1314.

[244] Antony Lewis and Sarah Bridle. "Cosmological Parameters from CMB and Other Data: A Monte Carlo Approach." In: *Physical Review* D66 (2002), p. 103511. DOI: 10.1103/PhysRevD.66.103511. arXiv: astro-ph/0205436.

[245] Antony Lewis. "Efficient Sampling of Fast and Slow Cosmological Parameters." In: *Physical Review* D87.10 (2013), p. 103529. DOI: 10.1103/PhysRevD.87.103529. arXiv: 1304.4473 [astro-ph.CO].

[246] Nicholas Metropolis et al. "Equation of State Calculations by Fast Computing Machines." In: *Journal of Cosmology and Astroparticle Physics* 21.6 (June 1953), pp. 1087–1092. DOI: 10.1063/1.1699114.

[247] R. M. Neal. "Taking Bigger Metropolis Steps by Dragging Fast Variables." In: *ArXiv Mathematics e-prints* (Feb. 2005). eprint: math/0502099.

[248] Stuart Geman and Donald Geman. "Stochastic Relaxation, Gibbs Distributions, and the Bayesian Restoration of Images." In: *IEEE Transactions on Pattern Analysis and Machine Intelligence* PAMI-6.6 (1984), pp. 721–741. DOI: 10.1109/TPAMI.1984.4767596.

[249] George Casella and Edward I. George. "Explaining the Gibbs Sampler." In: *The American Statistician* 46.3 (1992), pp. 167–174. ISSN: 0003-1305. DOI: 10.2307/2685208. JSTOR: 2685208.

[250] M. Galloway et al. "BeyondPlanck III. Commander3." In: *Astronomy & Astrophysics* 675 (July 2023), A3. ISSN: 0004-6361, 1432-0746. DOI: 10.1051/0004-6361/202243137. arXiv: 2201.03509 [astro-ph].

[251] Philip Bull et al. "A CMB Gibbs Sampler for Localized Secondary Anisotropies." In: *The Astrophysical Journal Supplement Series* 219.1 (July 2015), p. 10. ISSN: 0067-0049. DOI: 10.1088/0067-0049/219/1/10. arXiv: 1410.2544 [astro-ph.CO].

[252] Simon Duane et al. "Hybrid Monte Carlo." In: *Physics Letters B* 195.2 (1987), pp. 216–222. ISSN: 0370-2693. DOI: 10.1016/0370-2693(87)91197-X.

[253] Amir Hajian. "Efficient Cosmological Parameter Estimation with Hamiltonian Monte Carlo." In: *Physical Review D* 75.8 (2007), p. 083525. ISSN: 1550-7998, 1550-2368. DOI: 10.1103/PhysRevD.75.083525. arXiv: astro-ph/0608679.

[254] Antony Lewis. "GetDist: A Python Package for Analysing Monte Carlo Samples." In: (2019). arXiv: 1910.13970 [astro-ph.IM].

[255] R L Workman et al. "Review of Particle Physics." In: *Progress of Theoretical and Experimental Physics* 2022.8 (Aug. 2022), p. 083C01. DOI: 10.1093/ptep/ptac097.

[256] Adrià Gómez-Valent. "A Fast Test to Assess the Impact of Marginalization in Monte Carlo Analyses, and Its Application to Cosmology." In: *Physical Review D* 106.6 (Sept. 2022), p. 063506. ISSN: 2470-0010, 2470-0029. DOI: 10.1103/PhysRevD.106.063506. arXiv: 2203.16285 [astro-ph].

[257] Andreas Nygaard et al. "Fast and Effortless Computation of Profile Likelihoods Using CONNECT." In: *Journal of Cosmology and Astroparticle Physics* 11.11 (Nov. 2023), p. 064. ISSN: 1475-7516. DOI: 10.1088/1475-7516/2023/11/064. arXiv: 2308.06379 [astro-ph.CO].

[258] Gary J. Feldman and Robert D. Cousins. "A Unified Approach to the Classical Statistical Analysis of Small Signals." In: *Physical Review D* 57.7 (1998), pp. 3873–3889. ISSN: 0556-2821, 1089-4918. DOI: 10.1103/PhysRevD.57.3873. arXiv: physics/9711021.

[259] Giacomo Galloni et al. *Updated Constraints on Amplitude and Tilt of the Tensor Primordial Spectrum*. Nov. 2022. arXiv: 2208.00188. (Visited on 11/24/2022).

[260] Jesus Torrado and Antony Lewis. "Cobaya: Code for Bayesian Analysis of Hierarchical Physical Models." In: (May 2020). arXiv: 2005.05290 [astro-ph.IM].

[261] Antony Lewis, Anthony Challinor, and Anthony Lasenby. "Efficient Computation of Cosmic Microwave Background Anisotropies in Closed Friedmann-Robertson-Walker Models." In: *The Astrophysical Journal* 538.2 (Aug. 2000), pp. 473–476. DOI: 10.1086/309179. eprint: astro-ph/9911177.

[262] Cullan Howlett et al. "CMB Power Spectrum Parameter Degeneracies in the Era of Precision Cosmology." In: *Journal of Cosmology and Astroparticle Physics* 2012.04 (Apr. 2012), pp. 027–027. DOI: 10.1088/1475-7516/2012/04/027. eprint: 1201.3654.

[263] M. Tristram et al. "Improved Limits on the Tensor-to-Scalar Ratio Using BICEP and Planck Data." In: *Physical Review D: Particles and Fields* 105.8 (2022), p. 083524. DOI: 10.1103/PhysRevD.105.083524. arXiv: 2112.07961 [astro-ph.CO].

[264] F. Couchot et al. "Relieving Tensions Related to the Lensing of the Cosmic Microwave Background Temperature Power Spectra." In: *Astronomy & Astrophysics* 597 (Jan. 2017), A126. DOI: 10.1051/0004-6361/201527740. eprint: 1510.07600.

[265] F. Couchot et al. "Cosmology with the CMB Temperature-Polarization Correlation." In: *Astronomy & Astrophysics* 602 (June 2017), A41. ISSN: 0004-6361, 1432-0746. DOI: 10.1051/0004-6361/201629815. arXiv: 1609.09730 [astro-ph].

[266] Paolo Campeti and Eiichiro Komatsu. "New Constraint on the Tensor-to-Scalar Ratio from the Planck and BICEP/Keck Array Data Using the Profile Likelihood." In: (May 2022). arXiv: 2205.05617 [astro-ph.CO].

[267] Giovanni Cabass et al. "Updated Constraints and Forecasts on Primordial Tensor Modes." In: *Physical Review D* 93.6 (Mar. 2016). ISSN: 2470-0029. DOI: 10.1103/physrevd.93.063508. eprint: 1511.05146.

[268] P. A. R. Ade et al. "Planck 2015 Results XX: Constraints on Inflation." In: *Astronomy & Astrophysics* 594 (Sept. 2016), A20. DOI: 10.1051/0004-6361/201525898. eprint: 1502.02114.

[269] Martina Gerbino et al. "Likelihood Methods for CMB Experiments." In: *Frontiers in Physics* 8 (Feb. 2020), p. 15. ISSN: 2296-424X. DOI: 10.3389/fphy.2020.00015. arXiv: 1909.09375 [astro-ph].

[270] N. Aghanim et al. "Planck 2018 Results. V. CMB Power Spectra and Likelihoods." In: *Astronomy and Astrophysics* 641 (2020), A5. DOI: 10.1051/0004-6361/201936386. arXiv: 1907.12875 [astro-ph.CO].

[271] P. A. R. Ade et al. "Detection of B-Mode Polarization at Degree Angular Scales by BICEP2." In: *Physical Review Letters* 112.24 (June 2014). ISSN: 1079-7114. DOI: 10.1103/physrevlett.112.241101. eprint: 1403.3985.

[272] N. Aghanim et al. "Planck 2018 Results VIII Gravitational Lensing." In: *Astronomy & Astrophysics* 641 (Sept. 2020), A8. DOI: 10.1051/0004-6361/201833886. arXiv: 1807.06210 [astro-ph.CO].

[273] A. Mangilli, S. Plaszczynski, and M. Tristram. "Large-Scale CMB Temperature and Polarization Cross-Spectra Likelihoods." In: *Monthly Notices of the Royal Astronomical Society* 453.3 (Nov. 2015), pp. 3175–3190. ISSN: 0035-8711, 1365-2966. DOI: 10.1093/mnras/stv1733. arXiv: 1503.01347 [astro-ph].

[274] Sachiko Kuroyanagi and Tomo Takahashi. "Higher Order Corrections to the Primordial Gravitational Wave Spectrum and Its Impact on Parameter Estimates for Inflation." In: *Journal of Cosmology and Astroparticle Physics* 2011.10 (Oct. 2011), pp. 006–006. DOI: 10.1088/1475-7516/2011/10/006. eprint: 1106.3437.

[275] William Giarè, Fabrizio Renzi, and Alessandro Melchiorri. "Higher-Curvature Corrections and Tensor Modes." In: *Physical Review D* 103.4 (Feb. 2021). DOI: 10.1103/physrevd.103.043515. eprint: 2012.00527.

[276] William Giarè and Alessandro Melchiorri. "Probing the Inflationary Background of Gravitational Waves from Large to Small Scales." In: *Physics Letters B* 815 (Apr. 2021), p. 136137. DOI: 10.1016/j.physletb.2021.136137. eprint: 2003.04783.

[277] R. Abbott et al. "Upper Limits on the Isotropic Gravitational-Wave Background from Advanced LIGO and Advanced Virgo's Third Observing Run." In: *Physical Review D* 104.2 (July 2021). ISSN: 2470-0029. DOI: 10.1103/physrevd.104.022004. eprint: 2101.12130.

[278] Michele Maggiore. "Gravitational Wave Experiments and Early Universe Cosmology." In: *Physics Reports* 331.6 (2000), pp. 283–367. ISSN: 0370-1573. DOI: 10.1016/S0370-1573(99)00102-7. eprint: gr-qc/9909001.

[279] Shadab Alam et al. "Completed SDSS-IV Extended Baryon Oscillation Spectroscopic Survey: Cosmological Implications from Two Decades of Spectroscopic Surveys at the Apache Point Observatory." In: *Physical Review D* 103.8 (Apr. 2021). DOI: 10.1103/physrevd.103.083533.

[280] Andrew Gelman and Donald B. Rubin. "Inference from Iterative Simulation Using Multiple Sequences." In: *Statistical Science* 7.4 (Nov. 1992), pp. 457–472. ISSN: 0883-4237, 2168-8745. DOI: 10.1214/ss/1177011136.

[281] Masahiro Kawasaki and Hiromasa Nakatsuka. "Gravitational Waves from Type II Axion-like Curvaton Model and Its Implication for NANOGrav Result." In: *Journal of Cosmology and Astroparticle Physics* 2021.05 (May 2021), p. 023. ISSN: 1475-7516. DOI: 10.1088/1475-7516/2021/05/023. arXiv: 2101.11244 [astro-ph, physics:hep-ph].

[282] Tomohiro Fujita, Kaname Imagawa, and Kai Murai. "Gravitational Waves Detectable in Laser Interferometers from Axion-SU(2) Inflation." In: (2022). DOI: 10.48550/ARXIV.2203.15273. eprint: 2203.15273.

[283] Micol Benetti, Leila Lobato Graef, and Sunny Vagnozzi. "Primordial Gravitational Waves from NANOGrav: A Broken Power-Law Approach." In: *Physical Review D* 105.4 (Feb. 2022), p. 043520. ISSN: 2470-0010, 2470-0029. DOI: 10.1103/PhysRevD.105.043520. arXiv: 2111.04758 [astro-ph, physics:gr-qc, physics:hep-ph, physics:hep-th].

[284] Paolo Campeti et al. "Measuring the Spectrum of Primordial Gravitational Waves with CMB, PTA and Laser Interferometers." In: *Journal of Cosmology and Astroparticle Physics* 2021.01 (Jan. 2021), pp. 012–012. ISSN: 1475-7516. DOI: 10.1088/1475-7516/2021/01/012. arXiv: 2007.04241 [astro-ph, physics:gr-qc].

[285] Sunny Vagnozzi. "Implications of the NANOGrav Results for Inflation." In: *Monthly Notices of the Royal Astronomical Society: Letters* 502.1 (Dec. 2020), pp. L11–L15. DOI: 10.1093/mnrasl/slaa203. eprint: 2009.13432.

[286] Sachiko Kuroyanagi, Tomo Takahashi, and Shuichiro Yokoyama. "Blue-Tilted Inflationary Tensor Spectrum and Reheating in the Light of NANOGrav Results." In: *Journal of Cosmology and Astroparticle Physics* 2021.01 (Jan. 2021), pp. 071–071. ISSN: 1475-7516. DOI: 10.1088/1475-7516/2021/01/071. arXiv: 2011.03323 [astro-ph, physics:gr-qc, physics:hep-ph].

[287] John Ellis and Marek Lewicki. "Cosmic String Interpretation of NANOGrav Pulsar Timing Data." In: *Physical Review Letters* 126.4 (Jan. 2021). DOI: 10.1103/physrevlett.126.041304. eprint: 2009.06555.

[288] Amjad Ashoorioon, Kazem Rezazadeh, and Abasalt Rostami. *NANOGrav Signal from the End of Inflation and the LIGO Mass and Heavier Primordial Black Holes*. 2022. DOI: 10.48550/ARXIV.2202.01131. eprint: 2202.01131.

[289] Ligong Bian et al. "Evidence for Different Gravitational-Wave Sources in the NANOGrav Dataset." In: *Physical Review D* 103.8 (Apr. 2021). DOI: 10.1103/physrevd.103.l081301. eprint: 2009.13893.

[290] E. Allys et al. "Probing Cosmic Inflation with the LiteBIRD Cosmic Microwave Background Polarization Survey." In: (2022). DOI: 10.48550/ARXIV.2202.02773. eprint: 2202.02773.

[291] Y. Akrami et al. "*Planck* Intermediate Results: LVII. Joint *Planck* LFI and HFI Data Processing." In: *Astronomy & Astrophysics* 643 (Nov. 2020), A42. ISSN: 0004-6361, 1432-0746. DOI: 10.1051/0004-6361/202038073.

[292] Erik Rosenberg, Steven Gratton, and George Efstathiou. "CMB Power Spectra and Cosmological Parameters from Planck PR4 with CamSpec." In: *Monthly Notices of the Royal Astronomical Society* 517.3 (Nov. 2022), pp. 4620–4636. ISSN: 0035-8711, 1365-2966. DOI: 10.1093/mnras/stac2744. arXiv: 2205.10869 [astro-ph].

[293] Samira Hamimeche and Antony Lewis. "Likelihood Analysis of CMB Temperature and Polarization Power Spectra." In: *Physical Review D* 77.10 (May 2008), p. 103013. ISSN: 1550-7998, 1550-2368. DOI: 10.1103/PhysRevD.77.103013. arXiv: 0801.0554 [astro-ph].

[294] Julien Carron, Mark Mirmelstein, and Antony Lewis. "CMB Lensing from Planck PR4 Maps." In: *Journal of Cosmology and Astroparticle Physics* 09.09 (Sept. 2022), p. 039. ISSN: 1475-7516. DOI: 10.1088/1475-7516/2022/09/039. arXiv: 2206.07773 [astro-ph.CO].

[295] F. James and M. Roos. "Minuit: A System for Function Minimization and Analysis of the Parameter Errors and Correlations." In: *Comput. Phys. Commun.* 10 (1975), pp. 343–367. DOI: 10.1016/0010-4655(75)90039-9.

[296] Coralia Cartis et al. "Improving the Flexibility and Robustness of Model-Based Derivative-Free Optimization Solvers." In: (May 2018). DOI: 10.48550/arXiv.1804.00154. arXiv: 1804.00154 [math.OC].

[297] Pauli Virtanen et al. "SciPy 1.0: Fundamental Algorithms for Scientific Computing in Python." In: *Nature Methods* 17.3 (Mar. 2020), pp. 261–272. ISSN: 1548-7105. DOI: 10.1038/s41592-019-0686-2. eprint: 1907.10121.

[298] P. A. R. Ade et al. "Planck Intermediate Results. XVI. Profile Likelihoods for Cosmological Parameters." In: *Astronomy & Astrophysics* 566 (June 2014), A54. ISSN: 0004-6361, 1432-0746. DOI: 10.1051/0004-6361/201323003. arXiv: 1311.1657 [astro-ph].

[299] Robert D. Cousins. "Why Isn't Every Physicist a Bayesian?" In: *American Journal of Physics* 63.5 (1995), p. 398. ISSN: 0002-9505. DOI: 10.1119/1.17901.

[300] Maresuke Shiraishi. *Probing the Early Universe with the CMB Scalar, Vector and Tensor Bispectrum*. Springer Theses. Springer, 2013. ISBN: 978-4-431-54179-0. DOI: 10.1007/978-4-431-54180-6. arXiv: 1210.2518 [astro-ph.CO].

[301] R. Adam et al. "Planck Intermediate Results. XLVII. Planck Constraints on Reionization History." In: *Astronomy & Astrophysics* 596 (Dec. 2016), A108. ISSN: 0004-6361, 1432-0746. DOI: 10.1051/0004-6361/201628897. arXiv: 1605.03507 [astro-ph].